HAL
open science

Thermal Barrier Effect, Non-Fourier Effect and Inertia Effect on a Cracked Plate under Thermal Shock Loading

Wei Li

To cite this version:

Wei Li. Thermal Barrier Effect, Non-Fourier Effect and Inertia Effect on a Cracked Plate under Thermal Shock Loading. Other. Université Sorbonne Paris Cité, 2016. English. NNT : 2016USPCD089 . tel-02165931

HAL Id: tel-02165931

https://theses.hal.science/tel-02165931

Submitted on 26 Jun 2019

HAL is a multi-disciplinary open access archive for the deposit and dissemination of scientific research documents, whether they are published or not. The documents may come from teaching and research institutions in France or abroad, or from public or private research centers.

L'archive ouverte pluridisciplinaire **HAL**, est destinée au dépôt et à la diffusion de documents scientifiques de niveau recherche, publiés ou non, émanant des établissements d'enseignement et de recherche français ou étrangers, des laboratoires publics ou privés.

UNIVERSITE PARIS 13 SORBONNE PARIS CITE
N° attribué par la bibliothèque
|_|_|_|_|_|_|_|_|_|_|

THÈSE
pour obtenir le grade de

DOCTEUR DE L'UNIVERSITE PARIS 13 SORBONNE PARIS CITE

Spécialité : Mécanique des Matériaux

Préparée au **Laboratoire des Sciences et des Procédés des Matériaux**

Dans le cadre de l'**Ecole Doctorale Galilee**

par

Wei LI

Thermal Barrier Effect, Non-Fourier Effect and Inertia Effect on a Cracked Plate under Thermal Shock Loading

Composition du jury

M.	Sami El Borgi	Professeur	Rapporteur
M.	Yuri Lapusta	Professeur	Rapporteur
M.	Ioan Ionescu	Professeur	Examinateur
M.	Naman Recho	Professeur	Examinateur
M.	Oueslati Abdelbacet	Maitre de Conférences	Examinateur
M.	Jia LI	Professeur	Directeur de thèse
M.	Radhi Abdelmoula	Maitre de Conférences	Co-encadrant

Acknowledgements

I would like to express my deepest gratitude to my supervisor, professor Jia LI, whose encouragement and support from the initial to the final level enabled me to complete the subject. His professional guidance helped me in all the time of research and writing of this thesis. Thanks to my co-supervisor, Dr. Radhi ABDELMOULA, who helped me a lot in the numerical method and gave me a lot useful articles to reference.

My sincere thanks also goes my supervisor in China, Prof. Song Fan. He helped me to lay a good theoretical foundation, which is very important in my present work.

Besides my advisor, I would like to thank the rest of my thesis committee: Prof. Sami El Borgi, Prof. Yuri Lapusta, Prof. Ioan Ionescu, Prof. Naman Recho and Dr. Oueslati Abdelbacet, for their insightful comments and valuable suggestions.

Thanks to all in LSPM who have helped me during my PhD.

Last but not the least, I would like to thank my family: my parent Li Zhao-Yong and Zhang Lin-Xia, my sister Li Ying, whom have been supporting and encouraging me unconditionally throughout my life. Thanks to my wife Xia Xue, she took good care of the two families during the 3 years of my study and gave me a lot of encourage and support.

Paris

December, 2015

LI Wei

Résumé

Les chocs thermiques provoquent, en général, l'endommagement et la fissuration des matériaux. Ces phénomènes sont observés, par exemple, dans le revêtement de barrière thermique pour les moteurs des turbines, le traitement des surfaces ou la soudure par laser etc. Plusieurs travaux de recherche ont été réalisés au cours des dernières décennies dans l'objectif d'améliorer les performances thermiques et/ou mécaniques des matériaux sous chargement thermique. L'étude des dommages et de la fissuration des matériaux provoqués par les chocs thermiques, tels que le décollement des interfaces et de décohésion de revêtements, a reçu également une attention considérable par les chercheurs. La majorité de ces travaux utilisent les théories classiques, tels que la loi de Fourier de conduction thermique et l'hypothèse de quasi-statique. Malheureusement ces théories ne sont pas adaptées dans le cas de charges extrêmes provoqués par le choc thermique et dans le cas des matériaux micro-fissurés. En conséquence, les théories conventionnelles doivent être enrichies.

L'objectif de la thèse est de montrer le rôle crucial des termes non Fourier et les termes inertiels dans le cas de choc thermique sous conditions sévères et dans le cas où les fissures sont petites. Pour cela nous avons mené des études sur deux structures particulières soumises à des chocs thermiques. Chaque structure contient une fissure parallèle au bord libre de la structure située au voisinage de ce dernier. L'influence de la présence de fissure sur la conductivité thermique est prise en compte. Nous avons utilisé la théorie Hyperbolique de transfert de chaleur par conduction pour les champs thermique et mécanique à la place de la théorie traditionnelle classique de Fourier. Pour mener cette étude, nous avons utilisé les Transformées de Laplace et de Fourier aux équations de mouvement et à l'équation de transfert de chaleur. En s'intéressant en particulier aux champs de contrainte au voisinage de la pointe de fissure et aux facteurs d'intensité de contrainte dynamiques. Le problème se ramène à la résolution d'un système d'équations intégrales singulières dans l'espace de Laplace-Fourier. On utilise une méthode d'intégration numérique pour obtenir les différents champs. Nous résolvons ensuite un système d'équations algébriques linéaires. En effectuant des inversions numériques des transformées, nous obtenons les champs de contrainte de température et les facteurs d'intensité de contrainte dynamiques dans le domaine temporel.

Les résultats numériques montrent que la conductivité thermique du milieu est affectée par l'ouverture de la fissure ce qui perturberait fortement le champ de température ainsi que l'amplitude des facteurs d'intensité de contrainte dynamiques. Les amplitudes sont supérieures à celles obtenues à partir de la théorie classique de Fourier ainsi que dans le cadre de l'hypothèse quasi-statique. On constate également qu'elles oscillent au cours du temps. La prise en compte simultanément de l'influence de la fissure sur la conductivité thermique, de l'effet non-Fourier ainsi que les effets

d'inertie induit un couplage entre les trois phénomènes qui rendrait le problème de choc thermique très complexe. L'effet de barrière thermique induit par la fissure affecte d'une manière significative les champs de température et des contraintes. Les effets d'inertie, et des termes non-Fourier joueraient également un rôle non négligeable lorsque la longueur de la fissure est petite. Comme dans de nombreux problèmes d'ingénierie, l'initiation et la propagation des micro-fissures sont des mécanismes dont il faut tenir compte dans les prévisions de la rupture des structures. Ces effets non conventionnels ne sont plus négligeables et doivent être inclus dans l'analyse de la fracture des structures soumises à des chocs thermiques.

Mots Clés : Transformée de Laplace; Transformée de Fourier; Conduction thermique hyperbolique; Effet inertiel; Nombre de Biot; Équations intégrales singulières; Facteurs d'intensité de contrainte dynamiques

Abstract

Thermal shock problems occur in many engineering materials and elements, which are used in high temperature applications such as thermal barrier coatings (TBCs), solid propellant of rocket-engine, pulsed-laser processing of materials, and so on. The thermal shock resistance performance~~s~~ and the thermal shock damage~~s~~ of materials, especially the interface debonding and spallation of coatings, have received considerable attention in both analysis and design. Some conventional theories, such as the Fourier's law of thermal conduction and the quasi-static assumption of the thermoelastic body, may no longer be appropriate because of the extreme loads provoked by the thermal shock. Therefore, these conventional theories need to be enriched or revised.

The objective of this thesis is to develop the solutions of the transient temperature field and thermal stresses around a partially insulated crack in a thermoelastic strip under thermal shock loading. The crack lies parallel to the heated traction free surface. The thermal conductivity of the crack gap is taken into account. Hyperbolic heat conduction theory is used in solving the temperature field instead of the traditional Fourier thermal conduction theory. Equations of motion are applied to obtain the stress fields and the dynamic stress intensity factors of the crack. The Laplace and Fourier transforms are applied to solve the thermal-elastic governing equations such that the mixed boundary value problems are reduced to solving a singular integral equations system in Laplace-Fourier space. The numerical integration method is applied to get the temperature field and stress fields, respectively. The problems are then solved numerically by converting the singular integral equations to a linear algebraic equations system. Finally, numerical inversions of the Laplace transform are performed to obtain the temperature field and dynamic stress intensity factors in the time domain.

Numerical results show that the thermal conductivity of the crack gap strongly affects the uniformity of the temperature field and consequently, the magnitude of the dynamic stress intensity factors of the crack. The stress intensity factors would have higher amplitude and oscillating feature comparing to those obtained under the conventional Fourier thermal conduction and quasi-static hypotheses. It is also observed that the interactions of the thermal conductivity of the crack gap, the non-Fourier effect and the inertia effects would make the dynamic thermal shock problem more complex. The magnitude of the thermal barrier, non-Fourier and inertia effects is estimated for some practical cases.

Keywords: Thermal Shock; Laplace Transform; Fourier Transform; Hyperbolic Thermal Conduction; Inertia Effect; Biot Number; Singular Integral Equations; Stress Intensity Factors.

Table of Contents

Acknowledgements I

Résumé III

Abstract V

Table of Contents VI

List of Figures X

List of Tables XIV

Nomenclature XV

Letters XV

Greek letters XVII

Symbols XVIII

Acronyms XVIII

Chapter 1 Introduction 1

1.1 Thermal Shock Induced Cracks 1

1.2 Backgrounds 2

1.3 Study Method 6

1.3.1 Boundary Conditions 7

1.3.2 Thermal Conduction Theory 8

1.3.3 Dynamic Thermal Stress Equations 10

1.4 Overview 11

Chapter 2 Temperature Field Analysis 13

2.1 Introduction 13

2.1.1 Main Results 13

2.1.2 Statement of the Thermal Shock Problem 13

2.2 Formulations of the Heat Conduction Problem 15

2.2.1 Fourier's law – Parabolic Heat Conduction 15

2.2.2 Hyperbolic Heat Conduction 15

2.2.3 Boundary Conditions and Initial Conditions.....16

2.3 Analytical Procedure of Temperature Fields.....17

2.3.1 Nondimensionalization of Variables.....20

2.3.2 Integral Transforms.....22

2.3.3 General Solution of ODE.....23

2.4 Derivation of the Singular Integral Equation 25

2.5 Solution of the Singular Integral Equation 27

2.5.1 Fundamental Function of the Singular Integral Equation 27

2.5.2 Cauchy Integral.....28

2.5.3 Numerical Integration 30

2.6 Convergence Analysis 31

2.6.1 Numerical Integration Interval 31

2.6.2 Number of Gauss Points.....33

2.7 Numerical Inversion of the Laplace Transform 35

Chapter 3 Numerical Results on Temperature Field 39

3.1 Biot Number's Effects 39

3.1.1 Full Temperature Fields 40

3.1.2 Temperatures at the Mid-Points of the Crack Surfaces.....43

3.1.3 Temperatures at the Line $x = 0$ 46

3.1.4 Temperature at the Line $y = 0$.....48

3.2 Non-Fourier Effect.....49

3.2.1 Full Temperature Field.....51

3.2.2 Temperatures at the Mid-Points of the Crack Surfaces.....53

3.2.3 Temperatures at the Line $x = 0$ 55

3.2.4 Temperatures at the Line $y = 0$ 58

3.3 Interaction between the Biot Number and the NFF.....59

3.4 Summary 62

Chapter 4 Stress Field Analysis 65

4.1 Introduction 65

4.2 Formulation of the Crack Problem.....65

4.2.1 Basic Equations and Boundary Conditions.....65

4.2.2 Boundary Initial Conditions.....68

4.3 Analytical Resolution Procedure of the Stress Fields.....69

4.3.1 Nondimensionalization of Variables.....71

4.3.2 Integral Transforms.....72

4.3.3 General Solutions of the ODEs 74

4.4 Singular Integral Equations.....80

4.4.1 Derivation of the System of Integral Equations.....80

4.4.2 Solution of the Singular Integral Equations.....83

4.4.3 Stress Intensity Factors.....85

4.4.4 Crack Opening Displacements.....87

4.5 Convergence Analysis 90

4.6 Inverse Laplace Transform.....91

Chapter 5 Numerical Results on Stress Fields 93

5.1 Biot Number's Effect 93

5.1.1 Stress Intensity Factors.....94

5.1.2 Crack Opening Displacements.....96

5.2 Non-Fourier Effect.....101

5.2.1 Stress Intensity Factors.....101

5.2.2 Crack Opening Displacements.....103

5.3 Inertia Effect 107

5.3.1 Stress Intensity Factors.....107

5.3.2 Crack Opening Displacements.....110

5.4 Interaction among Bi, NFF and IF.....113

5.5 Heating Thermal Shock and Cooling Thermal Shock.....118

Chapter 6 Inner crack in a half plane 120

6.1 General consideration **120**

6.2 Influence of I_a **121**

6.3 Verification and Comparison of the Results **126**

Chapter 7 Conclusions and Future Works **129**

7.1 Conclusions **129**

7.2 Magnitude Estimation of Bi, Non-Fourier Factor and Inertia Factor **130**

7.2.1 The Biot Number 130

7.2.2 Non-Fourier Factor 132

7.2.3 Inertia Factor 133

7.3 Future Works **134**

References **137**

List of Figures

Figure 1.1-1 Heat thermal shock example and stresses 1

Figure 1.1-2 Cold thermal shock example and stresses 2

Figure 1.2-1 Anatomy of an electron-beam physical-vapor deposited (EB-PVD) TBC... 3

Figure 1.2-2 Cross-sectional SEM of a failed APS TBC 4

Figure 1.2-3 Thermal shock crack patterns on the interior surfaces of the stacked plate. 5

Figure 1.2-4 Transverse cracks observed at the cross section of the TiN coating following laser ablation 6

Figure 1.3-1 Large-scale buckling and crack morphology of EB-PDV. 7

Figure 2.1-1 Geometry of the cracked strip and the coordinate system 14

Figure 2.1-2 Boundary Conditions. 14

Figure 2.3-1 Solving procedure of the temperature field. 19

Figure 2.6-1 Temperature in Laplace space at the mid-point of the crack surfaces versus the number of Gauss points for Bi=0, τ_1=0.1, p=1 35

Figure 2.7-1 Appriximations for Equation (2-98) 37

Figure 3.1-1 Temperature fields in near crack domain for $t^*=\infty$ and NFF =0. (*a*): Bi = 0; (b): Bi = 0.2; (*c*): Bi = 1; (*d*): Bi = ∞. 41

Figure 3.1-2 Temperature field in near crack domain for Bi=0 and NFF =0 at (a): t^* = 0; (b): t^* = 0.2; (c): t^* = 1; (d): t^* = ∞ 42

Figure 3.1-3 Coordinate domain. $-2 \leq x \leq 2$ and $-1 \leq y \leq 2$. 42

Figure 3.1-4 Dimensionless temperatures at the mid-points of the crack surfaces versus dimensionless time for different Biot numbers. 44

Figure 3.1-5 Dimensionless temperature differences of the mid-points of the crack surfaces versus dimensionless time for different Biot numbers. 44

Figure 3.1-6 Dimensionless temperatures at the mid-points of the crack surfaces versus the Biot number for different dimensionless times. 46

Figure 3.1-7 Dimensionless temperatures along the line x = 0 for different Biot numbers when $t^* \rightarrow \infty$. 47

Figure 3.1-8 Dimensionless temperatures along the line x = 0 at different times when Bi = 0. 47

Figure 3.1-9 Temperatures along y = 0 for different Biot numbers when $t^* \to \infty$. 48
Figure 3.1-10 Temperatures along y = 0 at different dimensionless times for Bi = 0. ..49
Figure 3.2-1 Temperature fields for -2 < x < 2 and -1 < y < 2 when dimensionless time is 1 and Biot number is set to be 0. (a): τ_1 = 0; (b): τ_1 = 0.2; (c): τ_1 = 0.4; (d): τ_1 = 0.6. 52
Figure 3.2-2 Temperature field in the domain -2 < x < 2 and -1 < y < 2. The Biot number and τ_1 are set to be 0 and 0.4, respectively. (a): t^* = 0.2; (b): t^* = 1.4; (c): t^* = 3.5; (d): t^* = 5.3. 53
Figure 3.2-3 Dimensionless temperatures at the mid-points of the crack surfaces versus dimensionless time for different τ_1. 55
Figure 3.2-4 Dimensionless temperature differences between the mid-points of the crack surfaces versus dimensionless time for different τ_1. 55
Figure 3.2-5 Dimensionless temperatures along the line x=0 for different τ_1 when t^* = 1 and Bi = 0. 57
Figure 3.2-6 Dimensionless temperatures along the line x = 0 for different times when τ_1 = 0.5 and Bi = 0. 57
Figure 3.2-7 Temperatures along the line y=0 for different τ_1 when t^* = 1 58
Figure 3.2-8 Temperatures along the line y=0 for different dimensionless times when Bi = 0 and τ_1 = 0.7 59
Figure 3.3-1 Maximal and minimal temperatures at the point (0, 0^-) versus τ_1 for different Biot numbers. 61
Figure 3.3-2 Temperature differences between the midpoints of the crack surfaces versus τ_1 for different Biot number. 62
Figure 4.3-1 Solving procedure of the Stress fields. 70
Figure 4.4-1 Comparison of $F1$ and the Fitting functions. 89
Figure 4.4-2 Comparison of $F2$ and the Fitting functions. 90
Figure 5.1-1 Dimensionless stress intensity factors versus dimensionless time for different Biot numbers when $\tau_1 = \tau_2 = 0$. 94
Figure 5.1-2 Dimensionless stress intensity factors (a): K_I (b): K_{II} versus Biot number at different dimensionless times when $\tau_1 = \tau_2 = 0$. 95
Figure 5.1-3 Crack Opening Displacement for different Biot numbers and at different

dimensionless times when $\tau_1 = \tau_2 = 0$.....97
Figure 5.1-4 Maximum COD(u) for different Biot numbers 98
Figure 5.1-5 Crack Opening Displacements COD(v) for different Biot numbers and at different dimensionless times when $\tau_1 = \tau_2 = 0$.....99
Figure 5.1-6 Maximum COD(v) for different Biot numbers 99
Figure 5.1-7 The dimensionless time when TDM, K_I, K_{II}, COD(v) and COD(u) reach the peak value versus Biot number. 101
Figure 5.2-1 Normalized stress intensity factors (a) K_I and (b) K_{II} versus dimensionless time for different τ_1 when Bi = τ_2 = 0. 102
Figure 5.2-2 Crack Opening Displacement (u_2 - u_1) for different values of τ_1 when Bi = τ_2 = 0 at (a) t^* = 0.5, (b) t^* = 1.1, (c) t^* = 2 and (d) t^* = ∞ respectively 104
Figure 5.2-3 Maximum COD(u) for different values of τ_1 when Bi = τ_2 = 0. 105
Figure 5.2-4 Crack Opening Displacement (v_2 - v_1) for different values of τ_1 when Bi = τ_2 = 0 and t^* = 0.5, 1.1, 2 and infinity. 105
Figure 5.2-5 Maximum COD(v) for different values of τ_1 106
Figure 5.2-6 The dimensionless time when TDM, K_I, K_{II}, COD(v) and COD(u) reach the peak value versus τ_1 when Bi = τ_2 = 0. 107
Figure 5.3-1 Normalized stress intensity factors (a) for K_I and (b) for K_{II} versus dimensionless time for different τ_2 when Bi = τ_1 = 0. 109
Figure 5.3-2 Crack Opening Displacement (u_2 - u_1) for different τ_2 when Bi = τ_1 = 0 and t^* = 0.2, 1.1, 2 and ∞. 110
Figure 5.3-3 Crack Opening Displacement (v_2 - v_1) for different τ_1 when Bi = τ_1 = 0 and t^* = ∞. 111
Figure 5.3-4 Maximum COD(u) for different τ_2 112
Figure 5.3-5 Maximum COD(v) for different τ_2 112
Figure 5.4-1 Maximum K_I versus inertia factor for different τ_1 when Bi = 0 113
Figure 5.4-2 Maximum K_I versus inertia factor for different τ_1 when Bi = 0.2 114
Figure 5.4-3 Maximum K_I versus inertia factor for different τ_1 when Bi = 2 114
Figure 5.4-4 Maximum K_I versus inertia factor for different τ_1 when Bi = ∞ 115
Figure 5.4-5 Minimum K_{II} versus inertia factor for different non-Fourier factors when Bi = 0.....116
Figure 5.4-6 Minimum K_{II} versus inertia factor for different non-Fourier factors when

Bi = 0.2 116
Figure 5.4-7 Minimum K_{II} versus inertia factor for different non-Fourier factors when Bi = 2 117
Figure 5.4-8 Minimum K_{II} versus inertia factor for different non-Fourier factors when Bi → ∞ 117
Figure 5.5-1 Variation of peak-values of K_I^* versus τ_2 for different τ_1 (*a*) when $T_\infty - T_0 > 0$ (heating) and (*b*) when $T_\infty - T_0 < 0$ (cooling) 119
Figure 6.1-1 Geometry of the cracked half infinite plate and the coordinate system. 120
Figure 6.2-1 Variation of maximum K_I and K_{II} versus l_a for different τ_1 when Bi = 0 and τ_2 = 0.2. 123
Figure 6.2-2 Maximum CODs for different l_a when τ_1 = 0 and τ_2=0.2. 124
Figure 6.2-3 Variation of maximal normalized COD versus l_a for different τ_1 when Bi = 0 and τ_2=0.2. Max COD(*v*) is measured at the midpoints of the crack; Max COD(*u*) is measured at the points of the crack where COD(*u*) is maximal. 125
Figure 6.3-1 Temperature field of the mid-points of the crack surfaces obtained by different model. 127
Figure 6.3-2 Stress intensity factors obtained by different model. 127

List of Tables

Table 2.6-1 Numerical approximations, absolute and relative errors for different parameters when *p* and *M* are set to be 1 and 40, respectively. 33

Table 3.1-1 Maximal temperature differences at the mid-points of the crack surfaces and its corresponding dimensionless time for different Biot numbers 45

Table 3.2-1 Heat wave velocity and the dimensionless time when the wave front reaches to the crack surface for different τ_1. 50

Table 3.2-2 Periods of the heat wave propagation 51

Table 3.2-3 Maximal temperature differences at the mid-points of the crack surfaces and its corresponding dimensionless time for different τ_1. 54

Table 3.2-4 The maximum and minimum temperatures at the point $0,0-$ for different τ_1. 56

Table 3.3-1 Dimensionless times used for the temperature at $0,0-$ to reach the maximum value 60

Table 4.2-1 Relations among elastic constants. 67

Table 4.2-2 Elastic Moduli conversion between plane stress and plane strain for thermoelastic problems. 68

Table 4.4-1 Geometrical and materials parameters used in the pilot case. 88

Table 4.4-2 Discrete data for $F1$ and $F2$. 88

Table 4.5-1 Selected upper limit and the precisions for each integral 90

Table 7.2-1 Interface contact conductance for representative interfaces 131

Table 7.2-2 Element properties and its corresponding τ_2' 134

Nomenclature

Letters

a	thermal diffusivity
$\mathbf{A}$	matrix defined in Eq. (4-47)
Bi	Biot's number
B_i	function defined in Eq. (4-36)
C_p	specific heat capacity
$C_{D,\,i}$	coefficients used in the process of solving the displacement field
$C_{L,\,i}$	coefficients used in the inversion of the Laplace transform
$C_{T,\,i}$	coefficients used in the process of solving the temperature field
e	mathematical constant
E	Young's modulus
f_i	dislocation function
$g(\zeta)$	function defined in Eq. (2-90)
$g_1(x)$	function defined in Eq. (2-52)
$G(x)$	function defined in Eq. (2-55)
h	heat transfer coefficient
$H(x)$	Heaviside's step function
i	imaginary unit
i, j	subscripts
k	thermal conductivity
$k()$	function defined in Eq. (2-51)
$K_{i,j}$	function defined in Eq. (4-56)
l_a, l_b	distances between the crack and the boundaries

m	variable defined in Eq. (2-26)
m_0	variable defined in Eq. (2-41)
p	Laplace variable
$P_n^{(\alpha,\beta)}$	Jacobi's Polynomials
$\vec{\boldsymbol{q}}$	heat flux vector
r	crack length
t	time
T	temperature
T_0	initial temperature
T_∞	environment temperature of the strip
u, v	displacements
$\bar{u}, \bar{v}$	displacements in Laplace space
$\tilde{\bar{u}}, \tilde{\bar{v}}$	displacements in Laplace-Fourier space
V	Elastic wave velocity
$w(x)$	function defined in Eq. (2-60)
x, y	Cartesian coordinates
$Y(x)$	function defined in Eq. (2-68)

Greek letters

α	coefficient of linear thermal expansion
β	coefficient used in inversion of the Laplace transform
β_i	function defined in Eq. (4-27)
γ	function defined in Eq. (4-49)
δ	coefficient used in inversion of the Laplace transform
$\delta()$	Dirac delta function
ε_x, ε_y, ε_{xy}	strain vectors
ζ	function defined in Eq. (2-89)
η	integral variable
λ	Lame's constant
λ_i	function defined in Eq. (4-34)
μ	Shear modulus
ν	Poisson's ratio
ξ	Fourier variable
π	circumference ratio
ρ	mass density
σ_x, σ_y	normal stresses
τ_0	thermal relaxation time
τ_1	non-Fourier factor
τ_2	inertia factor
τ_{xy}	shear stress
$\varphi\ (x)$	dislocation density function
$\psi(x)$	unknown function defined in Eq. (2-61)
$\Psi(x)$	function defined in Eq. (2-62)
ω_i	function defined in Eq. (4-37)

Symbols

!	Factorial Operator
∇	Laplace's operator
¯	Laplace's transform
~	Fourier's transform

Acronyms

HHCE	**H**yperbolic **H**eat **C**onduction **E**quation
IF	**I**nertia **F**actor
IFT	**I**nverse **F**ourier **T**ransform
NFF	**N**on-**F**ourier **F**actor
ODE(s)	**O**rdinary **D**ifferential **E**quations(s)
PDE(s)	**P**artial **D**ifferential **E**quations(s)
SIE(s)	**S**ingular **I**ntegral **E**quation(s)
SIF(s)	**S**tress **I**ntensity **F**actor(s)
TBC(s)	**T**hermal **B**arrier **C**oating(s)
TDM	Dimensionless **T**emperature **D**ifferences of the **M**id-Point of the Crack Surfaces

Chapter 1 Introduction

1.1 Thermal Shock Induced Cracks

Thermal shock occurs when a temperature gradient causes different parts of an object to expand by different amounts. This differential expansion can be understood in terms of stress or of strain, equivalently. At some point, this stress can exceed the strength of the material, causing a crack to form. If nothing stops this crack from propagating through the material, it will cause the object's structure to fail. The thermal shock is in general a very rapid process. We can distinguish two types of thermal shock: heating thermal shock and cooling thermal shock.

(*a*) *A heating thermal shock example:*

Ice cubes placed in a glass of warm water crack by thermal shock as the exterior surface increases in temperature much faster than the interior. As the outer layer expands as it warms, whilst the interior remains largely unchanged. This rapid change in volume between different layers creates stresses in the ice until the force exceeds the strength of the ice, and a crack forms.

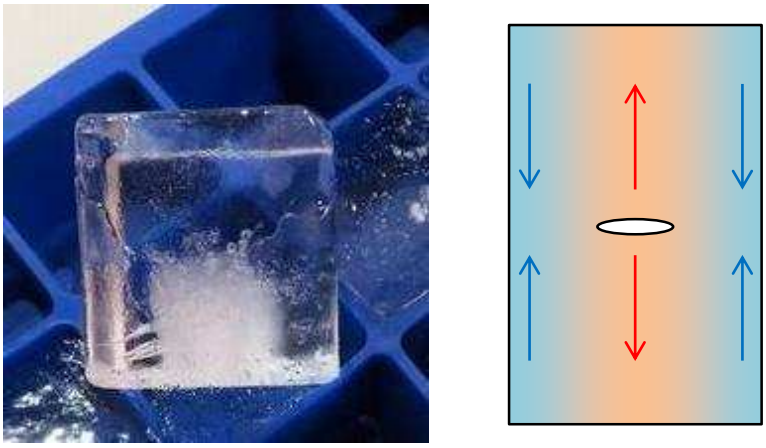

Figure 1.1-1 Heat thermal shock example and stresses

(*b*) *A cooling thermal shock example:*

The porcelain vases are heated in a kiln up to a high temperature, then quenching with water to induce a crackle surface.

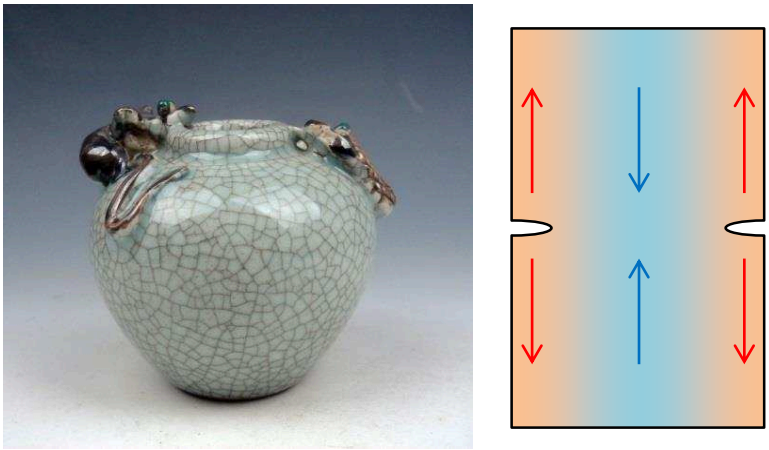

Figure 1.1-2 Cold thermal shock example and stresses

In these thermal shock processes, the heat flux enters into or goes out from the surface of the body, the temperature gradient vector lies along the normal direction of the surface. Consequently, the cracks also initiate and grow along this direction. The cracks normal to the surface of the body were largely studied in the literature [1-22]. However, this type of cracks is not the unique failure form of the solid under thermal shock. In the present thesis, we focus our attention to another type of cracks, the cracks parallel to the solid surface.

1.2 Backgrounds

Many engineering structure components subjected to server thermal loading suffer from cracking in paralleled direction of the heated surface. One of the examples is the thermal barrier coating (TBC). The TBC system, schemed in Figure 1.2-1 [23], is well known by its high performance in resistance of thermal shock damage and are widely used in gas-turbine engines for propulsion and power generations [23]. At the same time, the TBC is also an example of a material system where technology preceded largely scientific understanding [24].

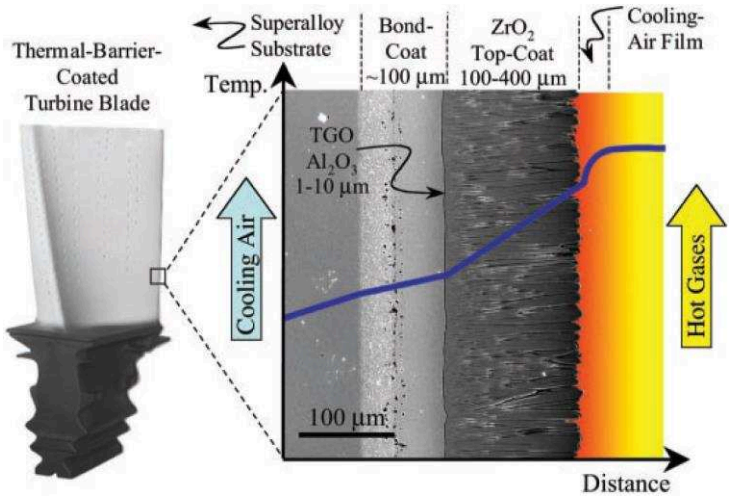

Figure 1.2-1 Anatomy of an electron-beam physical-vapor deposited (EB-PVD) TBC

Roughly speaking, the TBC system includes four different layers of materials, namely (1) the substrate, (2) the bound coat, (3) the thermally grown oxide and (4) the ceramic top-coat, as shown in Figure 1.2-1. During engine operation, several interrelated time-dependent phenomena take place within the TBC system which ultimately result in the TBC failure by cracking, as shown in Figure 1.2-2 [25]. Numeral previous studies demonstrate that the occurrence of the initial cracks at the interfaces between the ceramic coating and the alloy substrate play a key role in the failure of materials. The propagation of interface cracks will finally lead to the spallation of the top-coat. In the literature, the interface cracking was largely studied by means of numerical or theoretical modellings in order to reveal the failure mechanisms of the TBC in different aspects [25-45].

The existing studies state that one of the spallation failure mechanisms of layered materials is the thermal expansion mismatch stresses between the two different types of the materials, namely the ceramics and the alloys as in the layered materials [26, 27, 29-32, 46-51].

According to the fracture mechanics theory, the thermal expansion mismatch induced tensile stresses normal to the heated surfaces may be a source to yield the initial elementary cracks [24, 52, 53]. However, further studies showed that in the framework of the conventional thermal stress theories, the thermal expansion mismatch at the interfaces or inside the coating, does not usually provide high-enough stresses to initiate cracks when the surfaces are heated or cooled [52]. In order to

surmount this difficulty and based on the morphology of the interfacial imperfections in the TBCs, Evans and He [24, 54, 55] indicated that the undulations of interfaces can create local tensile stresses normal to the interfaces. They estimated that the order of the stresses could reach several GPa as the temperature difference applying to the coating surfaces approximated 1000 degree. Obviously, this statement explains with satisfaction the occurrence of some initial elementary interface crack in the TBCs. However, this model cannot explain the delamination of a perfectly straight interface. Moreover, initiation and growth of the transverse cracks inside the ceramic coating can also be observed, as shown in Figure 1.2-2. The above-mentioned interface delamination models cannot be used in this case.

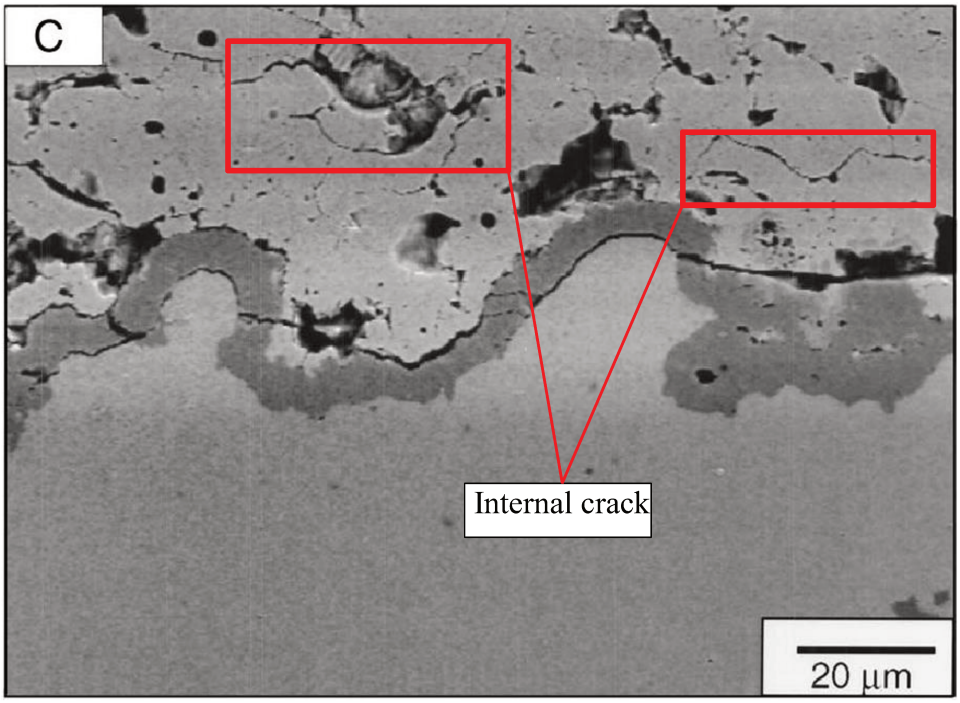

Figure 1.2-2 Cross-sectional SEM of a failed APS TBC

The crack initiation and growth in the direction parallel to the heated surface can also be observed in other thermal-shocked-structures. Figure 1.2-3 shows the crack patterns in a group of alumina samples under thermal shock [56]. The crack patterns were obtained by quenching the heated alumina plates (250 ~ 700℃) into water of the room temperature (20℃). We can observe that the cracks initiate in the normal direction of the surface, but transverse bifurcation, framed by the red lines in Figure 1.2-3, can occur, especially when the quenching temperature is high. Clearly, the conventional thermal stress theories are not capable to give satisfactory answers to

this phenomenon.

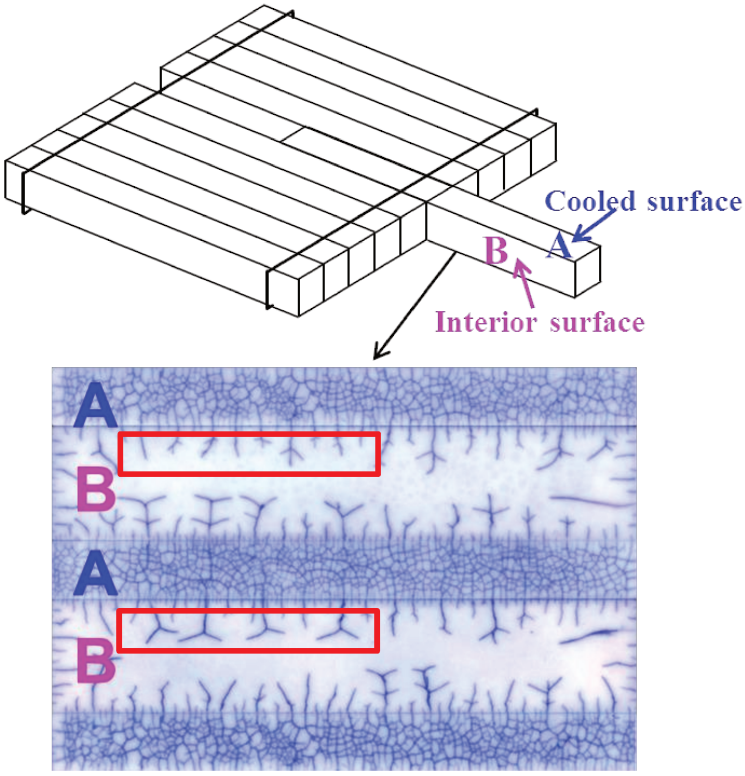

Figure 1.2-3 Thermal shock crack patterns on the interior surfaces of the stacked plate.

The third example is the crack propagation behavior of TiN coatings, deposited onto 304 stainless steel substrates, and related to a laser thermal shock experiment [57]. Under thermal shock produced by laser pulses on the coating surface, the cracks initiated at coating surface and propagated in a direction perpendicular to the substrate under low loads conditions. As shown in Figure 1.2-4, the cracks originated from coating-substrate interface began to appear with increasing laser pulse energy. The cracks from the interface also spread out transversely through the weak region of the columnar grains by repetitive laser shock. The change of crack propagation direction from perpendicular to horizontal is observed. After several laser pulses, delamination or spelling were observed at the coating-substrate interface region. Here again, the transverse cracks are the direct cause of the coating failure.

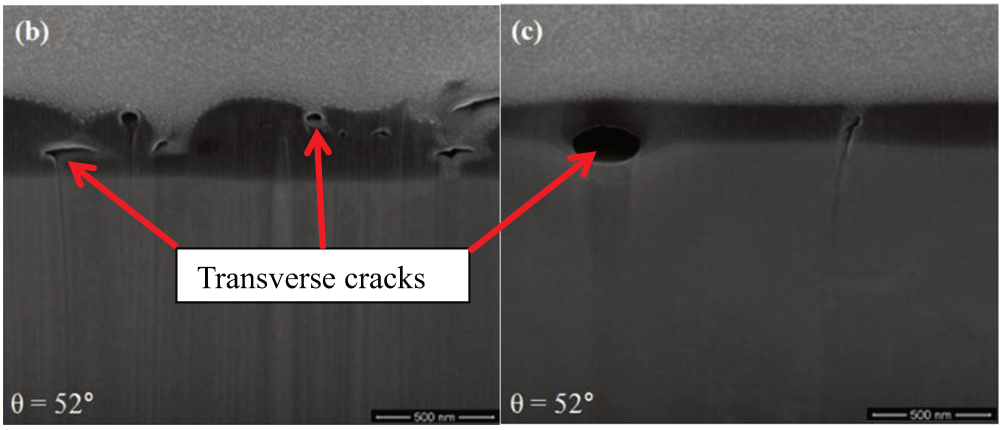

Figure 1.2-4 Transverse cracks observed at the cross section of the TiN coating following laser ablation

All these experimental observations show the importance of the cracks parallel to the heated surface in the fracture process of coatings or non-coated brittle materials. This fracture problem has not been properly resolved in the literature so far. This is the principal motivation of the present work.

1.3 Study Method

As we mentioned above, the conventional thermal stress theories and thermal shock models cannot be used to predict initiation and growth of transverse cracks parallel to the heated surface. Therefore, it is reasonable to believe that some physical factors, considered as insignificant and therefore neglected in these theories or models, may play an important role in the fracture procedure of materials under thermal shock. General speaking, these factors may be included in the consideration of the boundary conditions and the governing equations of the thermal and stress theories.

In this thesis we propose to study the driving forces governing the growth of a crack lied in the parallel direction of the surface of a plate under thermal shock. To this end, the temperature field and stress fields near the crack will be found by considering appropriately the boundary conditions, the thermal conduction theory and the thermal stress theory of the related problem.

1.3.1 Boundary Conditions

Solving the temperature and stress fields near the crack are the first and most important task to predict the crack propagation. However, existence of cracks can strongly influence the heat conductivity in the materials [58]

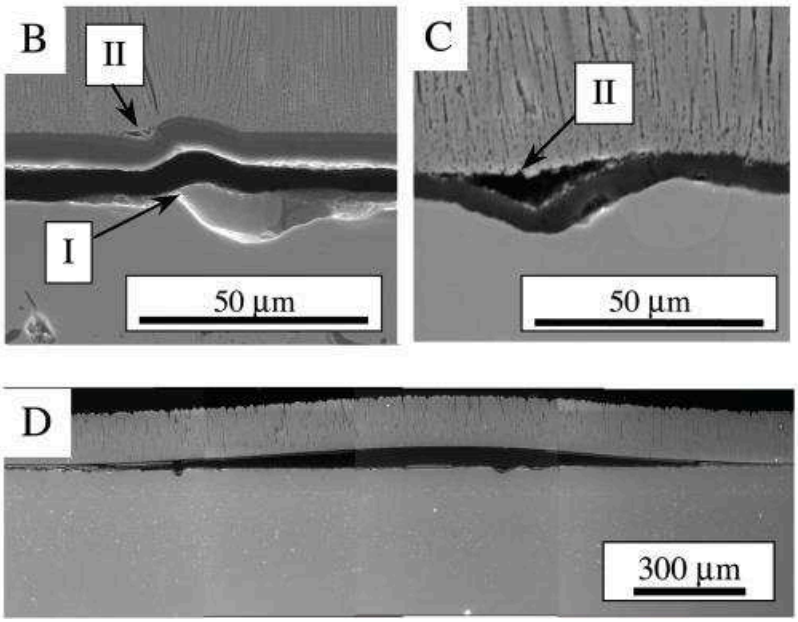

Figure 1.3-1 Large-scale buckling and crack morphology of EB-PDV.

As shown in Figure 1.3-1, the separation of the crack surface creates an empty space which gaz or liquid media can fill in. Thus the crack can be considered as a thermal barrier that resists the heat flux to pass across. However, the heat conductivity of a crack is not a basic material property. It may depend on numerous factors such as the temperature distribution near the crack, the volume of the crack gap or the medium filling in the crack gap and so on. So it will be more appropriate to define the thermal conductivity of the crack gap with an "inner heat transfer coefficient" h_c as follows:

$$q = h_c [T] \tag{1-1}$$

where q is the heat flux density across the crack, and $[T]$ is the temperature jump across the crack. h_c is also called *contact conductance* for the crack gap [59]

A small value of h_c of the crack gap would lead to a large temperature jump with strong nonlinear temperature gradients near the crack by means of what strong stress

concentrations near the crack tips are formed. In the contrary, a large value of h_c will lead to a small temperature jump and small stress concentrations near the crack tips. From this point of view, the importance of this heat transfer coefficient to the crack growth prediction is evident. In most of the literatures, this factor is often neglected (this is equivalent to $h_c \rightarrow \infty$). In this case, the temperature jump is nil, and no stress concentration is created. In other literatures [60], the crack was considered as totally thermally insulated (this is equivalent to $h_c = 0$). This hypothesis leads to an excessive stress concentration. In the present work, we consider h_c as an effective material parameter varying from zero to infinity.

1.3.2 Thermal Conduction Theory

The traditional thermal conduction theory was based on the famous Fourier law. It governs the relationship between the flow of heat and the temperature field. One of the advantages of Fourier's law is that its application is independent of the medium. In most engineering applications this theory agrees well with the experimental results when temperature doesn't change dramatically [59-62]. Nevertheless, numerous investigators pointed out that the Fourier law would lead to an infinite speed of the heat propagation [63-67], which is physically unrealistic. Boley [65] pointed out that the effect of the finite speed of heat propagation is negligible for most practical engineering applications. However, this assumption would make considerable error in the cases of the very small length and time scales [68, 69] or when the temperature changes very fast, such as in the cases of powerful laser impact or the ignition process of the turbines [70-72]. Maurer and Thompson [73] pointed out the surface temperature of a slab measured immediately after a sudden thermal shock is about 300 ℃ higher than that predicted by Fourier law. The Fourier heat conduction theory also breaks down at very low temperatures and when the applied heat flux is extremely large [74]. Peshkov [75] determined the heat relaxation time of liquid helium II experimentally at 1944. He found the finite propagation velocity heat wave to be 19 meters per sec at a temperature of 1.4 K and the order of magnitude is smaller than the ordinary velocity of sound in helium. In order to overcome this anomaly, the limiting speed on heat propagation was considered and hyperbolic heat conduction equation (HHCE) was developed. The HHCE, separately proposed by Vernotte [76] and Cattaneo [77], was based on the microscopic considerations [78-80] and by

introducing a new material property called thermal relaxation time. This proposed wave like propagation of heat is also named as the "*second sound wave*" due to its similarity with the acoustic wave.

Baumeister and Hamill [64] determined the effect of the propagation velocity of heat on the temperature and heat-flux distribution in a semi-infinite body. Özişik [81] studied the propagation and reflection of thermal waves in a finite slab and indicated that the release of a concentrated pulse of energy gives rise to a severe thermal wave front. The author pointed out that the wave travels through the medium with a finite speed and the energy dissipation during its propagation and reflecting from the insulated surfaces.

Zanchini and Pulvirenti [82] presented the effects of the relaxation time on the temperature field for steady-periodic heat conduction in an infinitely hollow cylinder. Lin and Chen [83] give a solution for hyperbolic heat conduction in both cylindrical and spherical objects using the Laplace transform technique. Babaei and Chen [84] investigated the functionally graded hollow cylinder.

Ali and Zhang [85] developed an alternative model for heat conduction, based on a weak interpretation of the theory of relativity and without any microscopic or material-specific considerations. Körner and Bergmann [79] inspected the HHCE on a microscopic level from a physical point of view and showed how the modified Fourier's law follows from approximations of the underlying transport equations.

All the previous models were developed under the continuity assumption. The materials were considered as perfectly continuous and non-cracked. In 2012, Chen [60] studied the transient thermal stress problem in a cracked elastic half-plane model with the HHCE. Laplace transforms and singular integral equations were applied to solve the temperature and thermal stress fields consecutively. Airy function technique was used to evaluate the stress concentration around cracks. The author found that the hyperbolic heat conduction has significant influence on the dynamic temperature and stress fields. In the same year, he extended this theory to the finite plate [86] and coating materials. However, if we introduce the inertia effect to the stress analysis, the equations of motion have to be used in the solution of the problem. The Airy function method is no longer applicable in this case. New solution techniques should be developed. This is what we proposed to study in this work.

1.3.3 Dynamic Thermal Stress Equations

The equilibrium equation, which is an approximate equation by neglecting the inertia item from the equation of motion, is one of the basic equations in thermoelasticity theory. The quasi static hypothesis agrees well with the experiment result when the temperature doesn't change very fast [87]. However, Kogawa [88] pointed out that the inertia effect should be considered in the case when the thermal stress is generated by thermal shock, especially when the samples are heated by laser beam shot.

In fact, the question of whether the inertia terms can be disregarded was considered by Duhamel [89] at as early as 1837. The author indicated that the time rate of temperature change is slow enough comparing to the stress wave velocity so that these terms should not be significant in equation of motion. Danilovskaya [90, 91] reexamined this question in more detail for the case of an elastic half-space in 1950. Her work can be taken as indicative of the importance of inertia effect in materials. Boley [92, 93] developed the theories for the case of beams and plates. The author found that the inertia effect is important to the beam only for the relatively thin samples. In such a thickness plate model are usually used rather than beam. Hetnarski [94] derived approximations for the stress and temperature fields in a small-time scale by using the Laplace transform method. Muki and Breuer [95] also investigated the temperature and stress fields under coupled theory by using the Laplace transform and gave exact solutions. Nyayadhish and Nariboli [96] noted the similarities between the dynamic thermal stress problem and the sound waves in certain plasmas and discussed the difficulties encountered in analytical analysis of such problems. Subsequently, Hetnarski and Ignaczak [97] also investigated laser induced thermos-elastic waves in a half-space of the Green and Lindsay type [98].

As discussed above, the importance of inertia effect to the thermal shock theory has been examined in both theory and experiments. However, little progress has been achieved in analysis of the cracked structures so far. In fact, the influences of the inertia effect on cracked materials should be considered carefully because the crack propagation is sensitive not only to the stress around the crack tips, but also to the stress wave reflected by the crack surfaces. The wave superposition and the strain rate effect will change a lot the stress intensity factors and the crack toughness.

Studies of the thermal stress distribution in a cracked elastic body have been

performed since 1950s [99-102]. In recent years, increasing investigations have been devoted to solve the crack problems under thermal loading in advanced materials [34, 103-109]. However, solving the temperature and stress fields by considering simultaneously the heat conduction barrier formed by a crack, the non-Fourier effect and the inertia effect is still rare in the literature due to the complexity of the problem.

We believed that the above-mentioned factors, namely the thermal barrier effect, the non-Fourier effect and the inertia effect, could play an important role in the crack initiation and failure process of the brittle materials under thermal shock loading. This motived us to study the interaction of all these factors in a specifically defined model in spite of the intrinsic mathematical difficulties of the problem.

1.4 Overview

In this work, we focus our attention on the stress analysis in a cracked plate under a thermal shock loading by taking both the non-Fourier effect and inertia forces into account. The crack lies in a parallel direction to the free surface. The thermal conductivity of the crack gap is regarded as a material property to improve the accuracy of the temperature distribution. In this work, we assume that the thermal fields and the mechanical fields are not coupled, which should not produce significant errors in most of engineering applications [110, 111]. The main objectives of this study can be summarized as follows:

(1) Develop a thermal stress model;

(2) Obtain the dimensionless solution of the temperature field;

(3) Investigate the influence of the crack on the temperature distribution;

(4) Develop a new method to obtain the dimensionless solutions of the thermal stresses, the dynamic stress intensity factors and the crack opening displacements;

(5) Study the crack behavior under the interaction of the thermal barrier effect, the non-Fourier effect and the inertia effect.

Chapter 2 Temperature Field Analysis

2.1 Introduction

2.1.1 Main Results

In this chapter, the evolution of the temperature field in a linear elastic strip containing a crack parallel to the heated surface is studied. A number of concepts are stated to enrich the traditional thermal conduction governing equations. In particular, the Biot number, the relaxation time and the non-Fourier factor (NFF) are introduced to improve the accuracy of the solutions of the temperature field. The Laplace transform and the Fourier transform are applied to eliminate the partial derivative with respect to the time variable t and the axis variable x, respectively, such that a non-linear ordinary differential equation system in y-coordinate can be obtained in Fourier-Laplace space. Boundary conditions are applied to obtain the singular integral equations. Furthermore, numerical integrate method and numerical inversion of the Laplace transform are used to obtain the temperature field in time domain. In this study, the thermal-elastic coupling term is neglected, that leads to an uncoupled problem [110, 112, 113].

2.1.2 Statement of the Thermal Shock Problem

The crack problem under thermal shock studied in this work is shown in Figure 2.1-1. We consider a thin plate under transient thermal loading which contains a straight crack of length $2r$ parallel to the free surface. A Cartesian coordinate system is established with the x-axis coincided with the crack plane and the origin at the crack center. The plate is assumed to be infinite in x direction. The distances between the crack and the bottom/up boundary surfaces are l_a and l_b, respectively, where l_a and l_b are strictly positive real. We assume that the material is homogeneous, isotropic and linearly elastic. In this work, only thermal loading is considered in evaluating the temperature and stress fields. The initial temperature is assumed to be uniform and equals to T_0 in the plate. Then the free surface $y = -l_a$ is suddenly heated to a fixed

temperature T_∞ and the temperature at the free surface $y = l_b$ stays unchanged, as is shown in Figure 2.1-2. The heat transfer coefficient between the crack surfaces is assumed to be h_c.

In the following, we present the detailed mathematical formulation for the resolution of the above-defined thermal shock problem.

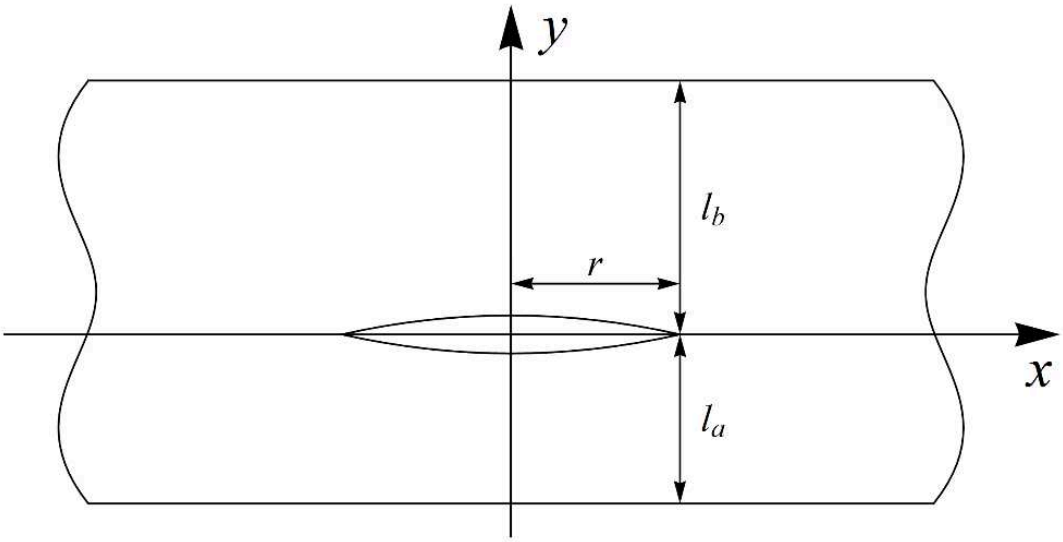

Figure 2.1-1 Geometry of the cracked strip and the coordinate system

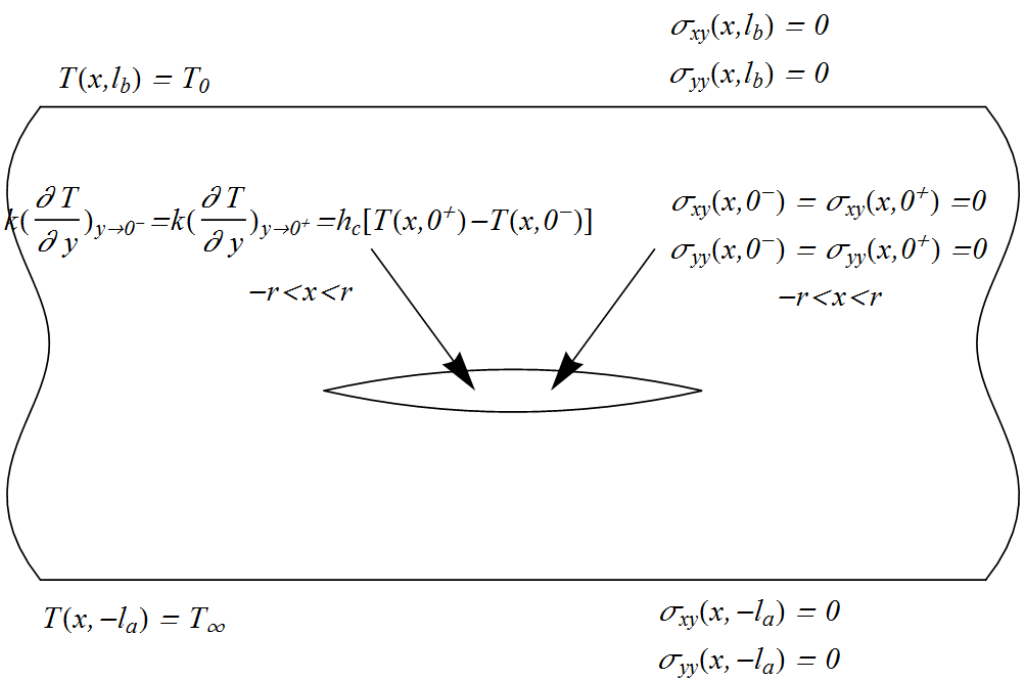

Figure 2.1-2 Boundary Conditions.

2.2 Formulations of the Heat Conduction Problem

2.2.1 Fourier's law – Parabolic Heat Conduction

Different theories on heat conduction in solids can be found in the literatures [63, 64, 66, 68, 114-117] . The famous Fourier law of heat conduction presents a linear relationship between the heat flux ($\vec{q}$) through a material and the gradient of temperature (T) which relates heat flux directly to the temperature gradient using thermal conductivity. For a homogeneous, isotropic solid, Fourier's law can be written in the form:

$$\vec{q} = -k\nabla T \tag{2-1}$$

where ∇ is the gradient operator, $T = T(x, y, t)$ is the temperature field and the temperature gradient ∇T is a vector normal to the isothermal surface, the heat flux vector $\vec{q}$ represents the heat flow per unit time, per unit area of the isothermal surface in the direction of decreasing temperature gradient, and k is the material thermal conductivity which is a positive, scalar for a homogeneous, isotropic material. In the SI units system, the unit of thermal conductivity is given as $\mathrm{W/(m \cdot K)}$.

The two components of the heat flux vector in x and y directions are

$$\begin{cases} q_x = -\dfrac{\partial T}{\partial x} \\ q_y = -\dfrac{\partial T}{\partial y} \end{cases} \tag{2-2}$$

2.2.2 Hyperbolic Heat Conduction

Normally the accuracy of Fourier's heat conduction law is sufficient for most practical engineering applications. However, there might be considerable error in the evaluation of the heat conduction, caused by highly-varying thermal loadings such as pulsed laser heating or the ignition process of turbine engines. In addition, Fourier's law also results in an infinite speed of thermal wave propagation because of its parabolic characteristics, which is physically unrealistic. To overcome this

contradiction, non-Fourier heat conduction theories have been developed. Amongst these theories, a hyperbolic model, named the Cattaneo-Vernotte model [70, 117] has been proposed by adding a time (t) dependent term in the Fourier equation.

The introduced time-derivative term describes a wave nature of heat propagation with a finite speed, which has been proved in both theory and experiments [70, 72, 118]. The non-Fourier thermal conduction equation writes:

$$\vec{q} + \tau_0 \frac{\partial \vec{q}}{\partial t} = -k \cdot \nabla T \tag{2-3}$$

where t is the time, τ_0 is the thermal relaxation time. The energy conservation equation of the thermal conduction without internal heat generation is expressed as:

$$\rho C_p \frac{\partial T}{\partial t} = -\nabla \vec{q} \tag{2-4}$$

where ρ and C_p are the mass density and the specific heat capacity, respectively. Substitution for $\vec{q}$ of Equation (2-3) from the energy balance Equation (2-4) leads to the governing equations of the hyperbolic thermal conduction:

$$\frac{1}{\rho C_p} \nabla \cdot \left(k \cdot \nabla T \right) = \tau_0 \frac{\partial^2 T}{\partial t^2} + \frac{\partial T}{\partial t} \tag{2-5}$$

In this study, the thermal conductivity k is assumed to be a constant, so the governing Equations (2-5) can be written as:

$$\Delta T = \frac{\tau_0}{a} \frac{\partial^2 T}{\partial t^2} + \frac{1}{a} \frac{\partial T}{\partial t} \tag{2-6}$$

where $\Delta = \nabla^2 = \frac{\partial^2}{\partial x^2} + \frac{\partial^2}{\partial y^2}$ and $a = \frac{k}{\rho C_p}$, is the thermal diffusivity.

2.2.3 Boundary Conditions and Initial Conditions

As shown in Figure 2.1-2, the hyperbolic heat conduction Equation (2-6) is subjected to the following conditions at the boundaries:

$$\begin{cases} T\left(x, -l_a, t\right) = T_\infty \\ T\left(x, l_b, t\right) = T_0 \end{cases} \tag{2-7}$$

Due to the presence of the crack, the material is in imperfect thermal contact between the crack surfaces $y = 0;\ |x| \le r$ as illustrated in Figure 2.1-2. The gap between the crack surfaces may be filled with air or other fluids and the thermal

conductivity of the surrounding fluid is normally smaller than that of the plate. This imperfect contact will lead to a steep temperature drop across the crack gap. In order to describe the boundary condition for the crack gap, we write the energy balance as follows

$$\begin{pmatrix}\text{Heat conduction}\\ \text{in the range } y<0\end{pmatrix}=\begin{pmatrix}\text{Heat transfer}\\ \text{across the gap}\end{pmatrix}=\begin{pmatrix}\text{Heat conduction}\\ \text{in the range } y>0\end{pmatrix} \tag{2-8}$$

Equation (2-8) can be rewritten in the form of formula:

$$\vec{q}=-k\left.\frac{\partial T}{\partial y}\right|_{y\to 0^-}=h_c\left[T\left(x,0^-,t\right)-T\left(x,0^+,t\right)\right]=-k\left.\frac{\partial T}{\partial y}\right|_{y\to 0^+},\quad |x|\le 1 \tag{2-9}$$

where h_c, in unit W/(m^2·K), is called *contact conductance* of the crack gap[59]. It is the proportionality coefficient between the heat flux and the thermodynamic driving force for the flow of heat. Equation (2-9) is called "*the homogeneous boundary condition of the third type*". It is obvious that thermal contact is perfect on the extension line of the crack, i.e., $h_c\to\infty$, and Equation (2-9) is reduced to the following

$$\begin{cases}k\left.\frac{\partial T}{\partial y}\right|_{y\to 0^-}=k\left.\frac{\partial T}{\partial y}\right|_{y\to 0^+},\quad |x>1|\\ T\left(x,0^-,t\right)=T\left(x,0^+,t\right)\end{cases} \tag{2-10}$$

The two equations in (2-10) stand for the continuity of heat flux and the continuity of temperature at the extension line of the crack, respectively.

The initial conditions of the thermal conduction problem are:

$$\begin{cases}T\left(x,y,0\right)=T_0\\ \left.\frac{\partial T}{\partial t}\right|_{t\to 0}=0\end{cases} \tag{2-11}$$

2.3 Analytical Procedure of Temperature Fields

In the following, we present the resolution procedure of the above-defined thermal conduction problem. The analytical-numerical methods used in [119, 120] are essentially followed in this work. The global procedure is illustrated in Figure 2.3-1 and can be briefly described as follows:

- After establishment of the heat conduction model as described above, we first eliminate the time variable *"t"* by means of the Laplace transform;

- Then we eliminate the coordinate variable *"x"* by using the Fourier transform. Thus we transform the partial differential equations to an ordinary differential equation (ODE) of the coordinate variable *"y"* in Laplace-Fourier space [60, 86, 121].
- The general solution of this ODE is readily found. By using the boundary conditions and by performing the inverse Fourier transform (IFT), a singular integral equation (SIE) can be obtained.
- The SIE is dealt with by using the numerical integration techniques and the Fourier transform convolution property. The numerical integration leads to solving a linear equation system then obtaining the temperature fields in Laplace space.
- The numerical inverse Laplace transform provides finally temperature field evolution.

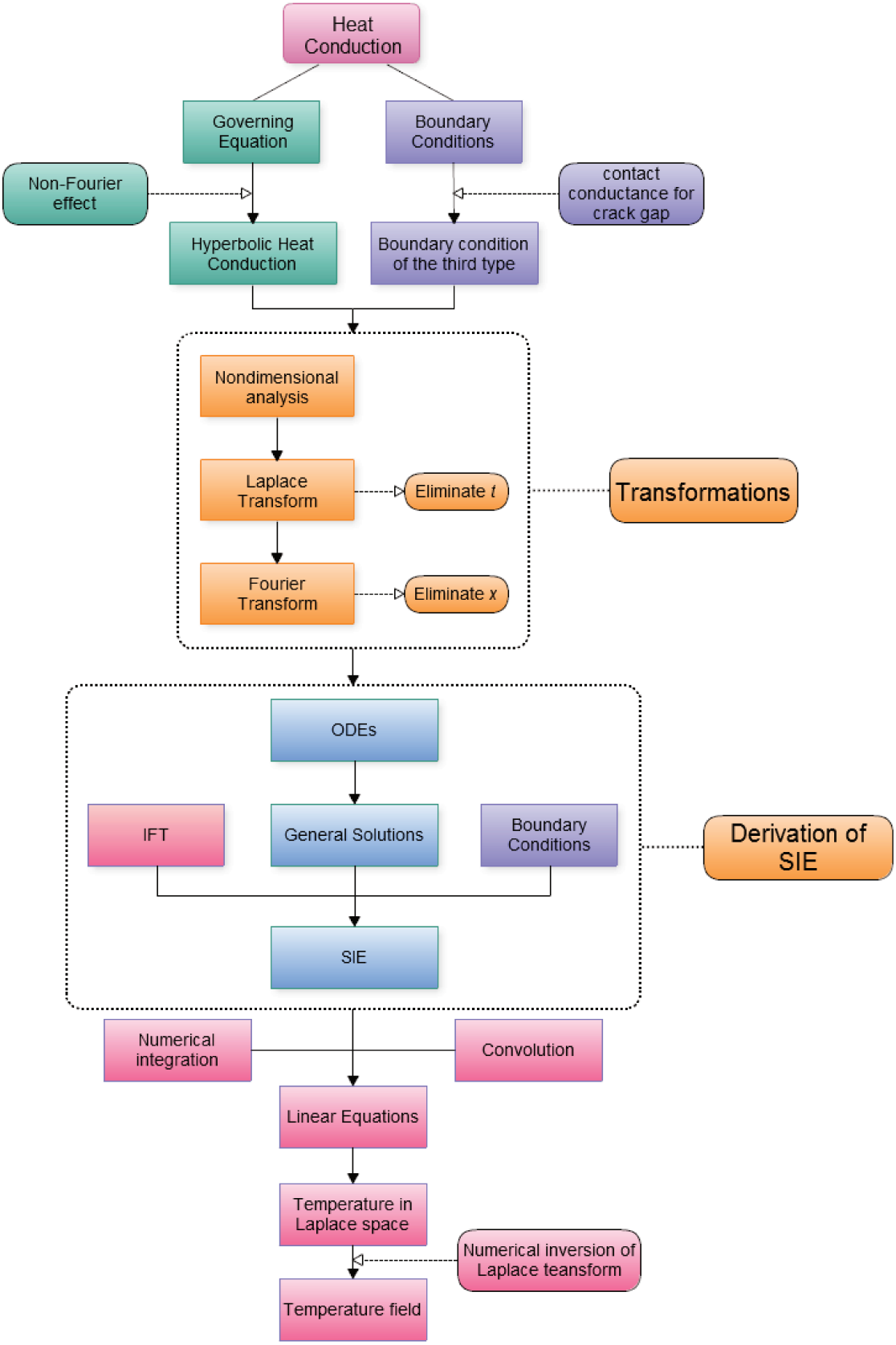

Figure 2.3-1 Solving procedure of the temperature field.

2.3.1 Nondimensionalization of Variables

In general, nondimensionalizing the governing equations would benefit the solution and analysis of engineering problems. This process often yields important dimensionless parameters and reduces the dependency of the solution on a potentially large number of dimensional parameters.

Since the numerical techniques used in section 2.5 and 4.4.2 are heavily based on the properties of the related Chebyshev and Jacobi polynomials, it would be useful to set the crack in the normalized coordinate interval $[-1,1]$. Hence, we define the dimension-independent variables as follows:

$$\begin{cases} \left(x^*, y^*\right) = \dfrac{(x, y)}{r} \\ t^* = \dfrac{at}{r^2} \\ Bi_c = \dfrac{h_c r}{k} = \dfrac{h_c l_a}{k}\dfrac{r}{l_a} = Bi \cdot \dfrac{r}{l_a} \\ T^* = \dfrac{T - T_0}{T_\infty - T_0} \end{cases} \tag{2-12}$$

where the dimensionless time is the ratio of the rate of heat transferred by conduction to the rate of energy stored[122]. This will become apparent if we rearrange t^* as follows:

$$t^* = \frac{at}{r^2} = \frac{\left(\dfrac{k}{r}\right) r^2}{\dfrac{\rho C_p r^3}{t}} = \frac{\text{Diffusive transport rate}}{\text{Storage rate}} \tag{2-13}$$

where the numerator denotes the rate of heat conducted across r in the reference volume r^3 while the denominator denotes the rate of energy storage in reference volume r^3. Therefore, the larger the dimensionless time is, the deeper the penetration of temperature into the solid over a given period of time will be.

Bi_c is the effective Biot number which gives a simple index of the heat transfer resistances of the crack gap and named after the physicist and mathematician Jean-Baptiste Biot.

The dimensionless length of the crack and the distances between the crack gap and the surfaces are

$$\begin{cases} r^* = \dfrac{r}{r} = 1 \\ l_a^* = \dfrac{l_a}{r} \\ l_b^* = \dfrac{l_b}{r} \end{cases} \tag{2-14}$$

The governing Equation (2-6) has the following dimensionless forms:

$$\nabla^2 T^* = \frac{\partial T^*}{\partial t^*} + \tau_1 \frac{\partial^2 T^*}{\partial t^{*2}} \tag{2-15}$$

where the gradient operator ∇ is related to the dimensionless coordinates x^* and y^*. τ_1 is the normalized thermal relaxation time which we named "***Non-Fourier factor***" (NFF) and is defined as:

$$\tau_1 = \frac{a\tau_0}{r^2} \tag{2-16}$$

The magnitude of τ_1 determines the strength of the non-Fourier effect. This point will be discussed in Chapter 5.

The boundary conditions (2-7), (2-9) and (2-10) can be written in the following forms:

$$\begin{cases} (a): T^*\left(x^*, -l_a^*, t^*\right) = 1 \\ (b): \left.\dfrac{\partial T^*}{\partial y^*}\right|_{y^*\to 0^-} = \left.\dfrac{\partial T^*}{\partial y^*}\right|_{y^*\to 0^+} = Bi_c\left[T^*\left(x^*, 0^+, t^*\right) - T^*\left(x^*, 0^-, t^*\right)\right] & \left|x^*\right| < 1 \\ \left.\begin{array}{l} (c): \left.\dfrac{\partial T^*}{\partial y^*}\right|_{y^*\to 0^-} = \left.\dfrac{\partial T^*}{\partial y^*}\right|_{y^*\to 0^+} \\ (d): T^*\left(x^*, 0^-, t^*\right) = T^*\left(x^*, 0^+, t^*\right) \end{array}\right\} & \left|x^*\right| \geq 1 \\ (e): T^*\left(x^*, l_b^*, t^*\right) = 0 \end{cases}$$

(2-17)

and the initial conditions (2-11) becomes:

$$\begin{cases} (a): T^*\left(x^*, y^*, 0\right) = 0 \\ (b): \left.\dfrac{\partial T^*}{\partial t^*}\right|_{t^*=0} = 0 \end{cases} \tag{2-18}$$

In the following the superscript "*" will be omitted for simplicity.

2.3.2 Integral Transforms

In heat conduction problems, the Laplace transform is generally applied to the time variable *t*.

To solve Equation(2-15), first we define the Laplace transform of the temperature field, as:

$$\bar{T}(x,y)=\int_0^{\infty} T(x,y,t)e^{-pt}dt \tag{2-19}$$

By definition, $T(x, y, t)$ can be expressed in term of $\bar{T}$

$$T(x,y,t)=\frac{1}{2\pi i}\int_{\gamma-i\infty}^{\gamma+i\infty}\bar{T}(x,y)e^{pt}dp \tag{2-20}$$

where the parameter "i" is the imaginary unit and γ is a real constant that exceeds the real part of all the singularities of $\bar{T}(x,y)$. The functions $T(x,y)$ and $\bar{T}(x,y)$ are called a Laplace transform pair[123].

By substituting the Laplace transform (2-20) to Equations (2-15), (2-17) and applying the initial conditions(2-18), we have the governing equation and boundary conditions in Laplace domain:

$$\nabla^2\bar{T}=(p+\tau_1 p^2)\bar{T}\quad \bar{T} \tag{2-21}$$

$$\begin{cases}(a):\bar{T}(x,-l_a)=\dfrac{1}{p} & \\ (b):\left.\dfrac{\partial\bar{T}}{\partial y}\right|_{y\to 0^-}=\left.\dfrac{\partial\bar{T}}{\partial y}\right|_{y\to 0^+}=Bi_c\left[\bar{T}(x,0^+)-\bar{T}(x,0^-)\right] & |x|<1 \\ \left.\begin{array}{l}(c):\left.\dfrac{\partial\bar{T}}{\partial y}\right|_{y\to 0^-}=\left.\dfrac{\partial\bar{T}}{\partial y}\right|_{y\to 0^+} \\ (d):\bar{T}(x,0^-)=\bar{T}(x,0^+)\end{array}\right\} & |x|\geq 1 \\ (e):\bar{T}(x,l_b)=0 & \end{cases} \tag{2-22}$$

Similarly, we define the Fourier transform of the Laplace-domain-temperature, $\tilde{\bar{T}}$, as:

$$\tilde{\bar{T}}(y)=\int_{-\infty}^{\infty}\bar{T}(x,y)e^{i\xi x}dx \tag{2-23}$$

And

$$\bar{T}(x,y)=\frac{1}{2\pi}\int_{-\infty}^{\infty}\tilde{\bar{T}}(y)e^{-i\xi x}d\xi \tag{2-24}$$

By substituting the Fourier transform (2-24) to Equations (2-21) and (2-22), we have the governing equation and boundary conditions in Laplace-Fourier domain:

$$\frac{d^2\tilde{\bar{T}}}{dy^2} = m^2\tilde{\bar{T}} \tag{2-25}$$

where

$$m = \sqrt{\xi^2 + p + \tau_1 p^2} \tag{2-26}$$

and

$$\begin{cases} (a): \tilde{\bar{T}}(-l_a) = \dfrac{\delta(\xi)}{p} \\ (b): \left.\dfrac{d\tilde{\bar{T}}}{\partial y}\right|_{y\to 0^-} = \left.\dfrac{d\tilde{\bar{T}}}{\partial y}\right|_{y\to 0^+} \\ (c): \tilde{\bar{T}}(l_b) = 0 \end{cases} \tag{2-27}$$

where $\delta(\xi)$ is the Dirac delta function. It is a generalized function on the real axes, equals to zero everywhere and to the infinity at $\xi = 0$:

$$\delta(\xi) = \begin{cases} \infty & \xi = 0 \\ 0 & \xi \neq 0 \end{cases} \tag{2-28}$$

and which is also constrained to satisfy the identity

$$\int_{-\infty}^{\infty} \delta(\xi)\, d\xi = 1 \tag{2-29}$$

It is clear that from (2-28) and (2-29), we have

$$\int_{-\infty}^{\infty} f(\xi)\delta(\xi)\, d\xi = f(0) \tag{2-30}$$

which would be useful in the following analysis.

2.3.3 General Solution of ODE

Equation (2-25) is a second order ordinary differential equation (ODE), whose general solution can be written as:

$$\tilde{\bar{T}} = \begin{cases} C_{T,1}e^{-my} + C_{T,2}e^{my} & -l_a < y < 0 \\ C_{T,3}e^{-my} + C_{T,4}e^{my} & 0 < y < l_b \end{cases} \tag{2-31}$$

where $C_{T,i}$ (i = 1, 2, 3, 4) are the coefficients to be determined by using the boundary conditions. It is also to notice that in this thesis, the italic letter "*i*" is used as a subscript order. It should not be confounded with the regular script "i", which stands for the imaginary unit.

We note that there are three boundary conditions (2-27) in Laplace-Fourier domain that can be applied by (2-31), whereas the number of the coefficients to be determined is four. The mixed boundary conditions (*b*) of (2-22) in Laplace space would give a dual integral equation to determine the last one.

We define a dimensionless density function as follow:

$$\phi(x,t)=\left.\frac{\partial T}{\partial x}\right|_{y\to 0^+}-\left.\frac{\partial T}{\partial x}\right|_{y\to 0^-} \tag{2-32}$$

It is clear that from the boundary condition (*b*) and (*c*) in (2-17), we have

$$\int_{-1}^{1}\phi(x)\,dx=0 \tag{2-33}$$

and

$$\phi(x)=0,\quad |x|>1 \tag{2-34}$$

These equations are direct results of the symmetry of the geometry and of the fact that $T(x,0^+)=T(x,0^-)$ outside of the crack. Equation (2-33) is also known as the single-valuedness condition. Physically it means that the temperatures are single-valued for the non-cracked portion along $y = 0$. By applying the Laplace and Fourier transforms to equation (2-32) successively, we can get

$$\tilde{\bar{\phi}}=-i\xi\left[\tilde{\bar{T}}(0^+)-\tilde{\bar{T}}(0^-)\right] \tag{2-35}$$

where, by definition and from (2-34), $\tilde{\bar{\phi}}$ is given by

$$\tilde{\bar{\phi}}=\int_{-a}^{a}\left[\int_{0}^{\infty}\phi(x,t)e^{-pt}dt\right]e^{i\xi x}dx \tag{2-36}$$

By substituting (2-31) into the boundary conditions (2-27) and (2-35) we obtained

$$\begin{bmatrix} e^{ml_a} & e^{-ml_a} & 0 & 0 \\ 0 & 0 & e^{-ml_b} & e^{ml_b} \\ 1 & -1 & -1 & 1 \\ -1 & -1 & 1 & 1 \end{bmatrix}\begin{bmatrix} C_{T,1} \\ C_{T,2} \\ C_{T,3} \\ C_{T,4} \end{bmatrix}=\begin{bmatrix} \dfrac{\delta(\xi)}{p} \\ 0 \\ 0 \\ \dfrac{\tilde{\bar{\phi}}}{i\xi} \end{bmatrix} \tag{2-37}$$

then we obtain C_i by solving the liner equations system (2-37)

$$\begin{cases} C_{T,1} = \dfrac{i\tilde{\bar{\phi}}\,p\left(1+e^{2ml_b}\right)+2\xi\delta(\xi)e^{m(l_a+2l_b)}}{2\left(-1+e^{2m(l_a+l_b)}\right)p\xi} \\ C_{T,2} = -\dfrac{ie^{ml_a}\left[\tilde{\bar{\phi}}\,pe^{ml_a}\left(1+e^{m2l_b}\right)-2i\xi\delta(\xi)\right]}{2\left(-1+e^{2m(l_a+l_b)}\right)p\xi} \\ C_{T,3} = \dfrac{e^{2ml_b}\left(i\tilde{\bar{\phi}}\,p\left(1+e^{2ml_a}\right)+2\xi\delta(\xi)e^{ml_a}\right)}{2\left(-1+e^{2m(l_a+l_b)}\right)p\xi} \\ C_{T,4} = -\dfrac{i\tilde{\bar{\phi}}\,p\left(1+e^{2ml_a}\right)+2\xi\delta(\xi)e^{ml_a}}{2\left(-1+e^{2m(l_a+l_b)}\right)p\xi} \end{cases} \tag{2-38}$$

The detailed expression of the temperature fields in Laplace – Fourier space in terms of $\tilde{\bar{\phi}}$ are given by

$$\begin{cases} \tilde{\bar{T}}_1 = \dfrac{i\tilde{\bar{\phi}}\,p\left(1+e^{2ml_b}\right)+2\xi\delta(\xi)e^{m(l_a+2l_b)}}{2\left(-1+e^{2m(l_a+l_b)}\right)p\xi}e^{-my} - \dfrac{ie^{ml_a}\left[\tilde{\bar{\phi}}\,pe^{ml_a}\left(1+e^{m2l_b}\right)-2i\xi\delta(\xi)\right]}{2\left(-1+e^{2m(l_a+l_b)}\right)p\xi}e^{my} \\ \tilde{\bar{T}}_2 = \dfrac{e^{2ml_b}\left(i\tilde{\bar{\phi}}\,p\left(1+e^{2ml_a}\right)+2\xi\delta(\xi)e^{ml_a}\right)}{2\left(-1+e^{2m(l_a+l_b)}\right)p\xi}e^{-my} - \dfrac{i\tilde{\bar{\phi}}\,p\left(1+e^{2ml_a}\right)+2\xi\delta(\xi)e^{ml_a}}{2\left(-1+e^{2m(l_a+l_b)}\right)p\xi}e^{my} \end{cases} \tag{2-39}$$

where $\tilde{\bar{T}}_1$ and $\tilde{\bar{T}}_2$ presents the temperature of the domain $-l_a < y < 0$ and $0 < y < l_b$, respectively.

2.4 Derivation of the Singular Integral Equation

Up to this point, we have used all of the boundary conditions except (*b*) in (2-22) on the crack surfaces, expressed in Laplace domain. The temperature fields in Laplace space can be obtained by applying the inverse Fourier transform to (2-39) and make use of the parity of the equations:

$$\begin{cases} \bar{T}_1 = \dfrac{1}{2\pi}\displaystyle\int_0^\infty \dfrac{e^{-my}\left(1+e^{2l_b m}\right)\left(1-e^{2m(l_a+y)}\right)}{\left(-1+e^{2(l_a+l_b)m}\right)\xi}\bar{\phi}\cos(\xi x)\,d\xi + \dfrac{e^{m_0(l_a+2l_b-y)}-e^{m_0(l_a+y)}}{\left(-1+e^{2(l_a+l_b)m_0}\right)p} \\ \bar{T}_2 = \dfrac{1}{2\pi}\displaystyle\int_0^\infty \dfrac{e^{-my}\left(1+e^{2l_a m}\right)\left(e^{2l_b m}-e^{2my}\right)}{\left(-1+e^{2(l_a+l_b)m}\right)\xi}\bar{\phi}\cos(\xi x)\,d\xi + \dfrac{e^{m_0(l_a+2l_b-y)}-e^{m_0(l_a+y)}}{\left(-1+e^{2(l_a+l_b)m_0}\right)p} \end{cases} \tag{2-40}$$

where

$$m_0 = \sqrt{p + \tau_1 p^2} \tag{2-41}$$

Here Euler's formula

$$e^{ix} = \cos(x) + i\sin(x) \tag{2-42}$$

is used to obtain (2-40). Note that $\tilde{\bar{\phi}}$ is the only undetermined function in (2-40), therefore, the boundary condition (*b*) in (2-22) is sufficient to determinate the unknown.

Substituting (2-40) into (*b*) in (2-22), we obtain the integral equation

$$\lim_{y\to 0}\int_{-\infty}^{\infty}\frac{i}{2}\cdot In_1\cdot\tilde{\bar{\phi}}e^{-i\xi x}d\xi = \lim_{y\to 0}\int_{-\infty}^{\infty}\frac{me^{m(-y+l_a)}\left(e^{2my}+e^{2ml_b}\right)\delta(\xi)}{\left(-1+e^{2m(l_a+l_b)}\right)p}e^{-i\xi x}d\xi \tag{2-43}$$

where In_1 is an integral function and expressed as

$$In_1 = -\frac{e^{-my}\left(\left(1+e^{2my}\right)\left(-1+e^{2m(l_a+l_b)}\right)Bi_c + \left(1+e^{2m(y+l_a)}\right)\left(1+e^{2ml_b}\right)m\right)}{\left(-1+e^{2m(l_a+l_b)}\right)\xi} \tag{2-44}$$

The lengthy integral function may be broken into two less complicated functions by using the Fourier transform convolution property

$$F^{-1}\left[\tilde{f}(\xi)\cdot\tilde{g}(\xi)\right] = f(x) * g(x) \tag{2-45}$$

Take advantage of Equation (2-45) and the delta function property (2-30), (2-43) can be written as

$$\int_0^{\infty}\bar{\phi}(\eta)\cdot\lim_{y\to 0}\int_{-\infty}^{\infty}\frac{i}{2}In_1e^{-i\xi(x-\eta)}d\eta = \frac{m_0e^{m_0l_a}\left(1+e^{2m_0l_b}\right)}{\left(-1+e^{2m_0(l_a+l_b)}\right)p} \tag{2-46}$$

It is clear that In_1 is an odd function with respect to ξ, by using Euler's formula, we obtain

$$\int_0^{\infty}\bar{\phi}(\eta)\cdot\lim_{y\to 0}\int_0^{\infty}In_1\sin\left[\xi(x-\eta)\right]d\eta = \frac{m_0e^{m_0l_a}e^{2m_0l_b}}{\left(-1+e^{2m_0(l_a+l_b)}\right)p} \tag{2-47}$$

It is worthy to point out that

$$\lim_{\substack{y\to 0\\ \xi\to\infty}} In_1 = -1 \tag{2-48}$$

Thus, using the relations[124]

$$\lim_{y\to 0}\int_0^{\infty} e^{-\xi y}\sin\left[\xi\left(x-\eta\right)\right]d\xi=\lim_{y\to 0}\frac{x-\eta}{y^2+\left(x-\eta\right)^2}=\frac{1}{x-\eta} \tag{2-49}$$

We readily obtain the following singular integral equation in which the only unknown is $\bar{\phi}$

$$\int_{-1}^{1}\bar{\phi}\left(\eta\right)\left[\frac{1}{\eta-x}+k\left(x,\eta\right)\right]d\eta=g_1\left(x\right) \tag{2-50}$$

where $k\,(x,\,\eta)$ is the Fredholm kernel and given by

$$k\left(x,\eta\right)=\int_0^{\infty}\left[1-\frac{2Bi}{\xi}-\frac{\left(1+e^{2l_a m}\right)\left(1+e^{2l_b m}\right)m}{\left(-1+e^{2(l_a+l_b)m}\right)\xi}\right]\sin\xi\left(x-\eta\right)d\xi \tag{2-51}$$

and

$$g_1\left(x\right)=\frac{2\pi m_0 e^{l_a m_0}\left(1+e^{2l_b m_0}\right)}{\left(-1+e^{2m_0(l_a+l_b)}\right)p} \tag{2-52}$$

Equation (2-50) is the singular integral equation of the first kind which arises from the formulation of the mixed boundary value conditions.

In addition, by applying the previous method to (2-40), we can rewrite the temperature field in the following form

$$\begin{cases}\bar{T}_1=\dfrac{1}{2\pi}\displaystyle\int_{-1}^{1}\bar{\phi}\left(\eta\right)\cdot\int_0^{\infty}\frac{e^{-my}\left(1+e^{2l_b m}\right)\left(1-e^{2m(l_a+y)}\right)}{\left(-1+e^{2(l_a+l_b)m}\right)\xi}\cos\left[\xi\left(x-\eta\right)\right]d\xi d\eta+\frac{e^{m_0(l_a+2l_b-y)}-e^{m_0(l_a+y)}}{\left(-1+e^{2(l_a+l_b)m_0}\right)p}\\ \bar{T}_2=\dfrac{1}{2\pi}\displaystyle\int_{-1}^{1}\bar{\phi}\left(\eta\right)\cdot\int_0^{\infty}\frac{e^{-my}\left(1+e^{2l_a m}\right)\left(e^{2l_b m}-e^{2my}\right)}{\left(-1+e^{2(l_a+l_b)m}\right)\xi}\cos\left[\xi\left(x-\eta\right)\right]d\xi d\eta+\frac{e^{m_0(l_a+2l_b-y)}-e^{m_0(l_a+y)}}{\left(-1+e^{2(l_a+l_b)m_0}\right)p}\end{cases} \tag{2-53}$$

2.5 Solution of the Singular Integral Equation

2.5.1 Fundamental Function of the Singular Integral Equation

Equation (2-50) can be rewritten as:

$$\int_{-1}^{1}\frac{\bar{\phi}\left(\eta\right)}{\eta-x}d\eta+\int_{-1}^{1}\bar{\phi}\left(\eta\right)\cdot k\left(x,\eta\right)d\eta=g_1\left(x\right) \tag{2-54}$$

which is called as *"Singular integral equations of the first kind"*. Since $\bar{\phi}(t)$ and $k(x, \eta)$ are Hausdorff continuous functions[125], the second term in Equation (2-54) is a bounded function of x. Hence, the singular behavior of $\bar{\phi}(t)$ may be obtained by studying the first term of (2-54) only. We define:

$$\int_{-1}^{1} \frac{\bar{\phi}(\eta)}{\eta - x} d\eta = G(x) \tag{2-55}$$

where $G(x)$ contains the input function $g_1(x)$ and the second term of the integral in Equation (2-56). We rewrite the solution form of the integral equation $\bar{\phi}(x)$ as:

$$\bar{\phi}(x) = \psi(x) w(x) \tag{2-57}$$

where $\psi(x)$ is the new unknown function; $w(x)$ is known as the "fundamental function" of the singular integral equation and expressed as

$$w(x) = (1-x)^{\frac{1}{2}+N} (1+x)^{-\frac{1}{2}+M} \tag{2-58}$$

where N and M can be obtained from the boundary condition (2-50). It is clear from the singles-value condition (2-33) and (2-34) that the function $\bar{\phi}(x)$ has integrable singularities at both end, (-1,0) and (1,0), then we have [126]:

$$\begin{cases} N = -1 \\ M = 0 \end{cases} \tag{2-59}$$

so Equation (2-58) and (2-57) lead to

$$w(x) = (1-x^2)^{-\frac{1}{2}} \tag{2-60}$$

and

$$\bar{\phi}(x) = \frac{\psi(x)}{\sqrt{1-x^2}} \tag{2-61}$$

2.5.2 Cauchy Integral

Following the method introduced by Muskhelishvili[127], we introduce a new function $\Psi(x)$ and let

$$\Psi(x) = \frac{1}{2\pi i} \int_{-1}^{1} \frac{\bar{\phi}(\eta)}{\eta - x} d\eta \tag{2-62}$$

where x is any point of the plane and $\Psi(x)$ is called the *Cauchy integral*[127]. The

Cauchy integral may naturally be defined for much larger class of functions $\bar{\phi}(\eta)$ at the line $(y=0,-1<x<1)$.

The boundary values of $\Psi(x)$ are related to the following Plemelj formulas[128] which were given by Plemelj Josip in 1908:

$$\begin{cases} \Psi^{+}(x)-\Psi^{-}(x)=\bar{\phi}(x) \\ \Psi^{+}(x)+\Psi^{-}(x)=\dfrac{1}{\pi i}\displaystyle\int_{-1}^{1}\dfrac{\bar{\phi}(\eta)}{\eta-x}dt \end{cases} \tag{2-63}$$

where $\Psi^{+}(x)$ and $\Psi^{-}(x)$ stands for

$$\begin{cases} \Psi^{+}(x)=\dfrac{1}{2}\bar{\phi}(x)+\dfrac{1}{2\pi i}\displaystyle\int_{-1}^{1}\dfrac{\bar{\phi}(\eta)}{t-x}d\eta \\ \Psi^{-}(x)=-\dfrac{1}{2}\bar{\phi}(x)+\dfrac{1}{2\pi i}\displaystyle\int_{-1}^{1}\dfrac{\bar{\phi}(\eta)}{t-x}d\eta \end{cases} \tag{2-64}$$

Substituting Equation(2-55) into (2-63), then we obtain the following Riemann-Hilbert problem to determine $\Psi(x)$:

$$\Psi^{+}(x)+\Psi^{-}(x)=\frac{1}{\pi i}G(x) \tag{2-65}$$

The solution of Equation (2-65) may easily be expressed as[127]

$$\Psi(x)=-\frac{Y(x)}{2}\int_{-1}^{1}\frac{G(\eta)}{(\eta-x)Y^{+}(\eta)}d\eta+c\cdot Y(x) \tag{2-66}$$

where c is a constant and $Y(x)$ is the fundamental solution of the problem. It is clear that $Y(x)$ satisfies the following homogeneous boundary conditions:

$$\begin{cases} Y^{+}(x)+Y^{-}(x)=0 & |x|<1 \\ Y^{+}(x)-Y^{-}(x)=0 & |x|>1 \end{cases} \tag{2-67}$$

By ignoring an arbitrary multiplicative holomorphic function, the most general solution of Equation (2-67) may be expressed as

$$Y(x)=\frac{w(x)}{i(-1)^{N}}=\frac{1}{\sqrt{x^{2}-1}} \tag{2-68}$$

By substituting (2-66) into (2-63) and by making use of the relations (2-67), the solution of the integral equation (2-55) is found to be

$$\begin{aligned}\bar{\phi} &= \Psi^{+}(x) - \Psi^{-}(x) \\ &= 2cY^{+}(x) - Y^{+}(x)\int_{-1}^{1}\frac{G(\eta)}{(\eta - x)Y(\eta)}d\eta \quad -1 < x < 1\end{aligned} \tag{2-69}$$

Due to the singular nature of the function $\bar{\phi}(x)$, an additional condition is needed to determine the constant c in Equations (2-66) and (2-69), and thus to obtain a unique solution. In the present case, this condition is the Laplace transform of Equation (2-33)

$$\int_{-1}^{1}\bar{\phi}(x)dx = 0 \tag{2-70}$$

2.5.3 Numerical Integration

An effective numerical solution of the Fredholm integral Equation (2-54) can be obtained by using a quadrature formula of the Gaussian type with appropriately selected orthogonal polynomial and values of x_j (j = 1, …, n). Thereby Equation (2-54) can be reduced to the following system of linear algebraic equations of the unknown function $\psi(\eta_i)$, written as

$$\sum_{i=1}^{n} W_i \psi(\eta_i)\left[\frac{1}{\eta_i - x_j} + k(x_j, \eta_i)\right] + R_n(x_j) = g(x_j) \qquad i = 1, \ldots, n \tag{2-71}$$

where W_i (i = 1, …, n) are the weights and R_n is the remainder. Normally R_n can be made sufficient small by choosing n large enough. The discrete points η_i (i = 1, …, n) correspond to the zeros of the orthogonal polynomials which related to the particular Gaussian quadrature[129, 130].

In fact, the fundamental function $w(x)$ in Equation (2-60) is the corresponding weight function in Equation (2-71) and the related orthogonal polynomial in (2-71) is the Jacobi polynomials $P_n^{(\alpha,\beta)}(x)$ [131].

$$P_n^{(\alpha,\beta)}(x) = \frac{(-1)^n}{2^n n!(1-x)^{\alpha}(1+x)^{\beta}}\frac{d^n}{dx^n}\left[(1-x)^{n+\alpha}(1+x)^{n+\beta}\right] \tag{2-72}$$

where the exclamation marker "!" stands for the factorial operation and

$$\begin{cases}\alpha = \dfrac{1}{2} + N \\ \beta = -\dfrac{1}{2} + M\end{cases} \tag{2-73}$$

It should be noticed that the Greek letter *"α"* used in Jacobi polynomial is a common parameter which should be distinguished from the thermal expansion coefficient.

It is clear that both the value of α and β is -1/2 in the case of N = -1 and M = 0 such that the orthogonal polynomial would be reduced to the Chebyshev polynomial of the first kind T_n (x). The integral equation (2-54) and the additional condition (2-70) may be expressed as[132]

.. (2-74)

where η_i and x_j can be obtained from the following equations

$$\begin{cases} T_n(\eta_i) = 0 \\ U_{n-1}(x_j) = 0 \end{cases} \tag{2-75}$$

then we have

$$\begin{cases} \eta_i = \cos\left(\dfrac{2i-1}{2n}\pi\right), & (i = 1, \ldots, n) \\ x_j = \cos\dfrac{j\pi}{n}, & (j = 1, \ldots, n-1) \end{cases} \tag{2-76}$$

The unknown function $\psi(\eta_i)(i = 1, 2, \ldots, n)$ can be determined by the n linear algebraic equations provided by (2-74). The temperature field in Laplace space can be obtained by substituting $\psi(\eta_i)$ into (2-57) then into (2-53)

2.6 Convergence Analysis

2.6.1 Numerical Integration Interval

Noting that the integration interval of (2-51) has an infinite upper border, therefore, the integral can also be expressed as:

$$k(x,\eta) = k^M(x,\eta) + O(0) \tag{2-77}$$

where

$$\begin{cases} k^M(x,\eta) = \displaystyle\int_0^{M\cdot T}\left[1 - \frac{2Bi}{\xi} - \frac{\left(1+e^{2l_a m}\right)\left(1+e^{2l_b m}\right)m}{\left(-1+e^{2(l_a+l_b)m}\right)\xi}\right]\sin\xi(x-\eta)\,d\xi \\ O(0) = \displaystyle\int_{M\cdot T}^{\infty}\left[1 - \frac{2Bi}{\xi} - \frac{\left(1+e^{2l_a m}\right)\left(1+e^{2l_b m}\right)m}{\left(-1+e^{2(l_a+l_b)m}\right)\xi}\right]\sin\xi(x-\eta)\,d\xi \end{cases} \tag{2-78}$$

where T is the oscillation period of the integrand and obtained by:

$$T = \frac{2\pi}{|x-\eta|}, \quad 0 < |x-\eta| < 2 \tag{2-79}$$

M is a large integer number which denotes the number of the periods contained in the integral interval. By considering the convergence and the periodicity of the integrand it is clear that

$$\begin{cases} k^{M}(x,\eta) < k(x,\eta) < k^{M+\frac{1}{2}}(x,\eta), & \text{integrand} < 0 \\ k^{M+\frac{1}{2}}(x,\eta) < k(x,\eta) < k^{M}(x,\eta), & \text{integrand} > 0 \end{cases} \tag{2-80}$$

where

$$k^{M+\frac{1}{2}}(x,\eta) = \int_{0}^{\left(M+\frac{1}{2}\right)T} \left[1 - \frac{2Bi}{\xi} - \frac{\left(1+e^{2l_a m}\right)\left(1+e^{2l_b m}\right)m}{\left(-1+e^{2(l_a+l_b)m}\right)\xi} \right] \sin\xi(x-\eta)\,d\xi \tag{2-81}$$

Then the error bounds can be expressed as:

$$|O(0)| < \text{error}_{max} = \left| k^{M+\frac{1}{2}} - k^{M} \right| = \left| \int_{M}^{\left(M+\frac{1}{2}\right)T} \left[1 - \frac{2Bi}{\xi} - \frac{\left(1+e^{2l_a m}\right)\left(1+e^{2l_b m}\right)m}{\left(-1+e^{2(l_a+l_b)m}\right)\xi} \right] \sin\xi(x-\eta)\,d\xi \right|$$

(2-82)

and the maximum relative error:

$$\text{Relative error} = \left| \frac{k^{M+\frac{1}{2}} - k^{M}}{k^{M}} \right| \tag{2-83}$$

First we take the total number of the Gauss points $n = 16$. The choice of n will be discussed in detail in the next subsection. By using Equation (2-76) it follows that

$$0.00548 < |x_j - \eta_i| < 1.99 \tag{2-84}$$

By selecting different values of the parameters as listed in Table 2.6-1, the results of the numerical integration and the error bonds are obtained.

Table 2.6-1 shows the absolute and relative errors and the numerical approximations for different parameters when the number of the oscillation periods in the integral interval, M, is set to be 40 and p is set to be 1. By comparing the values of the absolute errors and the approximations we can conclusion that the numerical integration has sufficient accuracy when $M = 40$.

$\lvert x_j-\eta_i \rvert$	Bi_c	τ_1	$\lvert k^M(x,\eta) \rvert$	Absolute error	Relative error
0.00548	0	0	0.019797	5.51E-08	2.78E-06
		0.2	0.023125	6.59E-08	2.85E-06
	1	0	3.155023	0.012669	0.004016
		0.2	3.158352	0.012669	0.004011
	1000	0	3135.246	12.66911	0.004041
		0.2	3135.25	12.66911	0.004041
0.5	0	0	0.678933	5.02E-06	7.39E-06
		0.2	0.75975	6.02E-06	7.92E-06
	1	0	3.81416	0.012674	0.003323
		0.2	3.894977	0.012675	0.003254
	1000	0	3135.906	12.66911	0.00404
		0.2	3135.986	12.66912	0.00404
1.99	0	0	1.340396	2E-05	1.49E-05
		0.2	1.455808	2.4E-05	1.65E-05
	1	0	4.475622	0.012689	0.002835
		0.2	4.591035	0.012693	0.002765
	1000	0	3136.567	12.66913	0.004039
		0.2	3136.682	12.66913	0.004039

Table 2.6-1 Numerical approximations, absolute and relative errors for different parameters when p and M are set to be 1 and 40, respectively.

2.6.2 Number of Gauss Points

In the previous section, the singular integral equation is successfully converted into a linear system of the size n by n, where n is the total terms that make up the density functions. The error analysis of Gaussian quadrature indicates that accuracy of

the integral would be improved by increasing the total number of the Gauss points, n. However, the computational task required for the higher order approximations increases quickly with n in a quadratic way. In order to determinate the appropriate n which gives sufficient accuracy and does not take too long computational time, we study the relations between the numerical accuracy and the number of terms n used in the approximation.

To this end, we just carry out a case study for the problem in Laplace space by taking the following parameter values: distances between the crack and the boundaries $l_a = 1$ and $l_b = 2$; the Biot number Bi = 0; the non-Fourier factor $\tau_1 = 0.1$ and the Laplace parameter $p = 1$.

The temperature of the mid-points of the crack surfaces in Laplace domain as a function of n is illustrated in Figure 2.6-1. Figure 2.6-1 shows that the accuracy would be sufficient if $n > 10$. Noting that the result of temperature field will be used in solving the stress fields, therefore, sufficient accuracy of the temperature field is required. We will use $n = 16$ in our analysis in order to ensure the accuracy of stress fields.

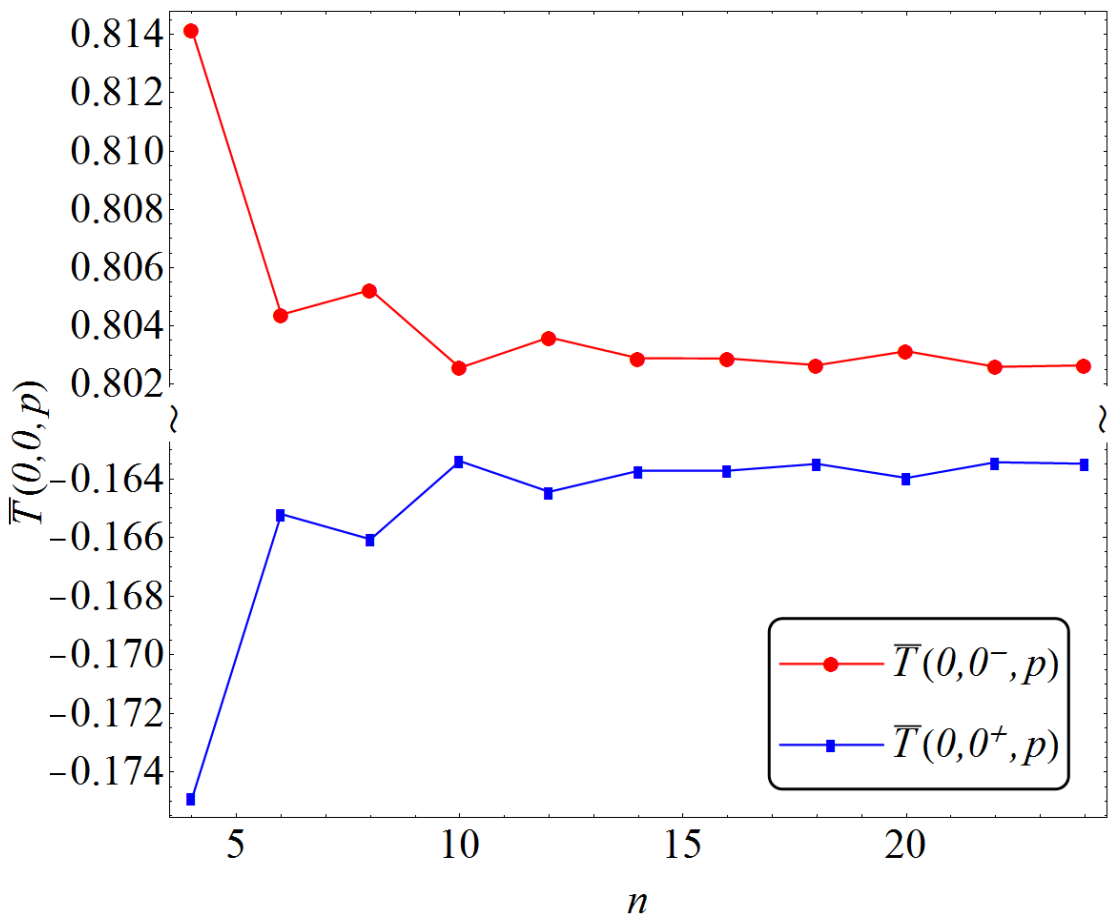

Figure 2.6-1 Temperature in Laplace space at the mid-point of the crack surfaces versus the number of Gauss points for Bi=0, τ_1=0.1, p=1

2.7 Numerical Inversion of the Laplace Transform

The previous sections give the solutions of the temperature field in Laplace space. Inversion of the transformed function from the Laplace variable p domain to the time variable t domain should be applied to obtain the actual temperature field. However, the available inversion tables of the Laplace transform don't provide explicit inversion formula of the present problem because of the complexity of the expression. Therefore, numerical methods for the inversion of the Laplace transform will be used in this section.

A number of numerical inversion methods have been proposed in the literature [119, 133-142]. However, there is no method that is efficient for all types of problems. In this thesis, the Jacobi polynomial method developed by Miller [119] is used. This method is characterized by its good accuracy and fast running speed on digital computers.

In Miller's method, the coefficient α and β used in Jacobi polynomial are usually appears to be

$$\begin{cases} \alpha = 0 \\ \beta > 1 \end{cases} \tag{2-85}$$

Then Equation (2-72) is reduced to be:

$$P_n^{(0,\beta)}(x) = \frac{(-1)^n}{2^n n!(1+x)^\beta} \frac{d^n}{dx^n}\left[(1-x)^n (1+x)^{n+\beta}\right] \tag{2-86}$$

We consider the Laplace transform of an arbitrary function $f(t)$

$$F(p) = \int_0^\infty f(t) e^{-pt} dt \tag{2-87}$$

From the definition(2-87), the inverse Laplace transform is

$$f(t) = \frac{1}{2\pi i} \int_{\gamma - i\infty}^{\gamma + i\infty} F(p) e^{pt} dp \tag{2-88}$$

First we transform the variable t to a new variable ζ, which is defined as

$$\zeta = 2e^{-\delta t} - 1 \tag{2-89}$$

where δ is a real positive number. Then the function in time domain can be redefined

as:

$$g(\zeta) = f(t) = f\left(-\frac{1}{\delta}\log\left(\frac{1+\zeta}{2}\right)\right) \tag{2-90}$$

In addition, g (1) and g (-1) are redefined to extend the domain of definition by

$$\begin{cases} g(1) = \lim\limits_{\zeta \to 1^-} g(x) \\ g(-1) = \lim\limits_{\zeta \to -1^+} g(x) \end{cases} \tag{2-91}$$

It is obvious from Equation (2-91) that $f(0) = \lim\limits_{t \to 0^+} f(0)$ and $f(\infty) = \lim\limits_{t \to \infty} f(\infty)$ should be limit.

Substituting (2-89) into (2-19) and applying the relation (2-90) then we have

$$F(p) = \frac{1}{2\delta}\int_{-1}^{1}\left(1+\frac{x}{2}\right)^{\frac{s}{\delta}-1} g(\zeta)d\zeta \tag{2-92}$$

Assume that $g(\zeta)$ can be expanded over $[-1, 1]$ in the terms of the Jacobi polynomials, then

$$g(\zeta) = \sum_{i=0}^{\infty} C_{L,i} P_i^{(0,\beta)}(\zeta) \tag{2-93}$$

where $C_{L,i}$ (i=0, 1, …, n) are determined by the following algebraic equations

$$\delta \cdot F\left(\delta(\beta+1+j)\right) = \sum_{i=0}^{j} \frac{j!(j+\beta)!}{(j-i)!(j+\beta+1+i)!} C_{L,i} \tag{2-94}$$

By allowing j = 0, 1, …, n, respectively, we have the following equations:

$$\begin{cases} \delta \cdot F\left(\delta(\beta+1)\right) = \dfrac{C_{L,0}}{\beta+1} \\ \delta \cdot F\left(\delta(\beta+2)\right) = \dfrac{C_{L,0}}{\beta+2} + \dfrac{C_{L,1}}{(\beta+2)(\beta+3)} \\ \delta \cdot F\left(\delta(\beta+3)\right) = \dfrac{C_{L,0}}{\beta+3} + \dfrac{2C_{L,1}}{(\beta+3)(\beta+4)} + \dfrac{2C_{L,2}}{(\beta+3)(\beta+4)(\beta+5)} \\ \quad \vdots \end{cases} \tag{2-95}$$

Thus $C_{L,i}$ can be obtained by solving the linear equations (2-95). Substituting Equations (2-90), (2-89) and the solution of $C_{T,i}$ into (2-93), finally we obtain

$$f(t) \approx \sum_{i=0}^{n} C_{L,i} P_i^{(0,\beta)}\left(2e^{-\delta t} - 1\right) \tag{2-96}$$

The error analysis was performed in detail by Miller [119]. Here we just verify the accuracy and the convergence of (2-96) by inverting a specific function as

follows:

$$F(p)=\frac{pe^{-a\sqrt{p}}}{\sqrt{p}+b} \tag{2-97}$$

The inverse Laplace transform of function (2-97) can be obtained analytically by using the table of the Laplace transform pairs[143]. The known inversion is

$$f(t)=\frac{1}{t\sqrt{\pi t}}\left(b^2t-\frac{1}{2}-\frac{1}{2}ab+\frac{a^2}{4t}\right)e^{-\frac{a^2}{4t}}-b^3e^{ab+b^2t}\operatorname{erfc}\left(\frac{a}{2\sqrt{t}}+b\sqrt{t}\right) \tag{2-98}$$

Now we take a = 1 and b = 3 for example. The parameter β_0 is set to be 0. Figure 2.1-1 shows the comparison of the exact and numerical inverse Laplace transforms of (2-97) for different n. It shows that n=19 gives already very satisfactory numerical result comparing with the analytical one.

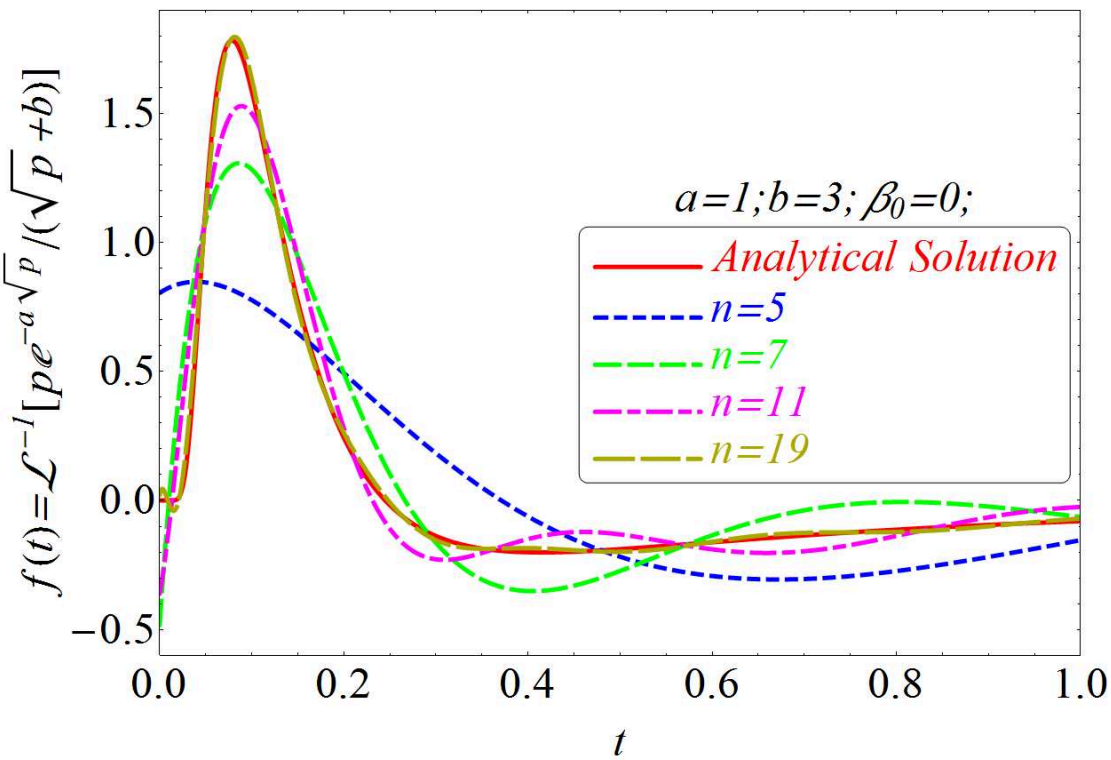

Figure 2.7-1 Appriximations for Equation (2-98)

Chapter 3 Numerical Results on Temperature Field

In the earlier chapter, we analyzed the heat conduction problem under mixed boundary condition. Particularly, hyperbolic heat conduction was used to develop the governing equation. The thermal contact resistance of the crack was considered by introducing appropriate boundary conditions. By following the numerical procedure described-above, this isothermal thermal conduction problem can be resolved. In this chapter, we will focus our attention on the physical implications of the Non-Fourier Factor (NFF) and the Biot number in the evolution of the temperature field.

The considered heat conduction problem was schemed in Figure 2.1-1. In this chapter the dimensionless distances between the crack surfaces and the boundary, l_a and l_b, are set to be 1 and 2, respectively. As a consequence, the value of Bi_c will be equal to the Biot number. In the following analysis, we will use Bi instead of Bi_c.

The material parameters k, a are included in Bi and NFF, respectively so their influences will not be discussed separately.

3.1 Biot Number's Effects

In this section we will investigate the behavior of the Biot number by omitting the non-Fourier effect, i.e., by setting $\tau_1 = 0$. Under this condition, the heat conduction problem is reduced to the Fourier heat conduction problem.

We recall that the Biot number is defined in Equation (2-12). This parameter gives a simple indication of the ratio of the heat transfer resistance of the crack gap.

When the Biot number equals zero, the boundary condition (b) in (2-17) can be reduced to

$$\left.\frac{\partial T}{\partial y}\right|_{y\to 0^-} = \left.\frac{\partial T}{\partial y}\right|_{y\to 0^+} = 0, \qquad |x| < 1 \tag{3-1}$$

which gives a perfectly adiabatic condition of the crack gap and is called as *the homogeneous boundary condition of the second kind*, or in mathematics, the *Neumann boundary condition*. While in the limit case when the Biot number tends to the

infinity, the boundary condition (*b*) in (2-17) yields:

$$T\left(x,0^{-},t\right)=T\left(x,0^{+},t\right),\quad |x|<1 \tag{3-2}$$

This equation denotes that the crack gap has a perfect thermal conductivity and is called as the *homogeneous boundary condition of the first kind*. In mathematics, boundary conditions of the first kind are also called the Dirichlet boundary conditions.

In the following analyses, the Biot number is chosen to be 0, infinity and some values between the two limits.

Our numerical calculations show that Bi > 1000 can be regarded as the infinity. In this case, the temperature field is reduced to that obtained with a non-crack model. That is, if the heat transfer coefficient satisfies the following condition

$$h > \frac{1000k}{r} \tag{3-3}$$

the influence of the crack can be neglected in solving the temperature field.

3.1.1 Full Temperature Fields

We first present the stationery temperature fields in the cracked strip for $t \to \infty$. The plot range of the domain is set to be $-2 \le x \le 2$ and $-1 \le y \le 2$ around the crack, as shown in Figure 3.1-3. The dimensionless time is set to be 1000, which can be considered as long enough such that the temperature fields become stationery. The temperature fields are shown in Figure 3.1-1 for different values of the Biot number, namely Bi = 0, 0.2 and 1 and infinity, respectively. In this figure and also in the following one, the temperature levels are represented by means of gradually changed colors, and more precisely, the iso-value lines of the temperature are indicated by the dot lines.

From Figure 3.1-1, we can observe that the temperature field is disturbed by introducing a crack into the strip. This distribution gets stronger as the Biot number decreases. In fact, Bi = 0 means that the crack is totally heat-insulated. In this case, we have the maximum temperature difference between the two crack surfaces. As the Biot number increases, the temperature jump between the crack surfaces deceases and finally disappears for Bi→∞. Physically speaking, the existence of a crack gap creates a heat barrier in the strip. As a result, a temperature jump between the crack surfaces is produced, which constitutes a principal source of stress concentration around the

crack tips.

The time-evolution of the dimensionless temperature field under the *homogeneous boundary condition of the second kind* at the crack surfaces, i.e., Bi = 0, is shown in Figure 3.1-2. The pictures are taken at the dimensionless times t^* = 0.1, 0.2, 0.5 and 1, respectively

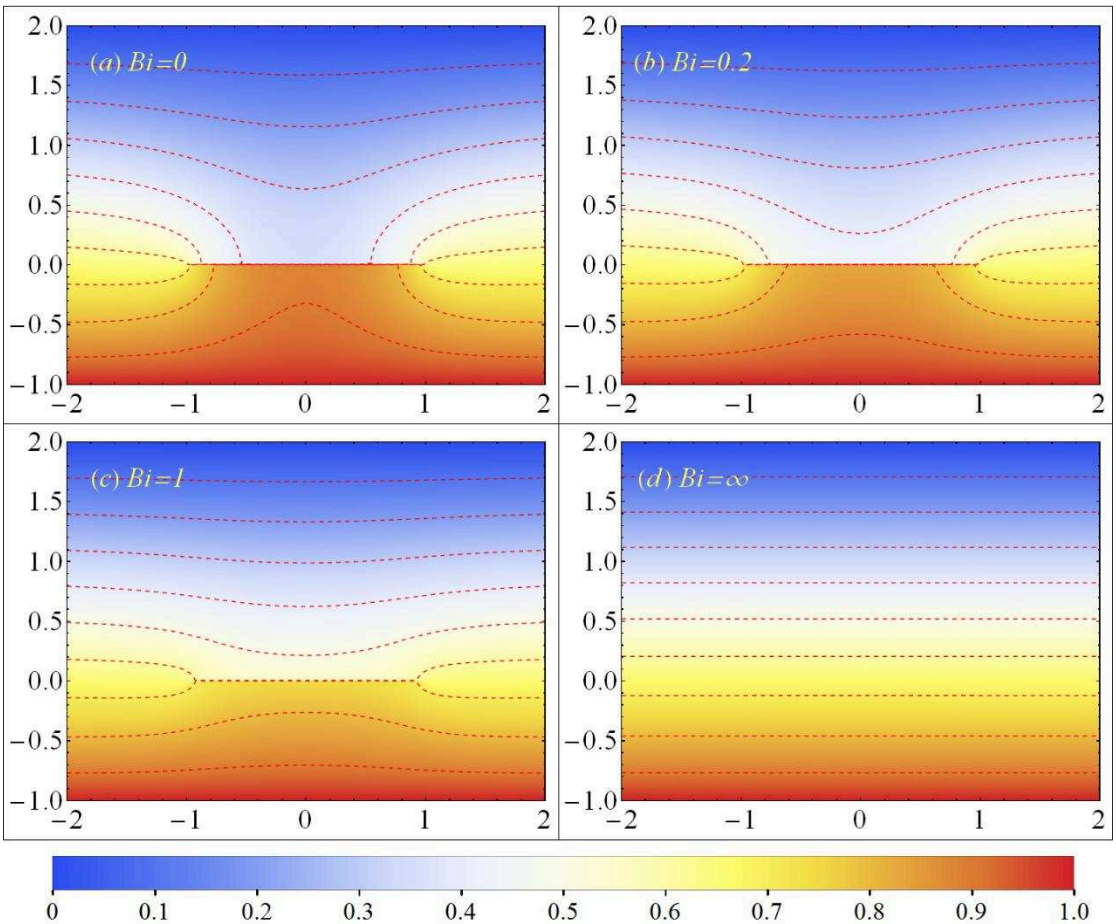

Figure 3.1-1 Temperature fields in near crack domain for t^*=∞ and NFF =0. (a): Bi = 0; (b): Bi = 0.2; (c): Bi = 1; (d): Bi = ∞.

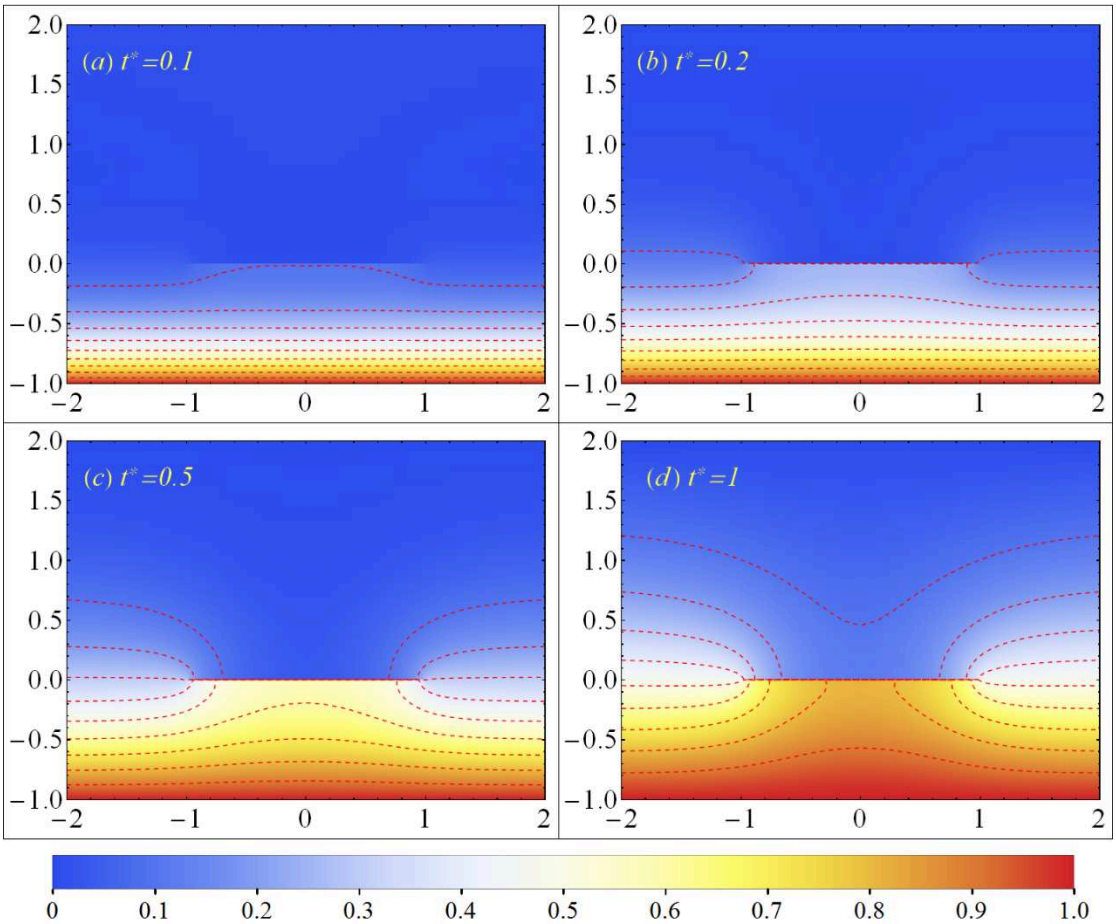

Figure 3.1-2 Temperature field in near crack domain for Bi=0 and NFF =0 at (a): $t^* = 0$; (b): $t^* = 0.2$; (c): $t^* = 1$; (d): $t^* = \infty$

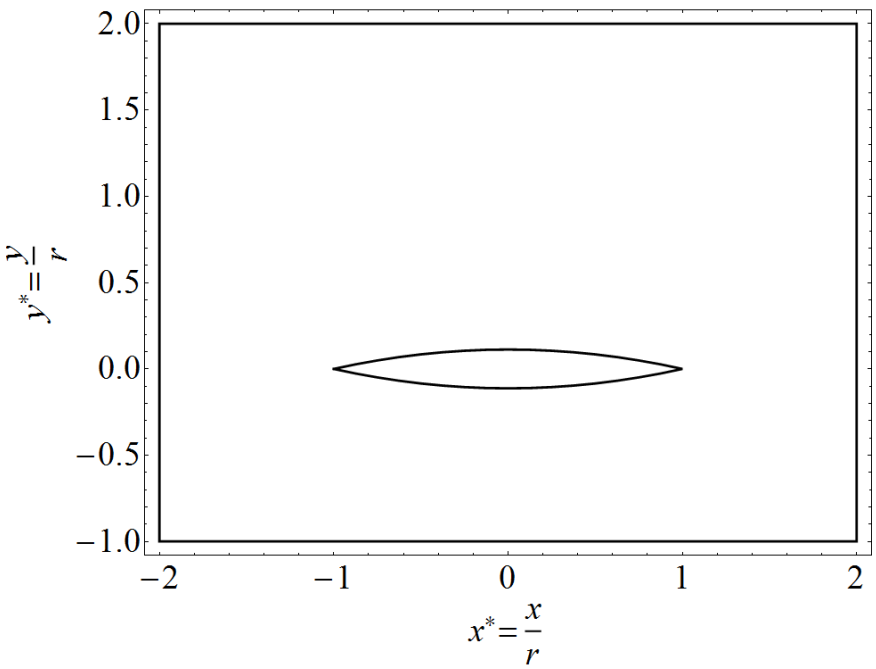

Figure 3.1-3 Coordinate domain. $-2 \leq x \leq 2$ and $-1 \leq y \leq 2$.

3.1.2 Temperatures at the Mid-Points of the Crack Surfaces

The variation of temperatures versus the dimensionless time at the mid-points of the crack surfaces is shown in Figure 3.1-4 for different Biot numbers. In Figure 3.1-4, the solid line and the dashed line denote the temperatures at the locations $(0, 0^-)$ and $(0, 0^+)$, respectively. The figure shows that the temperatures at these points gradually increase with the dimensionless time and finally converge to some asymptotic values. This gradually time-variation of the temperature is a characteristic feature of the Fourier law. It is shown that the temperature stays almost unchanged when $t^* > 8$. Consequently, it is reasonable to consider the $t^* = 1000$ as infinity in Figure 3.1-2.

From Figure 3.1-4, we can remark that the temperature jump between the crack surfaces is maximal for Bi=0, as shown by the red lines, that corresponds to a completely isolating crack gap. The temperature jump becomes gradually smaller as the Biot number increases. It tends to zero as the Biot number tends to the infinity, as shown by the black lines.

In order to better assess this temperature jump, we plot the temperature differences at the mid-point of the crack surfaces versus dimensionless time for different Biot numbers, as shown in Figure 3.1-5.

It is interesting to notice that even the temperatures at both the crack surfaces increase monotonically; their difference curves exhibit quite a different behavior. They first increase gradually at the early stage of the thermal shock, then decrease with time after reaching a peak value, and finally are flatten out. The main reason of this phenomenon is that the heating speeds of the two surfaces are different. It is clear that the thermal stresses around the crack essentially depend on the temperature jumps across the crack surfaces. Consequently, the peak value of the temperature jump will be a key factor that governs the maximal stress concentration. This point will be revised in stress analyses in Chapter 5.

From Figure 3.1-5, we can also observe that the peak value of the temperature jump decreases rapidly when the Biot number increases. Figure 3.1-6 shows the dimensionless temperatures at the mid-points of the crack surfaces versus the Biot number for different dimensionless times. It worthy to notice that the temperature jumps are already very small when Bi = 100 and almost nil when Bi = 1000.

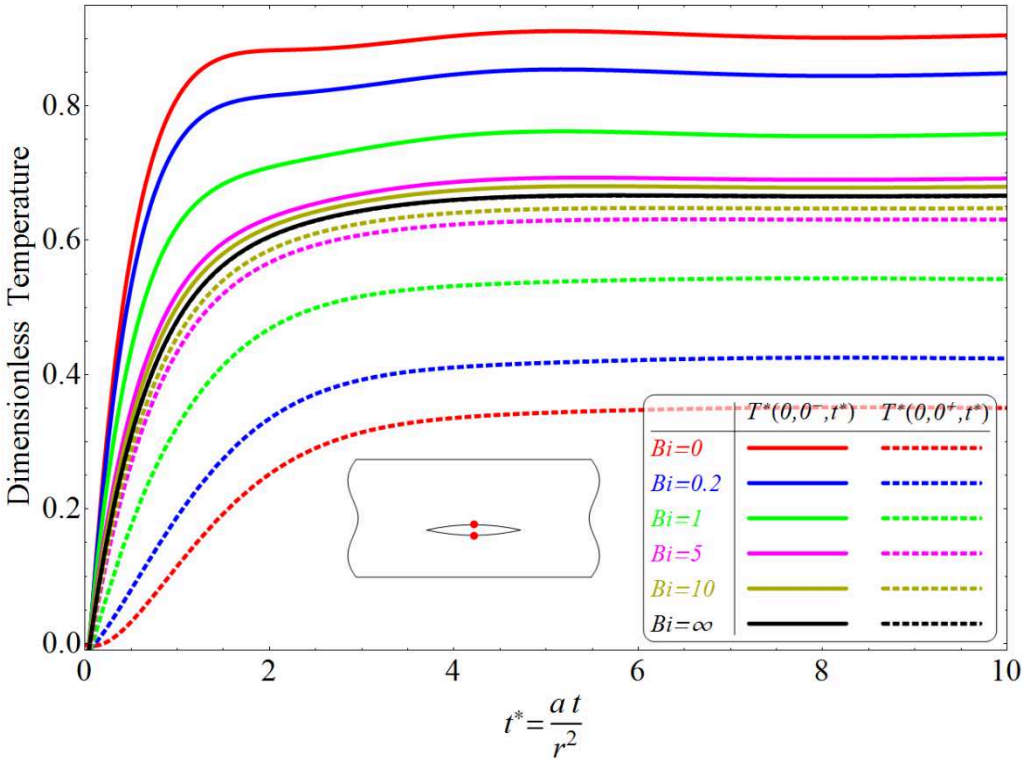

Figure 3.1-4 Dimensionless temperatures at the mid-points of the crack surfaces versus dimensionless time for different Biot numbers.

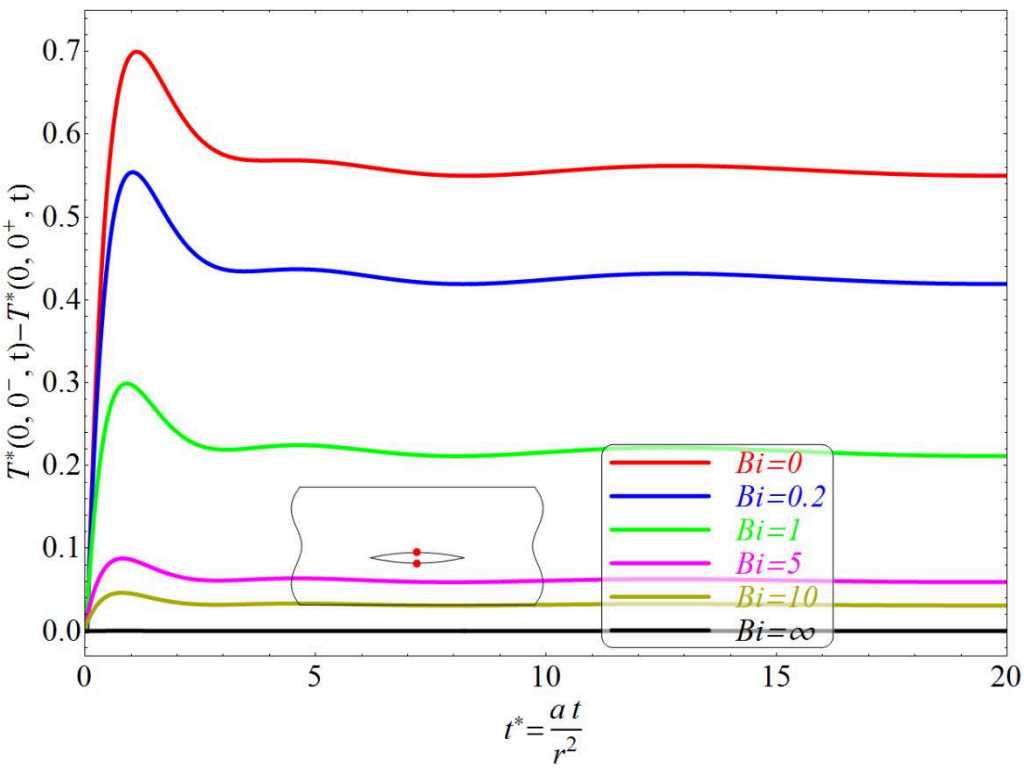

Figure 3.1-5 Dimensionless temperature differences of the mid-points of the crack surfaces versus dimensionless time for different Biot numbers.

Table 3.1-1 shows the maximal temperature differences of the point $(0, 0^-)$ and $(0, 0^+)$ and its corresponding dimensionless time to reach this value for different Biot numbers, where

$$dT = T\left(0, 0^- t\right) - T\left(0, 0^+ t\right) \tag{3-4}$$

The results show that the maximal of dT is brought forward by the increasing of Biot number. In other words, the higher the thermal conductivity of the crack gap is, the earlier the dT reach the maximal will be.

Bi	**Max(d*T*)**	t^*
0	0.699723	1.119692
0.2	0.554172	1.03199
0.4	0.457898	0.980545
0.6	0.389513	0.94671
0.8	0.338497	0.922721
1	0.299034	0.904794
2	0.187864	0.856504
5	0.087912	0.814326
10	0.046409	0.796537
100	0.004874	0.778151
1000	0.00049	0.776158

Table 3.1-1 Maximal temperature differences at the mid-points of the crack surfaces and its corresponding dimensionless time for different Biot numbers

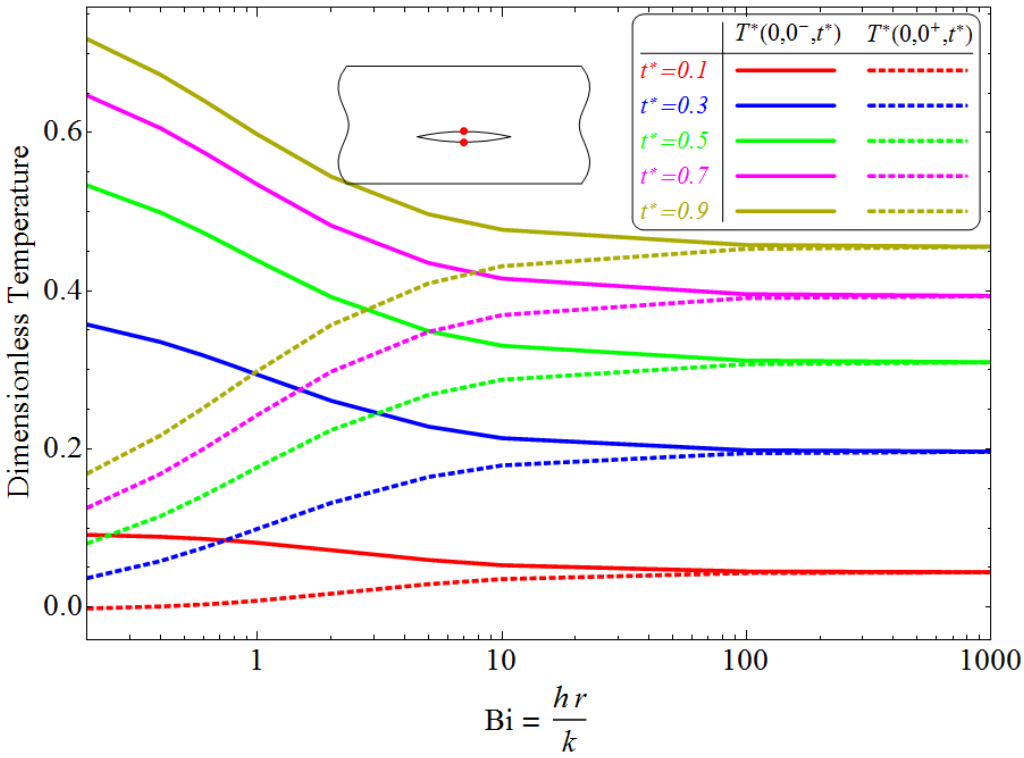

Figure 3.1-6 Dimensionless temperatures at the mid-points of the crack surfaces versus the Biot number for different dimensionless times.

3.1.3 Temperatures at the Line $x = 0$

The variation of temperature field versus the y coordinate at the line $x = 0$ is shown in Figure 3.1-7 and Figure 3.1-8. In Figure 3.1-7, the temperature variations are plotted for different Biot numbers with $t^* = \infty$; while in Figure 3.1-8 the Biot number is set to be 0 and the different curves stand for the different dimensionless times.

These two figures show that there is a temperature jump at the location (0, 0) across the crack line. This result agrees with the previous observations. It is noticeable that the closer the curves to the crack surfaces are, the less the temperature gradient will be.

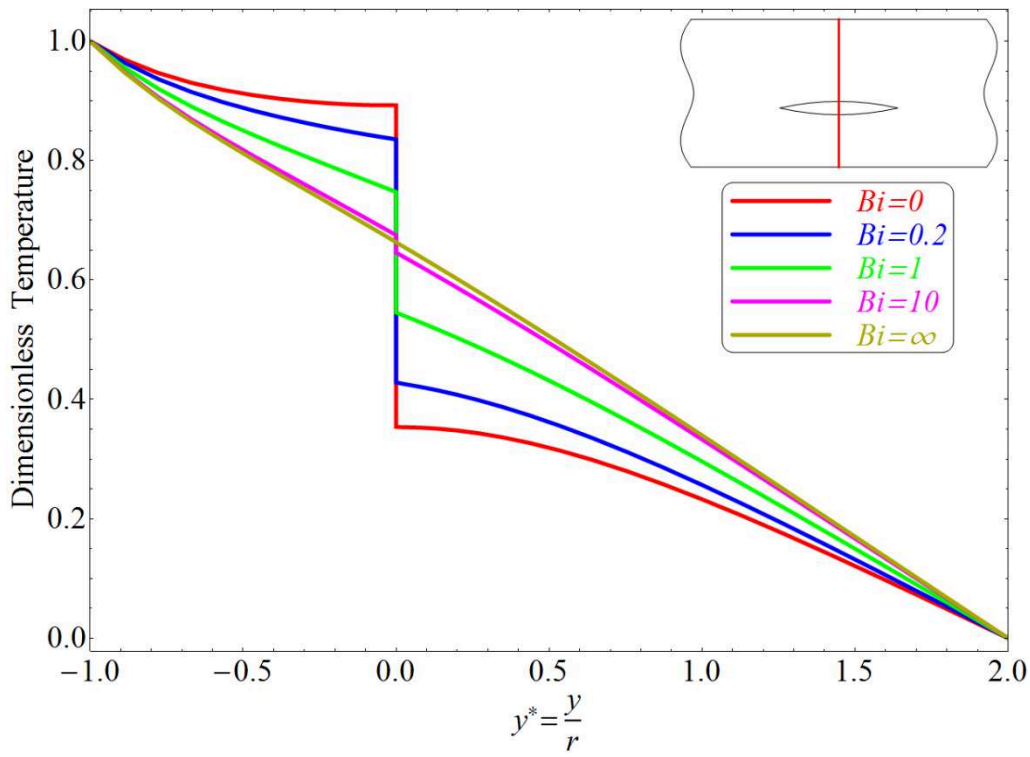

Figure 3.1-7 Dimensionless temperatures along the line x = 0 for different Biot numbers when $t^* \to \infty$.

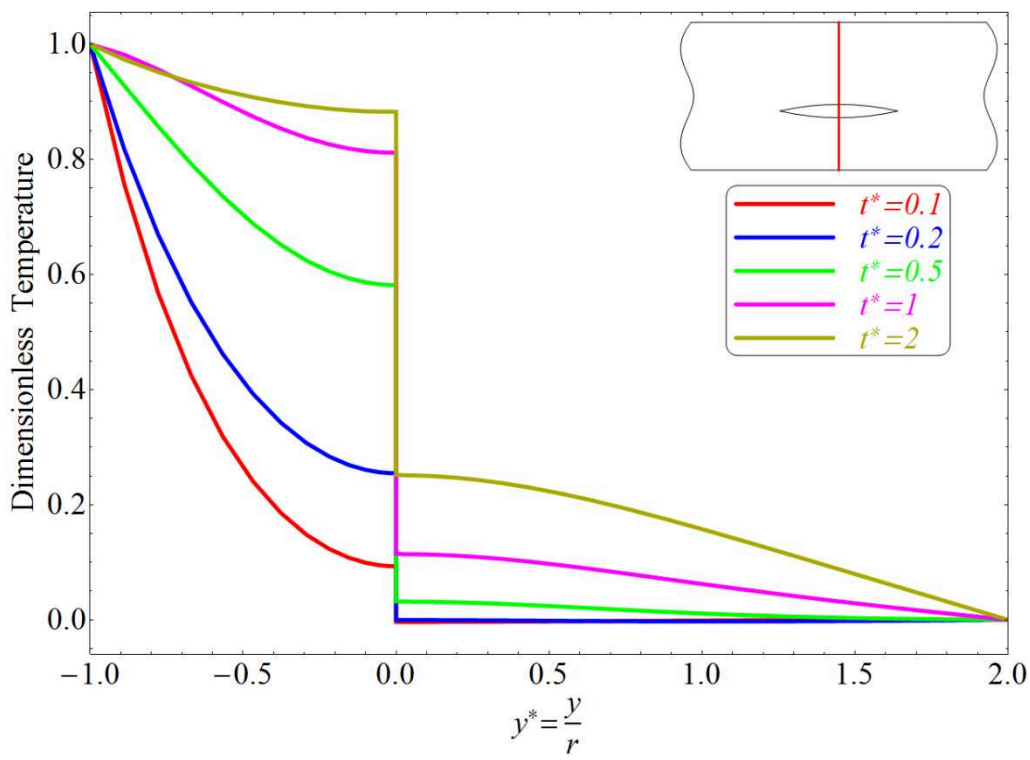

Figure 3.1-8 Dimensionless temperatures along the line x = 0 at different times when Bi = 0.

3.1.4 Temperature at the Line $y = 0$

The temperature variations along the line $y = 0$ are shown in Figure 3.1-9 and Figure 3.1-10. In Figure 3.1-9, the temperature variations are plotted for different Biot numbers with $t^* = \infty$; while in Figure 3.1-10 the Biot number is set to be 0 and the different curves stand for the different dimensionless times. These figures confirm the observations made previously in this section.

In summary, we can conclude that the Biot number plays a key role on the temperature distribution and evolution in the cracked strip subjected to thermal shock. The heat conduction barrier formed by the crack gap creates important temperature jump and consequently favorites the stress concentration at the crack tips.

The determination of the Biot number for a cracked plate involves a formidable challenge for experimental investigations. As this parameter depends on numerous factors such as the crack size, its location and orientation, the crack opening under loading, the working environment etc., judicious conception and careful manipulation in experiments should be necessary.

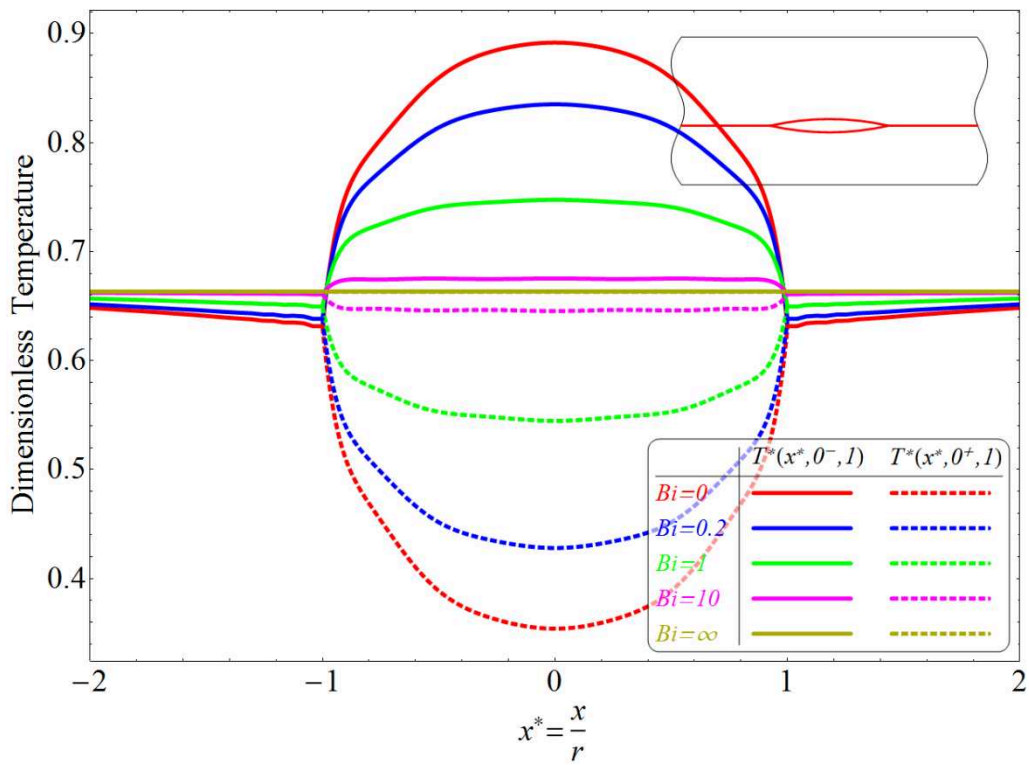

Figure 3.1-9 Temperatures along $y = 0$ for different Biot numbers when $t^* \to \infty$.

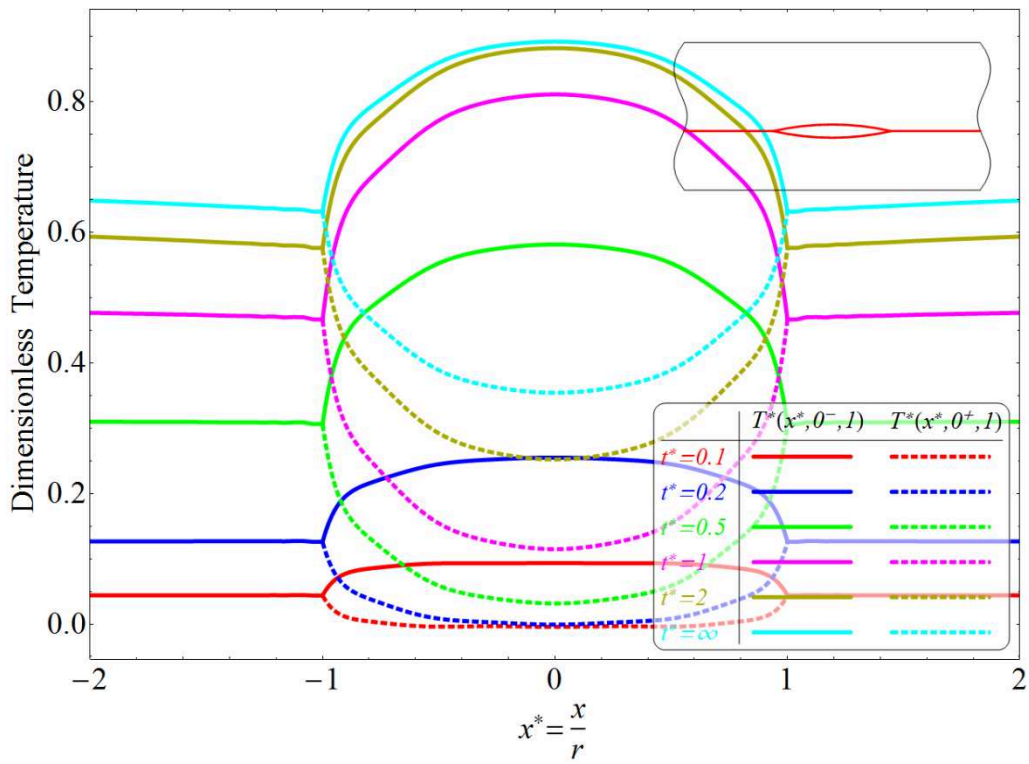

Figure 3.1-10 Temperatures along y = 0 at different dimensionless times for Bi = 0.

3.2 Non-Fourier Effect

In this section, we will consider the influence of the non-Fourier effect on the temperature field. Contrarily to the Biot number effect, the introduction of the non-Fourier effect changes fundamentally the governing equation of the thermal conduction problem. When the non-Fourier factor $\tau_1 = 0$, the governing equation of thermal conduction is a parabolic partial differential equation which corresponding to a diffusion equation; while $\tau_1 \neq 0$ leads to a hyperbolic governing equation which corresponds to a wave equation. Consequently, an oscillating property of the temperature field will be predicted. In this section, this point will be discussed in detail.

Equation (2-6) is a wave equation containing an attenuation term $\frac{\partial T}{\partial t}$. Consequently, one can expect a diminution of oscillation with respect to time.

By taking use of the properties of wave equation [144, 145] and by examining the form of Equation(2-6), it is clear that velocity of the heat wave c have the

following form

$$c = c(t) \tag{3-5}$$

$c(t)$ is a decreasing function of t and its value is less than c (0), which can be obtained by taking use of the initial condition (2-11)

$$c(0) = \sqrt{\frac{a}{\tau_0}} \tag{3-6}$$

The dimensionless form of (3-6) writes

$$c^*(0) = \sqrt{\frac{1}{\tau_1}} \tag{3-7}$$

where

$$c^*(0) = \frac{c(0)r}{a} \tag{3-8}$$

In the following analysis we omitted the superscript "*" for simplicity.

Equation (3-7) indicates when τ_1 is sufficiently small, the velocity of heat wave can be large enough to be considered as infinity in engineering application, which corresponds to the Fourier heat conduction.

In order to estimate the time used by the heat wave to reach to the crack surface, we neglect the attenuation item for simplify. Table 3.2-1 shows the heat wave velocities $c(0)$ for different τ_1. The last column is the dimensionless time, spent for a heat wave to move from the strip boundary to the lower crack surfaces.

τ_1	c(0)	t
0.1	3.16228	0.31623
0.2	2.23607	0.44721
0.3	1.82574	0.54772
0.4	1.58114	0.63246
0.5	1.41421	0.70711
0.6	1.29099	0.7746
0.7	1.19523	0.83666

Table 3.2-1 Heat wave velocity and the dimensionless time when the wave front reaches to the crack surface for different τ_1.

The heat wave can be reflected by the crack surfaces. We can distinguish the different time periods for the heat wave front to travel between the boundary and the crack lower surface, as indicated in Table 3.2-2. The heat wave is continuously spread out of the zone between the boundary and the crack in the process of wave propagation so that the wavy property will disappears gradually.

Time period	Heat wave direction	Information of wave front
$0 < t < t_1$	↑	Travelling to the crack surface
$t_1 < t < t_2$	↓	Reflect by the crack surface and travelling to the heated surface
$t_2 < t < t_3$	↑	Reflect by the heated surface again and travelling to the crack surface
……	……	……

Table 3.2-2 Periods of the heat wave propagation

In order to better observe the influence of NFF, the Biot number is set to be 0 in all the analyses performed in this section.

3.2.1 Full Temperature Field

Figure 3.2-1 and Figure 3.2-2 show the dimensionless temperature fields in the domain of $-2 < x^* < 2$ and $-1 < y^* < 2$, as defined in Figure 3.1-3.

The figures in Figure 3.2-1 are plotted at the same dimensionless time $t^* = 2$ for different values of τ_1, namely $\tau_1 = 0$, 0.2, 0.4 and 0.6 respectively. From these figures, we can observe quantitatively the τ_1 effect on the global temperature field. Roughly speaking, the non-zero τ_1 create a temperature concentration between the crack and the strip boundary. The principal reason of this result resides in the fact that the crack behaves as a reflecting boundary, especially in the case when Bi = 0. The heat wave reflected by the crack will be superposed to the non-wavy temperature field such that the temperature increases in this zone. For example, the peak value of the dimensionless temperature in figure (*d*) reaches 1.08; this is even higher that the thermal shock temperature imposed at the boundary.

In Figure 3.2-2, the non-Fourier factor is set to be 0.4 and the dimensionless time are 0.2, 1.4, 3.5 and 5.3, respectively. This figure illustrates the global evolution of the temperature field.

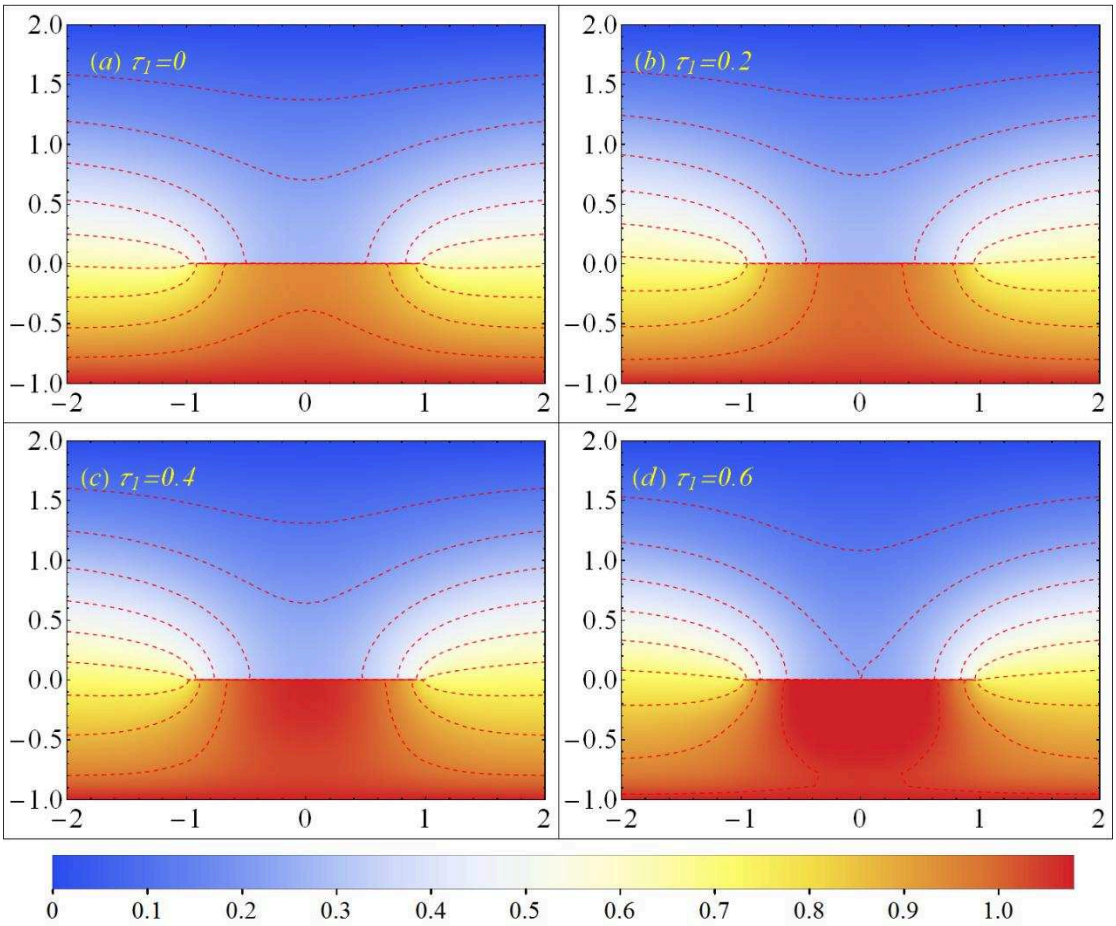

Figure 3.2-1 Temperature fields for -2 < x < 2 and -1 < y < 2 when dimensionless time is 1 and Biot number is set to be 0. (a): τ_1 = 0; (b): τ_1 = 0.2; (c): τ_1 = 0.4; (d): τ_1 = 0.6.

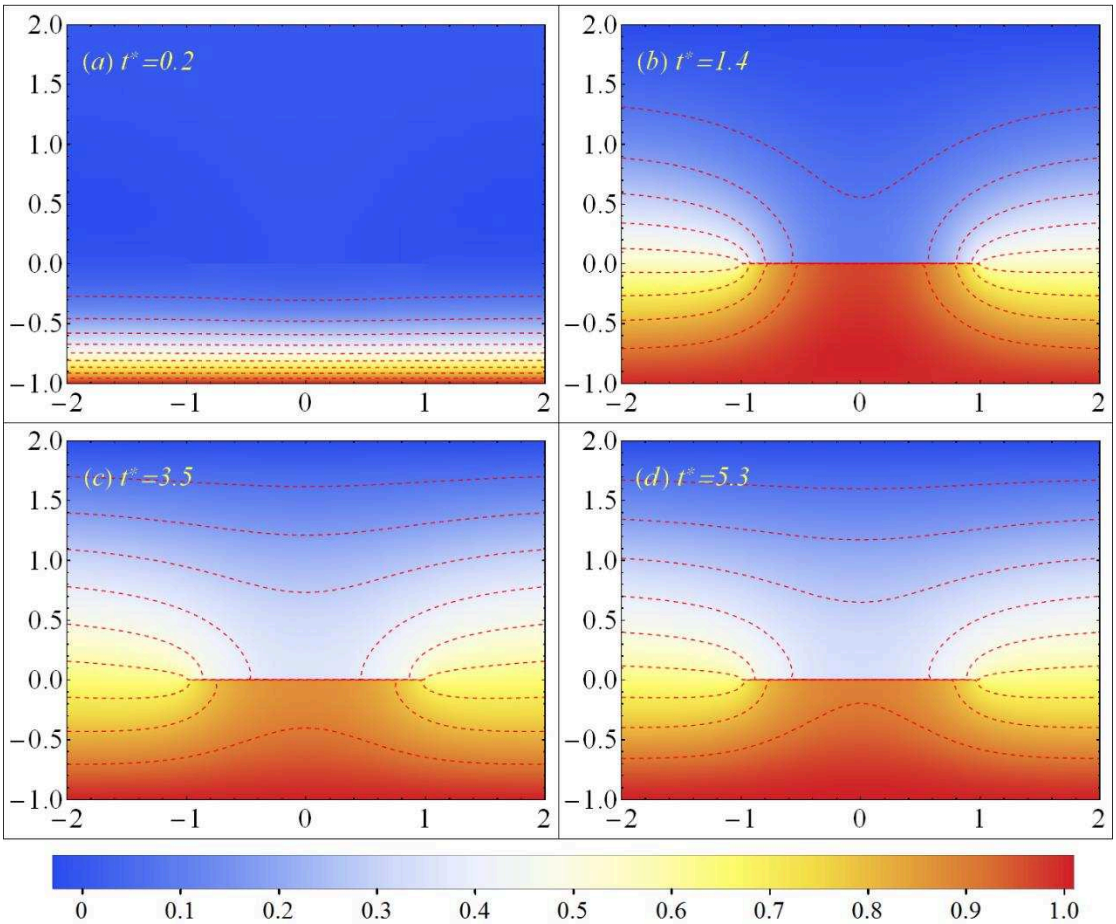

Figure 3.2-2 Temperature field in the domain -2 < x < 2 and -1 < y < 2. The Biot number and τ_1 are set to be 0 and 0.4, respectively. (a): t^* = 0.2; (b): t^* = 1.4; (c): t^* = 3.5; (d): t^* = 5.3.

3.2.2 Temperatures at the Mid-Points of the Crack Surfaces

Figure 3.2-3 shows the variations of the dimensionless temperature at the mid-points of the crack surfaces for different τ_1 values. The solid curves and the dashed curves stand for the values at the mid-points of the lower and upper crack surfaces, respectively.

The curves for τ_1 = 0, which correspond to the red curves in Figure 3.1-4, are monotonically increasing curves. However, this monotonic feature is no longer true in the cases when τ_1 is different from zero. In these cases, the temperature oscillation gradually appears and increases as τ_1 increases. It is clear that the bigger the value of τ_1 is, the higher the peak value of the temperature will be. It is possible that the peak value may be higher than the thermal shock temperature 1 and the minimum value

may be lower than the initial temperature 0.

Table 3.2-3 shows the maximal temperature differences of the point $(0, 0^-)$ and $(0, 0^+)$ and its corresponding dimensionless time to reach this value for different τ_1. Overall, the maximal of dT is delayed by the increasing of τ_1 if we neglect the value of $\tau_1 = 0$.

τ_1	Max(dT)	t^*
0	0.699723	1.119692
0.1	0.745777	1.071271
0.2	0.783199	1.110901
0.3	0.815667	1.197439
0.4	0.849799	1.310043
0.5	0.889649	1.424697
0.6	0.935229	1.52464
0.7	0.98435	1.60632

Table 3.2-3 Maximal temperature differences at the mid-points of the crack surfaces and its corresponding dimensionless time for different τ_1.

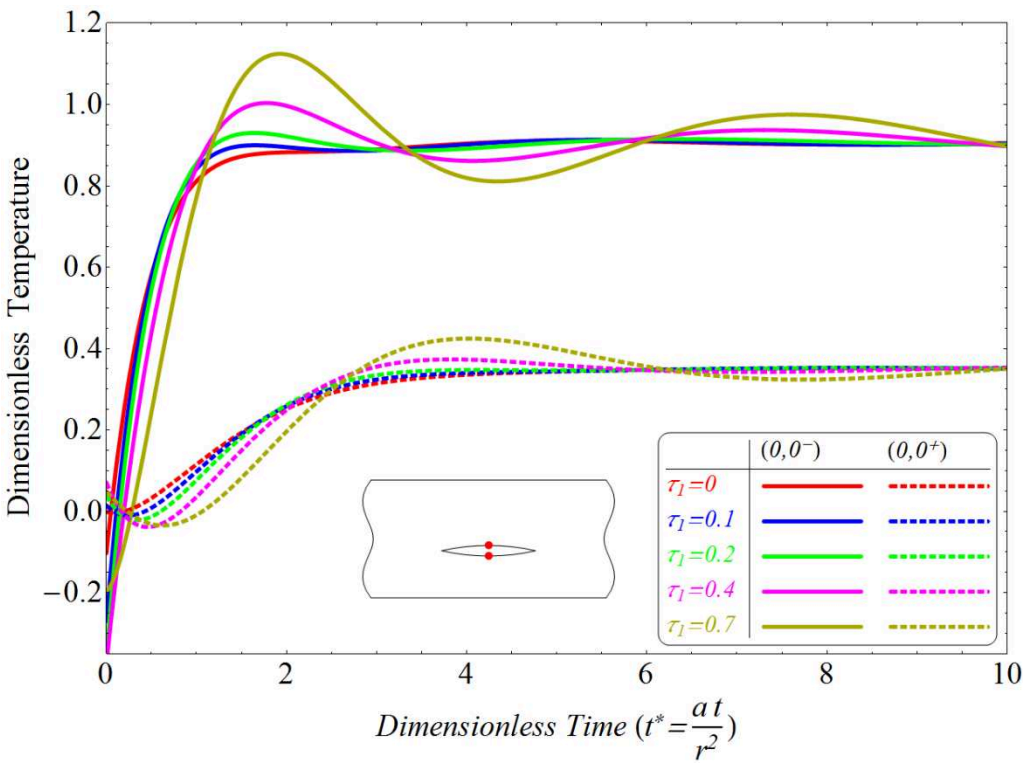

Figure 3.2-3 Dimensionless temperatures at the mid-points of the crack surfaces versus dimensionless time for different τ_1.

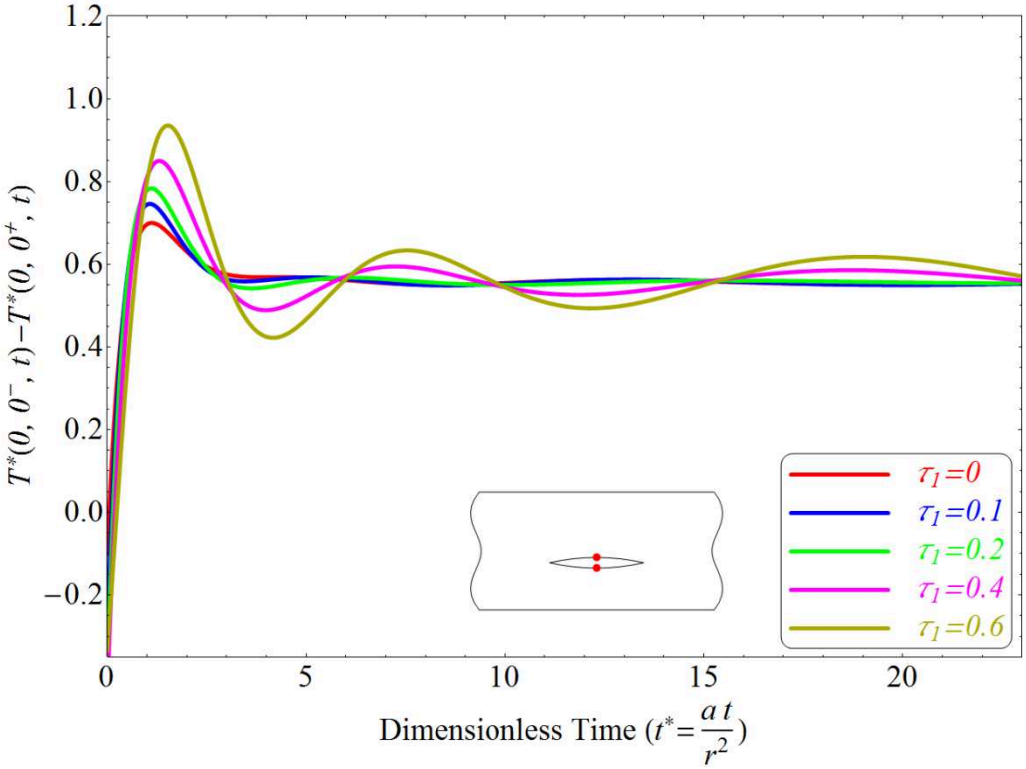

Figure 3.2-4 Dimensionless temperature differences between the mid-points of the crack surfaces versus dimensionless time for different τ_1.

Figure 3.2-4 illustrates the time variation of the dimensionless temperature differences between the mid-points of the crack surfaces for different τ_1. From this figure, we can see that the peak value of the temperature jump across the crack increases with τ_1. Moreover, its oscillation becomes more pronounced as τ_1 increases.

3.2.3 Temperatures at the Line $x = 0$

The dimensionless temperature field along the line $x = 0$ versus y are shown in Figure 3.2-5 and Figure 3.2-6.

In Figure 3.2-5 the dimensionless time is set to be 1, the τ_1 is set to be 0, 0.1, 0.2, 0.4 and 0.7, respectively. Compared with Figure 3.1-7 in which the non-Fourier effect is not taken into account, the temperature variations at $x = 0$ and $y \in [-1, 0]$ are not monotonically decreasing in y-direction. An increasing phase can be observed when τ_1

is different from zero. In the interval $y \in [0, 2]$, we observe that larger τ_1 leads to lower temperatures because of the wave shielding effect of the crack.

Figure 3.2-6 displays the temperature variations along the line $x = 0$ at different dimensionless times when τ_1 is set to be 0.5. As in Figure 3.2-5, the temperatures at the boundaries $y = -1$ and $y = 2$ stay unchanged because of the constraints of boundary conditions. However, the temperature in the interval $y \in [-1, 0]$ increases continuously with an oscillating feature. Moreover, since the crack behaves as a reflecting interface of the heat wave, the maximum and minimum values of the temperature at the lower crack surface can surpass the imposed thermal shock or initial temperatures.

The maximum and minimum temperatures at the point $(0, 0^-)$ for different τ_1 are shown in Table 3.2-4. It is clear from this table that the maximum temperature increases with τ_1 for $\tau_1 < 0.7$ while the absolute value of the minimum temperature increases with τ_1 until $\tau_1 = 0.5$ and then decrease.

τ_1	Maximum	Minimum
0	0.91114	0.09313
0.1	0.91312	-0.02548
0.2	0.92999	-0.10318
0.3	0.96507	-0.14987
0.4	1.00353	-0.17315
0.5	1.04386	-0.17889
0.6	1.08454	-0.17167
0.7	1.12433	-0.15506

Table 3.2-4 The maximum and minimum temperatures at the point $(0, 0^-)$ for different τ_1.

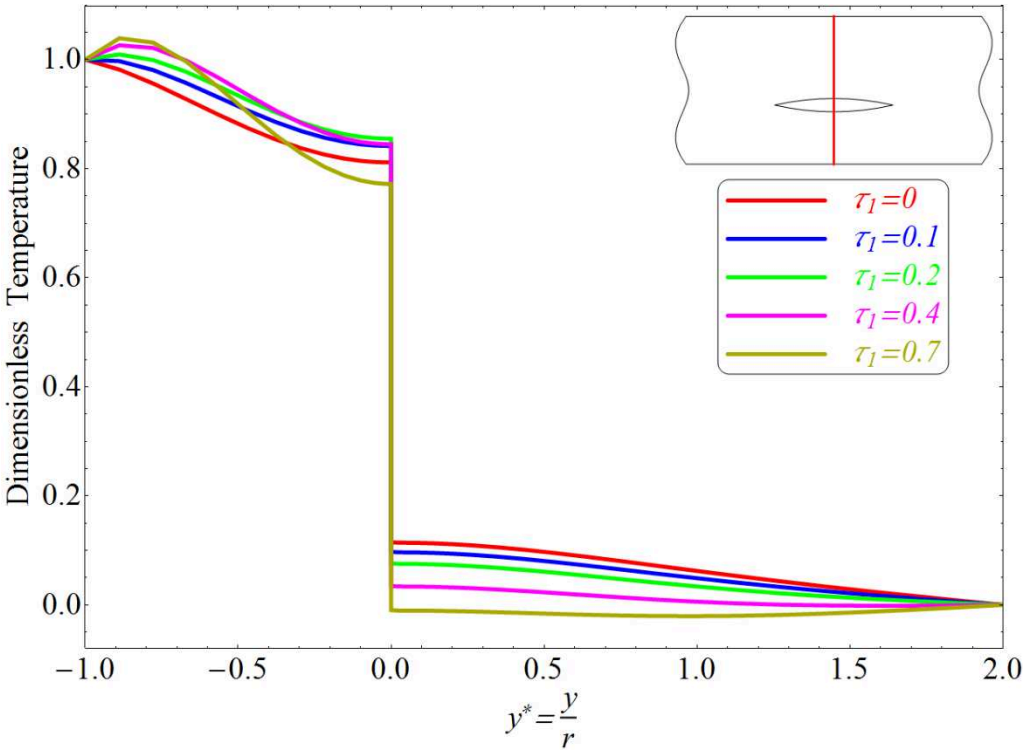

Figure 3.2-5 Dimensionless temperatures along the line x=0 for different τ_1 when t^* = 1 and Bi = 0.

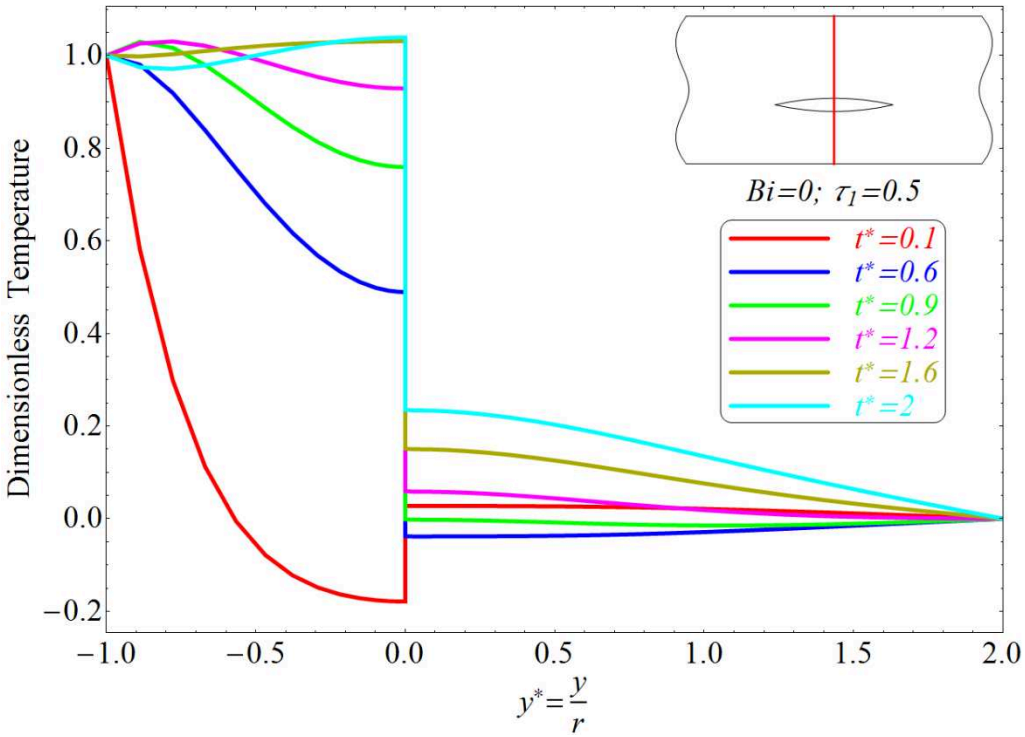

Figure 3.2-6 Dimensionless temperatures along the line x = 0 for different times when τ_1 = 0.5 and Bi = 0.

3.2.4 Temperatures at the Line y = 0

The temperature variations along the line y = 0 are shown in Figure 3.2-7 and Figure 3.2-8.

From Figure 3.2-7, we can remark that the temperature jump across the crack surfaces and the temperature gradient along the crack surfaces increase with τ_1.

In general, the temperature at the lower surface of the crack is higher than that at the upper crack surface. However, as shown in Figure 3.2-8, the contrary can occur at early stage of thermal shock when the τ_1 is large enough due to the oscillating aspect of the non-Fourier heat conduction.

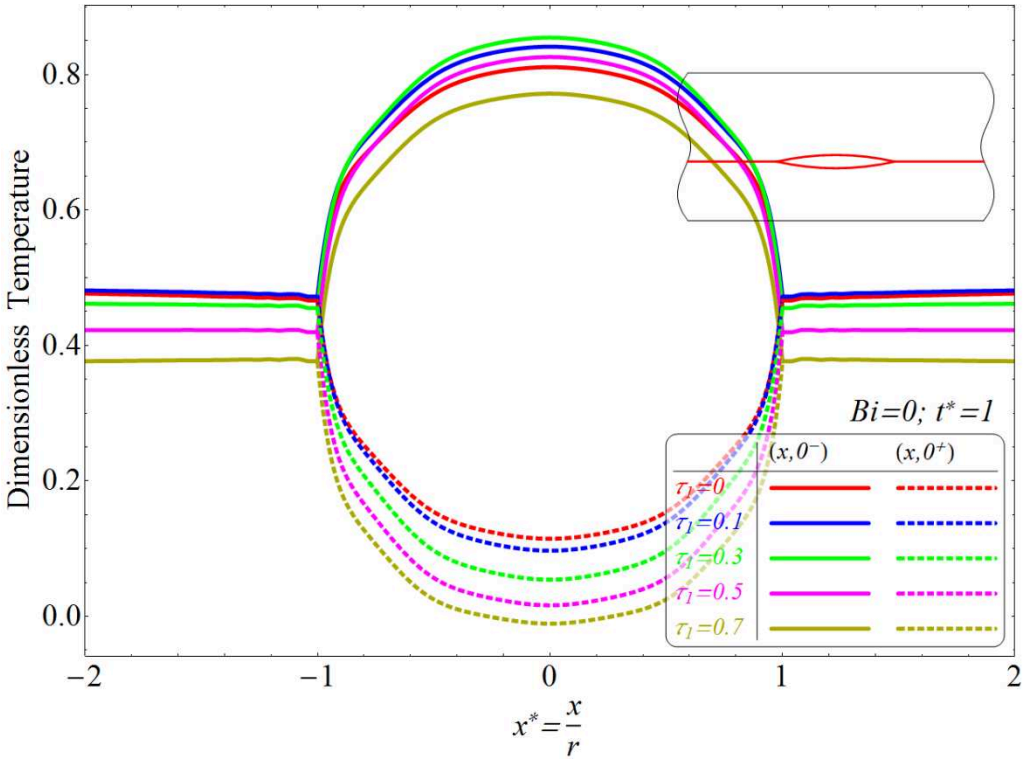

Figure 3.2-7 Temperatures along the line y=0 for different τ_1 when t^* = 1

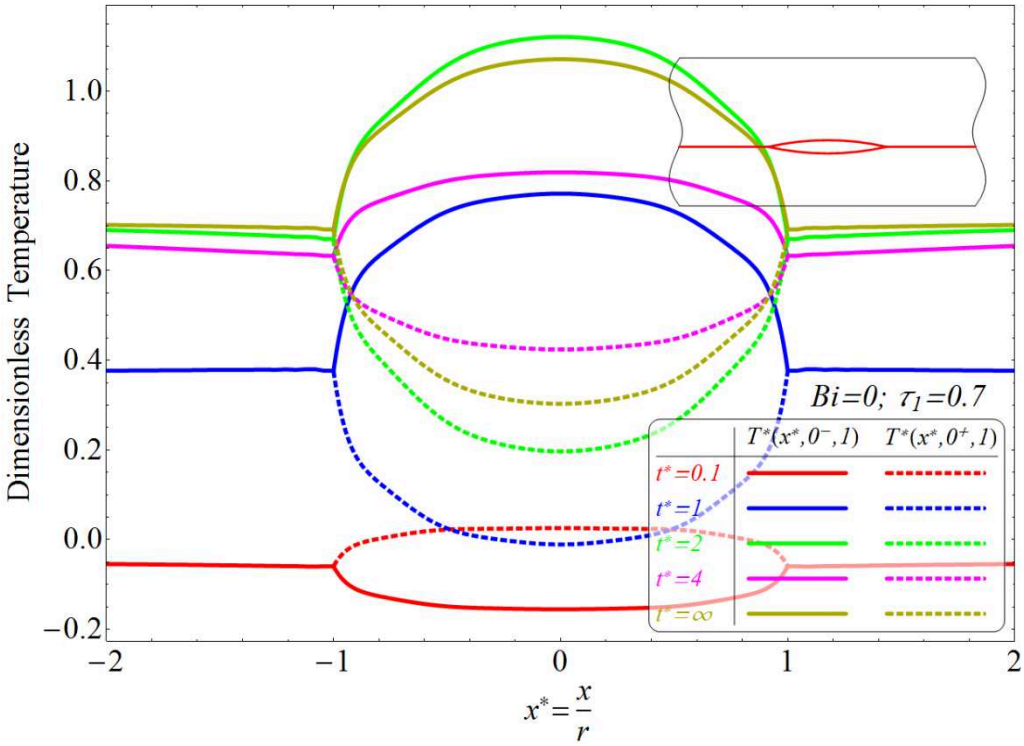

Figure 3.2-8 Temperatures along the line y=0 for different dimensionless times when Bi = 0 and τ_1 = 0.7

3.3 Interaction between the Biot Number and the NFF

Now let us consider the cases when both the Biot number and τ_1 have non-zero values. Figure 3.3-1 shows the maximum and minimum temperatures at the mid-point of the lower crack surface versus τ_1 for different Biot numbers. It is clear from Figure 3.3-1 (a) that the maximum temperature increases with τ_1 and decreases with the Biot number. This observation agrees well with the previous results. Moreover, the amplification of the maximal temperature by the non-Fourier effect is more pronounced with small Biot numbers.

The dimensionless times used for the temperature to reach the maximum value at the point $\left(0,0^-\right)$ are displayed in Table 3.3-1. Overall, this time increases as Bi increases. Its variation versus τ_1 is not monotonous and seems to be more complicated.

The interpretation of Figure 3.3-1 (b) is more complex. General speaking, the minimal temperature curves versus τ_1 appear to be a parabolic type. When τ_1 = 0, the minimum temperature which occurs at t^* = 0 stays at its initial level and entirely

unrelated to the Biot number. However, the minimal temperature can be lower than the initial level when $\tau_1 > 0$. Here again, this drop is more significant when the Biot number is small.

Figure 3.3-1 shows the maximal temperature differences between the midpoints of the crack surfaces versus τ_1 for different Biot numbers. From this figure, we can remark that the temperature jump across the crack is amplified by both the Biot number and τ_1. Nevertheless, the Biot number plays a more important role than τ_1 in augmentation of the temperature jump.

Bi \ τ_1	0	0.1	0.2	0.3	0.4	0.5	0.6	0.7
0	5.1809	5.4076	1.6408	1.7067	1.7768	1.8359	1.8846	1.926
0.2	5.1597	5.2727	6.0239	1.7524	1.8144	1.8681	1.9127	1.9506
0.4	5.1548	5.2123	5.8316	6.7442	1.882	1.9248	1.9622	1.995
0.6	5.1591	5.1847	5.7321	6.6698	1.9629	1.9916	2.0205	2.0477
0.8	5.1686	5.1743	5.6855	6.6404	2.0464	2.0593	2.0797	2.1017
1	5.1809	5.1736	5.671	6.6448	2.1252	2.1229	2.1357	2.1534
2	5.2526	5.2277	5.8181	6.8773	2.3825	2.3367	2.3313	2.3411
5	5.4115	5.4502	6.5983	7.3266	2.5476	2.5011	2.4996	2.5177
10	5.5368	5.6937	7.0466	7.4837	2.5798	2.5432	2.5486	2.5739
100	5.7365	6.1835	7.3384	7.5986	2.5945	2.5689	2.5819	2.6144
1000	5.7642	6.255	7.3605	7.6083	2.5952	2.5708	2.5845	2.6178

Table 3.3-1 Dimensionless times used for the temperature at $(0, 0^-)$ to reach the maximum value

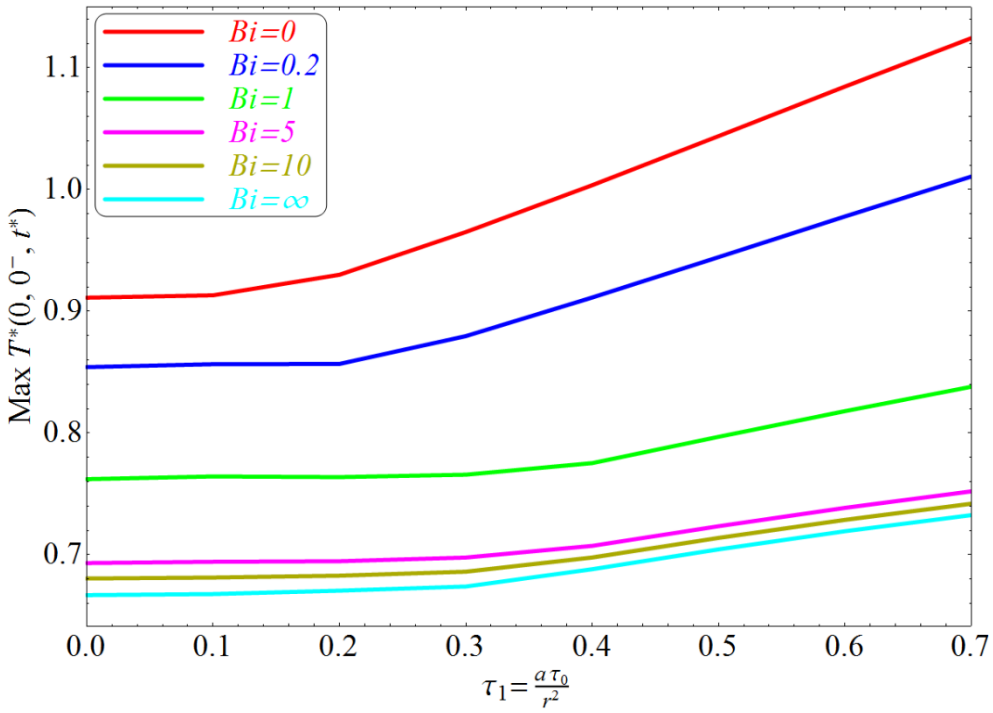

(a) The maximum temperature

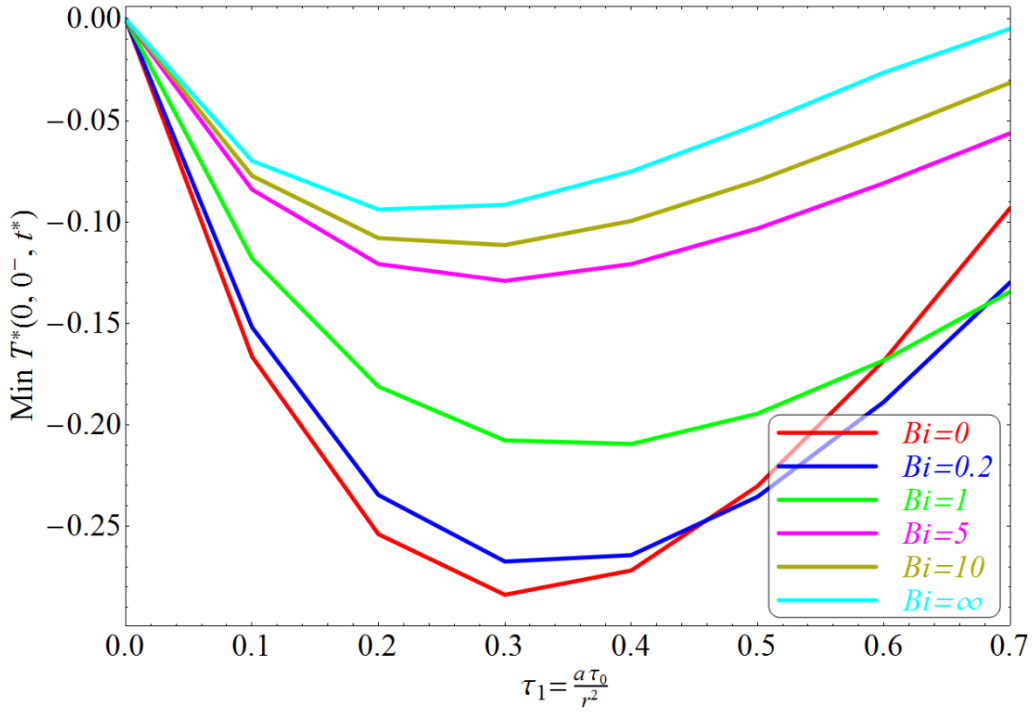

(b) The minimum temperature

Figure 3.3-1 Maximal and minimal temperatures at the point (0, 0^-) versus τ_1 for different Biot numbers.

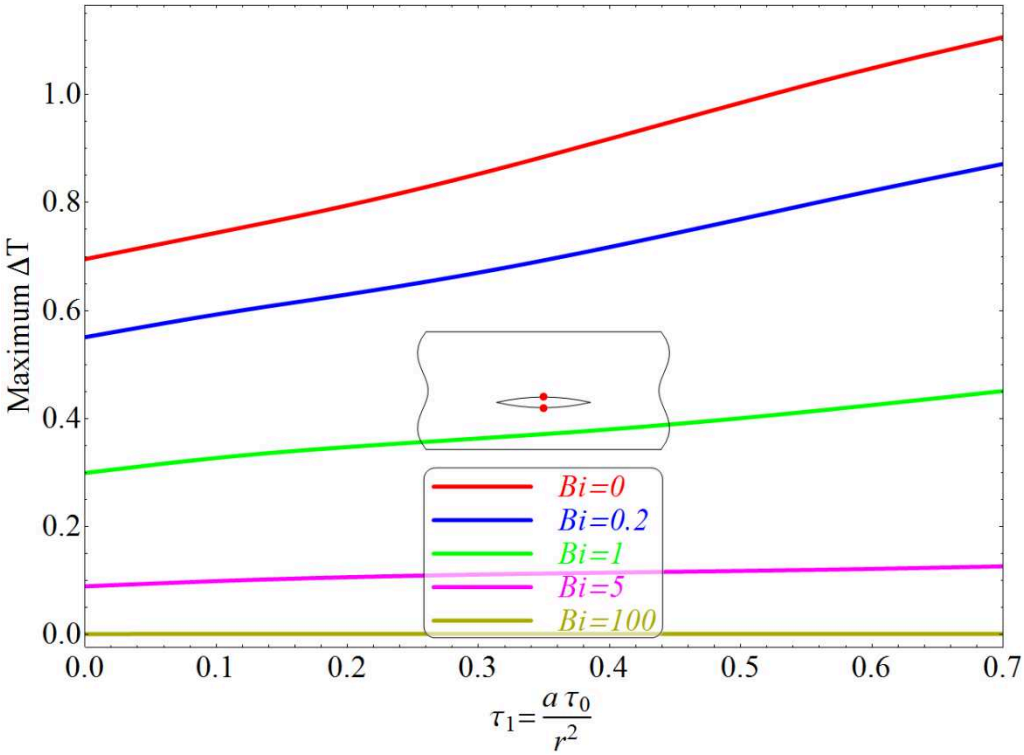

Figure 3.3-2 Temperature differences between the midpoints of the crack surfaces versus τ_1 for different Biot number.

3.4 Summary

In this chapter, numerical results on temperature field were presented in order to assess the influence of the Biot number and the non-Fourier factor. From the obtained results we may summarize the conclusions as follows

(1) The magnitude of the Biot number governs the uniformity of the temperature field near the crack. As the Biot number grows from 0 to infinite, the temperature difference between the two surfaces of the crack decreases gradually.

(2) Considering the finite speed of the heat propagation, i.e., introducing the non-Fourier effect in the heat conduction equation, would extend the temperature range of the strip. In heating process, the peak temperature may be larger than the thermal shock temperature and the minimum temperature may be smaller than the initial temperature, while the contrary will take place in cooling process.

(3) Another effect of the non-Fourier heat conduction is the wavy property of the temperature field. The velocity of the heat wave decreases with the

increasing of τ_1. Moreover, both the amplitude and velocity of the heat wave attenuate gradually with time.

The Biot number and the non-Fourier factor are physical parameters to be determined by experiments. In general, the thermal barrier formed by a macro-crack is experimentally evident, even though available experimental data in this topic are still rare so far [59]. However, the non-Fourier factors are often of small values for current engineering materials [65]. Consequently, we can reasonably say that the Biot number plays a key role in temperature distribution around the crack, which leads to stress concentrations near the crack tips.

Chapter 4 Stress Field Analysis

4.1 Introduction

In this chapter, we describe the resolution method used in studying the stress field in the cracked strip. Some new concepts and dimensionless parameters are introduced in order to understand better the crack growth mechanisms under thermal shock loading. In particular, the inertia terms are added to the equilibrium equations to assess the dynamic effects of the thermal shock on the stress fields. Furthermore, a new parameter named the inertia factor (IF) is defined to illustrate the mechanical relevance of the theoretical analyses. Since the inertia effect is introduced to the equilibrium equations, the resolution procedure becomes much more challenging comparing to the quasi-static problems. Special resolution techniques are developed in this chapter.

4.2 Formulation of the Crack Problem

4.2.1 Basic Equations and Boundary Conditions

The two-dimensional thermoelastic theory provides formulations involving the solution of boundary-value problems. In this class of problems two special cases, namely the plane stress and the plane strain should be distinguished. In the frame of the plane elasticity theory, the solution of a plane stress problem can be converted to that of the corresponding plane strain problem and vice versa. In this work, only the solution for plane stress problems is detailed.

In plane stress, the surfaces of the plate normal to the z-axis are assumed to be traction free, and thus

$$\sigma_z = \tau_{xz} = \tau_{yz} = 0 \tag{4-1}$$

Furthermore, the thickness of the plate is thin such that the other nonzero stress components have little variation with z. These arguments can then be summarized as follows

$$\begin{cases} \sigma_x = \sigma_x(x, y) \\ \sigma_y = \sigma_y(x, y) \\ \tau_{xy} = \tau_{xy}(x, y) \end{cases} \tag{4-2}$$

where $\sigma_x, \sigma_y, \sigma_z, \tau_{xy}, \tau_{yz}, \tau_{xz}$ are the components of the stress tensor. The basic equations of the plane thermos-elasticity for a homogeneous isotropic body are:

(1) Equations of motion in absence of the body forces:

$$\begin{cases} \dfrac{\partial \sigma_x}{\partial x} + \dfrac{\partial \tau_{xy}}{\partial y} = \rho \dfrac{\partial^2 u}{\partial t^2} \\ \dfrac{\partial \tau_{xy}}{\partial x} + \dfrac{\partial \sigma_y}{\partial y} = \rho \dfrac{\partial^2 v}{\partial t^2} \end{cases} \tag{4-3}$$

(2) Strain–displacement relations:

$$\begin{cases} \varepsilon_x = \dfrac{\partial u}{\partial x} \\ \varepsilon_y = \dfrac{\partial v}{\partial y} \\ \varepsilon_{xy} = \dfrac{1}{2}\left(\dfrac{\partial u}{\partial y} + \dfrac{\partial v}{\partial x}\right) \end{cases} \tag{4-4}$$

(3) Hooke's law:

$$\begin{cases} \varepsilon_x = \dfrac{1}{E}\left(\sigma_x - \nu\sigma_y\right) + \alpha\left(T - T_0\right) \\ \varepsilon_y = \dfrac{1}{E}\left(\sigma_y - \nu\sigma_x\right) + \alpha\left(T - T_0\right) \\ \varepsilon_{xy} = \dfrac{1+\nu}{E}\tau_{xy} \\ \varepsilon_z = -\dfrac{\nu}{E}\left(\sigma_x + \sigma_y\right) + \alpha\left(T - T_0\right) \\ \varepsilon_{xz} = \varepsilon_{yz} = 0 \end{cases} \tag{4-5}$$

(4) Compatibility equation

$$\frac{\partial^2 \varepsilon_x}{\partial y^2} + \frac{\partial^2 \varepsilon_y}{\partial x^2} = 2\frac{\partial^2 \varepsilon_{xy}}{\partial x \partial y} \tag{4-6}$$

where u and v are the displacement components; $\varepsilon_x, \varepsilon_y, \varepsilon_z, \varepsilon_{xy}, \varepsilon_{xz}, \varepsilon_{yz}$ are the components of the strain tensor; E, ν and α are Young's modulus, Poisson's ratio and the coefficient of linear thermal expansion, respectively.

For more convenience, we write the strain-stress relations as

$$\begin{cases} \sigma_x = \dfrac{E}{1-\nu^2}\left[\varepsilon_x + \nu\varepsilon_y - (1+\nu)\alpha(T-T_0)\right] \\ \sigma_y = \dfrac{E}{1-\nu^2}\left[\nu\varepsilon_x + \varepsilon_y - (1+\nu)\alpha(T-T_0)\right] \\ \tau_{xy} = \dfrac{E}{1+\nu}\varepsilon_{xy} \end{cases} \tag{4-7}$$

In fact, the equations of motion and the strain compatibility equations in plane strain are identical to those in plane stress. The Hooke's law in plane strain can be expressed as

$$\begin{cases} \sigma_x = \lambda\left(\dfrac{\partial u}{\partial x} + \dfrac{\partial v}{\partial y}\right) + 2\mu\dfrac{\partial u}{\partial x} - \alpha(3\lambda + 2\mu)(T-T_0) \\ \sigma_y = \lambda\left(\dfrac{\partial u}{\partial x} + \dfrac{\partial v}{\partial y}\right) + 2\mu\dfrac{\partial v}{\partial y} - \alpha(3\lambda + 2\mu)(T-T_0) \\ \tau_{xy} = \mu\left(\dfrac{\partial u}{\partial y} + \dfrac{\partial v}{\partial x}\right) \\ \sigma_z = \nu(\sigma_x + \sigma_y) - E\alpha(T-T_0) \\ \tau_{xz} = \tau_{yz} = 0 \end{cases} \tag{4-8}$$

where the elastic constant λ is called Lame's constant, and μ is referred to as the shear modulus. The relations of the four constants, E, ν, λ, μ are related as shown in Table 4.2-1.

In fact, the plane stress and plane strain theories are interchangeable with simple interchange of elastic moduli, as is shown in Table 4.2-2.

	$\boldsymbol{E}$	$\boldsymbol{\nu}$	$\boldsymbol{\mu}$	$\boldsymbol{\lambda}$
$\boldsymbol{E,\nu}$	E	ν	$\dfrac{E}{2(1+\nu)}$	$\dfrac{E\nu}{(1+\nu)(1-2\nu)}$
$\boldsymbol{\mu,\lambda}$	$\dfrac{\mu(3\lambda+2\mu)}{\lambda+\mu}$	$\dfrac{\lambda}{2(\lambda+\mu)}$	μ	λ

Table 4.2-1 Relations among elastic constants.

	E	ν	α
Plane stress to plane strain	$\frac{E}{1-\nu^2}$	$\frac{\nu}{1-\nu}$	$(1+\nu)\alpha$
Plane strain to plane stress	$\frac{E(1+2\nu)}{(1+\nu)^2}$	$\frac{\nu}{1+\nu}$	$\frac{1+\nu}{1+2\nu}\alpha$

Table 4.2-2 Elastic Moduli conversion between plane stress and plane strain for thermoelastic problems.

In the following, we focus our attention in resolving the plane-stress thermal-elastic problem. By substituting the equations of motion (4-3) with Equations(4-5) we obtain the equations of motion in terms of displacements:

$$\begin{cases} \frac{\partial^2 u}{\partial x^2}+\frac{1+\nu}{2}\frac{\partial^2 v}{\partial x\partial y}+\frac{1-\nu}{2}\frac{\partial^2 u}{\partial y^2}-\left(1-\nu^2\right)\frac{\rho}{E}\frac{\partial^2 u}{\partial t^2}=(1+\nu)\alpha\frac{\partial}{\partial x}(T-T_0) \\ \frac{\partial^2 v}{\partial y^2}+\frac{1+\nu}{2}\frac{\partial^2 u}{\partial x\partial y}+\frac{1-\nu}{2}\frac{\partial^2 v}{\partial x^2}-\left(1-\nu^2\right)\frac{\rho}{E}\frac{\partial^2 v}{\partial t^2}=(1+\nu)\alpha\frac{\partial}{\partial y}(T-T_0) \end{cases} \tag{4-9}$$

4.2.2 Boundary Initial Conditions

Equations (4-9) should be solved under the following boundary conditions and initial conditions, as schemed in Figure 2.1-2:

$$\begin{cases} (a):\sigma_y(x,-l_a,t)=0 \\ (b):\tau_{xy}(x,-l_a,t)=0 \\ \left.\begin{array}{l}(c):\sigma_y(x,0^+,t)=\sigma_y(x,0^-,t)=0 \\ (d):\tau_{xy}(x,0^+,t)=\tau_{xy}(x,0^-,t)=0\end{array}\right\} \quad |x|<r \\ \left.\begin{array}{l}(e):\tau_{xy}(x,0^+,t)=\tau_{xy}(x,0^-,t) \\ (f):\sigma_y(x,0^+,t)=\sigma_y(x,0^-,t)\end{array}\right\} \quad |x|\geq r \\ (g):\sigma_y(x,l_b,t)=0 \\ (h):\tau_{xy}(x,l_b,t)=0 \end{cases} \tag{4-10}$$

In (4-10), (*a*), (*b*), (*g*) and (*h*) translate the traction free conditions at the top and bottom surfaces of the strip; (*c*) and (*d*) describe the traction free conditions of the crack surfaces while (*e*) and (*f*) denote the stress continuity across the ligaments which extend the crack. The initial conditions are written as follows:

$$\begin{cases} u(x, y, 0) = v(x, y, 0) = 0 \\ \left.\dfrac{\partial u}{\partial t}\right|_{t=0} = \left.\dfrac{\partial v}{\partial t}\right|_{t=0} = 0 \\ \sigma_x(x, y, 0) = \sigma_y(x, y, 0) = \tau_{xy}(x, y, 0) = 0 \end{cases} \tag{4-11}$$

4.3 Analytical Resolution Procedure of the Stress Fields

For many two-dimensional linear elastic problems, the Airy stress function technique is a powerful tool to find an analytical solution. However, since the inertia effect is introduced in the equilibrium equations, this technique is no longer suitable to solve the proposed problem. A different resolution technique, namely the Laplace–Fourier transform technique, will be developed in this thesis. The flow chart of the solving procedure is shown in Figure 4.3-1.

In this section we first nondimensionalize the basic thermal stress equations. Then the Laplace transform with respect to t and the Fourier transform with respect to x are applied to these equations such that a non-linear ordinary differential equation system in y-coordinate can be obtained in Laplace - Fourier space. The solution of the ODE is similar to that described in Chapter 2. The main idea is to establish a pair of singular integral equations then to solve them with a numerical integration technique.

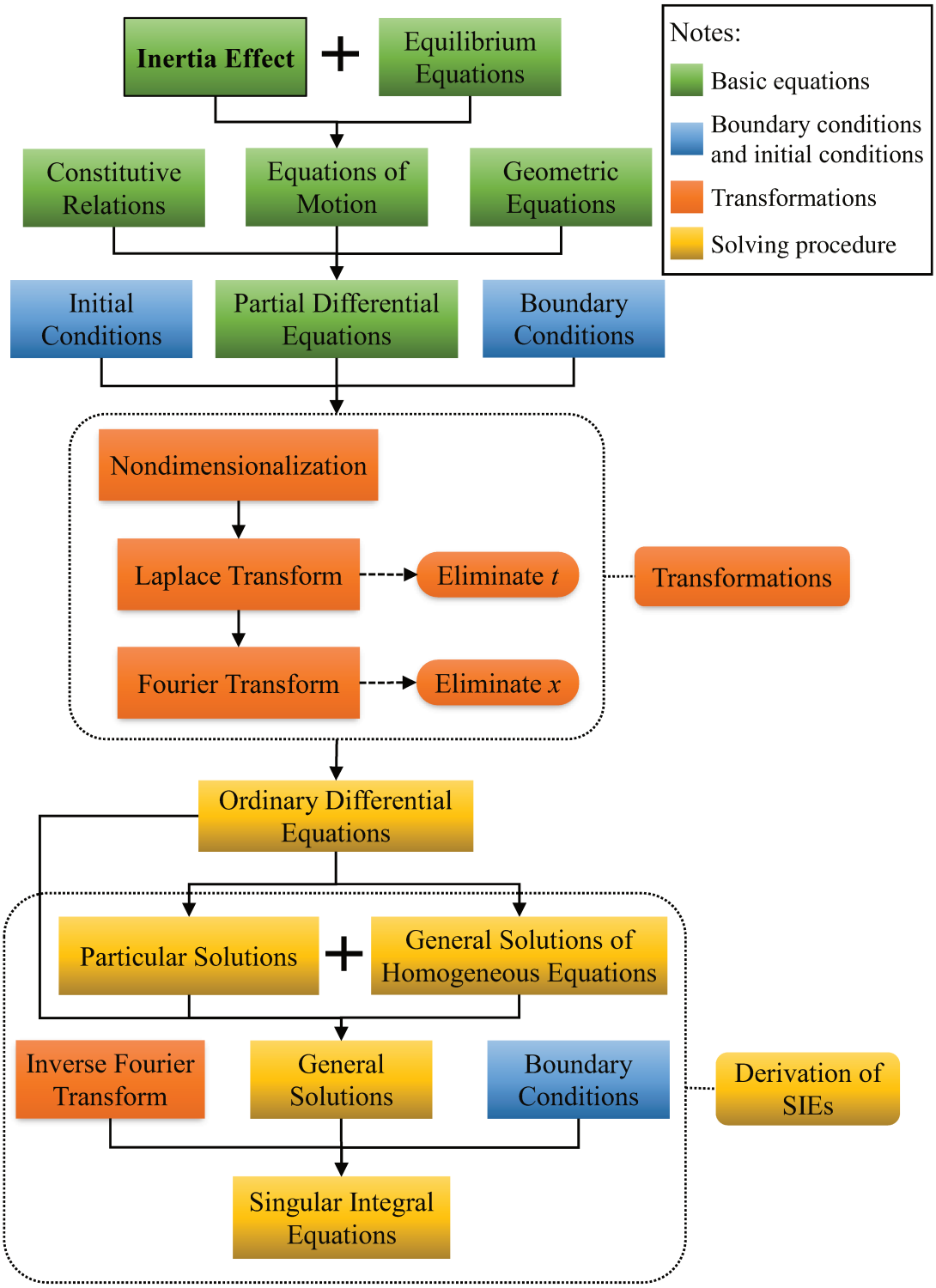

Figure 4.3-1 Solving procedure of the Stress fields.

4.3.1 Nondimensionalization of Variables

As is discussed in section 2.3.1, we now define some new dimension-independent quantities:

$$\begin{cases} \left(\sigma_x^*, \sigma_x^*, \tau_{xy}^*\right) = \dfrac{1-\nu}{E\alpha\left(T_\infty - T_0\right)}\left(\sigma_x, \sigma_x, \tau_{xy}\right) \\ \left(u^*, v^*\right) = \dfrac{1}{r\left(1+\nu\right)\alpha\left(T_\infty - T_0\right)}\left(u, v\right) \end{cases} \tag{4-12}$$

By introducing the dimensionless variables defined in (2-12) and (4-12) into (4-7) and (4-9) - (4-11), we obtain stress-strain relationships, the equations of motion written in terms of displacements, the boundary conditions and the initial conditions in dimensionless form:

$$\begin{cases} \sigma_x^* = \dfrac{\partial u^*}{\partial x^*} + \nu\dfrac{\partial v^*}{\partial y^*} - T^* \\ \sigma_y^* = \nu\dfrac{\partial u^*}{\partial x^*} + \dfrac{\partial v^*}{\partial y^*} - T^* \\ \tau_{xy}^* = \dfrac{1-\nu}{2}\left(\dfrac{\partial u^*}{\partial y^*} + \dfrac{\partial v^*}{\partial x^*}\right) \end{cases} \tag{4-13}$$

$$\begin{cases} \dfrac{\partial^2 u^*}{\partial x^{*2}} + \dfrac{1+\nu}{2}\dfrac{\partial^2 v^*}{\partial x^*\partial y^*} + \dfrac{1-\nu}{2}\dfrac{\partial^2 u^*}{\partial y^{*2}} - \tau_2^{\,2}\dfrac{\left(1-\nu\right)^2}{1-2\nu}\dfrac{\partial^2 u^*}{\partial t^{*2}} = \dfrac{\partial T^*}{\partial x^*} \\ \dfrac{\partial^2 v^*}{\partial y^{*2}} + \dfrac{1+\nu}{2}\dfrac{\partial^2 u^*}{\partial x^*\partial y^*} + \dfrac{1-\nu}{2}\dfrac{\partial^2 v^*}{\partial x^{*2}} - \tau_2^{\,2}\dfrac{\left(1-\nu\right)^2}{1-2\nu}\dfrac{\partial^2 v}{\partial t^{*2}} = \dfrac{\partial T^*}{\partial y^*} \end{cases} \tag{4-14}$$

$$\begin{cases} \left(a\right): \sigma_y^*\left(x^*, -l_a^*, t^*\right) = 0 \\ \left(b\right): \tau_{xy}^*\left(x^*, -l_a^*, t^*\right) = 0 \\ \left.\begin{array}{l} \left(c\right): \sigma_y^*\left(x^*, 0^+, t^*\right) = \sigma_y^*\left(x^*, 0^-, t^*\right) = 0 \\ \left(d\right): \tau_{xy}^*\left(x^*, 0^+, t^*\right) = \tau_{xy}^*\left(x^*, 0^-, t^*\right) = 0 \end{array}\right\} & \left|x^*\right| < 1 \\ \left.\begin{array}{l} \left(e\right): \tau_{xy}^*\left(x^*, 0^+, t^*\right) = \tau_{xy}^*\left(x^*, 0^-, t^*\right) \\ \left(f\right): \sigma_y^*\left(x^*, 0^+, t^*\right) = \sigma_y^*\left(x^*, 0^-, t^*\right) \end{array}\right\} & \left|x^*\right| \geq 1 \\ \left(g\right): \sigma_y^*\left(x^*, l_b^*, t^*\right) = 0 \\ \left(h\right): \tau_{xy}^*\left(x^*, l_b^*, t^*\right) = 0 \end{cases} \tag{4-15}$$

and

$$\begin{cases} u^*\left(x^*,y^*,0\right)=v^*\left(x^*,y^*,0\right)=0 \\ \left.\dfrac{\partial u^*}{\partial t^*}\right|_{t^*=0}=\left.\dfrac{\partial v^*}{\partial t^*}\right|_{t^*=0}=0 \\ \sigma_x^*\left(x^*,y^*,0\right)=\sigma_y^*\left(x^*,y^*,0\right)=\tau_{xy}^*\left(x^*,y^*,0\right)=0 \end{cases} \tag{4-16}$$

where $\tau_2=\dfrac{a}{Vr}$ with $V=\sqrt{\dfrac{E(1-\nu)}{\rho(1+\nu)(1-2\nu)}}$ being the stress wave velocity.

The dimensionless parameter τ_2 that we name the "***inertia factor***" (IF), plays an important role in describing the dynamic behavior of a cracked solid under thermal loading. The physical implication of this parameter in stress concentration near the crack tips will be discussed afterward in Chapter 5.

In the following analysis, the superscript "*" will be omitted for simplicity.

4.3.2 Integral Transforms

As we discussed previously in section 2.3.2, we define the displacement and stress fields in Laplace domain:

$$\left(\bar{u},\bar{v},\bar{\sigma}_x,\bar{\sigma}_y,\bar{\tau}_{xy}\right)=\int_0^\infty\left(u,v,\sigma_x,\sigma_y,\tau_{xy}\right)e^{-pt}dt \tag{4-17}$$

And the inverse Laplace transforms are:

$$\left(u,v,\sigma_x,\sigma_y,\tau_{xy}\right)=\frac{1}{2\pi i}\int_{\gamma-i\infty}^{\gamma+i\infty}\left(\bar{u},\bar{v},\bar{\sigma}_x,\bar{\sigma}_y,\bar{\tau}_{xy}\right)e^{pt}dp \tag{4-18}$$

The stress – strain relations, the equations of motion and the boundary conditions in Laplace space can be obtained by substituting Equation (4-18) into (4-13), (4-14) and (4-15), respectively and by applying the initial conditions(4-16), namely:

$$\begin{cases} \bar{\sigma}_x=\dfrac{\partial\bar{u}}{\partial x}+\nu\dfrac{\partial\bar{v}}{\partial y}-\bar{T} \\ \bar{\sigma}_y=\nu\dfrac{\partial\bar{u}}{\partial x}+\dfrac{\partial\bar{v}}{\partial y}-\bar{T} \\ \bar{\tau}_{xy}=\dfrac{1-\nu}{2}\left(\dfrac{\partial\bar{u}}{\partial y}+\dfrac{\partial\bar{v}}{\partial x}\right) \end{cases} \tag{4-19}$$

$$\begin{cases} \dfrac{\partial^2\bar{u}}{\partial x^2}+\dfrac{1+\nu}{2}\dfrac{\partial^2\bar{v}}{\partial x\partial y}+\dfrac{1-\nu}{2}\dfrac{\partial^2\bar{u}}{\partial y^2}-\tau_2^{\,2}p^2\dfrac{(1-\nu)^2}{1-2\nu}\bar{u}=\dfrac{\partial\bar{T}}{\partial x} \\ \dfrac{\partial^2\bar{v}}{\partial y^2}+\dfrac{1+\nu}{2}\dfrac{\partial^2\bar{u}}{\partial x\partial y}+\dfrac{1-\nu}{2}\dfrac{\partial^2\bar{v}}{\partial x^2}-\tau_2^{\,2}p^2\dfrac{(1-\nu)^2}{1-2\nu}\bar{v}=\dfrac{\partial\bar{T}}{\partial y} \end{cases} \tag{4-20}$$

$$\begin{cases} (a): \bar{\sigma}_y(x,-l_a)=0 \\ (b): \bar{\tau}_{xy}(x,-l_a)=0 \\ \left.\begin{array}{l}(c): \bar{\sigma}_y(x,0^+)=\bar{\sigma}_y(x,0^-)=0 \\ (d): \bar{\tau}_{xy}(x,0^+)=\bar{\tau}_{xy}(x,0^-)=0\end{array}\right\} \quad |x|<1 \\ \left.\begin{array}{l}(e): \bar{\tau}_{xy}(x,0^+,t)=\bar{\tau}_{xy}(x,0^-) \\ (f): \bar{\sigma}_y(x,0^+)=\bar{\sigma}_y(x,0^-)\end{array}\right\} \quad |x|\geq 1 \\ (g): \bar{\sigma}_y(x,l_b)=0 \\ (h): \bar{\tau}_{xy}(x,l_b)=0 \end{cases} \tag{4-21}$$

Similarly, we define the Fourier transform of the Laplace-domain-stresses and the Laplace-domain-displacements as follows:

$$\left\{\tilde{\bar{\sigma}}_x, \tilde{\bar{\sigma}}_y, \tilde{\bar{\tau}}_{xy}\right\}(y)=\int_{-\infty}^{\infty}\left\{\bar{\sigma}_x, \bar{\sigma}_y, \bar{\tau}_{xy}\right\}(x,y)e^{i\xi x}dx \tag{4-22}$$

and

$$\left\{\bar{\sigma}_x, \bar{\sigma}_y, \bar{\tau}_{xy}\right\}(x,y)=\frac{1}{2\pi}\int_{-\infty}^{\infty}\left\{\tilde{\bar{\sigma}}_x, \tilde{\bar{\sigma}}_y, \tilde{\bar{\tau}}_{xy}\right\}(y)e^{-i\xi x}d\xi \tag{4-23}$$

Then Equations (4-19) - (4-21) follow that

$$\begin{cases} \tilde{\bar{\sigma}}_x=-i\xi\tilde{\bar{u}}+\nu\dfrac{d\tilde{\bar{v}}}{dy}-\tilde{\bar{T}} \\ \tilde{\bar{\sigma}}_y=-i\xi\nu\tilde{\bar{u}}+\dfrac{d\tilde{\bar{v}}}{dy}-\tilde{\bar{T}} \\ \tilde{\bar{\tau}}_{xy}=\dfrac{1-\nu}{2}\left(\dfrac{d\tilde{\bar{u}}}{dy}-i\xi\tilde{\bar{v}}\right) \end{cases} \tag{4-24}$$

$$\begin{cases} \dfrac{d^2\tilde{\bar{u}}}{dy^2}+\beta_1\dfrac{d\tilde{\bar{v}}}{dy}+\beta_2\tilde{\bar{u}}=\beta_3\tilde{\bar{T}} \\ \dfrac{d^2\tilde{\bar{v}}}{dy^2}+\beta_4\dfrac{d\tilde{\bar{u}}}{dy}+\beta_5\tilde{\bar{v}}=\dfrac{d\tilde{\bar{T}}}{dy} \end{cases} \tag{4-25}$$

$$\begin{cases} (a): \tilde{\bar{\sigma}}_y(-l_a)=0 \\ (b): \tilde{\bar{\tau}}_{xy}(-l_a)=0 \\ (c): \tilde{\bar{\sigma}}_y(0^+)=\tilde{\bar{\sigma}}_y(0^-) \\ (d): \tilde{\bar{\tau}}_{xy}(0^+)=\tilde{\bar{\tau}}_{xy}(0^-) \\ (e): \tilde{\bar{\sigma}}_y(l_b)=0 \\ (f): \tilde{\bar{\tau}}_{xy}(l_b)=0 \end{cases} \tag{4-26}$$

where

$$\begin{cases} \beta_1 = -\dfrac{1+\nu}{1-\nu} i\xi \\ \beta_2 = -\dfrac{2}{1-\nu}\left(\xi^2 + \tau_2{}^2 \dfrac{(1-\nu)^2}{1-2\nu} p^2\right) \\ \beta_3 = -\dfrac{2i\xi}{1-\nu} \\ \beta_4 = -\dfrac{1+\nu}{2} i\xi \\ \beta_5 = -\left(\dfrac{1-\nu}{2}\xi^2 + \tau_2{}^2 \dfrac{(1-\nu)^2}{1-2\nu} p^2\right) \end{cases} \tag{4-27}$$

4.3.3 General Solutions of the ODEs

The equations in (4-25) are second order non-homogeneous ordinary differential equations. Their solutions can be expressed by adding the general solutions of their corresponding homogeneous ordinary differential equations $\tilde{\bar{u}}_g, \tilde{\bar{v}}_g$ to a pair of particular solutions $\tilde{\bar{u}}_p, \tilde{\bar{v}}_p$:

$$\begin{cases} \tilde{\bar{u}}(y) = \tilde{\bar{u}}_g(y) + \tilde{\bar{u}}_p(y) \\ \tilde{\bar{v}}(y) = \tilde{\bar{v}}_g(y) + \tilde{\bar{v}}_p(y) \end{cases} \tag{4-28}$$

where

$$\begin{cases} \left.\begin{aligned} \tilde{\bar{u}}_g(y) &= \sum_{i=1}^{4} C_{D,i}(\xi) e^{\lambda_i y} \\ \tilde{\bar{v}}_g(y) &= \sum_{i=1}^{4} B_i C_{D,i}(\xi) e^{\lambda_i y} \end{aligned}\right\} & -l_a < y < 0 \\ \left.\begin{aligned} \tilde{\bar{u}}_g(y) &= \sum_{i=5}^{8} C_{D,i}(\xi) e^{\lambda_i y} \\ \tilde{\bar{v}}_g(y) &= \sum_{i=5}^{8} B_i C_{D,i}(\xi) e^{\lambda_i y} \end{aligned}\right\} & 0 < y < l_b \end{cases} \tag{4-29}$$

and the particular solutions can be written in a similar form to the temperature field (2-31)

$$\begin{cases} \left.\begin{aligned} \tilde{\bar{u}}^*(y) &= \omega_1 e^{-my} + \omega_2 e^{my} \\ \tilde{\bar{v}}^*(y) &= \omega_3 e^{-my} + \omega_4 e^{my} \end{aligned}\right\} & -l_a < y < 0 \\ \left.\begin{aligned} \tilde{\bar{u}}^*(y) &= \omega_5 e^{-my} + \omega_6 e^{my} \\ \tilde{\bar{v}}^*(y) &= \omega_7 e^{-my} + \omega_8 e^{my} \end{aligned}\right\} & 0 < y < l_b \end{cases} \tag{4-30}$$

Then we have

$$\begin{cases} \tilde{\bar{u}}_1(y) = \sum_{i=1}^{4} C_{D,i}(\xi) e^{\lambda_i y} + \omega_1 e^{-my} + \omega_2 e^{my} \\ \tilde{\bar{v}}_1(y) = \sum_{i=1}^{4} B_i C_{D,i}(\xi) e^{\lambda_i y} + \omega_3 e^{-my} + \omega_4 e^{my} \\ \tilde{\bar{u}}_2(y) = \sum_{i=5}^{8} C_{D,i}(\xi) e^{\lambda_i y} + \omega_5 e^{-my} + \omega_6 e^{my} \\ \tilde{\bar{v}}_2(y) = \sum_{i=5}^{8} B_i C_{D,i}(\xi) e^{\lambda_i y} + \omega_7 e^{-my} + \omega_8 e^{my} \end{cases} \tag{4-31}$$

where the subscripts 1 and 2 of $\tilde{\bar{u}}$ and $\tilde{\bar{v}}$ denote the domain $-l_a < y < 0$ and $0 < y < l_b$, respectively. $C_{D,i}(\xi)(i = 1, 2, \cdots, 8)$ are unknown functions to be determined, $\lambda_i(i = 1, 2, \cdots, 8)$ and $B_i(i = 1, 2, \cdots, 8)$ can be obtained from the characteristic equation of (4-25), deduced by substituting Equation (4-31) into (4-25):

$$\begin{cases} \beta_1 \lambda_i B_i + \lambda_i^2 + \beta_2 = 0 \\ \left(\lambda_i^2 + \beta_5\right) B_i + \beta_4 \lambda_i = 0 \end{cases} \tag{4-32}$$

so λ_i (i=1, …,4) can be given by the roots of the equation

$$\lambda^4 + \left(\beta_2 + \beta_5 - \beta_1 \beta_4\right) \lambda^2 + \beta_2 \beta_5 = 0 \tag{4-33}$$

namely,

$$\begin{cases} \lambda_1 = -\sqrt{\xi^2 + \dfrac{2p^2 \tau_2^2}{1-\nu}} \\ \lambda_2 = -\sqrt{\xi^2 + p^2 \tau_2^2} \\ \lambda_3 = \sqrt{\xi^2 + \dfrac{2p^2 \tau_2^2}{1-\nu}} \\ \lambda_4 = \sqrt{\xi^2 + p^2 \tau_2^2} \end{cases} \tag{4-34}$$

λ_i (i=5, …,8) can be obtained in the same way and it is obvious that

$$\lambda_{i+4} = \lambda_i \qquad i = 1, 2, 3, 4 \tag{4-35}$$

From the first equation of (4-32), we have

$$B_i = -\frac{\lambda_i^{\,2} + \beta_2}{\beta_1 \lambda_i} \qquad i = 1, 2, \ldots 8 \tag{4-36}$$

Substituting the particular solutions (4-30) and the temperature field (2-31) into (4-25), it follows that

$$\begin{cases}
\omega_1 = \dfrac{-\left(1+e^{2l_b m}\right)\tilde{\bar{\phi}}\, p + 2i\xi e^{(l_a+2l_b)m}\delta(\xi)}{2p\left(1-e^{2(l_a+l_b)m}\right)\left(m^2-\xi^2-p^2\tau_2^2\right)} \\
\omega_2 = \dfrac{e^{l_a m}\left[\left(1+e^{2l_b m}\right)e^{l_a m}\, p\tilde{\bar{\phi}} - 2i\xi\cdot\delta(\xi)\right]}{2p\left(1-e^{2(l_a+l_b)m}\right)\left(m^2-\xi^2-p^2\tau_2^2\right)} \\
\omega_3 = \dfrac{im\left[\left(1+e^{2l_b m}\right)p\tilde{\bar{\phi}} - 2i\xi e^{(l_a+2l_b)m}\delta(\xi)\right]}{2p\xi\left(1-e^{2(l_a+l_b)m}\right)\left(m^2-\xi^2-p^2\tau_2^2\right)} \\
\omega_4 = \dfrac{ie^{l_a m}m\left[\left(1+e^{2l_b m}\right)e^{l_a m}\tilde{\bar{\phi}}\, p - 2i\xi\cdot\delta(\xi)\right]}{2p\xi\left(1-e^{2(l_a+l_b)m}\right)\left(m^2-\xi^2-p^2\tau_2^2\right)} \\
\omega_5 = \dfrac{e^{2l_b m}\left[-\left(1+e^{2l_a m}\right)p\tilde{\bar{\phi}} + 2i\xi e^{l_a m}\delta(\xi)\right]}{2p\left(1-e^{2(l_a+l_b)m}\right)\left(m^2-\xi^2-p^2\tau_2^2\right)} \\
\omega_6 = \dfrac{\left(1+e^{2l_a m}\right)\tilde{\bar{\phi}}\, p - 2i\xi e^{l_a m}\delta(\xi)}{2p\left(1-e^{2(l_a+l_b)m}\right)\left(m^2-\xi^2-p^2\tau_2^2\right)} \\
\omega_7 = \dfrac{ie^{2l_b m}m\left[\left(1+e^{2l_a m}\right)\tilde{\bar{\phi}}\, p - 2i\xi e^{l_a m}\delta(\xi)\right]}{2p\xi\left(1-e^{2(l_a+l_b)m}\right)\left(m^2-\xi^2-p^2\tau_2^2\right)} \\
\omega_8 = \dfrac{im\left[\left(1+e^{2l_a m}\right)\tilde{\bar{\phi}}\, p - 2i\xi e^{l_a m}\delta(\xi)\right]}{2p\xi\left(1-e^{2(l_a+l_b)m}\right)\left(m^2-\xi^2-p^2\tau_2^2\right)}
\end{cases} \tag{4-37}$$

By substituting the displacement field (4-31) and temperature field (2-31) into the stress – displacement relations (4-24), the stresses can be obtained as follows:

$$\begin{cases}
\tilde{\bar{\sigma}}_x = \sum_{i=1}^{4}\left(B_i\lambda_i\nu - i\xi\right)C_{D,i}e^{\lambda_i y} - i\xi\left(\omega_1 e^{-my} + \omega_2 e^{my}\right) + \nu\left(-m\omega_3 e^{-my} + m\omega_4 e^{my}\right) \\
\qquad -\left(C_{T,1}e^{-my} + C_{T,2}e^{my}\right) \\
\tilde{\bar{\sigma}}_y = \sum_{i=1}^{4}\left(B_i\lambda_i - i\xi\nu\right)C_{D,i}e^{\lambda_i y} - i\nu\xi\left(\omega_1 e^{-my} + \omega_2 e^{my}\right) - m\omega_3 e^{-my} + m\omega_4 e^{my} \\
\qquad -\left(C_{T,1}e^{-my} + C_{T,2}e^{my}\right) \\
\tilde{\bar{\tau}}_{xy} = \dfrac{1-\nu}{2}\left[\sum_{i=1}^{4}\left(\lambda_i - i\xi B_i\right)C_{D,i}e^{\lambda_i y} - m\omega_1 e^{-my} + m\omega_2 e^{my} - i\xi\left(\omega_3 e^{-my} + \omega_4 e^{my}\right)\right]
\end{cases} \tag{4-38}$$

for $-l_a < y < 0$ and

$$\begin{cases} \tilde{\bar{\sigma}}_x = \sum_{i=5}^{8}\left(B_i\lambda_i\nu - i\xi\right)C_{D,i}e^{\lambda_i y} - i\xi\left(\omega_5 e^{-my} + \omega_6 e^{my}\right) + \nu\left(-m\omega_7 e^{-my} + m\omega_8 e^{my}\right) \\ \qquad -\left(C_{T,3}e^{-my} + C_{T,4}e^{my}\right) \\ \tilde{\bar{\sigma}}_y = \sum_{i=5}^{8}\left(B_i\lambda_i - i\xi\nu\right)C_{D,i}e^{\lambda_i y} - i\nu\xi\left(\omega_5 e^{-my} + \omega_6 e^{my}\right) - m\omega_7 e^{-my} + m\omega_8 e^{my} \\ \qquad -\left(C_{T,3}e^{-my} + C_{T,4}e^{my}\right) \\ \tilde{\bar{\tau}}_{xy} = \frac{1-\nu}{2}\left[\sum_{i=5}^{8}\left(\lambda_i - i\xi B_i\right)C_{D,i}e^{\lambda_i y} - m\omega_5 e^{-my} + m\omega_6 e^{my} - i\xi\left(\omega_7 e^{-my} + \omega_8 e^{my}\right)\right] \end{cases} \tag{4-39}$$

for $0 < y < l_b$, respectively.

To solve the unknown functions $C_{D,i}$ $(i = 1, 2, \ldots, 8)$, the boundary conditions (4-26) can be used. This allows providing six equations. The other two equations are found by considering the mixed boundary conditions (c) and (d) in (4-21) which would give a pair of dual integral equations.

Now we define two dimensionless dislocation functions $f_i(x)$ $(i = 1, 2)$ along the crack line as follows:

$$\begin{cases} f_1(x) = \dfrac{\partial\langle u\rangle}{\partial x} \\ f_2(x) = \dfrac{\partial\langle v\rangle}{\partial x} \end{cases} \tag{4-40}$$

where $\langle u\rangle$ and $\langle v\rangle$ denote the displacement jumps across the crack lips $y = 0$, namely

$$\begin{cases} \langle u\rangle = u\left(x, 0^+, t\right) - u\left(x, 0^-, t\right) \\ \langle v\rangle = v\left(x, 0^+, t\right) - v\left(x, 0^-, t\right) \end{cases} \tag{4-41}$$

From the conditions (*c*) and (*d*) of (4-15), we know that $f_i(x)$ $(i = 1, 2)$ also satisfy the single-valued conditions:

$$\int_{-1}^{1} f_i(x)\,dx = 0 \ (i = 1, 2) \tag{4-42}$$

and

$$f_i(x) = 0 \ (i = 1, 2) \qquad |x| \geq 1 \tag{4-43}$$

Physically speaking, Equation (4-43) means that the displacements are single-valued for the non-cracked portion along $y = 0$. By applying the Laplace and Fourier transforms to Equation (4-40), we obtain:

$$\begin{cases} \tilde{\bar{f}}_1(\xi) = -i\xi\left[\tilde{\bar{u}}(0^+) - \tilde{\bar{u}}(0^-)\right] \\ \tilde{\bar{f}}_2(\xi) = -i\xi\left[\tilde{\bar{v}}(0^+) - \tilde{\bar{v}}(0^-)\right] \end{cases} \tag{4-44}$$

where by definition and from (4-42), $\tilde{\bar{f}}_1$ and $\tilde{\bar{f}}_2$ are given by:

$$\begin{cases} \tilde{\bar{f}}_1 = \int_0^\infty \left(\int_{-1}^{1} f_1 \cdot e^{i\xi x} dx \right) \cdot e^{-pt} dt \\ \tilde{\bar{f}}_2 = \int_0^\infty \left(\int_{-1}^{1} f_2 \cdot e^{i\xi x} dx \right) \cdot e^{-pt} dt \end{cases} \tag{4-45}$$

By substituting (4-30) and (4-38) into (4-26) and (4-44), we obtain a system of eight linear equations for the unknown functions $C_{D,\,i}$ in terms of the dislocation functions in Laplace-Fourier space as follows

$$\mathbf{A} \cdot \mathbf{C}_D = \gamma \tag{4-46}$$

where $\mathbf{C}_D$ is the undetermined coefficient column vector, $\mathbf{A}$ and $\boldsymbol{\gamma}$ are the coefficient matrix and the constant column vector of the liner equation system, respectively, and are given by

$$\mathbf{A} = \begin{bmatrix} a_{1,1} & a_{1,2} & a_{1,3} & a_{1,4} & 0 & 0 & 0 & 0 \\ 0 & 0 & 0 & 0 & a_{2,5} & a_{2,6} & a_{2,7} & a_{2,8} \\ a_{3,1} & a_{3,2} & a_{3,3} & a_{3,4} & a_{3,5} & a_{3,6} & a_{3,7} & a_{3,8} \\ a_{4,1} & a_{4,2} & a_{4,3} & a_{4,4} & a_{4,5} & a_{4,6} & a_{4,7} & a_{4,8} \\ 0 & 0 & 0 & 0 & a_{5,5} & a_{5,6} & a_{5,7} & a_{5,8} \\ 0 & 0 & 0 & 0 & a_{6,5} & a_{6,6} & a_{6,7} & a_{6,8} \\ -1 & -1 & -1 & -1 & 1 & 1 & 1 & 1 \\ -B_1 & -B_2 & -B_3 & -B_4 & B_1 & B_2 & B_3 & B_4 \end{bmatrix} \tag{4-47}$$

where

$$\begin{cases} a_{1,j} = \left(i\xi\nu + B_j\lambda_j\right)e^{-\lambda_j l_a} & j = 1,2,3,4 \\ a_{2j} = \left(i\xi B_j + \lambda_j\right)e^{-\lambda_j l_a} & j = 1,2,3,4 \\ a_{3,j} = (-1)^{H(j-4.5)}\left(i\xi\nu + B_j\lambda_j\right) & j = 1,2,\ldots 8 \\ a_{4,j} = (-1)^{H(j-4.5)}\left(i\xi B_j + \lambda_j\right) & j = 1,2,\ldots 8 \\ a_{5,j} = \left(i\xi\nu + B_j\lambda_j\right)e^{\lambda_j l_b} & j = 5,6,7,8 \\ a_{6,j} = \left(i\xi B_j + \lambda_j\right)e^{\lambda_j l_b} & j = 5,6,7,8 \end{cases} \tag{4-48}$$

and

$$\gamma = \begin{bmatrix} \dfrac{(1-\nu)\xi^2 + p^2\tau_2^2}{p(-m^2+\xi^2+p^2\tau_2^2)}\delta(\xi) \\ -\dfrac{2m\left[p\left(e^{l_a m}+e^{(l_a+2l_b)m}\right)\tilde{\tilde{\phi}} - i\xi\left(1+e^{2(l_a+l_b)m}\right)\delta(\xi)\right]}{\left(-1+e^{2(l_a+l_b)m}\right)p\left(-m^2+\xi^2+p^2\tau_2^2\right)} \\ \dfrac{i\tilde{\tilde{\phi}}\left((1-\nu)\xi^2+p^2\tau_2^2\right)}{\xi(m^2-\xi^2-p^2\tau_2^2)} \\ 0 \\ 0 \\ -\dfrac{2e^{l_b m}m\left[\left(1+e^{2l_a m}\right)\tilde{\tilde{\phi}}\,p - 2ie^{l_a m}\delta(\xi)\xi\right]}{\left(-1+e^{2(l_a+l_b)m}\right)p\left(-m^2+\xi^2+p^2\tau_2^2\right)} \\ \dfrac{\tilde{\tilde{\phi}}}{-m^2+\xi^2+p^2\tau_2^2} \\ 0 \end{bmatrix} \tag{4-49}$$

where $H(x)$ used in (4-48) is the Heaviside step function. It is a discontinuous function whose value is zero for negative argument and one for positive argument:

$$H(x) = \begin{cases} 0 & x<0 \\ 1 & x>0 \end{cases} \tag{4-50}$$

We can solve Equation (4-46) for $C_{D,i}\,(i=1,2,\ldots,8)$ in terms of $\tilde{\tilde{f}}_1$ and $\tilde{\tilde{f}}_2$ as

$$C_{D,i} = \mathbf{A}^{-1}{}_i \cdot \gamma + \frac{1}{i\xi}\mathbf{A}^{-1}{}_{i,7}\tilde{\tilde{f}}_1 + \frac{1}{i\xi}\mathbf{A}^{-1}{}_{i,8}\tilde{\tilde{f}}_2 \qquad i=1,2,\ldots,8 \tag{4-51}$$

where $\mathbf{A}^{-1}$ denotes the inverse matrix of $\mathbf{A}$ and the subscripts i, j (i = 1, 2, …,8; j = 7, 8) denote the i-th row and j-th column of the matrix. Note that $\mathbf{A}^{-1}{}_i$ is a row vector and $\boldsymbol{\gamma}$ is a column vector and the dot between them denotes vector multiplication. By substituting (4-51) into (4-31), the displacements in Laplace-Fourier space can be written as:

$$\begin{cases} \tilde{\tilde{u}}_1(y) = \sum_{i=1}^{4}\left(\mathbf{A}^{-1}{}_i \cdot \gamma + \frac{1}{i\xi}\mathbf{A}^{-1}{}_{i,7}\tilde{\tilde{f}}_1 + \frac{1}{i\xi}\mathbf{A}^{-1}{}_{i,8}\tilde{\tilde{f}}_2(\xi)\right)e^{\lambda_i y} + \omega_1 e^{-my} + \omega_2 e^{my} \\ \tilde{\tilde{v}}_1(y) = \sum_{i=1}^{4} -\frac{\lambda_i^2+\beta_2}{\beta_1\lambda_i}\left(\mathbf{A}^{-1}{}_i \cdot \gamma + \frac{1}{i\xi}\mathbf{A}^{-1}{}_{i,7}\tilde{\tilde{f}}_1 + \frac{1}{i\xi}\mathbf{A}^{-1}{}_{i,8}\tilde{\tilde{f}}_2(\xi)\right)e^{\lambda_i y} + \omega_3 e^{-my} + \omega_4 e^{my} \\ \tilde{\tilde{u}}_2(y) = \sum_{i=5}^{8}\left(\mathbf{A}^{-1}{}_i \cdot \gamma + \frac{1}{i\xi}\mathbf{A}^{-1}{}_{i,7}\tilde{\tilde{f}}_1 + \frac{1}{i\xi}\mathbf{A}^{-1}{}_{i,8}\tilde{\tilde{f}}_2(\xi)\right)e^{\lambda_i y} + \omega_5 e^{-my} + \omega_6 e^{my} \\ \tilde{\tilde{v}}_2(y) = \sum_{i=5}^{8} -\frac{\lambda_i^2+\beta_2}{\beta_1\lambda_i}\left(\mathbf{A}^{-1}{}_i \cdot \gamma + \frac{1}{i\xi}\mathbf{A}^{-1}{}_{i,7}\tilde{\tilde{f}}_1 + \frac{1}{i\xi}\mathbf{A}^{-1}{}_{i,8}\tilde{\tilde{f}}_2(\xi)\right)e^{\lambda_i y} + \omega_7 e^{-my} + \omega_8 e^{my} \end{cases} \tag{4-52}$$

4.4 Singular Integral Equations

4.4.1 Derivation of the System of Integral Equations

Substituting (4-52) into (4-24) and applying the inverse Fourier transform, we obtain the stress fields in Laplace domain

$$
\begin{cases}
\bar{\sigma}_x = \dfrac{1}{2\pi}\displaystyle\int_{-\infty}^{\infty}\sum_{i=1}^{4}\left(B_i\lambda_i\nu - i\xi\right)\left(\mathbf{A}^{-1}{}_i\cdot\gamma + \dfrac{1}{i\xi}\mathbf{A}^{-1}{}_{i,7}\tilde{\tilde{f}}_1 + \dfrac{1}{i\xi}\mathbf{A}^{-1}{}_{i,8}\tilde{\tilde{f}}_2(\xi)\right)e^{\lambda_i y} \\
\quad + \displaystyle\int_{-1}^{1}\bar{\phi}(\eta)\cdot\dfrac{1}{2\pi}\int_0^{\infty}\dfrac{ie^{-my}\left(1-e^{2m(y+l_a)}\right)\left(1+e^{2ml_b}\right)\left(m^2(1-\nu)-p^2\tau_2^2\right)}{\left(-1+e^{2m(l_a+l_b)}\right)\xi\left(-m^2+\xi^2+p^2\tau_2^2\right)}\cos\left[\xi(\eta-x)\right]d\xi d\eta \\
\quad + \dfrac{1}{2\pi}\dfrac{e^{-ym_0+l_a m_0}\left(e^{2ym_0}-e^{2l_b m_0}\right)\left((-1+\nu)m_0^2+p^2\tau_2^2\right)}{\left(-1+e^{2(l_a+l_b)m_0}\right)p\left(-m_0^2+p^2\tau_2^2\right)} \\
\bar{\sigma}_y = \dfrac{1}{2\pi}\displaystyle\int_{-\infty}^{\infty}\sum_{i=1}^{4}\left(B_i\lambda_i - i\xi\nu\right)\left(\mathbf{A}^{-1}{}_i\cdot\gamma + \dfrac{1}{i\xi}\mathbf{A}^{-1}{}_{i,7}\tilde{\tilde{f}}_1 + \dfrac{1}{i\xi}\mathbf{A}^{-1}{}_{i,8}\tilde{\tilde{f}}_2(\xi)\right)e^{\lambda_i y}e^{-i\xi x}d\xi \\
\quad + \displaystyle\int_{-1}^{1}\bar{\phi}(\eta)\cdot\dfrac{1}{2\pi}\int_0^{\infty}\dfrac{ie^{-my}\left(e^{2m(y+l_a)}-1\right)\left(1+e^{2ml_b}\right)\left((1-\nu)\xi^2+p^2\tau_2^2\right)}{\left(-1+e^{2m(l_a+l_b)}\right)\xi\left(-m^2+\xi^2+p^2\tau_2^2\right)}\cos\left[\xi(\eta-x)\right]d\xi d\eta \\
\quad + \dfrac{1}{2\pi}\dfrac{p^2\tau_2^2 e^{-ym_0+l_a m_0}\left(e^{2ym_0}-e^{2l_b m_0}\right)}{\left(e^{2(l_a+l_b)m_0}-1\right)p\left(p^2\tau_2^2-m_0^2\right)} \\
\bar{\tau}_{xy} = \dfrac{1}{2\pi}\displaystyle\int_{-\infty}^{\infty}\dfrac{1-\nu}{2}\left[\sum_{i=1}^{4}\left(\lambda_i - i\xi B_i\right)\left(\mathbf{A}^{-1}{}_i\cdot\gamma + \dfrac{1}{i\xi}\mathbf{A}^{-1}{}_{i,7}\tilde{\tilde{f}}_1 + \dfrac{1}{i\xi}\mathbf{A}^{-1}{}_{i,8}\tilde{\tilde{f}}_2(\xi)\right)e^{\lambda_i y}\right]e^{-i\xi x}d\xi \\
\quad + \displaystyle\int_{-1}^{1}\bar{\phi}(\eta)\cdot\dfrac{1}{2\pi}\int_0^{\infty}\dfrac{2me^{-my}\left(1+e^{2m(y+l_a)}\right)\left(1+e^{2ml_b}\right)}{\left(e^{2m(l_a+l_b)}-1\right)\left(-m^2+\xi^2+p^2\tau_2^2\right)}\cos\left[\xi(\eta-x)\right]d\xi d\eta
\end{cases}
\tag{4-53}
$$

for $-l_a < y < 0, |x| < 1$ and

$$
\begin{cases}
\bar{\sigma}_x = \dfrac{1}{2\pi}\displaystyle\int_{-\infty}^{\infty}\sum_{i=5}^{8}\left(B_i\lambda_i\nu - i\xi\right)\left(\mathbf{A}^{-1}{}_i\cdot\gamma + \dfrac{1}{i\xi}\mathbf{A}^{-1}{}_{i,7}\tilde{\bar{f}}_1 + \dfrac{1}{i\xi}\mathbf{A}^{-1}{}_{i,8}\tilde{\bar{f}}_2(\xi)\right)e^{\lambda_i y}e^{-i\xi x}d\xi \\
\quad + \displaystyle\int_{-1}^{1}\bar{\phi}(\eta)\cdot\dfrac{1}{2\pi}\int_0^{\infty}\dfrac{ie^{-my}\left(1+e^{2ml_a}\right)\left(e^{2ml_b}-e^{2my}\right)\left(m^2(1-\nu)-p^2\tau_2^2\right)}{\left(-1+e^{2m(l_a+l_b)}\right)\xi\left(-m^2+\xi^2+p^2\tau_2^2\right)}\cos\left[\xi(\eta-x)\right]d\xi d\eta \\
\quad + \dfrac{1}{2\pi}\dfrac{e^{-ym_0+l_a m_0}\left(e^{2ym_0}-e^{2l_b m_0}\right)\left((-1+\nu)m_0^2+p^2\tau_2^2\right)}{\left(-1+e^{2(l_a+l_b)m_0}\right)p\left(-m_0^2+p^2\tau_2^2\right)} \\
\bar{\sigma}_y = \dfrac{1}{2\pi}\displaystyle\int_{-\infty}^{\infty}\sum_{i=5}^{8}\left(B_i\lambda_i - i\xi\nu\right)\left(\mathbf{A}^{-1}{}_i\cdot\gamma + \dfrac{1}{i\xi}\mathbf{A}^{-1}{}_{i,7}\tilde{\bar{f}}_1 + \dfrac{1}{i\xi}\mathbf{A}^{-1}{}_{i,8}\tilde{\bar{f}}_2(\xi)\right)e^{\lambda_i y}e^{-i\xi x}d\xi \\
\quad + \displaystyle\int_{-1}^{1}\bar{\phi}(\eta)\cdot\dfrac{1}{2\pi}\int_0^{\infty}\dfrac{ie^{-my}\left(1+e^{2ml_a}\right)\left(e^{2my}-e^{2ml_b}\right)\left((1-\nu)\xi^2+p^2\tau_2^2\right)}{\left(-1+e^{2m(l_a+l_b)}\right)\xi\left(-m^2+\xi^2+p^2\tau_2^2\right)}\cos\left[\xi(\eta-x)\right]d\xi d\eta \\
\quad + \dfrac{1}{2\pi}\dfrac{p^2\tau_2^2 e^{-ym_0+l_a m_0}\left(e^{2ym_0}-e^{2l_b m_0}\right)}{\left(-1+e^{2(l_a+l_b)m_0}\right)p\left(-m_0^2+p^2\tau_2^2\right)} \\
\bar{\tau}_{xy} = \dfrac{1}{2\pi}\displaystyle\int_{-\infty}^{\infty}\dfrac{1-\nu}{2}\left[\left(\lambda_i - i\xi B_i\right)\sum_{i=5}^{8}\left(\mathbf{A}^{-1}{}_i\cdot\gamma + \dfrac{1}{i\xi}\mathbf{A}^{-1}{}_{i,7}\tilde{\bar{f}}_1 + \dfrac{1}{i\xi}\mathbf{A}^{-1}{}_{i,8}\tilde{\bar{f}}_2(\xi)\right)e^{\lambda_i y}\right]e^{-i\xi x}d\xi \\
\quad + \displaystyle\int_{-1}^{1}\bar{\phi}(\eta)\cdot\dfrac{1}{2\pi}\int_0^{\infty}\dfrac{2me^{-my}\left(1+e^{2ml_a}\right)\left(e^{2my}+e^{2ml_b}\right)}{\left(-1+e^{2m(l_a+l_b)}\right)\left(-m^2+\xi^2+p^2\tau_2^2\right)}\cos\left[\xi(\eta-x)\right]d\xi d\eta
\end{cases}
\tag{4-54}
$$

for $0 < y < l_b, |x| < 1$. The parity of the integral function, the Euler formula (2-42) and the properties of Delta function (2-30) are used to obtain (4-53) and (4-54). It is obvious that the solution of the density function f_i (x) $(i = 1, 2)$ is necessary to find finally the stress fields.

By substituting Equation (4-53) into the boundary conditions (c) and (d) in (4-21), it can be shown that f_i (x) $(i = 1, 2)$ satisfy the following singular integral equations:

$$
\begin{cases}
\displaystyle\int_{-1}^{1}\bar{f}_1(\eta)\left[\frac{1}{x-\eta}+K_{11}(x,\eta)\right]d\eta + \int_{-1}^{1}\bar{f}_2(\eta)K_{12}(x,\eta)d\eta = K_{1,3}(x) \\
\displaystyle\int_{-1}^{1}\bar{f}_1(\eta)K_{21}(x,\eta)d\eta + \int_{-1}^{1}\bar{f}_2(\eta)\left[\frac{1}{x-\eta}+K_{22}(x,\eta)\right]d\eta = K_{2,3}(x)
\end{cases}
\tag{4-55}
$$

where

$$
\begin{cases}
K_{1,1} = \dfrac{1}{2\pi}\dfrac{2}{1-\nu^2}\displaystyle\int_0^\infty 2\sum_{i=1}^{4}\left(\left(\dfrac{-ib_i\lambda_i}{\xi}-\nu\right)\mathbf{A}^{-1}_{i,7}\right)\cos\left[\xi\left(x-\eta\right)\right]d\xi \\
K_{1,2} = \dfrac{1}{2\pi}\dfrac{2}{1-\nu^2}\displaystyle\int_0^\infty\left(2\sum_{i=1}^{4}\left(\left(\dfrac{-b_i\lambda_i}{\xi}+i\nu\right)A_{i,8}\right)-\dfrac{1-\nu^2}{2}\right)\sin\left[\xi\left(x-\eta\right)\right]d\xi \\
K_{1,3} = \dfrac{1}{2\pi}\dfrac{2}{1-\nu^2}\displaystyle\int_0^\infty 2i\left[\sum_{i=1}^{4}\left(-\nu\xi-ib_i\lambda_i\right)\mathbf{A}^{-1}_{i}\cdot\gamma_\phi-\dfrac{\left(1-e^{2Lam}\right)\left(1+e^{2Lbm}\right)\left(\left(1-\nu\right)\xi^2-p^2\tau_2^2\right)}{2\xi\left(-1+e^{2(La+Lb)m}\right)\left(-m^2+\xi^2+p^2\tau_2^2\right)}\right]\tilde{\bar{\phi}}\cos\left(\xi x\right)d\xi \\
\qquad +\dfrac{2}{1-\nu^2}\left(\dfrac{e^{Lap\tau_2}\left(1-e^{2Lbp\tau_2}\right)\tau_2^2}{\left(-1+e^{2(La+Lb)p\tau_2}\right)\left(-1-p\tau_1+p\tau_2^2\right)}+\dfrac{e^{Lam_0}\left(-1+e^{2Lbm_0}\right)\tau_2^2}{\left(-1+e^{2(La+Lb)m_0}\right)\left(-1-p\tau_1+p\tau_2^2\right)}\right) \\
K_{2,1} = \dfrac{1}{2\pi}\dfrac{1}{1+\nu}\displaystyle\int_0^\infty\left(2\sum_{i=1}^{4}\left(\dfrac{i\xi B_i-\Lambda_i}{\xi}A_{i,7}\right)-\left(1+\nu\right)\right)\sin\left[\xi\left(x-\eta\right)\right]d\xi \\
K_{2,2} = \dfrac{1}{2\pi}\dfrac{1}{1+\nu}\displaystyle\int_0^\infty 2\sum_{i=1}^{4}\left(\left(\dfrac{-i\Lambda_i}{\xi}-B_i\right)A_{i,8}\right)\cos\left[\xi\left(x-\eta\right)\right]d\xi \\
K_{2,3} = \dfrac{1}{2\pi}\dfrac{1}{1+\nu}\displaystyle\int_0^\infty 2i\left[\sum_{i=1}^{4}\left(i\xi b_i-\lambda_i\right)\mathbf{A}^{-1}_{i}\cdot\gamma_\phi+\dfrac{\left(1+e^{2Lam}\right)\left(1+e^{2Lbm}\right)m}{\left(-1+e^{2(La+Lb)m}\right)\left(m^2-\xi^2-p^2\tau_2^2\right)}\right]\tilde{\bar{\phi}}\sin\left(\xi x\right)d\xi
\end{cases}
\tag{4-56}
$$

where γ_φ is the coefficient of $\tilde{\bar{\varphi}}$ in Equation (4-49) and expressed as following

$$
\gamma_\phi = \begin{bmatrix}
0 \\
\dfrac{2mp\left(e^{l_a m}+e^{(l_a+2l_b)m}\right)}{p\left(1-e^{2(l_a+l_b)m}\right)\left(-m^2+\xi^2+p^2\tau_2^2\right)} \\
\dfrac{i\left(\left(1-\nu\right)\xi^2+p^2\tau_2^2\right)}{\xi(m^2-\xi^2-p^2\tau_2^2)} \\
0 \\
0 \\
\dfrac{2mpe^{l_b m}\left(1+e^{2l_a m}\right)}{\left(1-e^{2(l_a+l_b)m}\right)p\left(-m^2+\xi^2+p^2\tau_2^2\right)} \\
\dfrac{1}{-m^2+\xi^2+p^2\tau_2^2} \\
0
\end{bmatrix}
\tag{4-57}
$$

It is noticed that the convolving option is not applied to the inverse Fourier transform $K_{1,3}$ and $K_{2,3}$. Mathematically speaking, this would help to reduce the amount of computational tasks by n times where n is the number of the Gauss points. $\tilde{\bar{\varphi}}$ can be obtained from the roots of the linear equations (2-74)

$$
\begin{aligned}
\tilde{\bar{\phi}} &= \int_{-1}^{1}\bar{\phi}e^{i\xi x}dx \\
&= \frac{\pi}{n}\sum_{i=1}^{n}\psi_i\, i\sin\left(\xi\eta_i\right)
\end{aligned}
\tag{4-58}
$$

4.4.2 Solution of the Singular Integral Equations

By following the same procedure described in Section 2.5, the solutions of (4-55) can be written as

$$\overline{f}_i(x)=\overline{F}_i(x)w(x)=\overline{F}_i(x)(1-x)^{\alpha}(1+x)^{\beta}\quad (i=1,2) \tag{4-59}$$

where α and β satisfying:

$$-1<\mathrm{Re}(\alpha,\beta)<0 \tag{4-60}$$

We define that

$$g_i(z)=\frac{1}{\pi}\int_{-1}^{1}\frac{1}{\eta-z}\overline{f}_i(\eta)\,d\eta \tag{4-61}$$

Substituting Equation (4-61) into (4-59), we obtain

$$g_i(z)=\frac{1}{\pi}\int_{-1}^{1}\frac{1}{\eta-z}\overline{F}_i(\eta)(1-x)^{\alpha}(1+x)^{\beta}\,d\eta \tag{4-62}$$

Regarding the behavior of the Cauchy integral kernel [127, 131], Equation (4-62) can be expressed as follows:

$$g_i(z)=\frac{2^{\alpha}e^{-i\pi\beta}(1+z)^{\beta}}{\sin(-\beta\pi)}\overline{F}_i(-1)-\frac{2^{\beta}e^{i\pi\alpha}(1-z)^{\alpha}}{\sin(-\alpha\pi)}\overline{F}_i(1)+g_0(z) \tag{4-63}$$

where the singularity of $g_0(z)$ is less than α and β. The function $g_0(z)$ is bounded everywhere except probably at the crack tips where

$$|g_0(z)|<\frac{1}{|z-c_i|^{d_i}}\quad i=1,2 \tag{4-64}$$

where d_i are real constants and satisfies $d_i<1$. Using the Plemelj formula, we obtain:

$$\frac{1}{2}\left[g_i^{+}(z)+g_i^{-}(z)\right]=\frac{1}{\pi}\int_{-1}^{1}\frac{1}{\eta-z}\overline{f}_i(\eta)\,d\eta \tag{4-65}$$

From Equations (4-63) and (4-65) we obtain:

$$\begin{aligned}&\frac{1}{\pi}\int_{-1}^{1}\frac{1}{\eta-z}\overline{f}_i(\eta)\,d\eta\\&=2^{\alpha}(1+z)^{\beta}\cot(-\beta\pi)\overline{F}_i(-1)-2^{\beta}(1-z)^{\alpha}\cot(-\alpha\pi)\overline{F}_i(1)+g_0(z)\end{aligned} \tag{4-66}$$

Substituting (4-66) into (4-61), we obtain:

$$2^{\alpha}(1+z)^{\beta}\cot(-\beta\pi)\overline{F}_i(-1)-2^{\beta}(1-z)^{\alpha}\cot(-\alpha\pi)\overline{F}_i(1)+g_0(z)=g(z) \tag{4-67}$$

Multiplying both sides of (4-67) by $(1+z)^{-\alpha}$ and let $z\to1$, and then by $(z-1)^{-\beta}$ and let $z\to$-1, the Characteristic equation for the unknown constants α and β are obtained as

follows:

$$\begin{cases} \cot(-\alpha\pi) = 0 \\ \cot(-\beta\pi) = 0 \end{cases} \tag{4-68}$$

By considering the restriction (4-60), it is clear that

$$\alpha = \beta = -\frac{1}{2} \tag{4-69}$$

Thus Equation (4-59) can be written as:

$$\overline{f}_i(x) = \frac{\overline{F}_i(x)}{\sqrt{1-x^2}} \quad (i = 1, 2) \tag{4-70}$$

So the dislocation function $\overline{f}_i(x)$ has square root singularities at the crack tips.

From Equation (4-42) it is clear that $\overline{F}_i(x) \quad (i = 1, 2)$ satisfy:

$$\int_{-1}^{1} \overline{F}_i(x)\,dx = 0 \ (i = 1, 2) \tag{4-71}$$

By following the same procedure as that described in 2.5.1 - 2.5.3 and by using the Lobatto-Chebyshev method [102, 146, 147], the resolution of the singular integral equations (4-55) and (4-71) allows reducing the integral equations to the following algebraic equations:

$$\begin{cases} \sum_{i=1}^{n} A_i \left[\frac{1}{x_j - \eta_i} + K_{11}(x_j, \eta_i) \right] \overline{F}_1(\eta_i) + \sum_{i=1}^{n} A_i K_{12}(x_j, \eta_i) \overline{F}_2(\eta_i) = K_{13}(x_j) \\ \sum_{i=1}^{n} A_i K_{21}(x_j, \eta_i) \overline{F}_1(\eta_i) + \sum_{i=1}^{n} A_i \left[\frac{1}{x_j - \eta_i} + K_{22}(x_j, \eta_i) \right] \overline{F}_2(\eta_i) = K_{23}(x_j) \\ \sum_{i=1}^{n} A_i \overline{F}_1(\eta_i) = 0 \\ \sum_{i=1}^{n} A_i \overline{F}_2(\eta_i) = 0 \end{cases}$$

(4-72)

where

$$\begin{cases} \eta_i = \cos\dfrac{(i-1)\pi}{n-1},\ i = 1,2,\ldots,n; \\ x_j = \cos\dfrac{(2j-1)\pi}{2(n-1)},\ j = 1,2,\ldots,n-1; \\ A_1 = A_n = \dfrac{\pi}{2(n-1)}; \\ A_i = \dfrac{\pi}{n-1},\ i = 2,3,\ldots,n-1. \end{cases} \tag{4-73}$$

where $\eta_i\,(i = 1,\ldots n)$ are the Gauss points that we choose to form the linear equations, n is the number of the discrete points that make up the dislocation functions. Equations (4-72) and (4-73) give a linear equation system of size of $2n$ by $2n$, Then the functions $\overline{F}_1$ and $\overline{F}_2$ at the crack line can be obtained discretely by solving the linear equations (4-72).

4.4.3 Stress Intensity Factors

We define the dimensionless stress intensity factors (SIFs) as:

$$\left(K_I^*, K_{II}^*\right) = \frac{1-\nu}{E\alpha\left(T_\infty - T_0\right)\sqrt{r}}\left(K_I, K_{II}\right) \tag{4-74}$$

Similarly, we omit the superscript "*" in the following analysis for brevity. Then the dimensionless stress intensity factors at the crack tip (1, 0) in Laplace space can be defined and evaluated as follows:

$$\begin{cases} \overline{K}_I(1) = \lim\limits_{x\to 1}\sqrt{2\pi(x-1)}\,\overline{\sigma}_y(x,0) \\ \overline{K}_{II}(1) = \lim\limits_{x\to 1}\sqrt{2\pi(x-1)}\,\overline{\tau}_{xy}(x,0) \end{cases} \tag{4-75}$$

where $\overline{K}_i(1)\quad (i = I, II)$ denote the stress intensity factors in Laplace space; x tends to 1 from the outside of the crack. It should be noted that the traction free condition in the range of $|x| < 0,\ y = 0$ gives the singular integral equation system, the solution of which gives the stress expression at the extension cord of the crack in the domain $|x| \geq 0,\ y = 0$. We recognize that both Equations (4-53) and (4-54) can be used in (4-75) to evaluate the stress intensity factors. With Equation (4-53), for example, the stress components $\overline{\sigma}_y$ and $\overline{\tau}_{xy}$ at the crack ligaments can be rewritten as

$$\begin{cases} \dfrac{4}{1-\nu^2}\bar{\sigma}_y(x,0)=\dfrac{1}{2\pi}\left[\displaystyle\int_{-1}^{1}\dfrac{1}{\eta-x}\bar{f}_2(\eta)d\eta+\sum_{i=1}^{2}\int_{-1}^{1}K_{\sigma,f_i}\bar{f}_i(\eta)d\eta+\int_{-1}^{1}K_{\sigma,\phi}\bar{\phi}(\eta)d\eta\right]+K_{\sigma,\delta} \\ \dfrac{2}{1+\nu}\bar{\tau}_{xy}(x,0)=\dfrac{1}{2\pi}\left[\displaystyle\int_{-1}^{1}\dfrac{1}{\eta-x}\bar{f}_1(\eta)d\eta+\sum_{i=1}^{2}\int_{-1}^{1}K_{\tau,f_i}\bar{f}_i(\eta)d\eta+\int_{-1}^{1}K_{\tau,\phi}\bar{\phi}(\eta)d\eta\right]+K_{\tau,\delta} \end{cases} \tag{4-76}$$

where

$$\begin{cases} K_{\sigma,f_1}=-\dfrac{8}{1-\nu^2}\displaystyle\int_0^\infty\sum_{i=1}^{4}\left(\dfrac{iB_i\lambda_1}{\xi}+\nu\right).\mathbf{A}^{-1}_{i,7}\cos(\xi x)d\xi \\ K_{\sigma,f_2}=2\displaystyle\int_0^\infty\sum_{i=1}^{4}\left(\dfrac{4}{1-\nu^2}\left(i\nu-\dfrac{bi\lambda i}{\xi}\right).\mathbf{A}^{-1}_{i,7}-1\right)\sin\left[\xi(\eta-x)\right]d\xi \\ K_{\sigma,\phi}=\dfrac{4}{1-\nu^2}\dfrac{i\left(1-e^{2ml_1}\right)\left(1+e^{2ml_b}\right)\left((1-\nu)\xi^2+p^2\tau_2^2\right)}{2\left(1-e^{2m(l_1+l_b)}\right)\xi\left(-m^2+\xi^2+p^2\tau_2^2\right)} \\ K_{\sigma,\delta}=\dfrac{4}{1-\nu^2}\dfrac{e^{ml_1}\left(1-e^{2ml_b}\right)\left((1-\nu)\xi^2-p^2\tau_2^2\right)}{\left(1-e^{2m(l_1+l_b)}\right)p\left(-m^2+\xi^2+p^2\tau_2^2\right)} \\ K_{\tau,f_1}=2\displaystyle\int_0^\infty\left(\dfrac{2}{1+\nu}\sum_{i=1}^{4}\left(i\nu-\dfrac{bi\lambda i}{\xi}\right).\mathbf{A}^{-1}_{i,7}-1\right)\sin\left[\xi(\eta-x)\right]d\xi \\ K_{\tau,f_2}=\dfrac{4}{1+\nu}\displaystyle\int_0^\infty\sum_{i=1}^{4}-\left(\dfrac{ibi\lambda i}{\xi}+\nu\right).\mathbf{A}^{-1}_{i,7}\cos(\xi x)d\xi \\ K_{\tau,\phi}=\dfrac{2}{1+\nu}\dfrac{\left(1+e^{2ml_a}\right)\left(1+e^{2ml_b}\right)m}{\left(1-e^{2m(l_a+l_b)}\right)\left(m^2-\xi^2-p^2\tau_2^2\right)} \\ K_{\tau,\delta}=\dfrac{2}{1+\nu}\dfrac{2ie^{ml_a}\left(1+e^{2ml_b}\right)m\xi}{\left(1-e^{2m(l_a+l_b)}\right)p\left(-m^2+\xi^2+p^2\tau_2^2\right)} \end{cases} \tag{4-77}$$

The stresses are expected to be singular at the crack tip. It is clear from the definition of the stress intensity factors (4-75) that no terms in (4-76) is more singular than the square root singularity. By omitting these less singular terms, we deduce the stress intensity factors as follows:

$$\begin{cases} K_I(1)=\lim\limits_{x\to1}\sqrt{2\pi(x-1)}\sigma_y(x,0)=\sqrt{\pi(x-1)}\dfrac{1-\nu^2}{4\sqrt{2}}\dfrac{1}{\pi}\lim\limits_{x\to1}\displaystyle\int_{-1}^{1}\dfrac{1}{\eta-x}f_2(\eta)d\eta \\ K_{II}(1)=\lim\limits_{x\to1}\sqrt{2\pi(x-1)}\tau_{xy}(x,0)=\sqrt{\pi(x-1)}\dfrac{1+\nu}{2\sqrt{2}}\dfrac{1}{\pi}\lim\limits_{x\to1}\displaystyle\int_{-1}^{1}\dfrac{1}{\eta-x}f_1(\eta)d\eta \end{cases} \tag{4-78}$$

Regarding the behavior of the Cauchy integral [127], the integrals in Equations (4-78) can be expressed as follows

$$\frac{1}{\pi}\int_{-1}^{1}\frac{f_i(\eta)}{\eta-x}d\eta=\frac{F_i(-1)e^{\frac{i\pi}{2}}}{\sqrt{2}\sqrt{1+x}}-\frac{F_i(1)e^{-\frac{i\pi}{2}}}{\sqrt{2}\sqrt{1-x}}+g_0(x)\quad i=1,2;|x|>1 \tag{4-79}$$

Substituting Equation (4-79) into (4-78), we obtain:

$$\begin{cases} K_I(1) = \lim\limits_{x\to 1}\sqrt{2\pi(x-1)}\sigma_y(x,0) = -\dfrac{(1-\nu^2)\sqrt{\pi}}{8}F_2(1) \\ K_{II}(1) = \lim\limits_{x\to 1}\sqrt{2\pi(x-1)}\tau_{xy}(x,0) = -\dfrac{(1+\nu)\sqrt{\pi}}{4}F_1(1) \end{cases} \tag{4-80}$$

4.4.4 Crack Opening Displacements

Apart from the dynamic SIFs, the crack opening displacements (CODs) are also important parameters for predicting crack growth. The CODs can be defined in different manners. Whatever the definition, they can be calculated when knowing the displacement jumps between the crack-lips, which can be calculated by integrating the dislocation density function found from Equation(4-72), then by performing the Laplace inverse transform.

Once the solution of the dislocation functions obtained, the crack opening shape can be deduced from Equation (4-40):

$$\begin{cases} \langle \bar{u}(x)\rangle = \bar{u}_2(x) - \bar{u}_1(x) = \int_{-1}^{x} \bar{f}_1(\eta)\,d\eta \\ \langle \bar{v}(x)\rangle = \bar{v}_2(x) - \bar{v}_1(x) = \int_{-1}^{x} \bar{f}_2(\eta)\,d\eta \end{cases} \tag{4-81}$$

By using the relationship (4-70), Equation (4-81) can be expressed as:

$$\begin{cases} \langle \bar{u}(x)\rangle = \bar{u}_2(x) - \bar{u}_1(x) = \int_{-1}^{x} \dfrac{\bar{F}_1(\eta)}{\sqrt{1-\eta^2}}\,d\eta \\ \langle \bar{v}(x)\rangle = \bar{v}_2(x) - \bar{v}_1(x) = \int_{-1}^{x} \dfrac{\bar{F}_2(\eta)}{\sqrt{1-\eta^2}}\,d\eta \end{cases} \tag{4-82}$$

Noting that the solution of $\bar{F}_i(\eta)\,(i=1,2)$ are represented by the numerical values at the discrete points. In order to calculate the integral of the right-hand side of Equation (4-82), it would be convenient if we fit these discrete values by continue curves. By considering the parity of the dislocation functions and the symmetry of the problem, as is shown in Figure 2.1-1, polynomial functions are used to this end for simplicity. Noting that $\bar{F}_1$ is an even function and $\bar{F}_2$ is an odd function, therefore, the corresponding polynomials for $\bar{F}_1$ and $\bar{F}_2$ may be given as:

$$\begin{cases} P_{f1}(x,n) = a_0 + a_2x^2 + a_4x^4 + \ldots + a_{2(n-1)}x^{2(n-1)} \\ P_{f2}(x,n) = a_1x + a_3x^3 + a_5x^5 + \ldots + a_{2k-1}x^{2n-1} \end{cases} \tag{4-83}$$

where a_i are the polynomials coefficients, with i = 0, 2, … 2(n-1) for $P_{f1}(x, n)$ and i = 1, 3, … 2n-1 for $P_{f2}(x, n)$); n is the degree of the polynomials. Theoretically, the accuracy of series approximation of the dislocation function would be higher if we increase the degree of the polynomial. Fortunately, because of the smoothness and parity of the dislocation functions, the polynomial fitting functions convergent fast as the n increasing.

The convergence and accuracy of the fitting are illustrated by considering the following pilot case. The geometrical and material parameters are given in Table 4.4-1 and the raw data for $\bar{F}_1$ and $\bar{F}_2$ are shown in Table 4.4-2.

parameters	l_a	l_b	**Poisson's ratio**	**Biot number**	τ_1	τ_2
Values	1	2	0.3	0	0.2	0.1

Table 4.4-1 Geometrical and materials parameters used in the pilot case.

x	-1	-0.9781	-0.9135	-0.809	-0.6691	-0.5	-0.309	-0.1045
$\bar{F}_1$	0.1442	0.134	0.0939	0.0312	-0.0279	-0.0712	-0.1066	-0.1256
$\bar{F}_2$	-0.0027	-0.0021	-0.0005	0.0014	0.0028	0.0031	0.0024	0.0009
x	0.1045	0.309	0.5	0.6691	0.809	0.9135	0.9781	1
$\bar{F}_1$	-0.1256	-0.1066	-0.0712	-0.0279	0.0312	0.0939	0.134	0.1442
$\bar{F}_2$	-0.0009	-0.0024	-0.0031	-0.0028	-0.0014	0.0005	0.0021	0.0027

Table 4.4-2 Discrete data for $\bar{F}_1$ and $\bar{F}_2$.

By using the *"Fit"* function in mathematica, we obtain the fitting functions for different n:

$$\begin{cases} P_{f1}(x,2) = -0.13763 + 0.27603x^2 \\ P_{f1}(x,4) = -0.12614 + 0.18524x^2 + 0.09210x^4 - 0.00392x^6 \\ P_{f1}(x,5) = -0.12957 + 0.29401x^2 - 0.44576x^4 + 0.84709x^6 - 0.42072x^8 \\ P_{f1}(x,6) = -0.12821 + 0.22655x^2 + 0.08953x^4 - 0.63952x^6 + 1.26434x^8 - 0.66845x^{10} \end{cases} \tag{4-84}$$

and

$$\begin{cases} P_{f2}(x,2) = -0.00940x + 0.01203x^3 \\ P_{f2}(x,4) = -0.00838x + 0.00688x^3 + 0.00678x^5 - 0.00256x^7 \\ P_{f2}(x,5) = -0.00835x + 0.00651x^3 + 0.00810x^5 - 0.00430x^7 + 0.000767x^9 \\ P_{f2}(x,6) = -0.00835x + 0.00649x^3 + 0.00825x^5 - 0.00465x^7 + 0.001108x^9 - 0.000123x^{11} \end{cases} \tag{4-85}$$

The comparison between the discrete points and the fitting polynomials for $\bar{F}_1$ and $\bar{F}_2$ is illustrated in Figure 4.4-1 and Figure 4.4-2. It can be seen that the fitting functions are almost overlapped for n = 5 and n = 6 and agree already well with the original data by taking n = 6. Therefore, n = 6 will be used afterward for polynomial fitting of the crack shape.

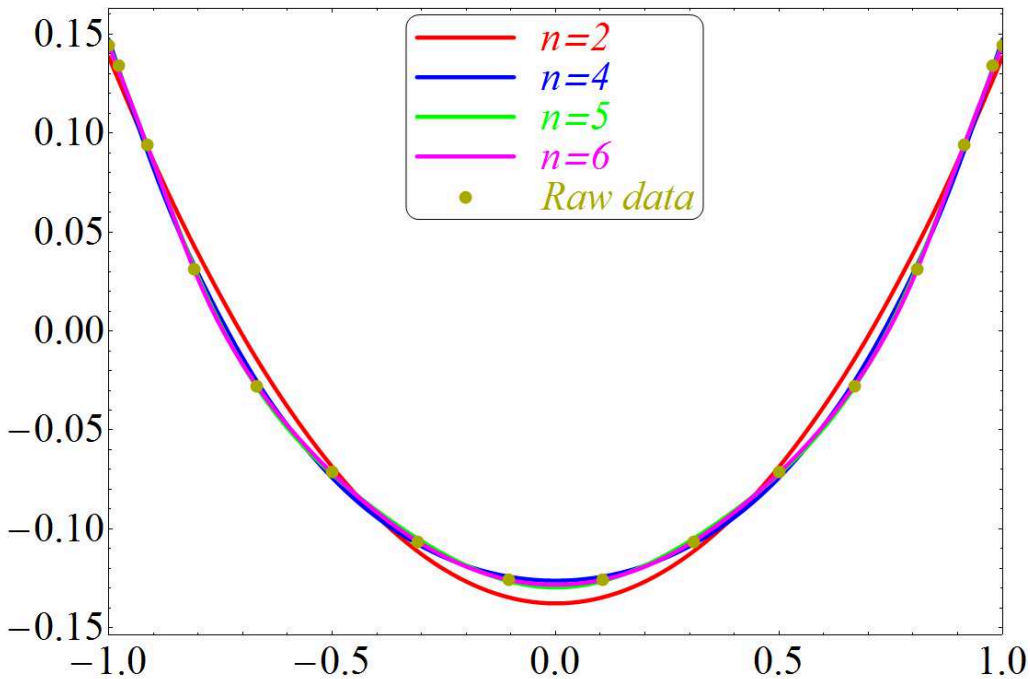

Figure 4.4-1 Comparison of $\bar{F}_1$ and the Fitting functions.

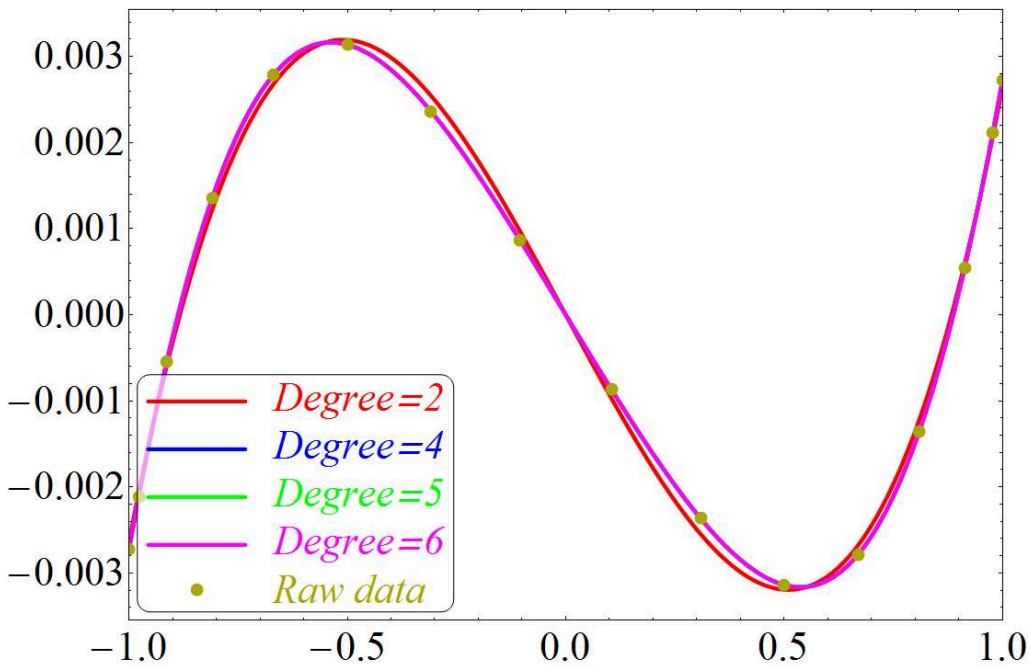

Figure 4.4-2 Comparison of $\bar{F}_2$ and the Fitting functions.

4.5 Convergence Analysis

The convergence analysis for the temperature field has been investigated in section 2.6. Similar analysis for the stress fields is carried out in this section.

As processed in section 2.6, the numerical integration interval $\xi \in [0, \infty)$ is split into two parts: $\xi \in [0, \mathrm{M} \cdot \mathrm{T}]$ and $\xi \in (\mathrm{M} \cdot \mathrm{T}, \infty)$. The integer M should be large enough such that the integral over the second part of the interval could be negligible. As there are 6 numerical integrations in Equation(4-55), namely $\mathrm{K}_{\mathrm{i,j}}$ $(\mathrm{i} = 1, 2; \mathrm{j} = 1, 2, 3)$, and the integrands are different in each integral, the upper border of the numerical integrations should be determined separately. Table 4.5-1 shows the upper border and the effective floating number for each integral under which all the relative errors are less than 0.004.

	K_{11}	K_{12}	K_{13}	K_{21}	K_{22}	K_{23}
Upper border (*M*)	6	8	5	8	6	160
Effective floating number	27	30	29	28	28	38

Table 4.5-1 Selected upper limit and the precisions for each integral

The process of determining n in Equation (4-72) and (4-73) is similar to that

described in section 2.6.2. In this work, the number of the Gauss points for all the numerical integrations is set to be 16.

4.6 Inverse Laplace Transform

Once the stress intensity factors and crack opening shape in Laplace space are obtained, fields in time domain can be derived by applying the inverse Laplace transform, as is shown in section 2.7.

Chapter 5 Numerical Results on Stress Fields

The analytical analyses performed in Chapter 4 allow obtaining the numerical solutions on stress intensity factors (SIFs) and crack opening displacements (CODs) of the crack, which enable the assessment of the crack toughness. In this chapter, we will focus our attention on the influence of different factors on these parameters. The factors we considered include the Biot number (Bi), the non-Fourier factor (NFF) and the inertia factor (IF), representing different physical mechanisms existing during the thermal shock process. In traditional thermal stress analyses, these factors are often neglected. This simplification does not permit to predict crack initiation and growth in the parallel direction of the heated surface, observed in engineering structure as mentioned in Chapter 1. We will demonstrate that such a cracking process is predictable if these factors are taken into account.

It is necessary to notice that there is no displacement constraint on the crack surfaces so both the stress intensity factors K_I and the crack opening displacement in y-direction may be negative. It is clear that this result is physically unreasonable as the overlapping of the crack surfaces is not allowed in real structures. However, the consideration of the non-overlapping condition leads to a too much complex mathematical formulation which makes its solution too difficult or impossible. As a consequence, we only study the opening phases of the crack and assume that this simplification will not lead to unacceptable errors in the solution of the thermal shock problem.

5.1 Biot Number's Effect

In this section we will discuss the influence of the Biot number on the SIFs and CODs with both τ_1 and τ_2 set to be 0. The physical meaning of $\tau_2 > 0$ will be discussed in Section 5.3. It is clear that when $\tau_2 = 0$, the stress fields are obtained from the quasi-static theory. Under this condition the stress concentration near the crack tips is provoked by the existence of the temperature gradient, which is, in turn, provoked by the thermal barrier formed by the crack. Consequently, the stress concentration level near the crack tips are directly related to the temperature distribution.

In fact, both the SIFs and CODs can be used to describe the stress concentration at the crack tips. The trend of SIFs versus different physical parameters is similar to that of the CODs. However, the CODs are easily measureable quantities in engineering applications and also help to understand the behavior of crack propagation. Therefore, the CODs will be discussed together with the SIFs in this section.

5.1.1 Stress Intensity Factors

The dimensionless stress intensity factors are defined in Equation (5-1). Figure 5.1-1 shows the evolution of the dimensionless stress intensity factors for different Biot numbers. The solid and dashed curves represent the evolution of K_{I} and K_{II} respectively and the use of different Biot numbers can be distinguished by colors. Here the absolute values of K_{II} are presented even though they are plotted as negative values: we plot the curves in this manner just for more clarity. In a similar manner, Figure 5.1-2 shows the dimensionless stress intensity factors versus Biot number for different dimensionless times.

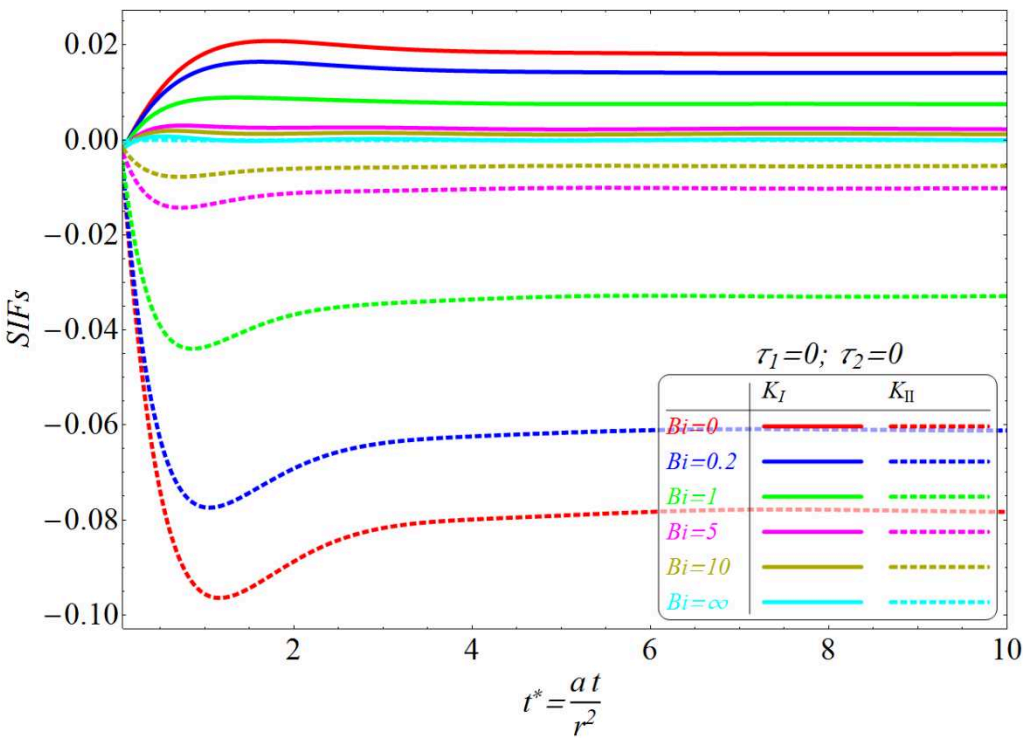

Figure 5.1-1 Dimensionless stress intensity factors versus dimensionless time for different Biot numbers when $\tau_1 = \tau_2 = 0$.

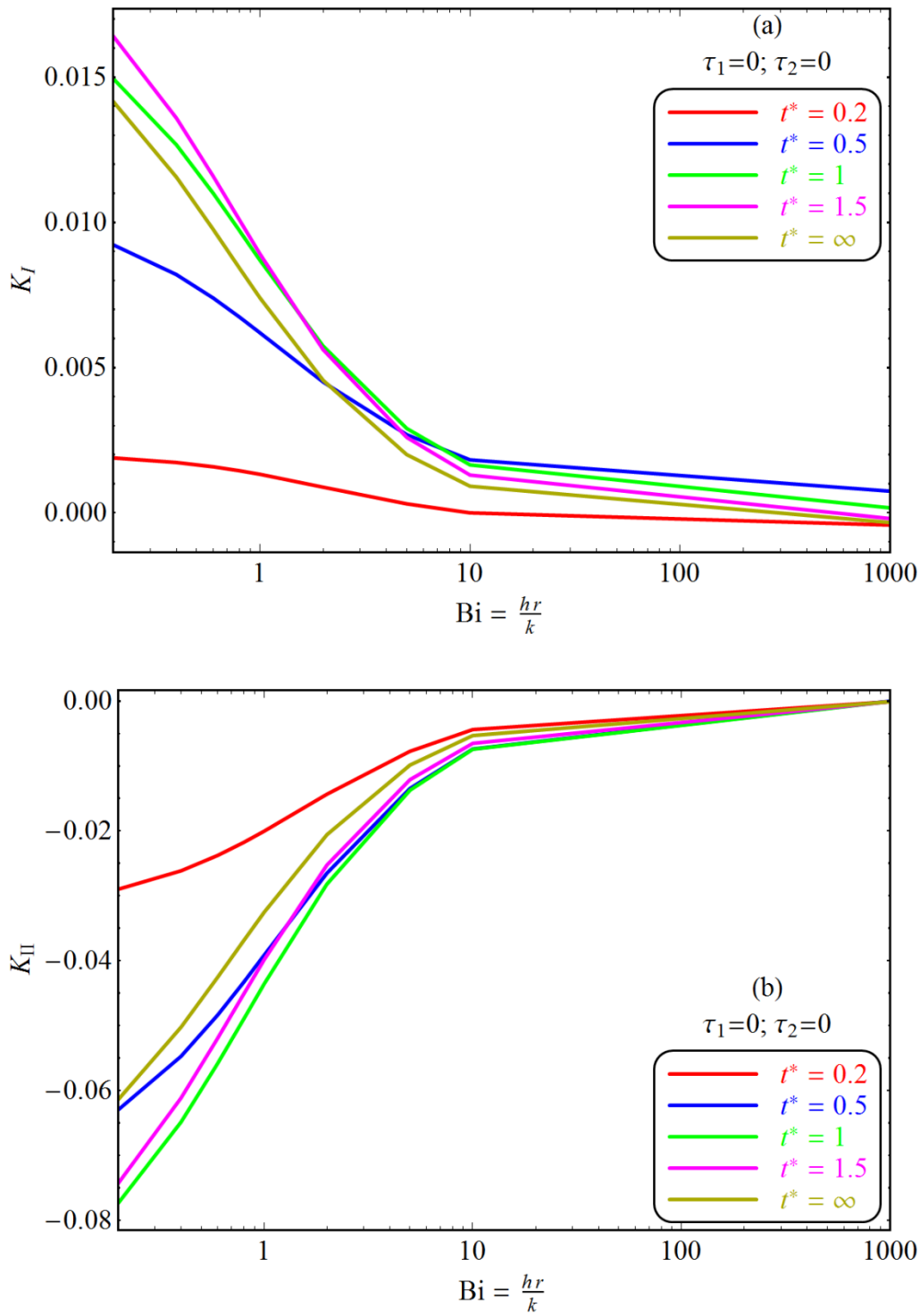

Figure 5.1-2 Dimensionless stress intensity factors (a): K_{I} (b): K_{II} versus Biot number at different dimensionless times when $\tau_1 = \tau_2 = 0$.

From these two figures, the following remarks can be made:

- As the Biot number increases, the values of the SIFs decrease gradually. This trend is directly related to the dependence of the temperature field on the Biot number. As discussed above, the crack behaves as a thermal

resistance: smaller Biot numbers signify bigger thermal resistance. Therefore, the smaller the Biot number is, the higher the temperature gradient is around the crack and as a consequence, the higher the SIFs are.

- The curves of the SIFs versus t^* do not cross each other for all $t^* > 0$. This means that larger Biot numbers always correspond to lower SIFs during all the thermal shock process.
- The absolute values of both K_I and K_{II} increase then decrease with time. A peak value for each SIF evolution can be reached during the thermal shock. It is clear that this peak value is a crucial measure for crack growth prediction.
- In general, $K_{II} > K_I$ for all the Biot numbers.
- In heating process, the crack tips are subjected to a mixed mode loading as both K_I and K_{II} are not nil. However, in cooling process, only the mode-II loading exists as the crack surfaces are closed and in contact.

It is notable that the magnitude of the SIFs change significantly as the Biot number goes from 0 to infinity. This proves that the thermal resistance of the crack plays a major role in the crack propagation under thermal shock.

5.1.2 Crack Opening Displacements

In this work, the crack opening displacements (CODs) are defined as the displacement jumps between all the opposed points of the two crack surfaces. The components COD(u) and COD(v) stand for the displacement jumps in x- and y-directions respectively. This definition is different from that usually used in the literature, in which the acronym COD stands for the crack opening distance between two special opposite points.

It is predictable from the definition of CODs that the influence of physical parameters to the CODs follows the similar rules as those to the SIFs. However, the CODs display the deformed crack shape in a displacement perspective, which helps to understand the process of thermal shock in an intuitive manner. Moreover, the CODs are observable and measurable quantities. This property makes it more advantageous comparing to the SIFs in some engineering applications. In this section we will discuss the influence of Biot number to the CODs.

In Figure 5.1-3, we plot the crack opening displacements COD(u) in x-direction for different Biot numbers at different dimensionless times. The vertical coordinate denotes the displacement differences between the two crack surfaces. The abscissa denotes the dimensionless coordinates of points at the crack surfaces. The displacement directions of these points in a heating process are indicated in small sketches included in the figures.

The maximum COD(u) during all the thermal shock process are plotted in Figure 5.1-4.

Similarly, in Figure 5.1-5, we plot the crack opening displacements COD(v) in y-direction for different Biot numbers at different dimensionless times. The maximum COD(v) during all the thermal shock process are plotted in Figure 5.1-6.

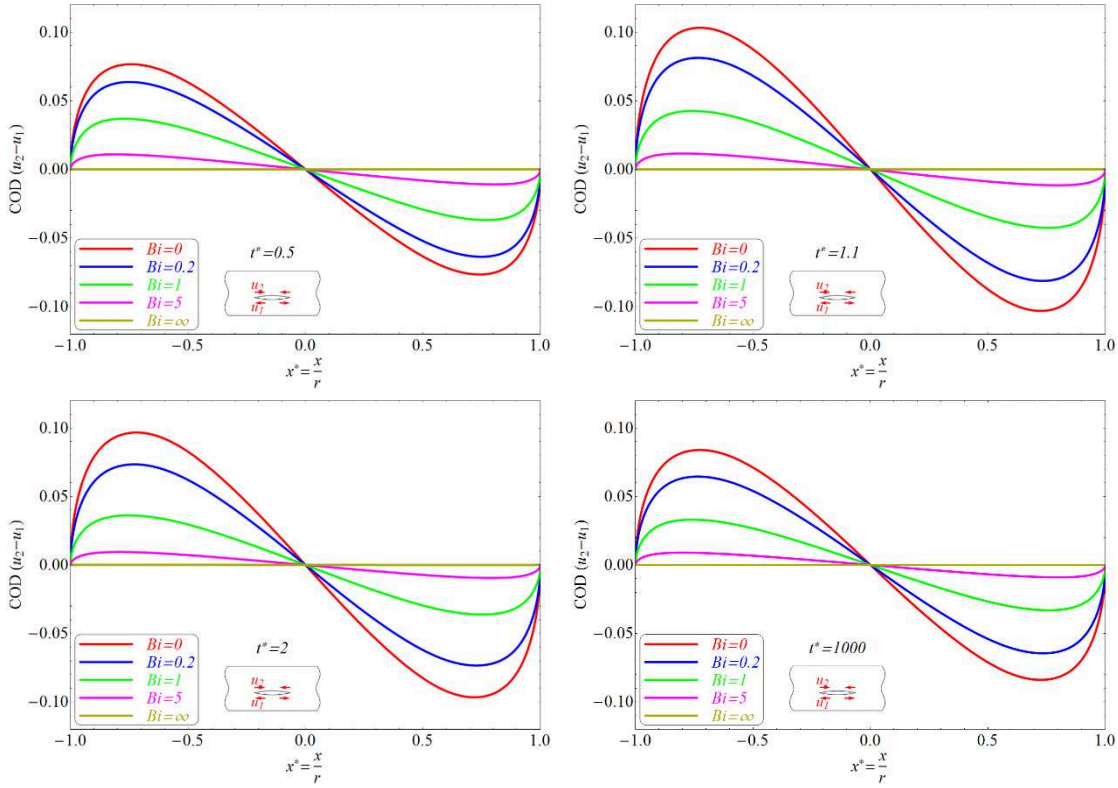

Figure 5.1-3 Crack Opening Displacement for different Biot numbers and at different dimensionless times when $\tau_1 = \tau_2 = 0$

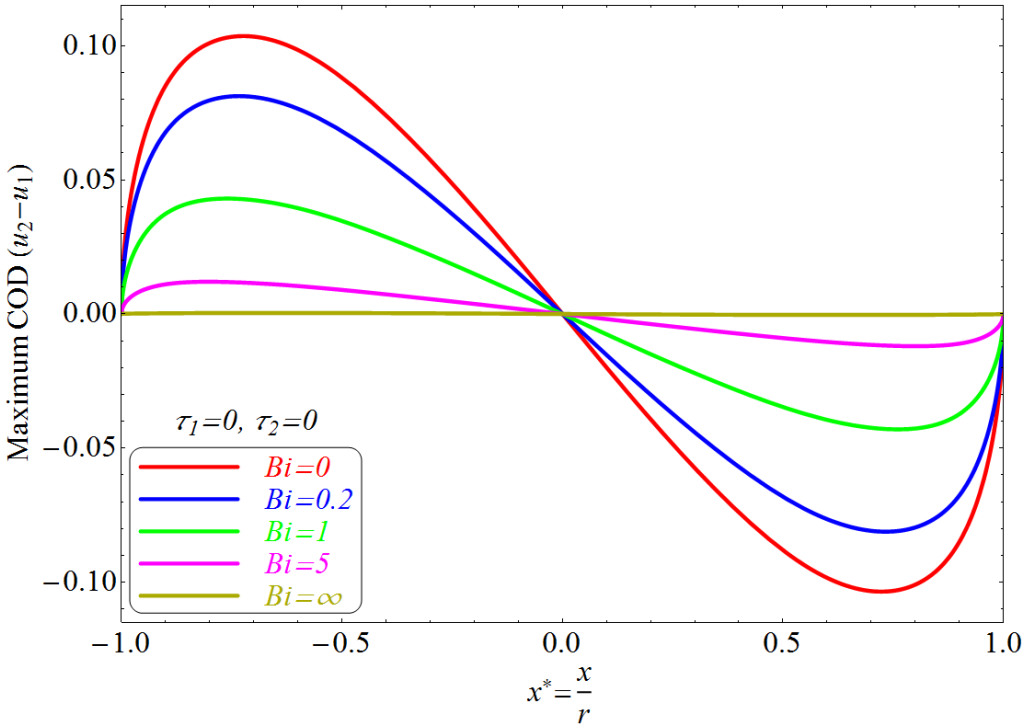

Figure 5.1-4 Maximum COD(u) for different Biot numbers

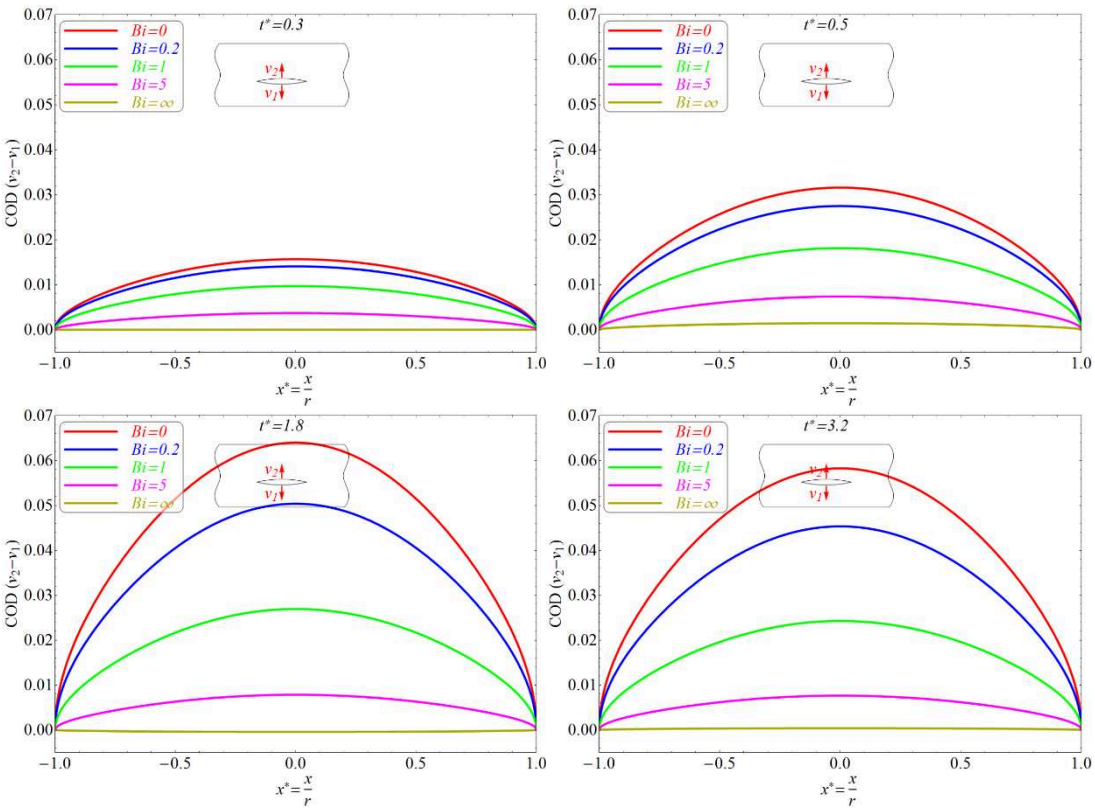

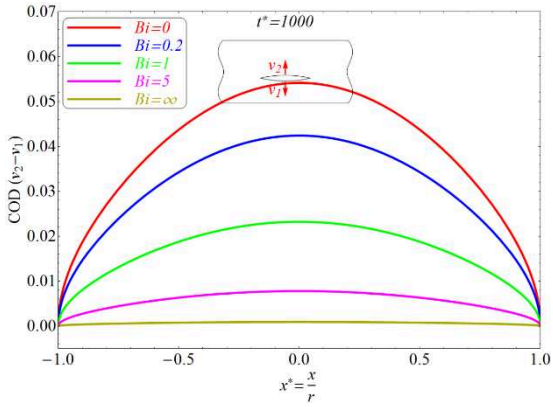

Figure 5.1-5 Crack Opening Displacements COD(v) for different Biot numbers and at different dimensionless times when $\tau_1 = \tau_2 = 0$

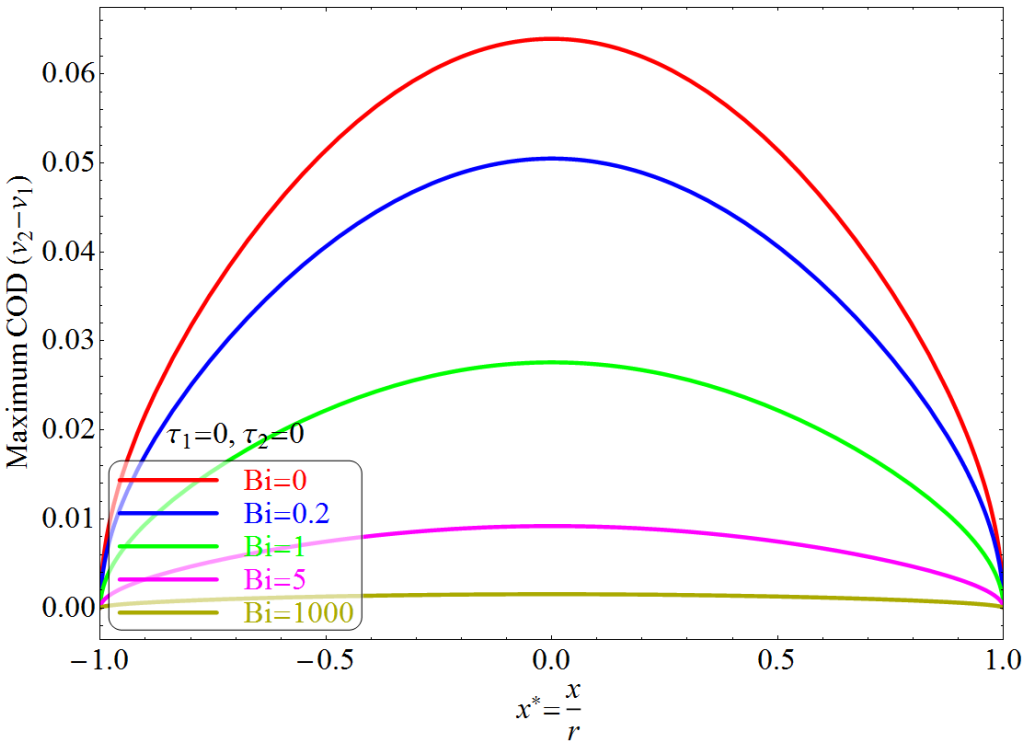

Figure 5.1-6 Maximum COD(v) for different Biot numbers

Observation of these figures leads us to obtain the similar conclusions as those indicated in Section 5.1.1. It confirms the role played by the Biot number in thermal shock induced fractures. Also, these figures show that the curves of COD(u) are of a sinus-form and the maximums of COD(u) are always located in the range of $x^* = [-1, -0.5]$. For COD(v), parabolic-form curves are obtained. The maximums of COD(v) are always situated at the mid-point of the crack line.

Moreover, these figures provide deformed crack shapes that enable us to easily

describe the fracture scenarios in two different situations:

- Heating thermal shock: In this case, COD(v) is positive, therefore, both the mode-I and mode-II are activated on the crack tips during the thermal shock. The fracture energy release rate G can be amplified due to this fact according to $G = \left(K_I^2 + K_{II}^2\right)/E$. The crack growth direction will be oriented to the interior of the strip according to the maximum circumferential stress criterion [148]
- Cooling thermal shock. In this case, COD(v) is negative. Only the mode-II is activated as the crack surfaces are closed. The stress intensity factor K_{II} should be attenuated by the friction between the crack surfaces. However, the crack growth direction will be oriented toward the surface of the strip. As the distance l_a can be very small, this crack growth direction favorites the fracture of the coating. It is worthy to repeat that the surface contact scenario is not considered in this work and the crack surface overlapping is not a physically reasonable result. Consequently, only qualitative indications can be made in the case when this result is applied to a cooling thermal shock.

These discussions show the complexity of the crack growth scenarios during the thermal shock process. It is difficult to quantify the harmfulness of the near-surface crack in an incisive manner; detailed analysis should be made case by case in order to obtain correct conclusions.

As we know, the stress concentrations in a solid subjected to thermal loading are essentially generated by the temperature gradient. The results in the previous sections indicate that the evolution of the stress field, characterized here by SIFs and CODs, is highly related to that of the temperature field. Therefore, it will be interesting to compare the evolution of these two fields and find an eventual correlation between them.

Here we compare the times used for different thermal and mechanical quantities to reach their maximal values. Figure 5.1-7 shows the dimensionless times used for different variables, namely, TDM, K_I, K_{II}, COD(v) and COD(u), to reach the peak values. These dimensionless times are plotted as function of the Biot number which is scaled in a logarithmic abscissa.

Figure 5.1-7 shows that all the curves decrease as Biot number decreases. This means that the bigger the Biot number is, the earlier the fields reach the maximum

will be. On other words, the thermal barrier created by the crack will delay the times used for all the considered variables to reach their maximal values. On the one hand, the curves of Max(K_{I}) and Max(COD(v)) are very close each other, exactly like those of Max(K_{II}) and Max(COD(u)). This is because that the parameters K_I and COD(v) are related to the mode-I loading while K_{II} and COD(u) are related to the mode-II loading. It is interesting to notice that Max(K_{II}) and Max(COD(u)) are closer to Max(TDM) than Max(K_{I}) and Max(COD(v)) when Bi < 10 while the contrary takes place when Bi > 10.

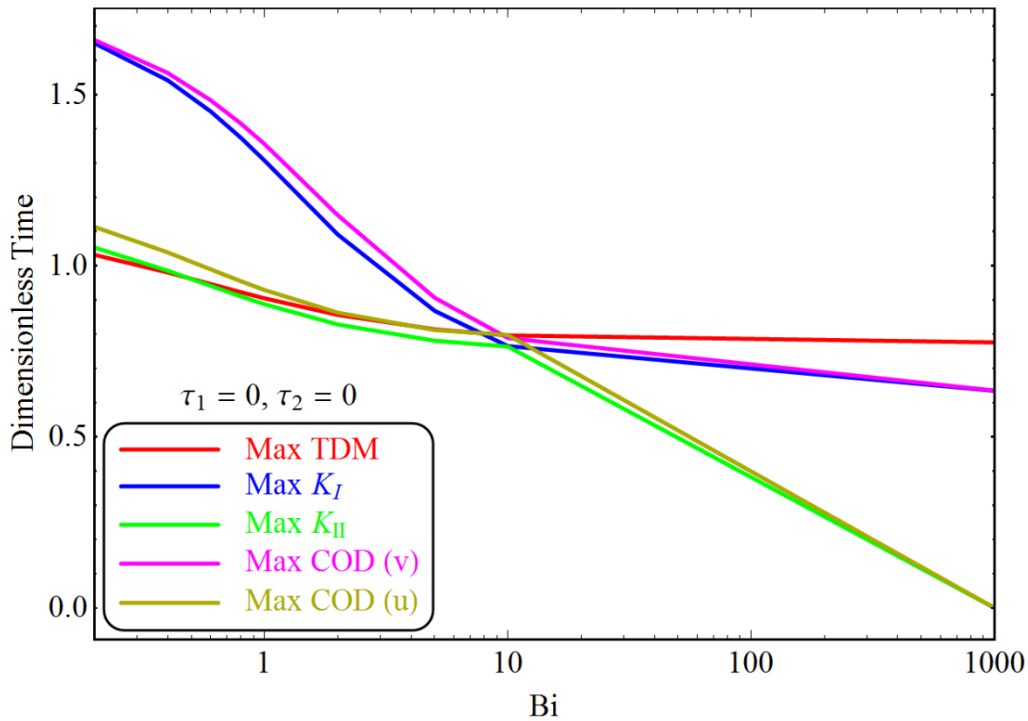

Figure 5.1-7 The dimensionless time when TDM, K_{I}, K_{II}, COD(v) and COD(u) reach the peak value versus Biot number.

5.2 Non-Fourier Effect

The influence of the non-Fourier effect on the SIFs and CODs will be discussed under the condition Bi = τ_2 = 0 in this section.

5.2.1 Stress Intensity Factors

Figure 5.2-1 shows the curves of dimensionless stress intensity factors versus

dimensionless time for different τ_1.

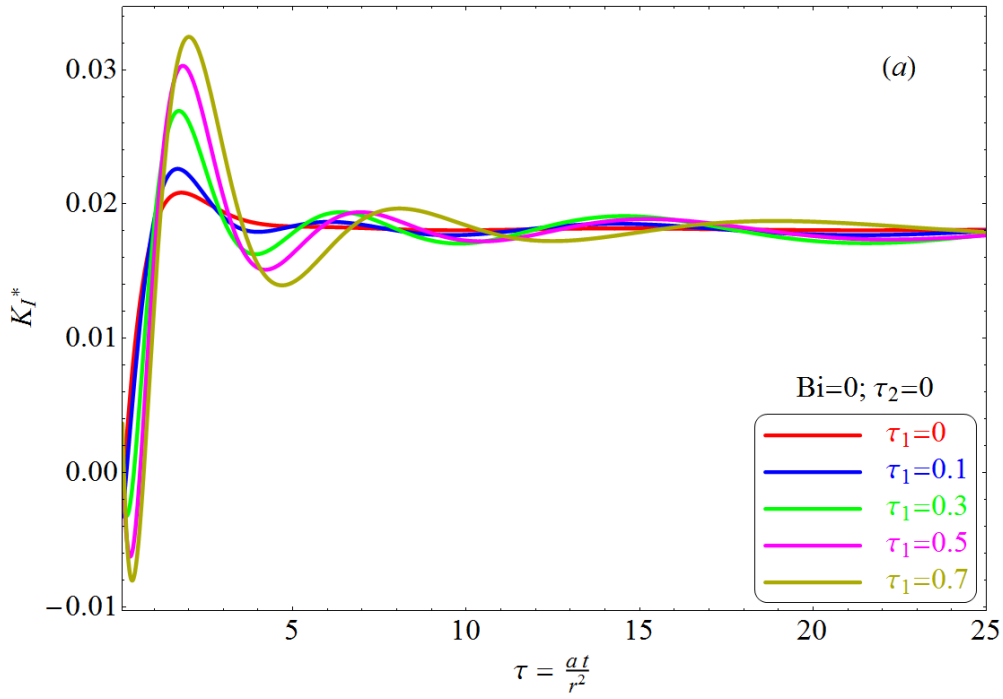

.

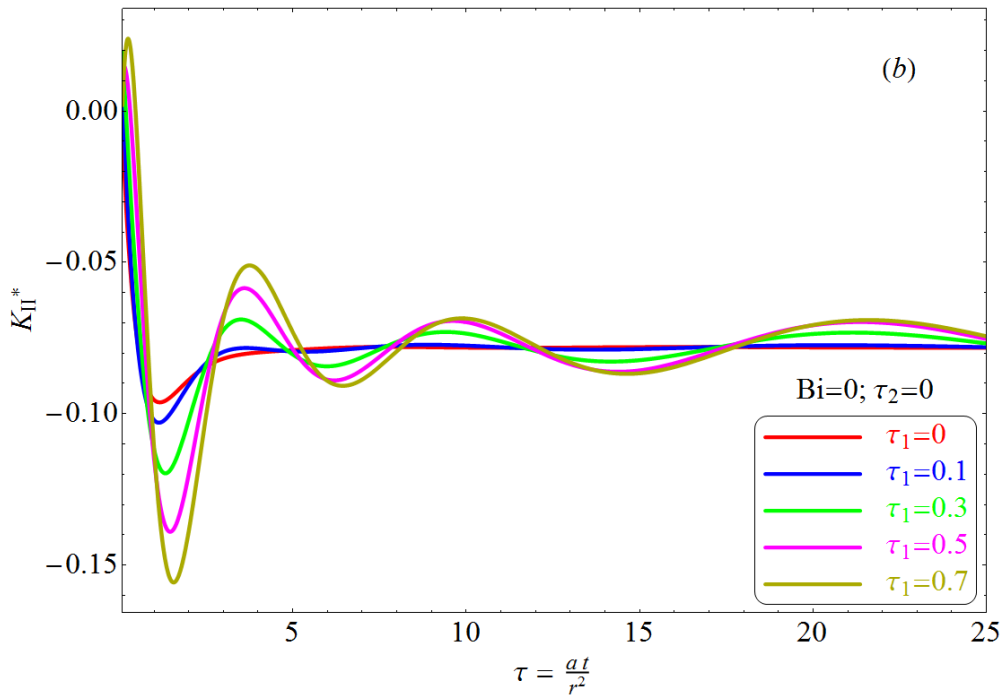

Figure 5.2-1 Normalized stress intensity factors (a) K_I and (b) K_{II} versus dimensionless time for different τ_1 when Bi = τ_2 = 0.

From Figure 5.2-1, we can remark that

- As τ_1 growing, the oscillation property appears in the evolution curves of the SIFs, similarly to that of the temperature field.

- The oscillation amplitude increases with τ_1. The first oscillation is the biggest. After that, the oscillation amplitude decreases as time increases.
- The oscillation period also increases with τ_1. It increases gradually as time increases.
- The oscillation of K_I is not synchronized with that of K_{II}. They follow their evolution with different periods and phases.
- A crack closure phase (negative K_I) at the first moment just after a heating thermal shock, or an opening phase (positive K_I) after a cooling thermal shock, can be found.

These phenomena related to the temperature oscillation are typical effects of the non-Fourier factor.

5.2.2 Crack Opening Displacements

Following the same analysis as in the preceding section, we now examine the influence of the non-Fourier factor on the CODs of the crack.

Figure 5.2-2 shows the crack opening displacement in x-direction (COD(u)) for different values of τ_1 at the dimensionless times 0.5, 1.1, 2 and infinity respectively. The behaviors of COD(u) are similar to those of the SIF K_{II}. The oscillation effect of NFF is obvious. At the beginning of the thermal shock, the CODs with $\tau_1 > 0$ are smaller to that with $\tau_1 = 0$. Then they quickly surpass the amplitude of the conventional COD.

Figure 5.2-3 shows the maximum COD(u) for different values of τ_1. It is clear that the maximum COD(u) increases with τ_1.

The variations of COD(v) for different τ_1 are illustrated in Figure 5.2-4 at different dimensionless times, namely t^*= 0.5, 1.1, 2 and infinity. The behaviors of COD(v) are similar to those of the SIF K_I. The oscillating effect of τ_1 can also be observed in these figures. It is to notice that the negative values of COD(v) at the early stage of the thermal shock are not physically reasonable. This is resulting from the fact that the displacement constraint at the crack surfaces is not taken into account in our analysis.

Figure 5.2-5 shows the maximum COD(v) for different values of τ_1. Here again, maximum COD(v) increases as τ_1 increases.

From these figures, we can conclude that the principal effect of the non-Fourier analysis is the oscillation of the stress field during the thermal shock process. It is clear that the stress oscillation occurs as the consequence of the temperature wave. More importantly, the maximum SIFs or CODs can be much higher than those obtained with a conventional Fourier heat conduction analysis.

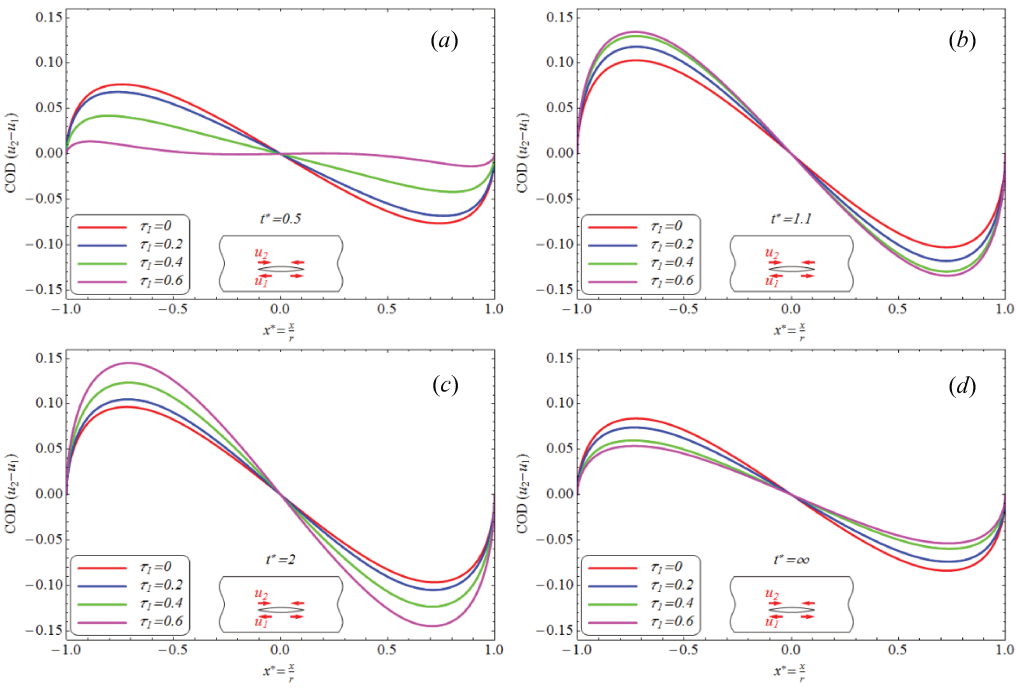

Figure 5.2-2 Crack Opening Displacement (u_2 - u_1) for different values of τ_1 when Bi = τ_2 = 0 at (a) t^* = 0.5, (b) t^* = 1.1, (c) t^* = 2 and (d) t^* = ∞ respectively

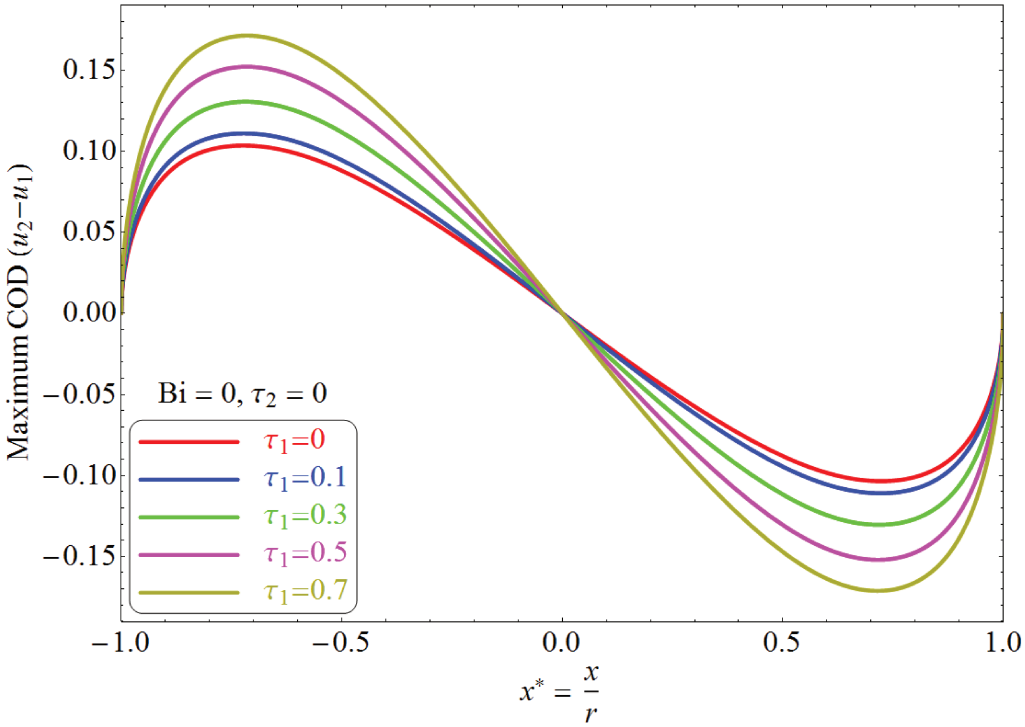

Figure 5.2-3 Maximum COD(u) for different values of τ_1 when Bi = τ_2 = 0.

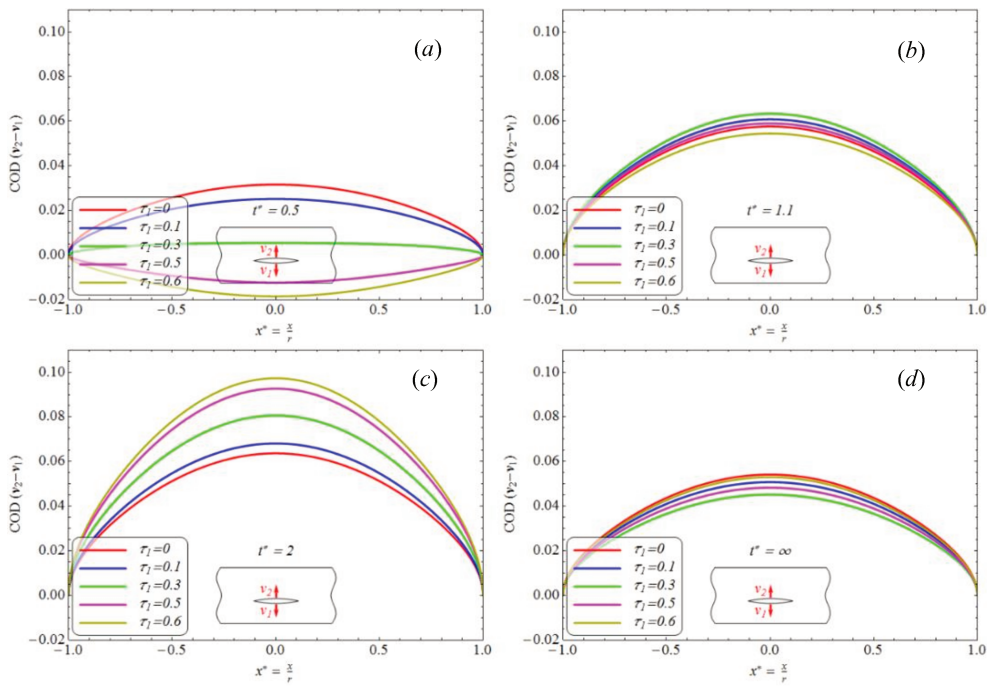

Figure 5.2-4 Crack Opening Displacement (v_2 - v_1) for different values of τ_1 when Bi = τ_2 = 0 and t^* = 0.5, 1.1, 2 and infinity.

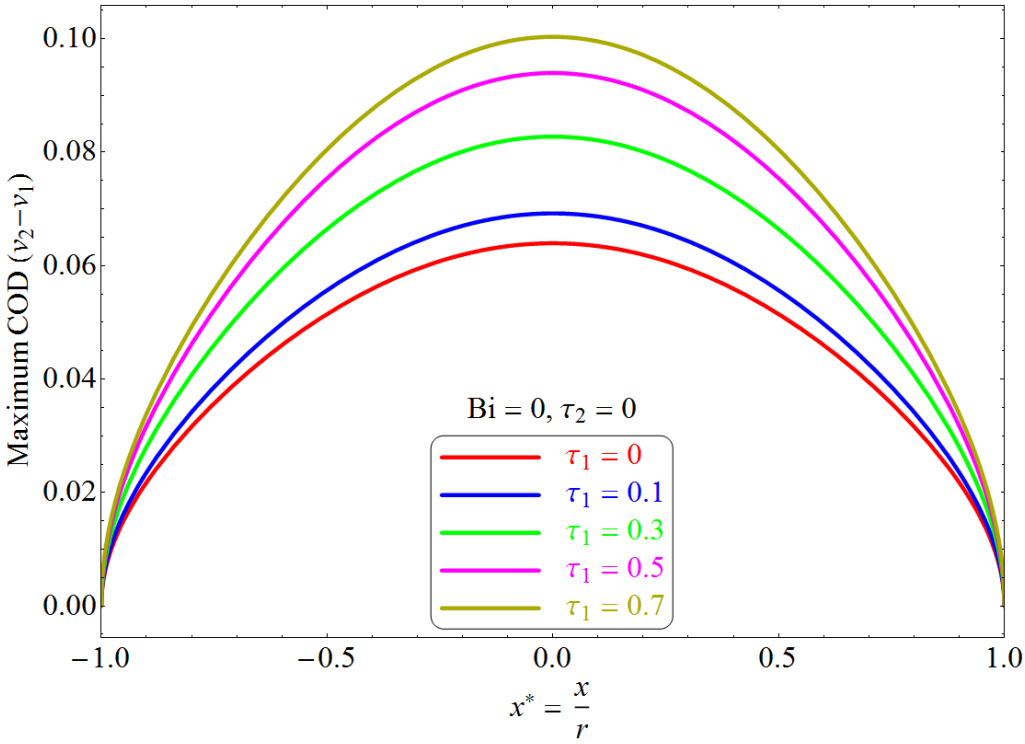

Figure 5.2-5 Maximum COD(v) for different values of τ_1

Figure 5.2-6 shows the dimensionless times used by different thermal and mechanical quantities to reach the peak values versus τ_1. Differently from the Biot number effect as shown in Figure 5.1-7, these curves are not monotonically increasing. They decrease at the early stage of the thermal shock, and become increasing afterward. Roughly speaking, all the mechanical quantities follow the variation of the thermal variable TDM. We also remark that the curve of max(K_I) and that of the max(COD(v)) almost overlap and the curves of max(K_{II}) and the that of max(COD(u)) are very close.

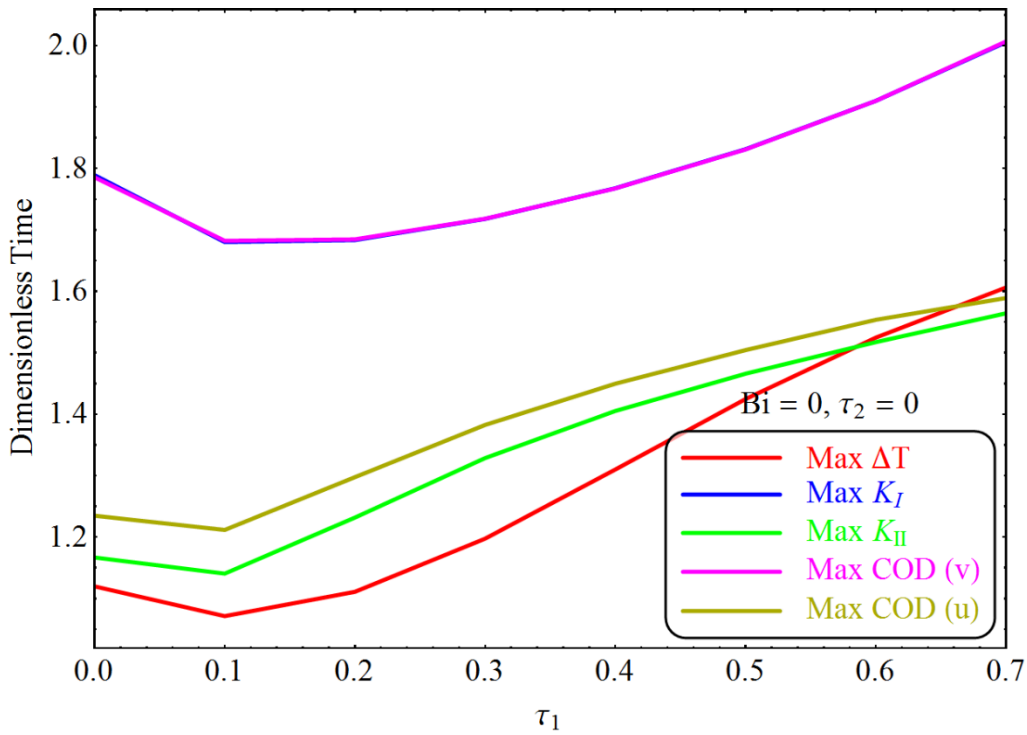

Figure 5.2-6 The dimensionless time when TDM, K_I, K_{II}, COD(v) and COD(u) reach the peak value versus τ_1 when Bi = τ_2 = 0.

5.3 Inertia Effect

In this section we will study the influence of the inertia factor on the stress concentration during the thermal shock. When the inertia factor τ_2 is different from zero, the governing Equations (4-14) become the wave equations. In this case, the time evolution of the stresses is not only caused by the variation of the temperature gradient, but also by the stress wave generated by the thermal shock. Physically speaking the stress waves are longitudinal waves. The direction of the wave propagation is essentially perpendicular to the heated surface.

In this section we will study in detail the behavior of τ_2 with τ_1 = Bi = 0.

5.3.1 Stress Intensity Factors

The normalized stress intensity factors versus dimensionless time for different τ_2 are shown in Figure 5.3-1. This figure leads us to make the following remarks:

- Both K_I and K_{II} present a time-dependent oscillating feature. The oscillation behavior is much more obvious for K_I than for K_{II}.

- Caused by additional source of stress, the crest of K_I curve can be much higher than that in the quasi-static cases when $\tau_2 = 0$.
- In comparison, the oscillation amplitude of K_{II} is much smaller. The reason of this difference is that the wave propagation is essentially along the *y*-axis which changes little the shear stresses along the *x*-axis. Consequently, K_{II} is not so sensitive to τ_2, as shown in Figure 5.3-1 (*b*).
- As τ_2 increases, it appears a time interval in which $K_I < 0$. This is senseless for heating thermal shock as the crack surfaces are in contact. However, for cooling thermal shock, the values of K_I in this interval are positive and cannot be neglected if τ_2 is large enough. This is an important difference from the quasi-static analysis according to which the mode-I crack growth can be neglected in cooling thermal shock.
- The oscillation amplitude decreases while the oscillation period increases with time;
- In comparison with Figure 5.3-1, we can see that the oscillation period of an inertia effect induced stress wave is comparable to that of a non-Fourier effect induced stress wave.

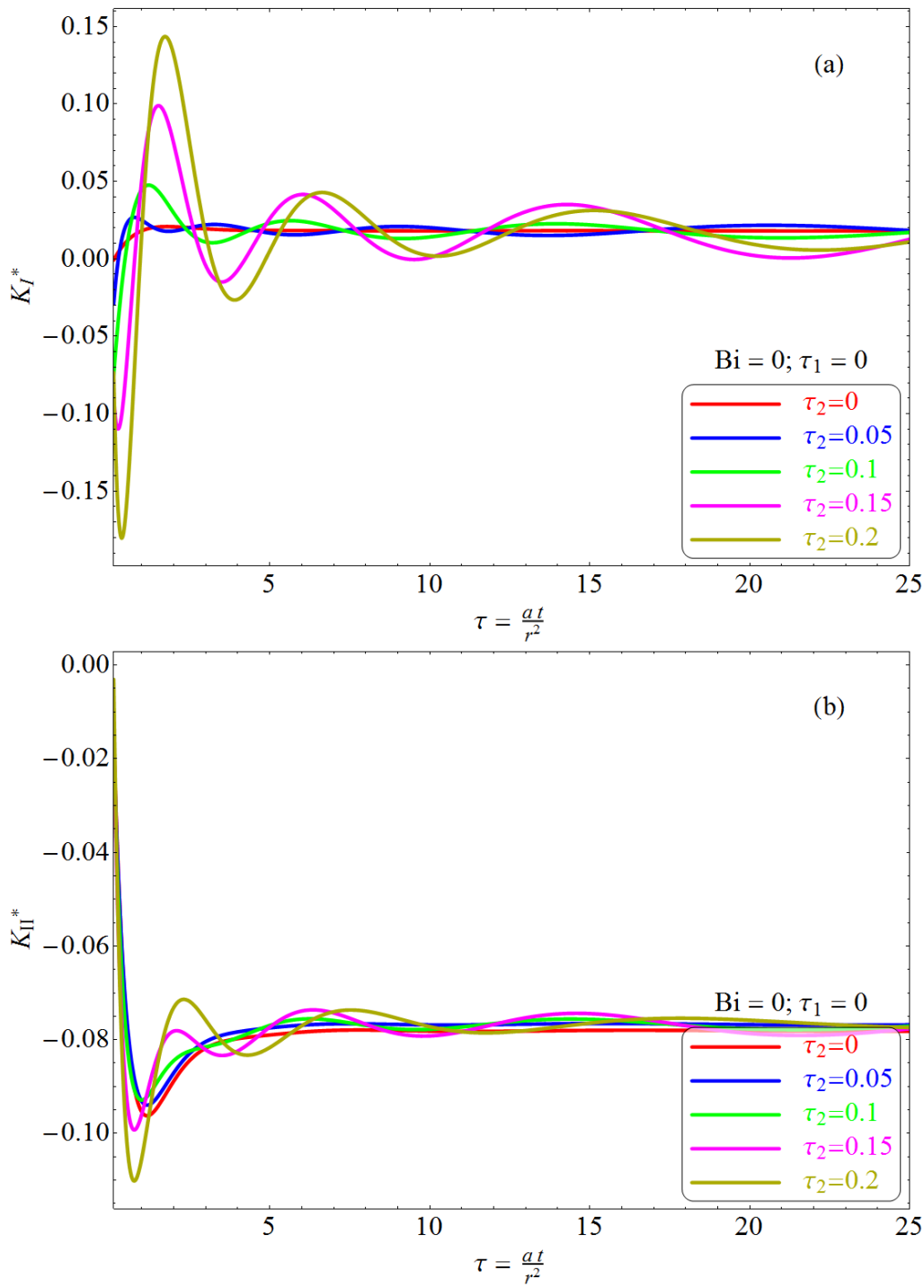

Figure 5.3-1 Normalized stress intensity factors (a) for K_{I} and (b) for K_{II} versus dimensionless time for different τ_2 when Bi = τ_1 = 0.

5.3.2 Crack Opening Displacements

The COD(u) for different inertia factors when the dimensionless time is set to be 0.2, 1.1, 2 and infinity respectively are shown in Figure 5.3-2. From these figures, we can observe that as in the case of K_{II} and for the same reason, the COD(u) remains almost unchanged in a large range of inertia factor's values.

The COD(v) for different inertia factors when the dimensionless time is set to be 0.5, 1.1, 2 and infinity respectively are shown in Figure 5.3-4. As in the case of K_I, the amplification of the COD(v) by the inertia factor is much more significant than that of COD(u).

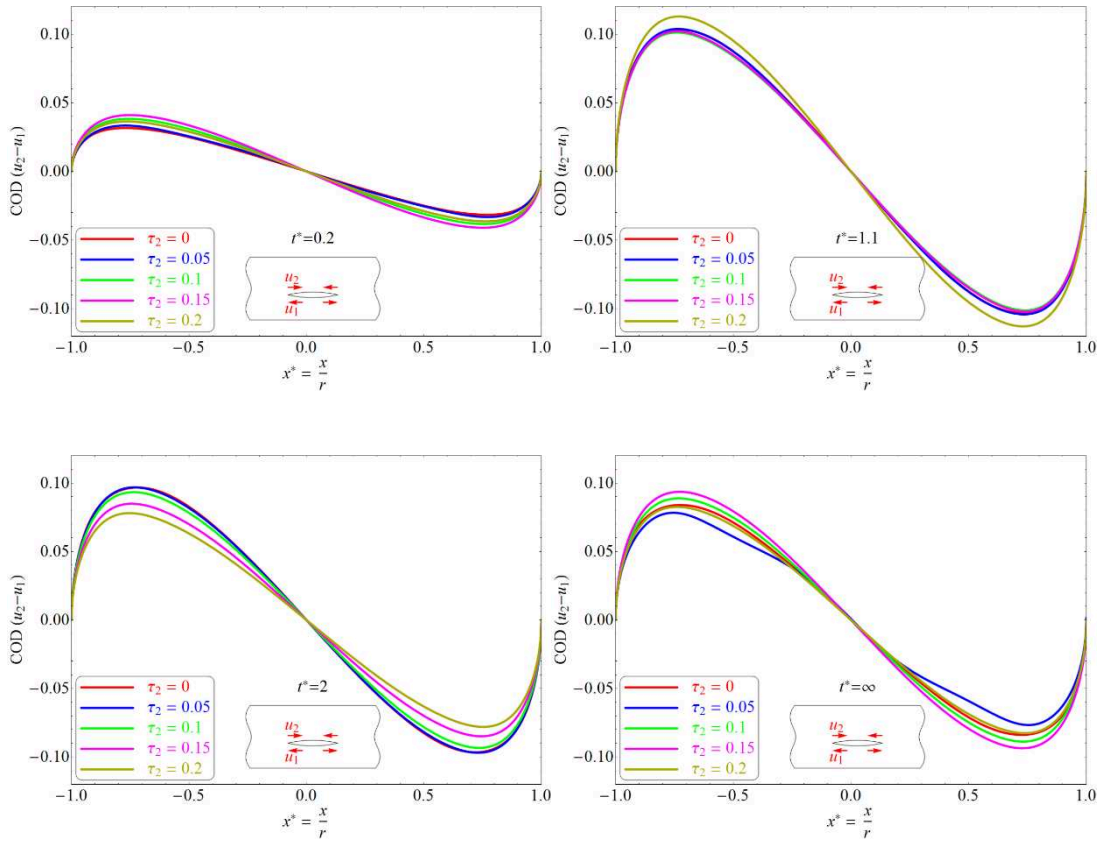

Figure 5.3-2 Crack Opening Displacement (u_2 - u_1) for different τ_2 when Bi = τ_1 = 0 and t^* = 0.2, 1.1, 2 and ∞.

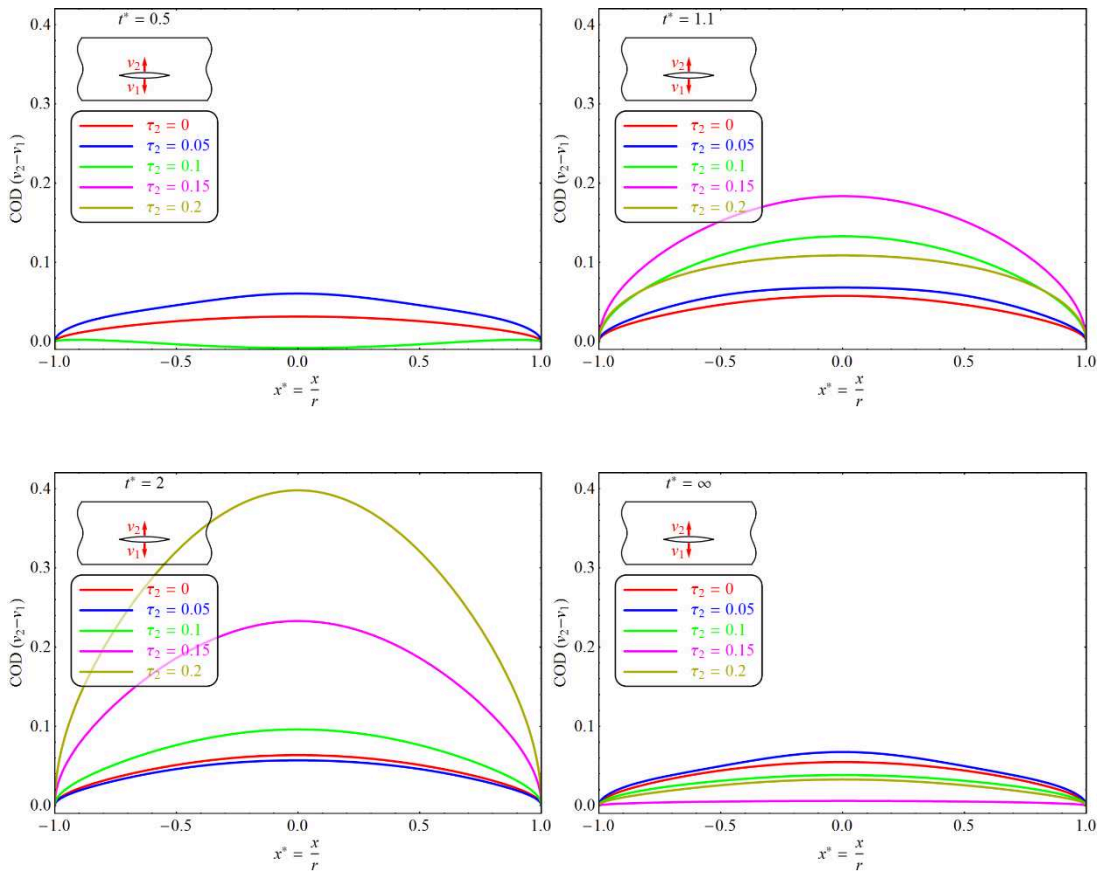

Figure 5.3-3 Crack Opening Displacement (v_2 - v_1) for different τ_1 when Bi = τ_1 = 0 and t^* = ∞.

These figures also show that amplifications by different inertia factors are not synchronized; the periods of oscillations are different from one IF to another. As a consequence, we cannot state what the most influencing IF is at an arbitrary time. For observing better the influence of IF on CODs, we plot only the maximum CODs for different inertia factors during all the thermal shock. Figure 5.3-4 and Figure 5.3-5 show respectively the maximum COD(u) and the maximum COD(v) for different inertia factors. Comparing these two figures leads us to confirm the crushing influence of τ_2 on COD(v) than on COD(u).

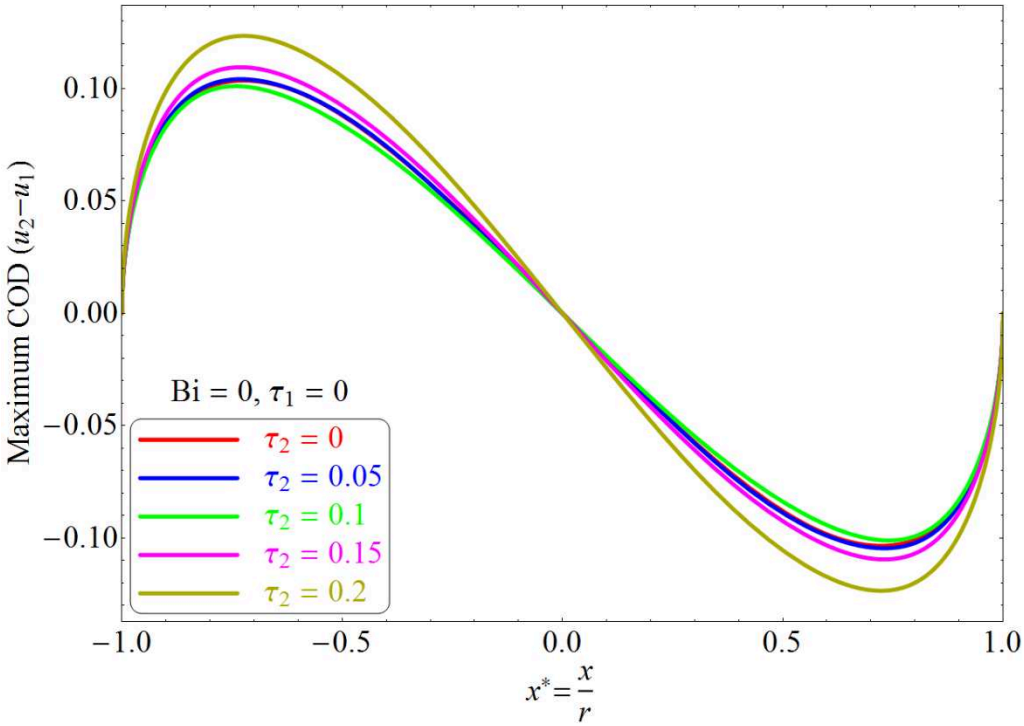

Figure 5.3-4 Maximum COD(u) for different τ_2

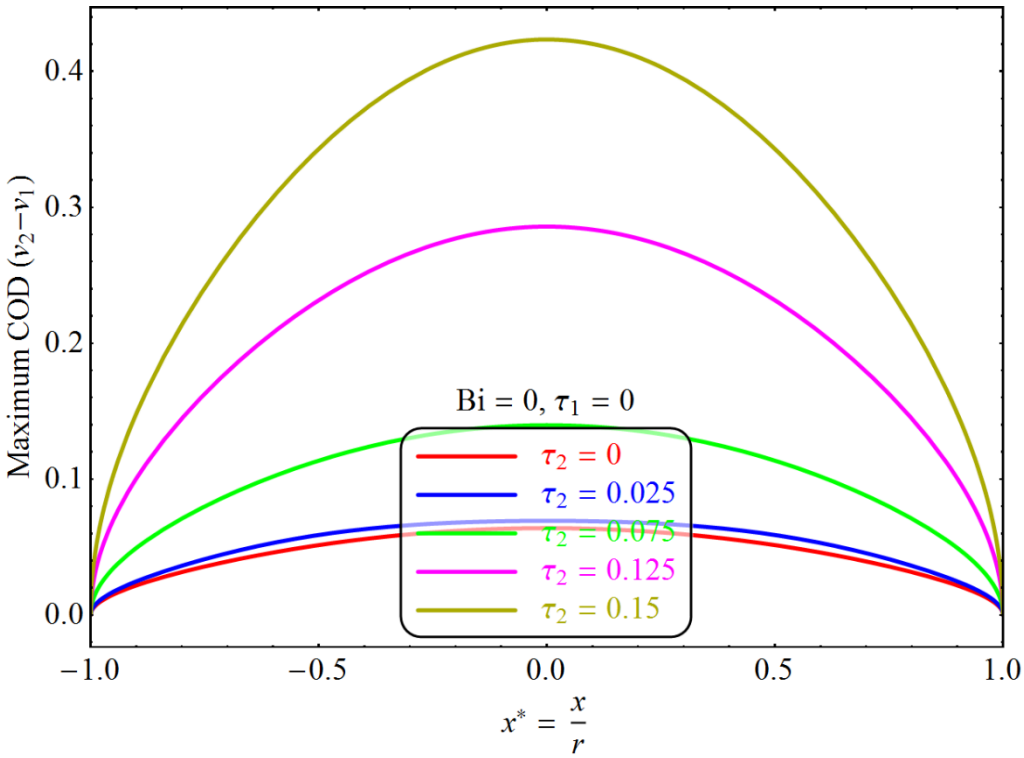

Figure 5.3-5 Maximum COD(v) for different τ_2

5.4 Interaction among Bi, NFF and IF

Now we consider the situations when the cracked induced thermal barrier, the non-Fourier effect and the inertia effect act together during the thermal shock process. The interaction of all these factors on the stress distribution and evolution can be particularly complex. In practice, the peak values of the dynamic SIFs during the time evaluation are the most significant quantities in predicting the crack growth. In this section we will evaluate the interaction among the parameters Bi, τ_1 and τ_2 on the maximum absolute values of K_I and K_{II}.

The peak values of K_I as function of τ_2 for different Bi and τ_1 are illustrated in Figure 5.4-1 - Figure 5.4-4. These figures are plotted in a same ordinate scale in order to facilitate comparison. At first glance, the inertia factor τ_2 has the greatest impact on the peak values of K_I. The maximum K_I increases more than 10 times as τ_2 grows from 0 to 0.3. This statement should be toned-down for the values of τ_2 are in general small for current engineering materials. In this case, the contribution of the Biot number to K_I is more significant. When τ_2 is small, a sufficiently large Biot number would lead to a small K_I, while a small Biot number would result in a noticeable value of K_I. In contrast, τ_1 plays a sufficiently important role only when τ_2 is large enough.

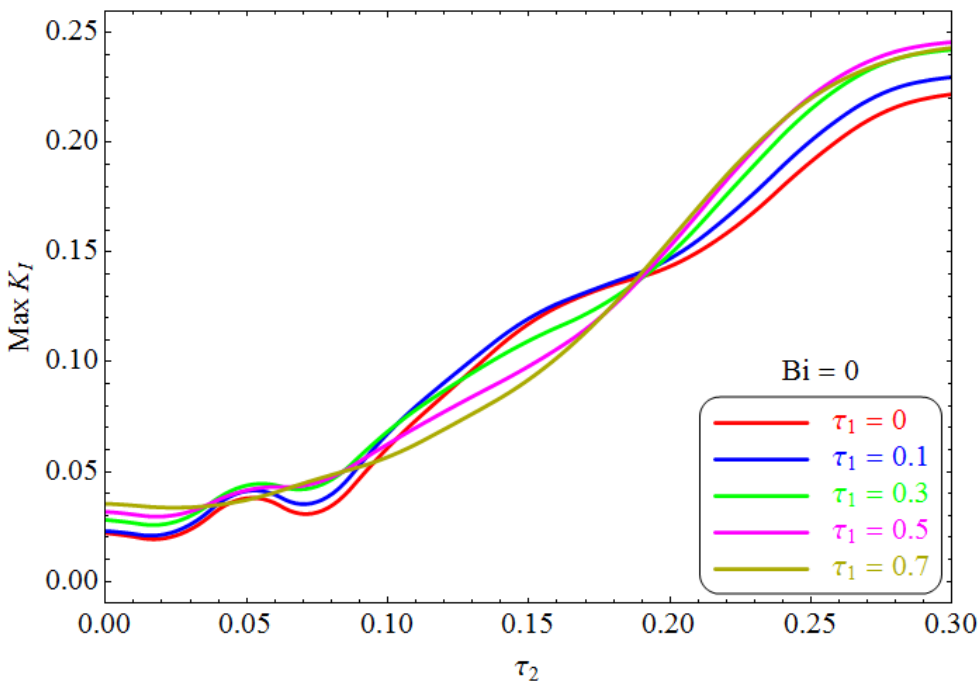

Figure 5.4-1 Maximum K_I versus inertia factor for different τ_1 when Bi = 0

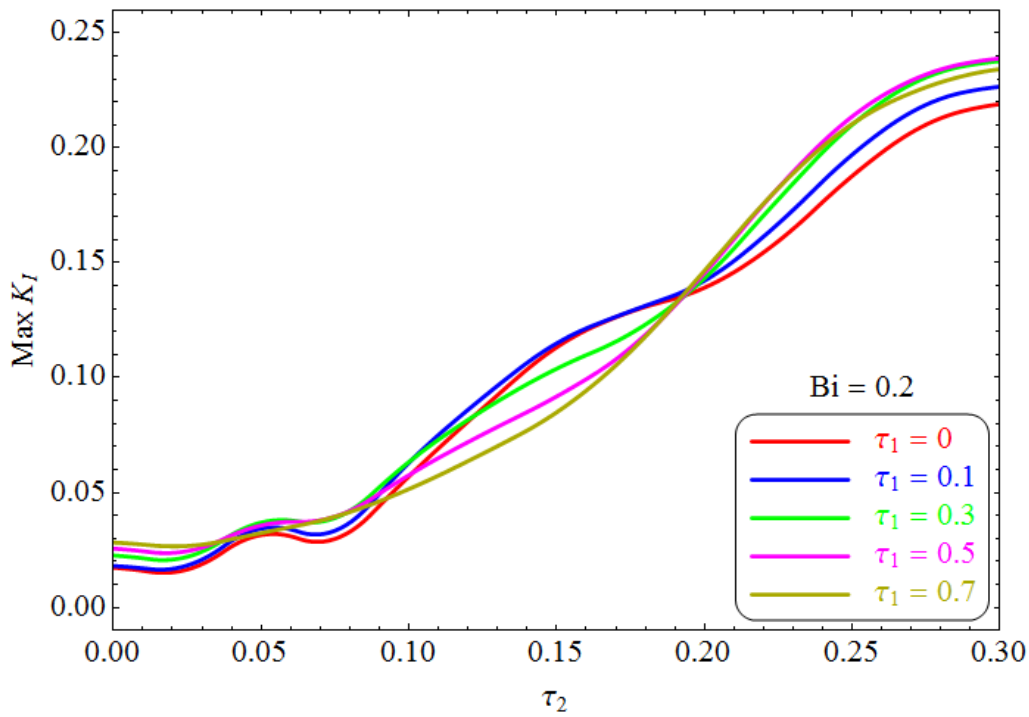

Figure 5.4-2 Maximum K_I versus inertia factor for different τ_1 when Bi = 0.2

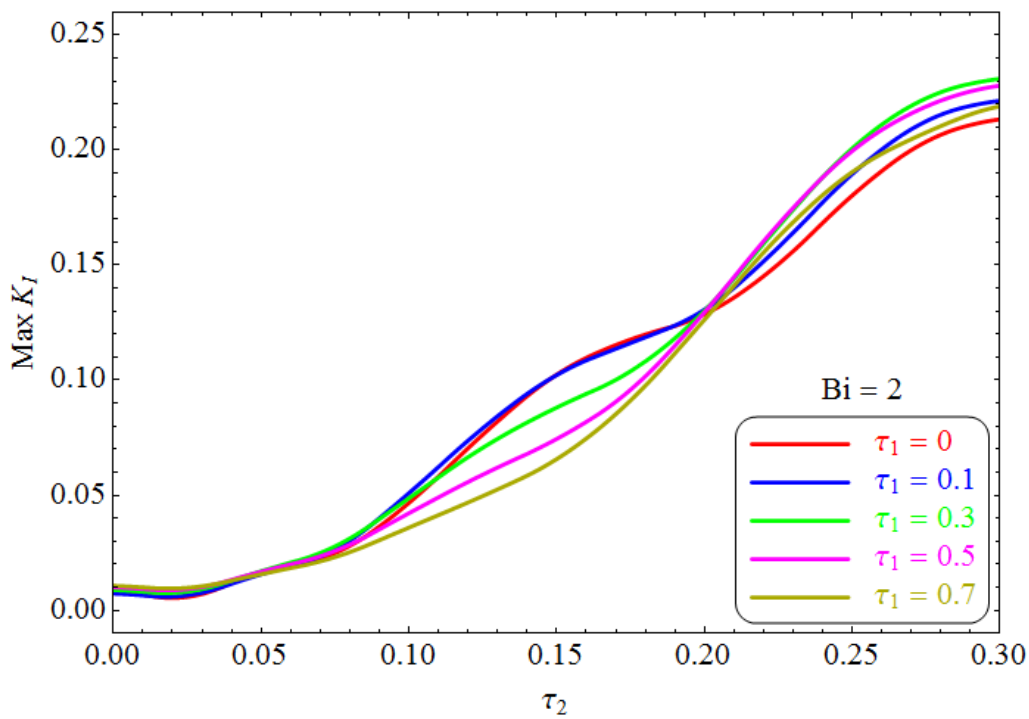

Figure 5.4-3 Maximum K_I versus inertia factor for different τ_1 when Bi = 2

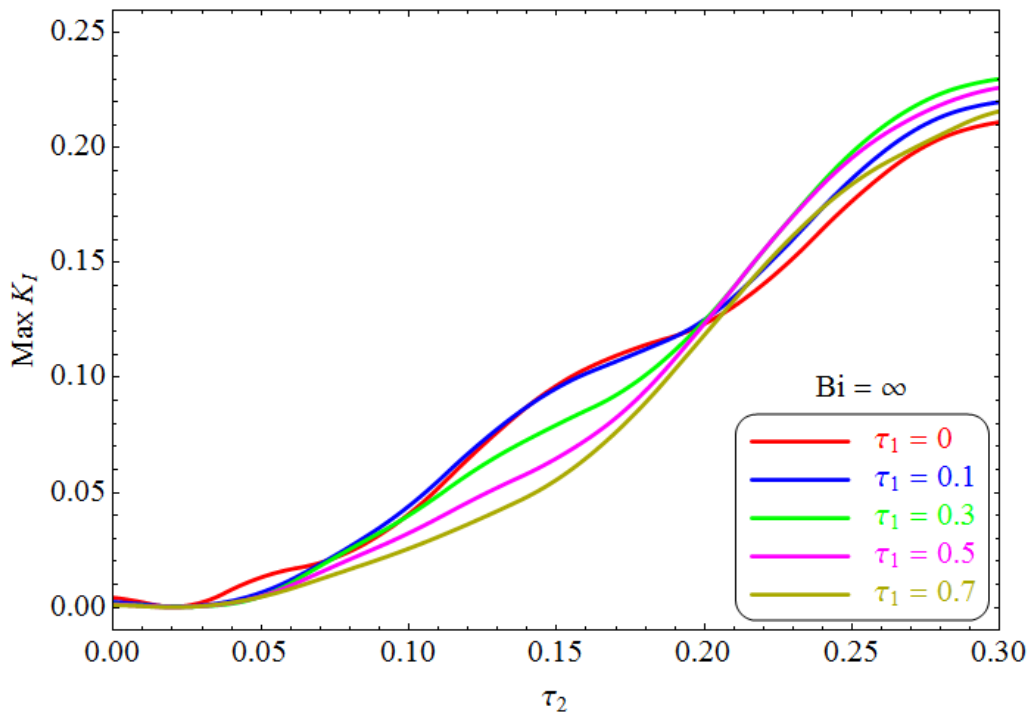

Figure 5.4-4 Maximum K_I versus inertia factor for different τ_1 when Bi = ∞

Similarly, the peak values of K_{II} as function of τ_2 for different Bi and τ_1 are illustrated in Figure 5.4-5 - Figure 5.4-8. We can see that the behaviors of K_{II} are very different from those of K_I with respect to these parameters. The influence of inertia effect on K_{II} is nearly unnoticeable within a large range of τ_2. Conversely, the Biot number and τ_1 become more significant parameters for amplifying the peak values of K_{II}. Similar with the behaviors of K_I, Bi = infinity results in the zero-K_{II}. As Bi → 0, the effect of τ_1 becomes increasingly important.

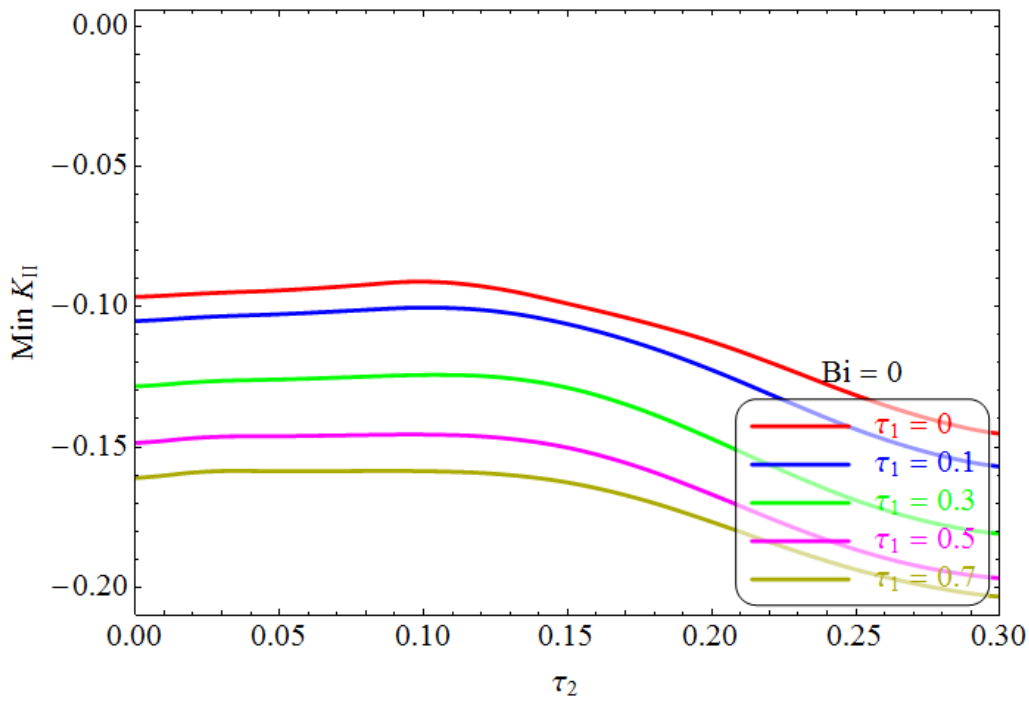

Figure 5.4-5 Minimum K_{II} versus inertia factor for different non-Fourier factors when Bi = 0

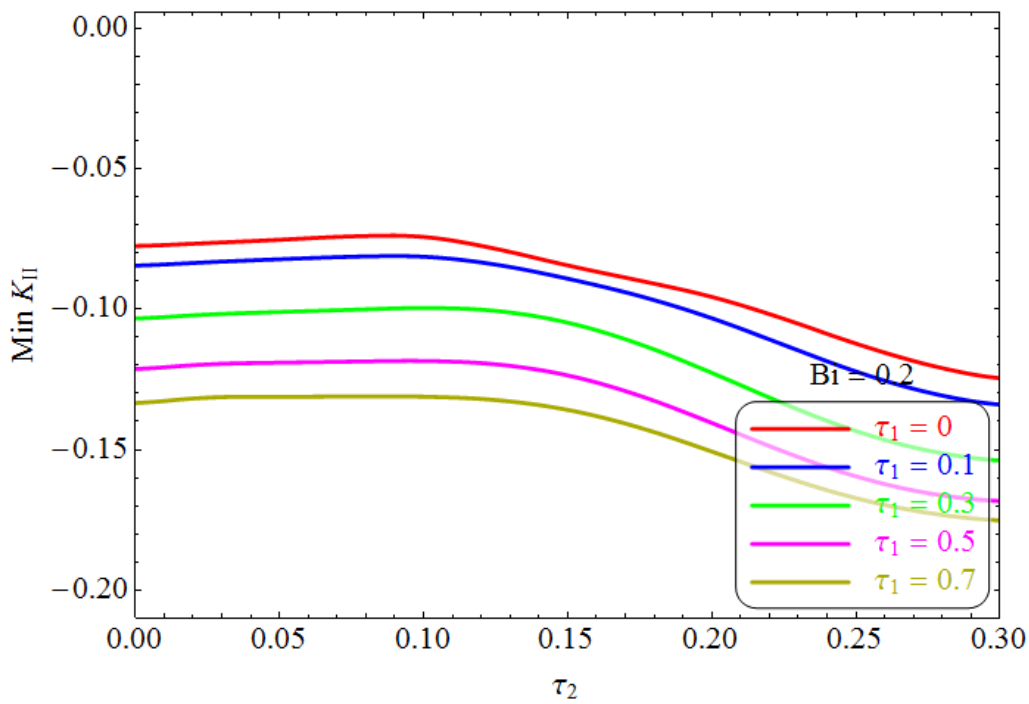

Figure 5.4-6 Minimum K_{II} versus inertia factor for different non-Fourier factors when Bi = 0.2

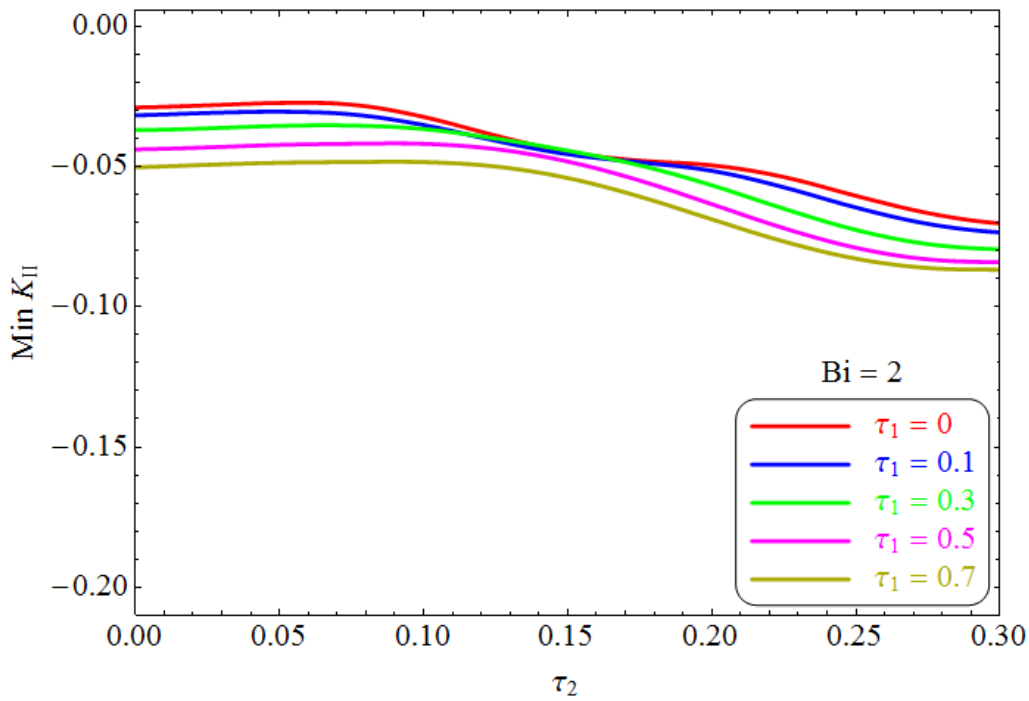

Figure 5.4-7 Minimum K_{II} versus inertia factor for different non-Fourier factors when Bi = 2

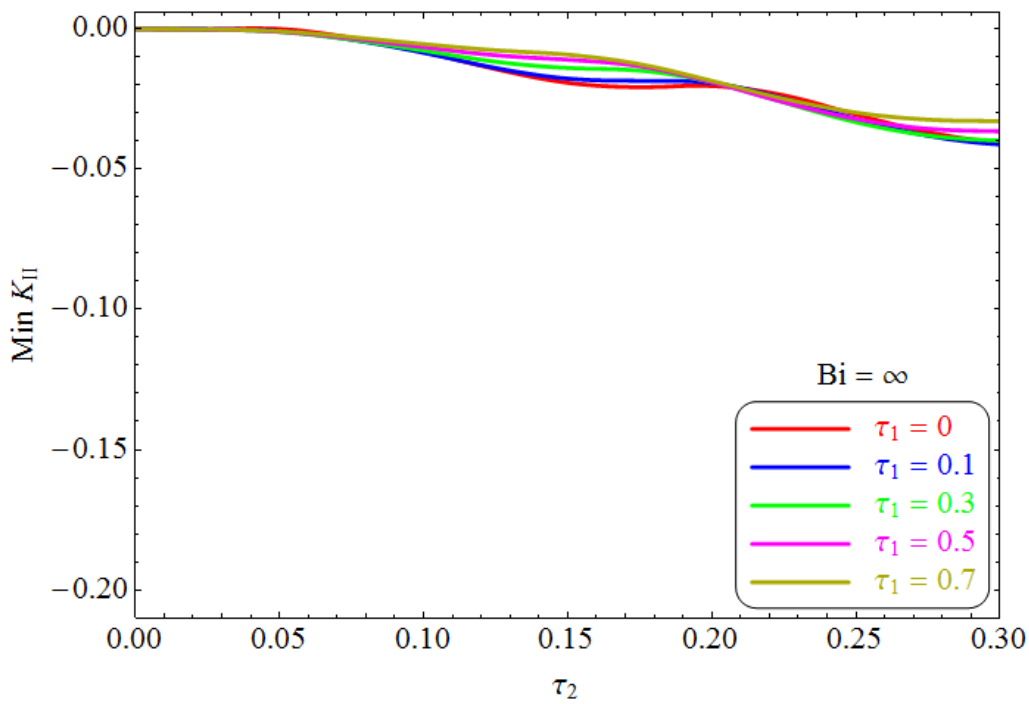

Figure 5.4-8 Minimum K_{II} versus inertia factor for different non-Fourier factors when Bi → ∞

5.5 Heating Thermal Shock and Cooling Thermal Shock

According to the results shown in the previous sections, the stress intensity factor K_I is a monotonic function of time when the non-Fourier factor τ_1 and the inerta factor τ_2 are not taken into account. However, K_I will exhibit an oscillation feature when τ_1 and τ_2 are larger than zero. The dangerousness of this oscillation is different for the two types of thermal shock, namely the "heating thermal shock" and the "cooling thermal shock". For the heating thermal shock, the positive peak value of the oscillation is the most dangerous, while the negative peak value is not effective as the crack surfaces are closed in this case. The contrary is true for the cooling thermal shock. Consequently, it will be helpful to consider separately the oscillation effect on these two different situations.

Figure 5.5-1 shows the absolute peak values of K_I evaluated for different τ_1 and τ_2. The effective K_I for heating thermal shock is plotted in Figure 5.5-1 (a) while the effective K_I for cooling thermal shock is plotted in Figure 5.5-1 (b). Noting that when the materials are cooled from the surface, the temperature difference between the environment and the initial temperature of the plate is smaller than 0. Thus the dimensionless K_I will take the opposite sign.

It is clear from Figure 5.5-1 that maximum K_I increases as τ_2 increases under both heating and cooling thermal shock conditions. When we neglect the inertia effect by setting $\tau_2 = 0$, the absolute values of K_I in heating thermal shock are larger than those of cooling thermal shock. Progressively as τ_2 grows, the situation becomes reverse: cooling shock provokes larger K_I than heating shock. These results agree with those presented in previous sections.

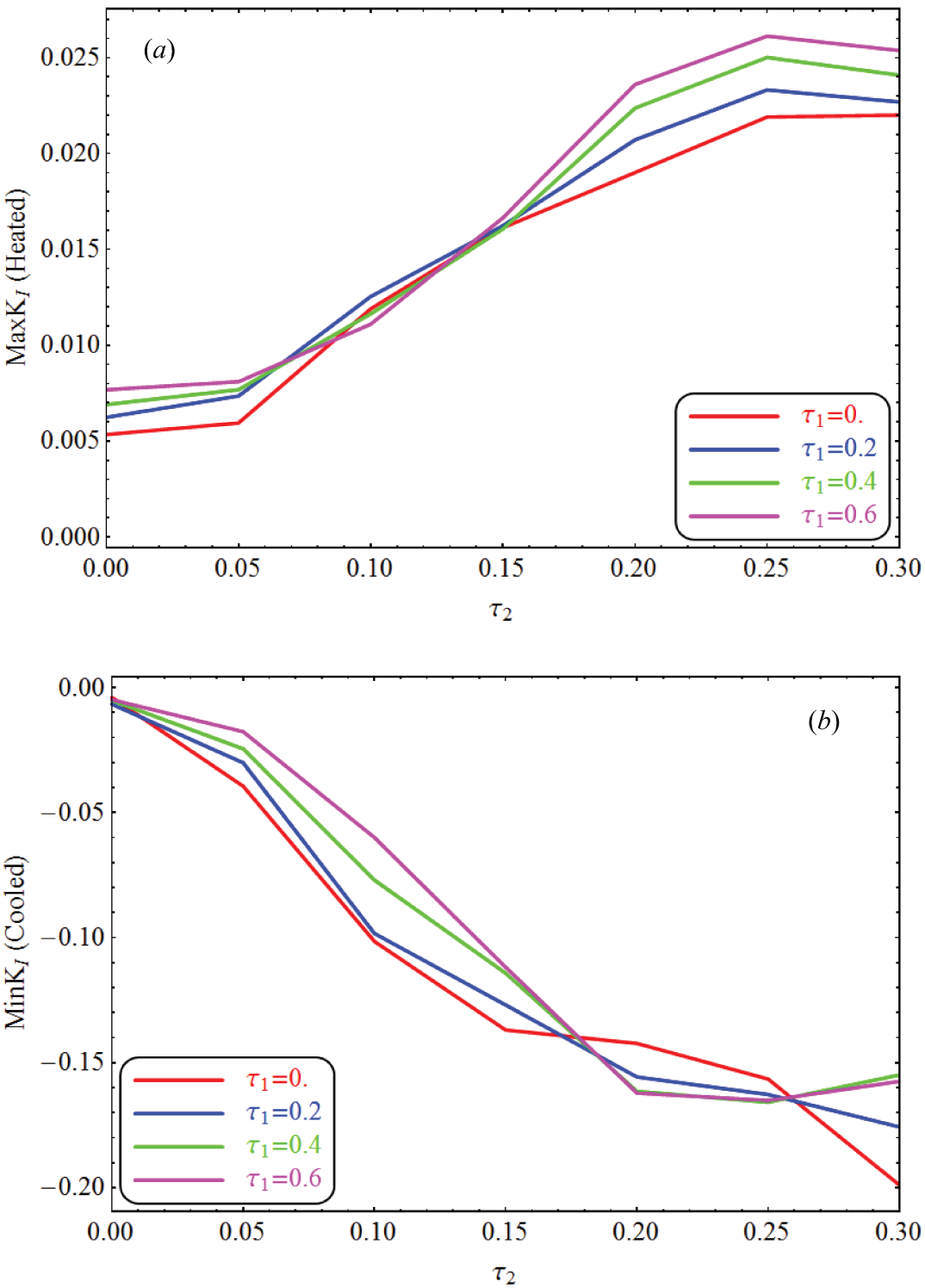

Figure 5.5-1 Variation of peak-values of K_I^* versus τ_2 for different τ_1 (*a*) when $T_\infty - T_0 > 0$ (heating) and (*b*) when $T_\infty - T_0 < 0$ (cooling)

Chapter 6 Inner crack in a half plane

6.1 General consideration

In the precedent analyses, we considered an inner crack in a strip of a particular dimension. Some significant factors influencing the crack initiation and propagation were discovered and discussed. However, the discussions are limited in a qualitative scope as only a particular geometry of the cracked strip with l_a = 1 and l_b = 2 was studied.

In this chapter we will study the problem with a more general geometry. In the case when the crack is located much closer to one surface than to the other, i.e., when l_a is much smaller than l_b, the cracked strip of Figure 2.1-1 is degenerated to a half semi-infinite plane, as shown in Figure 6.1-1 [149].

This geometry presents a particular importance in engineering applications. For example, in a coating failure problem, the thickness of the substrate is in general much larger than that of the coating. The delamination failure mainly occurs at the coating-substrate interface which is very close to the heated surface.

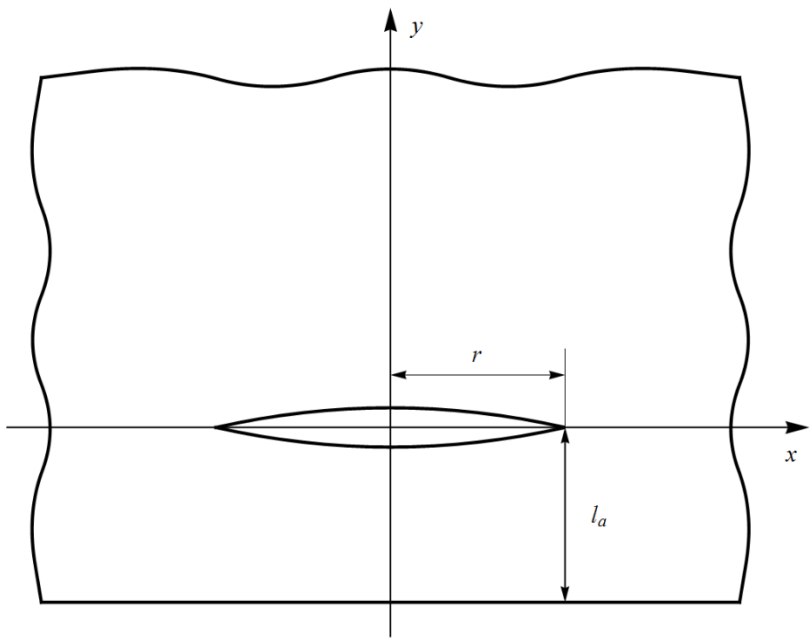

Figure 6.1-1 Geometry of the cracked half infinite plate and the coordinate system.

In this case, the boundary conditions (2-7) and (4-10) at $y = l_b$ are respectively reduced to

$$T(x,\infty,t) = T_0 \tag{6-1}$$

and

$$\begin{cases} (g): \sigma_y(x,\infty,t) = 0 \\ (h): \tau_{xy}(x,\infty,t) = 0 \end{cases} \tag{6-2}$$

In order to ensure a finite solution of Equations (2-31) and (4-31) when $y \to \infty$, the general solutions of the temperature and displacement fields for $y > 0$ in Laplace-Fourier space should be rewritten as follows:

$$\tilde{\bar{T}} = C_{T,3} e^{-my}, \quad 0 < y < \infty \tag{6-3}$$

and

$$\begin{cases} \tilde{\bar{u}}_2(y) = \sum_{i=5}^{6} C_{D,i}(\xi) e^{\lambda_i y} + \omega_5 e^{-my} \\ \tilde{\bar{v}}_2(y) = \sum_{i=5}^{6} B_i C_{D,i}(\xi) e^{\lambda_i y} + \omega_7 e^{-my} \end{cases} \tag{6-4}$$

while the solutions of the range $-l_a < y < 0$ stay unchanged. The size of the coefficient matrix defined in Equation (4-47) would be reduced to be 6 by 6. Then the temperature and stress fields, the SIFs and CODs can be obtained by following the similar solution procedures as described in Chapter 2 and Chapter 4.

As a consequence of these simplifications, the computation tasks are also largely reduced in terms of the time consummation.

6.2 Influence of l_a

An obvious benefit of this analysis is the possibility to assess the influence of l_a on the stress concentration near the crack tips. From the engineering point of view, it is interesting to know the most unfavorable value l_a for which the crack stress concentration is maximal. Figure 6.2-1 - Figure 6.2-3 show the influence of this parameter on the stress intensity factors and on the crack opening displacements. In these figures, the Biot number is assumed to be 0 and the inertia factor τ_2 is taken to be 0.2. Using other values of Bi and τ_2 will give similar results and will not be presented here. However, the interaction between l_a and τ_1 exhibits some complex

features. Therefore, the numerical results will be plotted as function of these two parameters.

The variation of the maximal normalized SIFs versus l_a is shown in Figure 6.2-1 for different τ_1. Noting that the starting abscissa is $l_a = 0.1$ instead of 0.

From this figure, we observe that the absolute values of the SIFs are not a monotonous function of l_a. We can remark that their maximal values occur at $l_a \cong 1$ for both mode-I and mode-II curves for almost all values of τ_1 considered. This result shows that the intuition is not always correct: smaller l_a does not always lead to larger SIFs. This critical value $l_a \cong 1$ indicates that the thermal shock is most dangerous for near surface cracks when its semi-length is close to its distance to the surface.

Figure 6.2-2 shows the maximum CODs versus the dimensionless coordinate for different l_a when $\tau_1 = 0$ and $\tau_2 = 0.2$. It appears that the mode-I COD decreases as l_a increases. However, this tendency is no longer true for the mode-II case. In order to better observe the influence of l_a on CODs, we plot in Figure 6.2-3 the maximum of the CODs versus l_a for different τ_1 under the condition τ_2 =0.2. We can observe that the mode-II COD first increases and then decreases as l_a increases. The maximal displacement jumps for different values of τ_1 are located at points between $0.2 < l_a < 0.5$. For the mode-I case, overall, the maximum displacement jumps decrease as l_a increases whereas small oscillations can appear with the increase of τ_1. Both the mode-I and mode-II CODs monotonously decrease with l_a when $l_a > 0.5$. This result agrees well with that found in the literature [60, 86].

An important remark is that the critical values of l_a are different for SIFs and CODs, especially for mode-I crack. In fact, there is no a veritable critical l_a for the mode-I CODs, even though the mode-I SIFs reach the maximum values at about $l_a \cong 1$. This is because of the small thickness between the crack and the surface as l_a is small, which makes this part of the material acting as a beam: the large CODs represent just the flexion of the beam under relatively small thermal stresses.

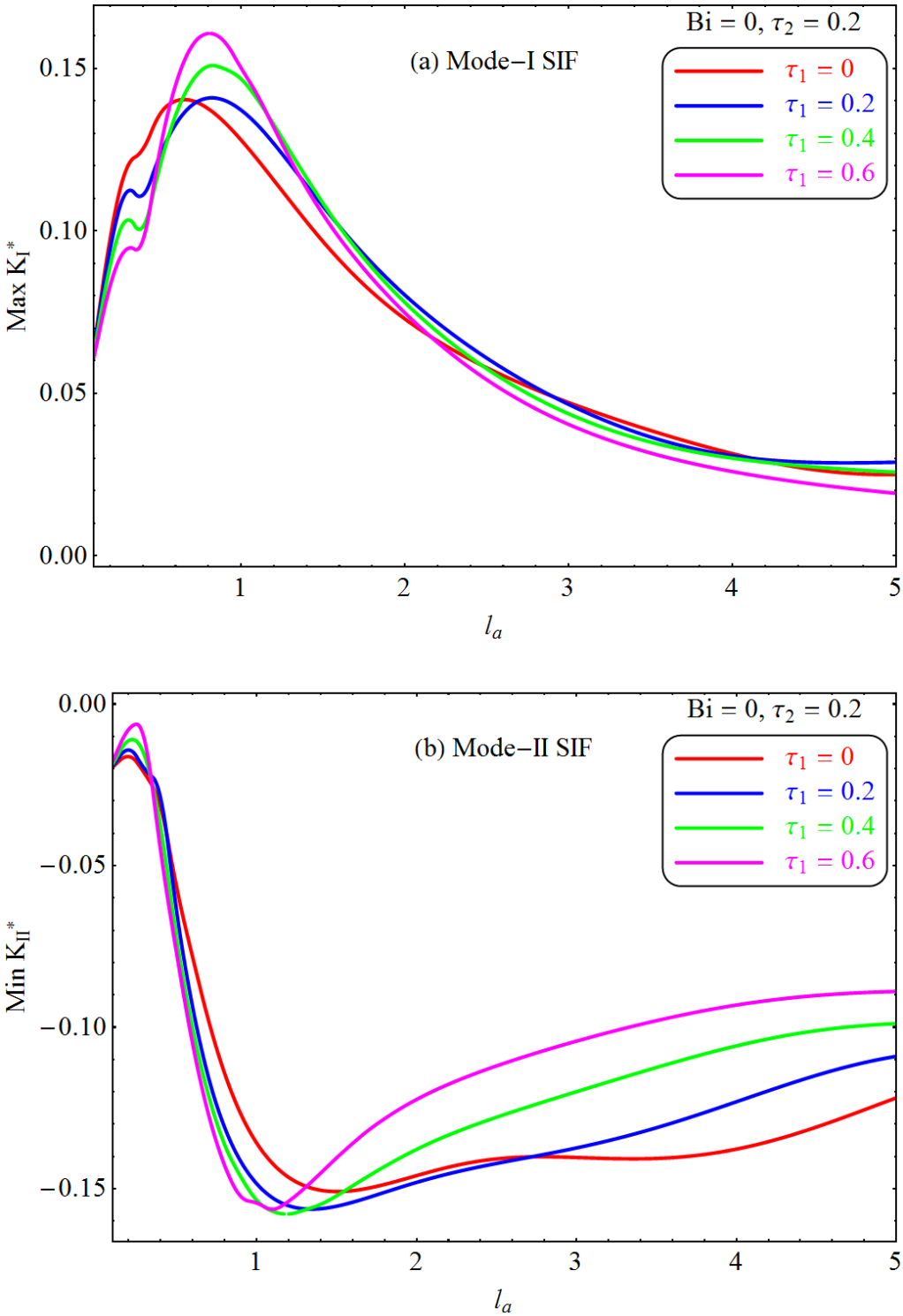

Figure 6.2-1 Variation of maximum K_I and K_{II} versus l_a for different τ_1 when Bi = 0 and τ_2 = 0.2.

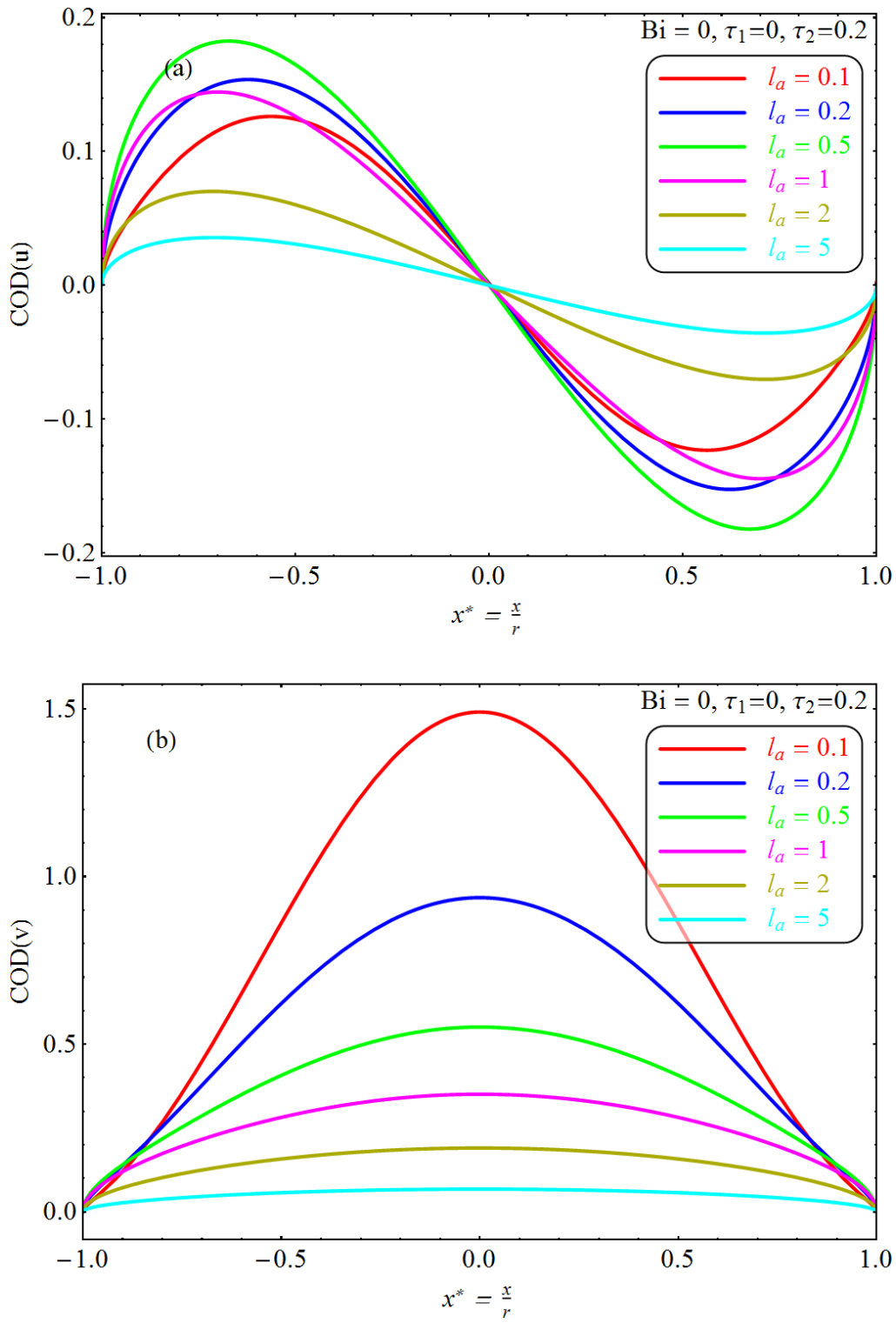

Figure 6.2-2 Maximum CODs for different l_a when τ_1 = 0 and τ_2=0.2.

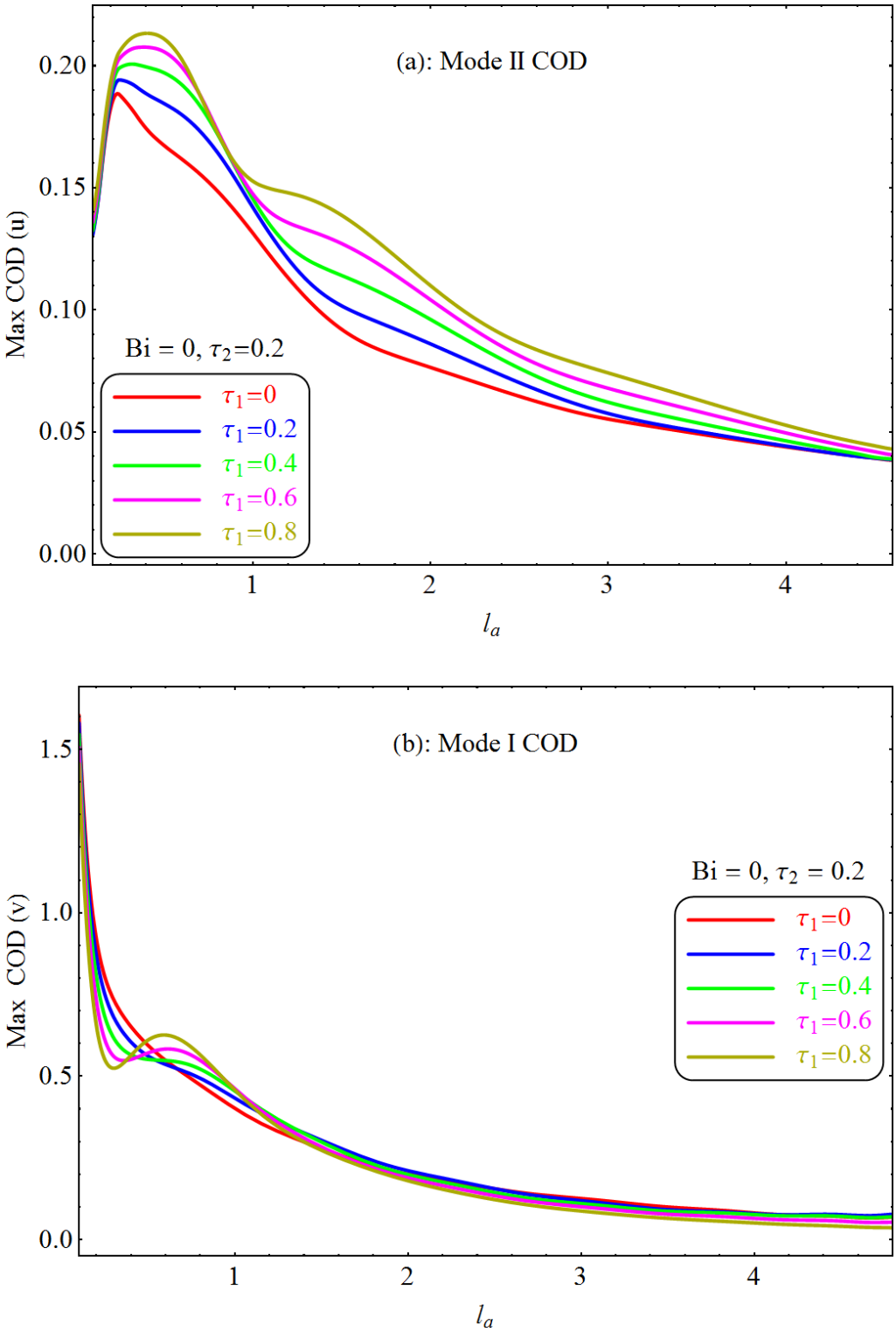

Figure 6.2-3 Variation of maximal normalized COD versus l_a for different τ_1 when Bi = 0 and τ_2=0.2. Max COD(v) is measured at the midpoints of the crack; Max COD(u) is measured at the points of the crack where COD(u) is maximal.

6.3 Verification and Comparison of the Results

In 2012, Chen and Hu [60] carried out the similar investigation under the model shown in Figure 6.1-1. In their study, the non-Fourier effect was considered while the inertia effect was not taken into account. The crack gap was considered as totally thermal isolated. Numerical results of temperature field and stress intensity factors were investigated in their published paper.

In this section we will compare the numerical results obtained from different models, namely: The Chen and Hu model with $\tau_1 = 0.5$ and $l_a = 1$; the half-infinite plate model studied in the present work with $\tau_1 = 0.5$, $\tau_2 = 0$ and $l_a = 1$; the strip model studied in the present work with $\tau_1 = 0.5$, $\tau_2 = 0$, $l_a = 1$ and $l_b = 100$.

Figure 6.3-1 and Figure 6.3-2 shows the temperature field of the mid-points of the crack surfaces and the stress intensity factors obtained by different models, respectively. In the two figures, the red curves represent the results of Chen and Hu [60]. The Blue curves are plotted with the results of the half-infinite plate model and the magenta curves are obtained from the strip model. The results show that as the increasing of l_b, the strip model is reduced to the half infinite plate model. In the case when the inertia effect is neglected, the results of both the models studied in the present work agree well with the results obtained by Chen and Hu [60].

Noting that because of the different dimensionless methods, the dimensionless SIFs between Chen's paper and those in this thesis are slightly different by a factor of $1-\nu$:

$$\begin{cases} K_I = (1-\nu)\, K_I^{(\mathrm{Chen})} \\ K_{II} = (1-\nu)\, K_{II}^{(\mathrm{Chen})} \end{cases} \tag{6-5}$$

In Figure 6.3-2, the convention of Chen was used in plotting the stress intensity factors.

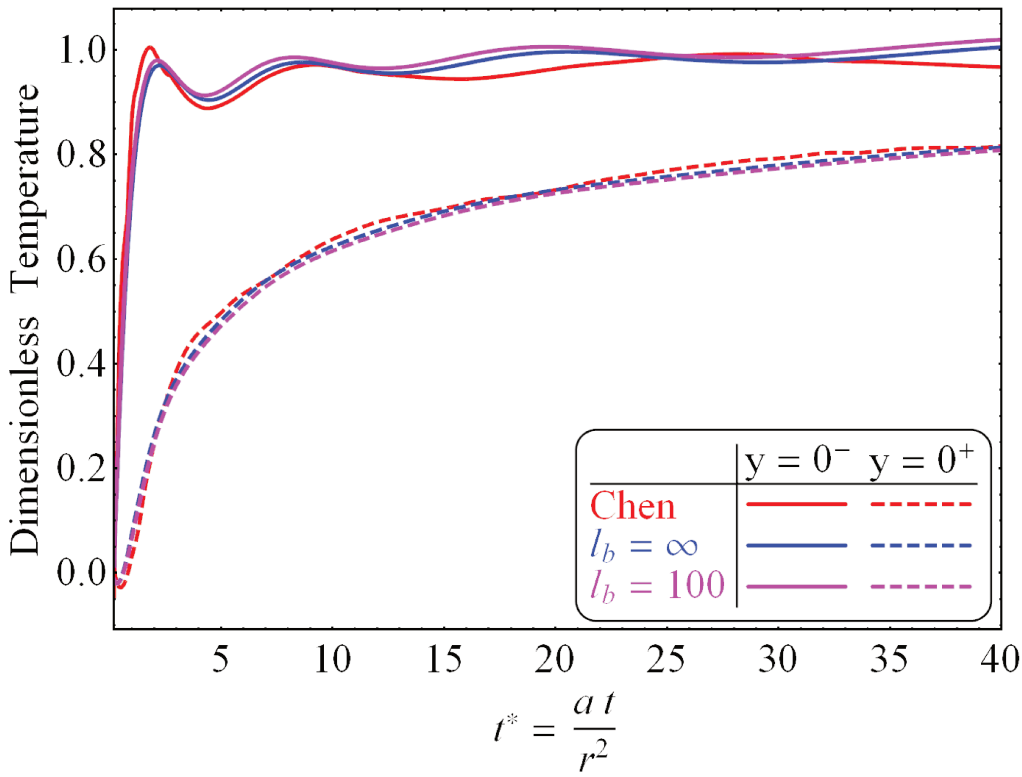

Figure 6.3-1 Temperature field of the mid-points of the crack surfaces obtained by different model.

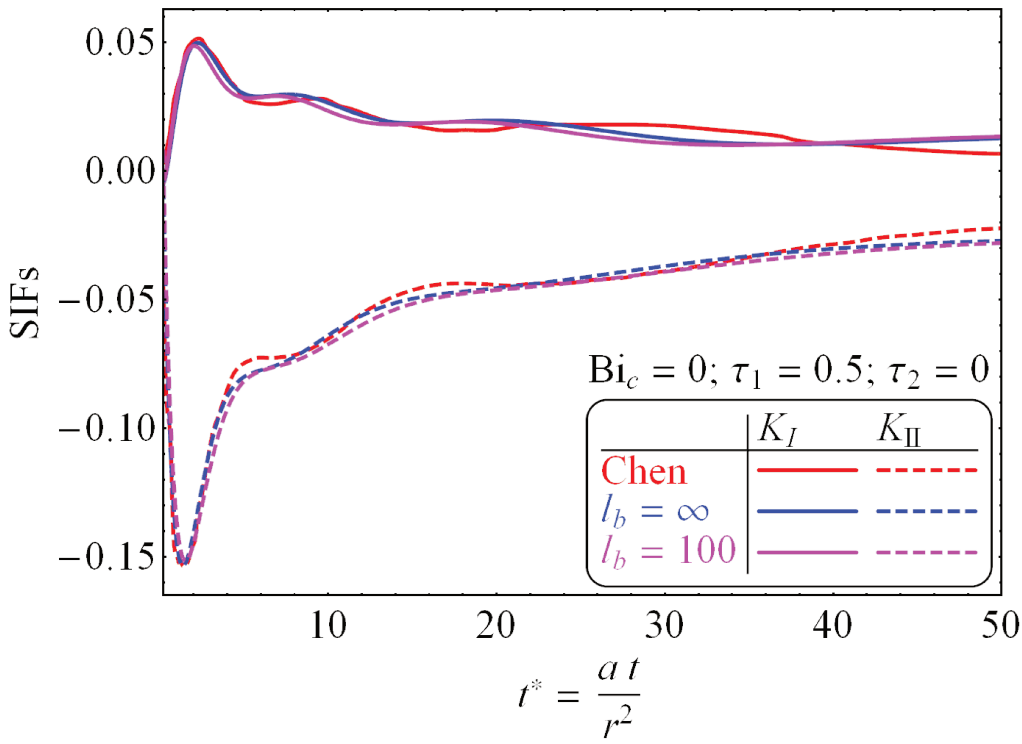

Figure 6.3-2 Stress intensity factors obtained by different model.

Chapter 7 Conclusions and Future Works

7.1 Conclusions

In this study, the crack problem of a two-dimensional strip under thermal shock loading is examined. The thermal barrier effect of the crack gap, the finite speed of the heat wave and the inertia force are taken into consideration to investigate the transient thermal stress problem. Corresponding to these physical mechanisms, three special parameters, namely the Biot number (Bi), the non-Fourier factor (τ_1) and the inertia factor (τ_2) are defined. The Laplace transform and Fourier transform techniques are applied to transform the governing partial differential equations to ordinary differential equations, which are transformed in turn to singular integral equations by applying the mixed-boundary conditions. The established singular integral equations are solved by using the Gauss-Chebyshev numerical integration method. Finally, the numerical inverse Laplace transform is used to obtain the temperature and stress fields in time domain. The temperature field and the dynamic stress intensity factors are evaluated for different values of the parameters Bi, τ_1 and τ_2.

From the mathematical point of view, the solution methods chosen and used in the present work is efficient. The main reason of choosing the present analytical resolution strategy is its possibility of obtaining an “exact” solution with which the further numerical solutions can compare. Moreover, in spite of the theoretical and numerical difficulties encountered in the resolution process, this approach ensures an accurate solution of the problem, which is not guaranteed by using pure numerical approaches such like the finite element modelling due to the complexity of the posed problem.

The obtained results show that the physical parameters Bi, τ_1 and τ_2 can really play an amplificatory role in the crack propagation process. Qualitative discussions were made on this point in Chapter 5 and Chapter 6. However, one can pose some crucial questions, for examples: what is the real impact of these parameters in engineering applications? Are the errors induced by neglecting these effects acceptable? In which circumstance these factors lead to structural failures? To answer these questions, we give some estimation of the magnitudes of these parameters for

some commonly used materials.

7.2 Magnitude Estimation of Bi, Non-Fourier Factor and Inertia Factor

7.2.1 The Biot Number

From the numerical results illustrated in Chapter 3 and Chapter 5, we concluded that the Biot number of the crack gaps has great influence for both the temperature field and stress intensity factors. The dependence of these fields on the Biot number is obvious, i.e., as the Biot number varies from the infinity to zero, the temperature jump across the crack becomes larger and larger and so does the stress intensity factors at the crack tips. Especially, the mode-II SIFs can reach until very large values as shown in Figure 5.1-1.

The Biot number of the crack gap, defined as $\mathrm{Bi} = \frac{h_c l_a}{k}$, is determined by many complex factors, such as the thermal properties of the materials, the surface roughness, the crack opening displacement, the temperature distributions around the crack, the gas component filling the crack gap and the gas pressure on the crack surface, the distance between the crack and the surface, etc. These factors lead the values of the Biot number to vary widely from one situation to another.

Most experimental data for the interface thermal contact conductance h_c are focused on metals. Reference data for nonmetallic materials are still rare. Table 7.2-1 shows some interface contact conductance for representative interfaces [150-154].

As might be expected, the interface conductance is higher with a softer material (e.g., aluminum) than with a harder material (e.g., stainless steel). As the thermal conductivity k is of the order of 50 W/(m·K) for metals, for a l_a = 1mm, the Biot numbers of the above-listed interfaces are close to zero when the contact pressure is small. This estimation indicates that, according to the discussions made in Section 5.1.1, the Biot number is a major factor in generating stress concentration near the crack tips.

At the same time, some of the factors determining the magnitude of the Biot number, such like k or l_a, are controllable in material design. This makes the Biot

number a very important parameter in improving the thermal shock resistance of the materials.

Materials	Contact pressure (atm)	Interface medium	h_c W/(m^2·K)
Stainless steel (0.76 μm roughness)	10	Air	9000 – 11500
	20	Air	10000 – 12000
Stainless steel (2.5 μm roughness)	10	Air	2800 – 4000
	20	Air	3100 – 4200
Aluminum (3 μm roughness)	10	Air	6000 – 15000
	20	Air	10500 – 28000
Stainless steel	1	Vacuum	400 – 1600
	100	Vacuum	2500 – 14000
Copper	1	Vacuum	1000 – 10000
	100	Vacuum	20000 – 100000
Aluminum	1	Vacuum	2000 – 6600
	100	Vacuum	25000 – 50000
Aluminum (10 μm roughness)	1	Air	3600
	1	Helium	10000
Aluminum	1	Silicone oil	19000
	1	Dow corning 340 grease	140000
Stainless steel	35	Dow corning 340 grease	250000

Table 7.2-1 Interface contact conductance for representative interfaces

7.2.2 Non-Fourier Factor

Generally speaking, the non-Fourier effect has the similar impact to both the temperature and the SIFs as the Biot number and the inertia factor. The increasing of the thermal relaxation time will lead the temperature and SIFs to present an oscillating property. Their peak values are higher comparing to those obtained without considering the finite speed of the heat wave. This result agrees well with the experimental observations [73, 75, 118].

Normally the thermal relaxation time is very small for most of the engineering materials [65], which would lead to an insignificant τ_1 according to its definition $\tau_1 = \frac{a\tau_0}{r^2}$. The relaxation time for most engineering materials is of the order of $10^{-14} \sim 10^{-6}$ s and the thermal diffusivity is ranged from 10^{-8} to 10^{-3} m²/s, which indicates that τ_1 is ranged from 10^{-16} to 10^{-3} for a crack of 1mm. In these cases, the parabolic heat conduction model can give good results. However, this argument can be challenged by the following facts:

Firstly, there are experimental evidences that the thermal relaxation time is not always very small, the value of which can be up to 10s for some non-homogeneous materials [117]. The thermal relaxation time of this magnitude will lead to a very large non-Fourier factor of the order of 1 when the crack length is of the order of 1mm. Polymeric and vitreous materials, which are almost thermal insulators, are widely used in engineering structures However, no available experimental result support that the heat wave in these materials can be seen as infinity [85]. There is no reason to believe that the thermal relaxation time for these materials should be as small as for metallic conductors.

Secondly, the thermal conductivity in biological materials is complex because of its heterogeneous nature. The thermal behaviors study of human tissue such as skin and muscle is an important issue in medicine research. Some experiment results show that the thermal conduction in meat is not accommodated by the classical Fourier model [155]. Of cause in this situation, the thermal conduction problem is much important than the thermal stress problem.

Lastly, it is obvious from the definition of τ_1 that its magnitude NFF can greatly be amplified if the crack length is very small. For example, the failure of TiN coatings deposited onto 304 stainless steel substrates by laser thermal shock shows that the

cracks initiate with a half-length of about 100nm while the coating thickness is 500nm [57], as shown in Figure 1.2-4. Thus τ_1 will be 10^8 times higher than that for a crack of 1mm. In this case, the non-Fourier effect may become significant in the failure mechanism of the coating.

7.2.3 Inertia Factor

It is obvious from the numerical results of Chapter 5 that the τ_2 has a significant influence on the SIFs, especially for mode I cracks. The value of K_I can be very large if τ_2 is bigger than 0.1. According to its definition $\tau_2 = \frac{a}{Vr}$, τ_2 is less than 0.01 for most macro-cracks in engineering materials.

According to Equation (4-14), the coefficients of $\frac{\partial^2 u^*}{\partial t^{*2}}$ and $\frac{\partial^2 v^*}{\partial t^{*2}}$ are not only τ_2^2 but also a Poisson's ratio item, $\frac{(1-\nu)^2}{1-2\nu}$. This term will not change much the nature of the inertia effect. If we would not neglect the influence of this term, we can define a new parameter τ_2' as follows:

$$\tau_2'(\tau_2, \nu) = \frac{1-\nu}{\sqrt{1-2\nu}}\tau_2 = \frac{k}{\rho C_p r}\sqrt{\frac{\rho(1-\nu^2)}{E}} \tag{7-1}$$

Table 2.6-1 [156] shows the τ_2' values and the materials parameters of some elements whose boiling point is higher than 500 Celsius. The crack length is set to be 1mm in the calculations. In the macro level, the initial effect can be neglected for most of materials. It is clear from Equation (7-1) that the value of τ_2' is inversely proportional to the crack length. Obviously τ_2' could become considerable in the case of micro-cracks, such as those lying at the interface of thin coatings. As in the example mentioned above, the micro-cracks of lengths smaller than 1μm existing in the TBCs [23] or the TiN coatings [57] can considerably be affected by the inertia effect.

Overall, the Biot number is a very important parameter for both macro- and micro-cracks. The non-Fourier effect and inertia effect would play a non-negligible role when the crack length is small. As in numerous engineering problems, the initiation and growth of the micro-cracks are predominant mechanism in the failure

process; these unconventional effects are no longer negligible and should be included in the fracture analysis.

Element	k(W/m·K)	ρ(Kg/m^3)	C_P(J/Kg·K)	E(GPa)	ν	$\tau_2'(10^{-5})$
Au	320	19300	129.1	78	0.44	5.736844
Ag	430	10490	235	85	0.37	5.692905
Ca	200	1550	631	20	0.31	5.412277
Tl	46	11850	129	8	0.45	3.270614
Cu	400	8960	384.4	130	0.34	2.867314
Yb	39	6570	154	24	0.21	1.971795
Cd	96	8650	230	50	0.3	1.914569
Pb	35	11340	127	16	0.44	1.83727
Al	235	2700	904	70	0.35	1.7713
Mg	160	1738	1020	45	0.29	1.697511
Sn	67	7310	217	50	0.36	1.506714
Th	54	11724	118	79	0.27	1.44785
W	170	19250	132	411	0.28	1.389984
Zn	120	7140	388	108	0.25	1.078386
Rh	150	12450	240	275	0.26	1.031407

Table 7.2-2 Element properties and its corresponding τ_2'

7.3 Future Works

The behavior of the Biot number, the non-Fourier effect and the inertia effect are investigated in this work. The results will help to better understand the thermal shock failure of materials. Actually, the failure mechanisms of engineering materials, such as those in the TBCs, are multiple and complex, due to different interrelated time- and cycle-dependent phenomena. The present work represents just our first effort in enlightening the secrets in this topic. Further studies are necessary to progress in this

this direction. Further works are necessary to provide more satisfactory answers for engineering applications.

We believe that several research works can be performed on the basis of the methodology established in this thesis:

(1) Modelling of layered structures and functional graded materials

The present work deals with an inner crack in a homogeneous material. However, the most frequent failure mechanism in this class of problems is the interface debonding of the layered structures, especially the delamination of thin coatings, because of the weakness of the interface and the mismatch of the materials properties. Even though the solutions given in the present work provides useful indications for the interface delamination, it cannot replace a properly defined interface fracture analysis. We believe that the mathematical tool developed in this work can directly be extended to resolve the interface fracture problems.

The functionally graded materials (FGM) are also widely used in engineering applications because of its high performances. Thus the model shown in Figure 2.1-1 can be replaced by a FGM structure.

These analyses will not increase too much the difficulty of the mathematical formulation and numerical calculating tasks.

(2) Introduction of the crack surface constraint

In the present work, the displacement constraint at the crack surfaces is not taken into account. As a consequence, the mode-I stress intensity factor and COD(v) may appears to be negative. This result is not physically reasonable. In future works, this point should be considered even though additional mathematical difficulties could appear in the analytical solution of the problem. From this point of view, the pure numerical methods such like the finite element method should be more advantageous, as the contact problem can properly be dealt with by using the FEM.

(3) Solution in very small time scales

In experiments related to a laser thermal shock or to a quenching, the duration of the effective action is extremely short. The time scale of these thermal shock processes is about 10^{-3} second or less. In this time scale, the accuracy of the numerical results obtained in the present work is debatable.

In fact, according to the article [119], the numerical inverse Laplace transform developed by Miller is accurate when the dimensionless time is of the order of 1. Therefore, most of the results obtained by using this method are quite accurate except when the dimensionless time is close to 0. Therefore, new numerical methods of the inverse Laplace transform should be tried to investigate the temperature field and SIFs of the early stage immediately after the thermal shock.

It is clear that the experimental measures of the physical parameters and their influences on the fracture of the structures under thermal shock are also indispensable to understand the failure mechanisms and to validate the developed theory. As our principal preoccupation remains essentially in the theoretical and numerical domain, the experimental topic will not be developed here.

References

[1]. S. Manson, R. Smith. Theory of thermal shock resistance of brittle materials based on Weibull's statistical theory of strength. Journal Of The American Ceramic Society, 1955(38): 18-27

[2]. D. Hasselman. Elastic energy at fracture and surface energy as design criteria for thermal shock. Journal Of The American Ceramic Society, 1963(46): 535-540

[3]. D. P. H. Hasselman. Unified Theory of Thermal Shock Fracture Initiation and Crack Propagation in Brittle Ceramics. Journal Of The American Ceramic Society, 1969(52): 600-604

[4]. Hasselma.Dp. Thermal Stress Resistance Parameters For Brittle Refractory Ceramics: A Compendium. American Ceramic Society Bulletin, 1970(49): 1033-1034

[5]. T. Gupta. Strength Degradation and Crack Propagation in Thermally Shocked Al2O3. Journal Of The American Ceramic Society, 1972(55): 249-253

[6]. J. Gupta. Resistance to crack propagation in ceramics subjected to thermal shock. Journal Of Materials Science, 1973(8): 1283-1286

[7]. J. P. Singh, Y. Tree, D. P. H. Hasselman. Effect of Bath and Specimen Temperature on the Thermal-Stress Resistance of Brittle Ceramics Subjected to Thermal Quenching. Journal Of Materials Science, 1981(16): 2109-2118

[8]. W. P. Rogers, A. F. Emery, R. C. Bradt, A. S. Kobayashi. Statistical study of thermal fracture of ceramic materials in the water quench test. Journal Of The American Ceramic Society, 1987(70): 406-412

[9]. H. A. Bahr, H. J. Weiss, H. Maschke, F. Meissner. Multiple crack propagation in a strip caused by thermal shock. Theoretical and Applied Fracture Mechanics, 1988(10): 219-226

[10]. H. A. Bahr, H. J. Weiss, H. G. Maschke, F. Meissner. Multiple Crack-Propagation in a Strip Caused by Thermal-Shock. Theoretical and Applied Fracture Mechanics, 1988(10): 219-226

[11]. M. Saâdaoui, G. Fantozzi. Crack growth resistance under thermal shock loading of alumina. Materials Science and Engineering A, 1998(247): 142-151

[12]. R. Mindlin, D. Cheng. Thermoelastic Stress in the Semi-Infinite Solid. Journal Of Applied Physics, 2009(21): 931-933

[13]. S. Meng, G. Liu, S. Sun. Prediction of crack depth during quenching test for an ultra high temperature ceramic. Materials & Design, 2010(31): 556-559

[14]. N. M. Rendtorff, L. B. Garrido, E. F. Aglietti. Thermal shock resistance and fatigue of Zircon-Mullite composite materials. Ceramics International, 2011(37): 1427-1434

[15]. D. Mendelsohn, J. Achenbach, L. Keer. Scattering of elastic waves by a surface-breaking crack. Wave Motion, 1980(2): 277-292

[16]. H. F. Nied. Thermal shock fracture in an edge-cracked plate. Journal of Thermal stresses, 1983(6): 217-229

[17]. H. Nied. Thermal shock in an edge-cracked plate subjected to uniform surface heating. Engineering Fracture Mechanics, 1987(26): 239-246

[18]. J. Li, F. Song, C. Jiang. Direct numerical simulations on crack formation in ceramic materials under thermal shock by using a non-local fracture model. Journal Of The European Ceramic Society, 2013(33): 2677-2687

[19]. C. Jiang, X. Wu, J. Li, F. Song, Y. Shao, X. Xu, P. Yan. A study of the mechanism of formation and numerical simulations of crack patterns in ceramics subjected to thermal shock. Acta Materialia, 2012(60): 4540-4550

[20]. J. Li, F. Song, C. Jiang. A non-local approach to crack process modeling in ceramic materials subjected to thermal shock. Engineering Fracture Mechanics, 2015(133): 85-98

[21]. Y. Liu, X. Wu, Q. Guo, C. Jiang, F. Song, J. Li. Experiments and numerical simulations of thermal shock crack patterns in thin circular ceramic specimens. Ceramics International, 2015(41): 1107-1114

[22]. F. Song, S. Meng, X. Xu, Y. Shao. Enhanced Thermal Shock Resistance of Ceramics through Biomimetically Inspired Nanofins. Physical Review Letters, 2010(104)

[23]. N. P. Padture, M. Gell, E. H. Jordan. Thermal barrier coatings for gas-turbine engine applications. Science, 2002(296): 280-284

[24]. A. G. Evans, D. Mumm, J. Hutchinson, G. Meier, F. Pettit. Mechanisms controlling the durability of thermal barrier coatings. Progress In Materials Science, 2001(46): 505-553

[25]. A. Rabiei, A. Evans. Failure mechanisms associated with the thermally grown oxide in plasma-sprayed thermal barrier coatings. Acta Materialia, 2000(48): 3963-3976

[26]. J. Y. Kwon, S. I. Jung, S. Y. Lee, P. H. Lee, J. H. Lee, Y. G. Jung, U. Paik, H. Cho, J. C. Chang. Interfacial stability and contact damage resistance by incorporating buffer layer in thermal barrier coatings. Progress In Organic Coatings, 2010(67): 95-101

[27]. S. Krämer, S. Faulhaber, M. Chambers, D. Clarke, C. Levi, J. Hutchinson, A. Evans. Mechanisms of cracking and delamination within thick thermal barrier systems in aero-engines subject to calcium-magnesium-alumino-silicate (CMAS) penetration. Materials Science and Engineering: A, 2008(490): 26-35

[28]. A. Feuerstein, J. Knapp, T. Taylor, A. Ashary, A. Bolcavage, N. Hitchman. Technical and economical aspects of current thermal barrier coating systems for gas turbine engines by thermal spray and EBPVD: A review. Journal Of Thermal Spray Technology, 2008(17): 199-213

[29]. A. Evans, J. Hutchinson. The mechanics of coating delamination in thermal gradients. Surface and Coatings Technology, 2007(201): 7905-7916

[30]. D. Balint, T. Xu, J. Hutchinson, A. Evans. Influence of bond coat thickness on the cyclic rumpling of thermally grown oxides. Acta Materialia, 2006(54): 1815-1820

[31]. T. Wakui, J. Malzbender, R. W. Steinbrech. Strain analysis of plasma sprayed thermal barrier coatings under mechanical stress. Journal Of Thermal Spray Technology, 2004(13): 390-395

[32]. J. Malzbender, R. Steinbrech. Mechanical properties of coated materials and multi-layered composites determined using bending methods. Surface and Coatings Technology, 2004(176): 165-172

[33]. Y. Liu, C. Persson, J. Wigren. Experimental and numerical life prediction of thermally cycled thermal barrier coatings. Journal Of Thermal Spray Technology, 2004(13): 415-424

[34]. S. Chi. Cracking in coating–substrate composites with multi-layered and FGM coatings. Engineering Fracture Mechanics, 2003(70): 1227-1243

[35]. H. Chen, X. Zhou, C. Ding. Investigation of the thermomechanical properties of a plasma-sprayed nanostructured zirconia coating. Journal Of The European Ceramic Society, 2003(23): 1449-1455

[36]. Y. C. Zhou, T. Hashida. Thermal fatigue in thermal barrier coating. Jsme International Journal Series a-Solid Mechanics and Material Engineering, 2002(45): 57-64

[37]. A. Karlsson, A. Evans. A numerical model for the cyclic instability of thermally grown oxides in thermal barrier systems. Acta Materialia, 2001(49): 1793-1804

[38]. E. Busso, J. Lin, S. Sakurai. A mechanistic study of oxidation-induced degradation in a plasma-sprayed thermal barrier coating system.:: Part II: Life prediction model. Acta Materialia, 2001(49): 1529-1536

[39]. A. Evans, J. Hutchinson, M. He. Micromechanics model for the detachment of residually compressed brittle films and coatings. Acta Materialia, 1999(47): 1513-1522

[40]. W. Beele, G. Marijnissen, A. van Lieshout. The evolution of thermal barrier coatings - status and upcoming solutions for today's key issues. Surface & Coatings Technology, 1999(120): 61-67

[41]. Y. Tsui, T. Clyne. An analytical model for predicting residual stresses in progressively deposited coatings Part 3: Further development and applications. Thin Solid Films, 1997(306): 52-61

[42]. Y. Tsui, T. Clyne. An analytical model for predicting residual stresses in progressively deposited coatings Part 2: Cylindrical geometry. Thin Solid Films, 1997(306): 34-51

[43]. Y. Tsui, T. Clyne. An analytical model for predicting residual stresses in progressively deposited coatings Part 1: Planar geometry. Thin Solid Films, 1997(306): 23-33

[44]. A. G. Evans, M. Y. He, J. W. Hutchinson. Effect of interface undulations on the thermal fatigue of thin films and scales on metal substrates. Acta Materialia, 1997(45): 3543-3554

[45]. D. Zhu, R. A. Miller, paper presented at the Fundamental Aspects of High Temperature Corrosion 1996.

[46]. S. Ahmaniemi, J. Tuominen, M. Vippola, P. Vuoristo, T. Mantyla, F. Cernuschi,

C. Gualco, A. Bonadei, R. Di Maggio. Characterization of modified thick thermal barrier coatings. Journal Of Thermal Spray Technology, 2004(13): 361-369

[47]. U. Schulz, B. Saruhan, K. Fritscher, C. Leyens. Review on advanced EB-PVD ceramic topcoats for TBC applications. International Journal of Applied Ceramic Technology, 2004(1): 302-315

[48]. A. G. Evans, N. A. Fleck, S. Faulhaber, N. Vermaak, M. Maloney, R. Darolia. Scaling laws governing the erosion and impact resistance of thermal barrier coatings. Wear, 2006(260): 886-894

[49]. W. Mao, Y. Zhou, L. Yang, X. Yu. Modeling of residual stresses variation with thermal cycling in thermal barrier coatings. Mechanics Of Materials, 2006(38): 1118-1127

[50]. R. S. Lima, B. R. Marple. Thermal spray coatings engineered from nanostructured ceramic agglomerated powders for structural, thermal barrier and biomedical applications: A review. Journal Of Thermal Spray Technology, 2007(16): 40-63

[51]. R. G. Wellman, J. R. Nicholls. A review of the erosion of thermal barrier coatings. Journal Of Physics D-applied Physics, 2007(40): R293-R305

[52]. W. D. Kingery. Factors affecting thermal stress resistance of ceramic materials. J. Am. Ceram. Soc, 1955(38): 3-15

[53]. M. He, J. Hutchinson, A. Evans. Simulation of stresses and delamination in a plasma-sprayed thermal barrier system upon thermal cycling. Materials Science and Engineering: A, 2003(345): 172-178

[54]. M. He, A. Evans, J. Hutchinson. The ratcheting of compressed thermally grown thin films on ductile substrates. Acta Materialia, 2000(48): 2593-2601

[55]. M. He, J. Hutchinson, A. Evans. Large deformation simulations of cyclic displacement instabilities in thermal barrier systems. Acta Materialia, 2002(50): 1063-1073

[56]. Y. F. Shao, X. H. Xu, S. H. Meng, G. H. Bai, C. P. Jiang, F. Song. Crack Patterns in Ceramic Plates after Quenching. Journal Of The American Ceramic Society, 2010(93): 3006-3008

[57]. Y. Choi, S. Jeon, M.-s. Jeon, H.-G. Shin, H. H. Chun, Y.-s. Lee, H. Lee. Crack propagation behavior of TiN coatings by laser thermal shock experiments. Applied Surface Science, 2012(258): 8752-8757

[58]. I. Sevostianov, M. Kachanov. Anisotropic thermal conductivities of plasma-sprayed thermal barrier coatings in relation to the microstructure. Journal Of Thermal Spray Technology, 2000(9): 478-482

[59]. D. W. Hahn, M. N. Ozisik. Heat Conduction. 3. 2012

[60]. Z. T. Chen, K. Q. Hu. Thermo-Elastic Analysis of a Cracked Half-Plane Under a Thermal Shock Impact Using the Hyperbolic Heat Conduction Theory. Journal of Thermal stresses, 2012(35): 342-362

[61]. H. S. Carslaw, J. C. Jaeger. Conduction of heat in solids Clarendon Press, 1959

[62]. J. P. Holman. Heat Transfer. 6. McGraw-Hill, 1986

[63]. A. Luikov. Application of irreversible thermodynamics methods to investigation of heat and mass transfer. International Journal Of Heat and Mass Transfer, 1966(9): 139-152

[64]. K. J. Baumeister, T. D. Hamill. Hyperbolic Heat-Conduction Equation-A Solution for the Semi-Infinite Body Problem. Journal Of Heat Transfer, 1969(91): 543-548

[65]. B. A. Boley, paper presented at the High temperature structures and materials, Columbia University, New York 2013.

[66]. Y. Taitel. On the parabolic, hyperbolic and discrete formulation of the heat conduction equation. International Journal Of Heat and Mass Transfer, 1972(15): 369-371

[67]. D. D. Joseph, L. Preziosi. Heat waves. Reviews Of Modern Physics, 1989(61): 41

[68]. L. Hector, W.-S. Kim, M. Özisik. Hyperbolic heat conduction due to a mode locked laser pulse train. International Journal Of Engineering Science, 1992(30): 1731-1744

[69]. M. Babaei, Z. Chen. Hyperbolic heat conduction in a functionally graded hollow sphere. International Journal Of Thermophysics, 2008(29): 1457-1469

[70]. A. Graßmann, F. Peters. Experimental investigation of heat conduction in wet sand. Heat and Mass Transfer, 1999(35): 289-294

[71]. H. Herwig, K. Beckert. Experimental evidence about the controversy concerning Fourier or non-Fourier heat conduction in materials with a nonhomogeneous inner structure. Heat and Mass Transfer, 2000(36): 387-392

[72]. W. Roetzel, N. Putra, S. K. Das. Experiment and analysis for non-Fourier conduction in materials with non-homogeneous inner structure. International Journal Of Thermal Sciences, 2003(42): 541-552

[73]. M. Maurer, H. Thompson. Non-Fourier effects at high heat flux. Journal Of Heat Transfer, 1973(95): 284-286

[74]. N. Ozisik. Finite difference methods in heat transfer CRC press, 1994

[75]. V. Peshkov. The Second sound in Helium II. Journal of Physics-USSR, 1944(166

[76]. P. Vernotte. Les paradoxes de la théorie continue de léquation de la chaleur. Comptes Rendus Hebdomadaires Des Seances De L Academie Des Sciences, 1958(246): 3154-3155

[77]. C. Cattaneo. Sulla conduzione del calore, 1948

[78]. M. Chester. Second sound in solids. Physical Review, 1963(131): 2013-2015

[79]. C. Körner, H. Bergmann. The physical defects of the hyperbolic heat conduction equation. Applied Physics A, 1998(67): 397-401

[80]. A. H. Ali. Statistical mechanical derivation of Cattaneo's heat flux law. Journal Of Thermophysics and Heat Transfer, 1999(13): 544-545

[81]. M. Özişik. Propagation and reflection of thermal waves in a finite medium. International Journal Of Heat and Mass Transfer, 1984(27): 1845-1854

[82]. E. Zanchini, B. Pulvirenti. Periodic heat conduction with relaxation time in cylindrical geometry. Heat and Mass Transfer, 1998(33): 319-326

[83]. J.-Y. Lin, H.-T. Chen. Numerical solution of hyperbolic heat conduction in cylindrical and spherical systems. Applied Mathematical Modelling, 1994(18): 384-390

[84]. M. H. Babaei, Z. Chen. Transient hyperbolic heat conduction in a functionally graded hollow cylinder. Journal Of Thermophysics and Heat Transfer, 2010(24): 325-330

[85]. Y. M. Ali, L. C. Zhang. Relativistic heat conduction. International Journal Of Heat and Mass Transfer, 2005(48): 2397-2406

[86]. K. Hu, Z. Chen. Thermoelastic analysis of a partially insulated crack in a strip under thermal impact loading using the hyperbolic heat conduction theory. International Journal Of Engineering Science, 2012(51): 144-160

[87]. B. A. Boley, J. H. Weiner. Theory of thermal stresses Courier Corporation, 2012

[88]. H. Kogawa, M. Futakawa, S. Isikura, K. Kikuchi, R. Hino, M. Eto. Inertia effect on thermal shock by laser beam shot. International Journal of Impact Engineering, 2001(25): 17-28

[89]. J. M. Duhamel. Second memoire sur les phenomenes thermo-mecaniques. Journal de l'École polytechnique, 1837(15): 1-57

[90]. V. I. Danilovskaya. thermal stress in an elastic half space arising after a sudden heating of its boundary. Prikladnaya Matematika i Mechanika, 1950(14)

[91]. V. I. Danilovskaya. On a Dynamical Problem of Thermoelasticity. Prikladnaya Matematika i Mechanika, 1952(16): 341

[92]. B. A. Boleyt. Thermally induced vibrations of beams. Journal of the Aero/Space Sciences, 1956(23): 179-181

[93]. B. Boley, A. Barber. Dynamic response of beams and plates to rapid heating. Journal Of Applied Mechanics, 1957(24): 413-425

[94]. R. B. Hetnarski. Coupled One-Dimensional Thermal Shock Problem for Small Times. Archiwum Mechaniki Stosowanej, 1961(13): 295-306

[95]. R. Muki, S. Breuer. Coupling Effects in a Transient Thermoelastic Problem. Archiwum Mechaniki Stosowanej, 1962(16): 349-368

[96]. G. Nariboli, V. Nyayadhish. One-dimensional thermo-elastic wave. The Quarterly Journal of Mechanics and Applied Mathematics, 1963(16): 473-482

[97]. R. B. Hetnarski, J. Ignaczak. Generalized thermoelasticity: response of semi-space to a short laser pulse. Journal of Thermal stresses, 1994(17): 377-396

[98]. A. Green, K. Lindsay. Thermoelasticity. Journal Of Elasticity, 1972(2): 1-7

[99]. M. Williams. The stresses around a fault or crack in dissimilar media. Bulletin Of The Seismological Society Of America, 1959(49): 199-204

[100]. G. C. Sih. On the singular character of thermal stresses near a crack tip. Journal Of Applied Mechanics, 1962(29): 587-589

[101]. G. D. Gupta. An Integral Equation Approach to the Semi-Infinite Strip Problem. Journal Of Applied Mechanics, 1973(40): 948-954

[102]. P. Theocaris, N. Ioakimidis. Numerical integration methods for the solution of singular integral equations(for crack tip stress intensity factor evaluation in elastic media). Quarterly Of Applied Mathematics, 1977(35): 173-183

[103]. Z.-H. Jin, N. Noda. An internal crack parallel to the boundary of a nonhomogeneous half plane under thermal loading. International Journal Of Engineering Science, 1993(31): 793-806

[104]. Y. Chen, F. Erdogan. The interface crack problem for a nonhomogeneous coating bonded to a homogeneous substrate. Journal Of The Mechanics and Physics Of Solids, 1996(44): 771-787

[105]. F. Erdogan, B. Wu. Crack problems in FGM layers under thermal stresses. Journal of thermal stresses, 1996(19): 237-265

[106]. S. Itou. Thermal stresses around a crack in the nonhomogeneous interfacial layer between two dissimilar elastic half-planes. International Journal Of Solids and Structures, 2004(41): 923-945

[107]. Y. Zhou, X. Li, J. Qin. Transient thermal stress analysis of orthotropic functionally graded materials with a crack. Journal of Thermal Stresses, 2007(30): 1211-1231

[108]. S. Dag, F. Erdogan. A surface crack in a graded medium under general loading conditions. Journal Of Applied Mechanics, 2002(69): 580-588

[109]. R. Bagheri, M. Ayatollahi. Multiple moving cracks in a functionally graded strip. Applied Mathematical Modelling, 2012(36): 4677-4686

[110]. N. Naotake, M. Yasuhiro, N. Hiroshi. Coupled thermoplastic problem of an infinite solid containing a penny-shaped crack. International Journal Of Engineering Science, 1990(28): 347-353

[111]. B. Boley, J. Weiner. Theory of thermal stresses Dover Pubns, 1997

[112]. B. A. Boley, I. S. Tolins. Transient Coupled Thermoelastic Boundary Value Problems in the Half-Space. Journal Of Applied Mechanics, 1962(29): 637-646

[113]. L. A. Aghalovyan, R. S. Gevorgyan. Asymptotic solutions of coupled dynamic problems of thermoelasticity for thin bodies of anisotropic inhomogeneous-in-plan materials. Journal of Applied Mathematics and Mechanics, 2011(75): 601-611

[114]. C. Cattaneo. A form of heat conduction equation which eliminates the paradox of instantaneous propagation. Compte Rendus, 1958(247): 431-433

[115]. P. Vernotee. Les Paradoxes De La Theorie Continue De L'equation De La Chaleur. Comptes Rendus Hebdomadaires Des Seances De L Academie Des Sciences, 1958(246): 3154-3155

[116]. D. Glass, M. Özişik, D. McRae, B. Vick. Hyperbolic heat conduction with temperature - dependent thermal conductivity. Journal Of Applied Physics, 1986(59): 1861-1865

[117]. W. Kaminski. Hyperbolic heat conduction equation for materials with a nonhomogeneous inner structure. Journal Of Heat Transfer, 1990(112): 555-560

[118]. I. Keles, C. Conker. Transient hyperbolic heat conduction in thick-walled

FGM cylinders and spheres with exponentially-varying properties. European Journal of Mechanics-A/Solids, 2011(30): 449-455

[119]. M. K. Miller, J. Guy, WT. Numerical inversion of the Laplace transform by use of Jacobi polynomials. Siam Journal On Numerical Analysis, 1966(3): 624-635

[120]. Z. Chen. Interfacial coplanar cracks in piezoelectric bi-material systems under pure mechanical impact loading. International Journal Of Solids and Structures, 2006(43): 5085-5099

[121]. K. Q. Hu, Z. T. Chen. Thermoelastic analysis of a partially insulated crack in a strip under thermal impact loading using the hyperbolic heat conduction theory. International Journal of Engineering Science, 2012(51): 144-160

[122]. M. N. Ozisik. Heat conduction. 3. Canada:John Wiley & Sons, 2012

[123]. A. Jeffrey, D. Zwillinger. Table of integrals, series, and products Academic Press, 2007

[124]. H. Ferdjani, R. Abdelmoula, J.-J. Marigo, S. El Borgi. Study of size effects in the Dugdale model through the case of a crack in a semi-infinite plane under anti-plane shear loading. Continuum Mechanics and Thermodynamics, 2009(21): 41-55

[125]. R. Anguelov, S. Markov, in Numerical Methods and Applications. (Springer, 2007) pp. 279-286.

[126]. E. Brown, F. Erdogan. Thermal stresses in bonded materials containing cuts on the interface. International Journal Of Engineering Science, 1968(6): 517-529

[127]. N. I. Muskhelishvili, J. R. M. Radok. Singular integral equations: boundary problems of function theory and their application to mathematical physics. 2. Courier Corporation, 2008

[128]. J. Plemelj. Ein ergänzungssatz zur cauchyschen integraldarstellung analytischer funktionen, randwerte betreffend. Monatshefte Fur Mathematik, 1908(19): 205-210

[129]. A. H. Stroud, D. Secrest. Gaussian quadrature formulas Prentice-Hall Englewood Cliffs, NJ, 1966

[130]. M. Abramowitz, I. A. Stegun. Handbook of mathematical functions. Applied Mathematics Series, 1966(55): 62

[131]. F. Erdogan, G. D. Gupta, T. Cook, in Methods of analysis and solutions of crack problems. (Springer, 1973) pp. 368-425.

[132]. F. Erdogan, G. D. GUPTA. On the numerical solution of singular integral equations(Singular integral equations numerical solution from Gauss-Chebyshev formulas for mixed boundary value problems). Quarterly Of Applied Mathematics, 1972(29): 525-534

[133]. H. Dubner, J. Abate. Numerical inversion of Laplace transforms by relating them to the finite Fourier cosine transform. Journal of the ACM (JACM), 1968(15): 115-123

[134]. H. Stehfest. Algorithm 368: Numerical inversion of Laplace transforms [D5]. Communications Of The Acm, 1970(13): 47-49

[135]. H. Stehfest. Remark on algorithm 368: numerical inversion of Laplace transforms. Communications Of The Acm, 1970(13): 624

[136]. F. Durbin. Numerical inversion of Laplace transforms: an efficient improvement to Dubner and Abate's method. The Computer Journal, 1974(17): 371-376

[137]. J. McWhirter, E. R. Pike. On the numerical inversion of the Laplace transform and similar Fredholm integral equations of the first kind. Journal of Physics A: Mathematical and General, 1978(11): 1729-1745

[138]. B. Davies, B. Martin. Numerical inversion of the laplace transform: a survey and comparison of methods. Journal Of Computational Physics, 1979(33): 1-32

[139]. G. Honig, U. Hirdes. A method for the numerical inversion of Laplace transforms. Journal Of Computational and Applied Mathematics, 1984(10): 113-132

[140]. J. Abate, W. Whitt. The Fourier-series method for inverting transforms of probability distributions. Queueing Systems, 1992(10): 5-87

[141]. R. G. Airapetyan, A. G. Ramm. Numerical Inversion of the Laplace Transform from the Real Axis. Journal Of Mathematical Analysis and Applications, 2000(248): 572-587

[142]. H. Hassanzadeh, M. Pooladi-Darvish. Comparison of different numerical Laplace inversion methods for engineering applications. Applied Mathematics and Computation, 2007(189): 1966-1981

[143]. I. N. Bronshtein, K. A. Semendyayev, G.Musiol, H.Muehlig. Handbook of Mathematics. 5. New York:Springer, 2007

[144]. M. A. Shubin. Partial Differential Equations IV: Microlocal Analysis and Hyperbolic Equations Springer, 1993

[145]. S. Alinhac. Hyperbolic partial differential equations Springer Science & Business Media, 2009

[146]. F. Delale, F. Erdogan. Effect of transverse shear and material orthotropy in a cracked spherical cap. International Journal Of Solids and Structures, 1979(15): 907-926

[147]. F. Erdogan, G. D. Gupta, amp, T. Cook, in Methods of analysis and solutions of crack problems. (Springer, 1973) pp. 368-425.

[148]. F. Erdogan, G. Sih. On the crack extension in plates under plane loading and transverse shear. Journal of Fluids Engineering, 1963(85): 519-525

[149]. W. Li, J. Li, R. Abdelmoula, F. Song, C. P. Jiang. Inertia effect analysis of a half - plane with an induced crack under thermal loading using hyperbolic heat conduction. ZAMM - Journal of Applied Mathematics and Mechanics, 2015(DOI: 10.1002/zamm.201500133)

[150]. M. Barzelay, K. Tong, G. Holloway, “Effects of pressure on thermal conductance of contact joints” (Note 3295, 1955).

[151]. E. Fried. Interface thermal contact resistance problem in space vehicles. ARS Journal, 1962(32): 237-243

[152]. H. Atkins, E. Fried. Interface thermal conductance in a vacuum. Journal Of Spacecraft and Rockets, 1965(2): 591-593

[153]. E. Fried. Thermal conduction contribution to heat transfer at contacts. Thermal conductivity, 1969(2): 253-274

[154]. B. Snaith, P. O'Callaghan, S. Probert. Interstitial materials for controlling thermal conductances across pressed metallic contacts. Applied Energy, 1984(16): 175-191

[155]. P. J. Antaki. New interpretation of non-Fourier heat conduction in processed meat. Transactions of the ASME-C-Journal of Heat Transfer, 2005(127): 189-193

[156]. http://www.wolframalpha.com/.